
Thermodynamic stability and solid solution hardening effects of CrMnFeCoNi based high entropy alloys



TECHNISCHE
UNIVERSITÄT
DARMSTADT

**Department of Materials and Earth Science
Technical University of Darmstadt**

Dissertation approved in fulfilment of the requirements
for the degree of Doctor of Engineering / Doktor Ingenieur

(Dr.-Ing.)

M.Sc. Tom Christopher Keil

1st Referee:

Prof. Dr. Karsten Durst

2nd Referee:

Prof. Dr. Gerhard Wilde

Darmstadt 2022

Thermodynamic stability and solid solution hardening effects of CrMnFeCoNi based high entropy alloys

Thermodynamische Stabilität und Mischkristallhärtungseffekte von CrMnFeCoNi basierten Hochentropielegierungen

Zur Erlangung des akademischen Grades Doktor-Ingenieur (Dr.-Ing.)
Genehmigte kumulative Dissertation von M.Sc. Tom Christopher Keil

1. Gutachter: Prof. Dr. Karsten Durst

2. Gutachter: Prof. Dr. Gerhard Wilde

Tag der Einreichung: 03.06.2022

Tag der Prüfung: 27.07.2022

Fachbereich Material- und Geowissenschaften
Technische Universität Darmstadt
Alarich-Weiss-Straße 2
64287 Darmstadt

Declaration of authorship

I herewith formally declare that I, Tom Christopher Keil, have written the submitted thesis independently pursuant to § 22 paragraph 7 of APB TU Darmstadt. I did not use any outside support except for the quoted literature and other sources mentioned in the thesis. I clearly marked and separately listed all of the literature and all of the other sources which I employed when producing this academic work, either literally or in content. This thesis has not been handed in or published before in the same or similar form.

In the submitted thesis the written copies and the electronic version for archiving are pursuant to § 23 paragraph 7 of APB identical in content.

Darmstadt, 03.06.2022

Tom Christopher Keil

Table of contents

Declaration of authorship	III
Table of contents	V
Acknowledgements	VII
List of publications	VIII
List of abbreviations and symbols	IX
1. Motivation	1
2. Fundamentals	3
2.1. Concept of high entropy alloys	3
2.2. Thermodynamics and diffusion of high entropy alloys	4
2.2.1. Entropic stabilisation	4
2.2.2. Phase stability models	5
2.2.3. Thermal stability	8
2.2.4. Diffusion	9
2.3. Structure and defects in high entropy alloys	10
2.3.1. Lattice structure and short-range order	10
2.3.2. Dislocations	12
2.3.3. Structure evolution during severe plastic deformation	13
2.3.4. Grain boundary structure	15
2.4. Deformation behaviour and hardening	16
2.4.1. Solid solution hardening and related models	17
2.4.2. Hall-Petch hardening	21
2.4.3. Mechanical properties of nanocrystalline HEAs	22
3. Objective of the work	25
4. List of selected publications	27
5. Synopsis of publications	31
5.1. Thermodynamic stability and solid solution hardening in single-phase HEAs	32



5.1.1.	Compositional parameter space	33
5.1.2.	Solid solution hardening effects	38
5.2.	Microstructural stability and mechanical properties after high pressure torsion	45
5.2.1.	Steady-state microstructure after high pressure torsion	46
5.2.2.	Thermal stability and related properties	50
6.	Summary	61
7.	References	65
8.	Cumulative part of the thesis	77
8.1.	Statement of personal contribution – Credit (Contributor Roles Taxonomy)	77
8.2.	Selected reprints	81

Acknowledgements

First of all, I thank my supervisor **Prof. Dr. Karsten Durst** for giving me the opportunity to do my PhD research in his group. I appreciate his constant support and great scientific guidance.

I would like to express my gratitude to the second referee of this thesis, **Prof. Dr. Gerhard Wilde** for fruitful collaborations, helpful discussions and feedback. Moreover, I thank all further members of the examination committee **Prof. Dr. Karsten Albe** and **Prof. Dr. Christian Kübel**.

I want to thank my project partners **Dr. Daniel Utt**, **Dr. Alexander Stukowski**, **Prof. Dr. Karsten Albe**, **Shabnam Taheriniya**, **Josua Kottke**, **Prof. Dr. Gerhard Wilde** and **Dr. Mathilde Laurent-Brocq** for the exciting and valuable collaborations within the last years.

I would like to express my thanks to all members of the group **Physikalische Metallkunde** for the wonderful time. Especially, I thank **Dr. Enrico Bruder**, who introduced me to the world of high entropy alloys, for the excellent support and the helpful discussions. I am very grateful to “**die Jungs**” – **Christian Minnert**, **Sebastian Bruns** and **Paul Braun** for fruitful discussions, the enjoyable time during and after work and the great adventures

I wish to express my deepest thanks to my **family** and my **friends** for continuous encouragement. Thank you for all the support and patience. Especially I would like to thank **Ina** for the great support and the assistance with Photoshop.

I gratefully acknowledge the financial support by the Deutsche Forschungsgemeinschaft (DFG) within the framework “**SPP2006 Compositionally Complex Alloys – High Entropy Alloys**” under Grant No. DU424-13/1 – 52300548.

List of publications

1. **Keil T.**, Bruder E., Durst K., *Exploring the compositional parameter space of high-entropy alloys using a diffusion couple approach*. *Materials & Design*, 176 (2019) 107816. DOI: 10.1016/j.matdes.2019.107816.
2. **Keil T.**, Utt D., Bruder E., Stukowski A., Albe K., Durst K., *Solid solution hardening in CrMnFeCoNi-based high entropy alloy systems studied by a combinatorial approach*. *Journal of Materials Research*, 36 (2021) 2558. DOI: doi.org/10.1557/s43578-021-00205-6.
3. **Keil T.**, Bruder E., Laurent-Brocq M., Durst K., *From diluted solid solutions to high entropy alloys: Saturation grain size and mechanical properties after high pressure torsion*. *Scripta Materialia*, 192 (2021) 43. DOI: 10.1016/j.scriptamat.2020.09.046.
4. **Keil T.**, Taheriniya S., Bruder E., Wilde G., Durst K., *Effects of solutes on thermal stability, microstructure and mechanical properties in CrMnFeCoNi based alloys after high pressure torsion*. *Acta Materialia*, 227 (2022) 117689. DOI: 10.1016/j.actamat.2022.117689.
5. Auernhammer J., **Keil T.**, Lin B., Schäfer JL., Xu BX., Biesalski M., Stark R.W., *Mapping Humidity-dependent mechanical properties of a single cellulose fibre*, *Cellulose*, 28 (2021) 8313.
6. Auernhammer J., Langhans M., Schäfer JL., **Keil T.**, Meckel T., Biesalski M., Stark R. W., *Nanomechanical subsurface characterisation of cellulosic fibres*. *SN Applied Sciences* 4, 160 (2022). DOI: 10.1007/s42452-022-05017-9.
7. **Keil T.**, Minnert C., Bruder E., Durst K., *Solid solution hardening effects on structure evolution and mechanical properties of nanostructured binary and high entropy alloys after high pressure torsion*. Submitted to IOP Conference Series: Microstructural variability: Processing, analysis, mechanisms and properties (42nd Risø International Symposium), 2022.

List of abbreviations and symbols

$\dot{\epsilon}_0$	Reference strain rate
$\dot{\epsilon}$	Strain rate
σ_0	Friction stress
APT	Atom Probe Tomography
b	Burgers vector
bcc	Body centered cubic
BSE	Backscattered Electrons
C	Constraint factor
CCA	Complex Concentrated Alloy
c_n	Mole fraction of the n-th element
d	Grain size
d_0	Initial grain size
E	Young's modulus
EBS	Electron Backscatter Diffraction
EDX	Energy Dispersive X-ray Spectroscopy
EELS	Electron Energy Loss Spectroscopy
fcc	Face centered cubic
G_{mix}	Gibbs free energy of mixing
H	Hardness
HAADF	High-angle Annular Dark-field
hcp	Hexagonal close-packed
HEA	High Entropy Alloy
H_{mix}	Enthalpy of mixing
HPT	High Pressure Torsion
ISE	Indentation Size Effect
k_b	Boltzmann constant
k_y	Hall-Petch constant
m	Strain rate sensitivity exponent
MEA	Medium Entropy Alloy
MPEA	Multi-principal Element Alloys
n	Grain growth exponent
nc	Nanocrystalline
Q	Activation energy

R	Gas Constant
SFE	Stacking Fault Energy
S_{mix}	Entropy of mixing
SPD	Severe Plastic Deformation
SRO	Short-range order
SRS	Strain Rate Sensitivity
SSH	Solid solution hardening
STEM	Scanning Transmission Electron Microscopy
T	Temperature
TEM	Transmission Electron Microscopy
UFG	Ultrafine-grained
V^*	Activation volume
VEC	Valence Electron Concentration
XRD	X-ray diffraction
α	Line tension parameter
δ	Atomic size mismatch
ΔE_b	Energy barrier
ΔV_n	Atomic size misfit volume of element n
ϵ_r	Representative strain
μ	Shear modulus
ν	Poisson's ratio
σ_r	Representative strength
σ_y	Yield stress
τ_y	Flow stress
τ_{y0}	Zero temperature flow stress

1. Motivation

The development of novel and superior materials has been pursued by humans for thousands of years. Since the Bronze age, alloying is used to alter the properties of metals [1, 2]. The general strategy was based on the addition of small amounts of alloying elements to a principal matrix element. This conventional alloy development strategy limits the total number of possible compositions, but has led to tremendous knowledge about alloys with only one principle element [2-5]. Metals are mostly used as alloys to adjust a variety of characteristics such as mechanical, chemical or physical properties [6]. For example in steel, which consist primarily of iron, a large number of different alloying elements such as carbon or chromium were used to achieve widely varying and outstanding properties (strength, corrosion resistance etc.) [2]. In addition to binary or diluted alloys, chemically complex compositions are used to achieve specific properties like high strength at high temperatures. Prominent examples are Ni-based and Co-based superalloys, where up to 15 different alloying elements are added to the primary element [7, 8].

Triggered by Yeh et al. [3] and Cantor et al. [4] in 2004, a new alloying concept emerged. A multitude of principle elements are combined to form a novel type of alloy called high entropy alloy (HEA). Due to the vast compositional range and enormous number of possible compositions, properties like the mechanical behaviour at low [9, 10], ambient [5, 11-14] or elevated temperatures [15, 16], fracture toughness [14, 17], corrosion [18-20] and oxidation resistance [21, 22] can be specifically tailored to exceed those of conventional alloys. However, the new compositional space also emphasizes one of the challenges, namely, *“to investigate the unexplored central region of multicomponent alloy phase space”* – B. Cantor et al. (2004) [4].

The concept of HEAs opens up a vast composition space and leads to an incredibly large number of potential alloys [23, 24]. In the past decade, just approx. 80 alloy systems have been investigated experimentally to identify HEAs with novel property combinations [13, 23]. Many equiatomic compositions with a different number of elements were studied, but compositions far away from equimolarity received only little attention [25]. The transition from dilute solid solutions to HEAs has been covered in a few studies, but aspects like the thermodynamic stability, segregation formation, the evolution of lattice parameter or solid solution hardening effects are not yet fully understood [25-30].

In this context, the DFG priority programme “SPP2006 Compositionally Complex Alloys – High Entropy Alloys” offers a broad, coordinated platform in Germany to develop alloys with outstanding mechanical properties. The present thesis was carried out in this framework and

focuses on the thermodynamic stability and solid solution hardening effects in chemical gradients. The following questions will be addressed in this work:

- I. Is there a continuous transition in behaviour by changing the composition towards the central region of multicomponent alloy systems or is it characterized by discontinuities?
- II. Do the specific properties emerge from a cocktail of multicomponent alloying with unexpected, synergistic response, coupled in a non-linear manner?
- III. Are there relevant parameters to differentiate HEAs from conventional alloys? Up to which compositions are the classical solid solution hardening models still applicable and when does the picture of solvent and solute atoms break down?
- IV. How do solutes, if differentiable at all, contribute to the defect storage as well as the microstructural stability? What are the kinetics and thermodynamics of segregation and phase decomposition and what is the role of grain boundaries?

To shed light on these questions, the phase stability including thermal stability and solid solution hardening is investigated in CrMnFeCoNi based high entropy alloys. The phase stability regarding effective solubility limits of individual elements and solid solution hardening is investigated using diffusion couples. Ni-enriched derivatives of the Cantor alloy in form of $(\text{CrMnFeCo})_x\text{Ni}_{1-x}$ show single-phase face-centered cubic (fcc) structures throughout the full concentration range and are therefore well suited to study the transition from high entropy-type alloys to dilute solid solutions. The discrete sample compositions in combination with high pressure torsion (HPT) deformation and subsequent annealing experiments allow to elucidate the effects of solutes on the saturation grain size, the thermal stability and on the mechanical properties.

2. Fundamentals

2.1. Concept of high entropy alloys

A novel class of alloys – high entropy alloys (HEAs) – have attracted extensive research interest in the last decade, especially in the last five years [2]. An early definition by Yeh et al. [3] describes HEAs as alloys “composed of five or more principal elements”, each with concentrations between 5 and 35 atomic percent (at.%). Yeh et al. [3, 31] hypothesized that the tendency to form solid solutions is increased by an increased configurational entropy and thus by the presence of multiple elements. This principal idea of entropy maximization led to a further definition of HEAs based on the configurational entropy, given by the Boltzmann equation. Yeh et al. [31] claims a minimum configurational entropy of 1.5 times the gas constant R ($8.31 \text{ J}/(\text{K}\cdot\text{mol})$) for HEAs. A common interpretation is a single-phase solid solution criterion, which differs from the primary definitions. This emphasizes the motivation to produce single-phase solid solutions, even it is not required by definition [24]. As described in recent reviews from George et al. [2] or Miracle and Senkov [24], the configurational entropy is not the main factor responsible for the crystal structure and properties of HEAs. Although the term HEA is currently under debate and alternative names such as complex concentrated alloys (CCAs) or multi-principal element alloys (MPEAs) have been suggested, it is the most common term in literature and is suspected to endure [2, 24].

Most of the HEA research and discourse in the academic community was significantly influenced by publications from the group of J.W. Yeh [5, 31-33] and shaped the research in the last years [29]. Based on their work, Yeh and co-workers proposed four core effects present in HEAs [5, 31, 32], which are briefly summarized below and are discussed later in the chapter. The formulation of these core effects played a decisive role in initiating an enormous interest in this research field, yet, the influence of these HEA core effects appears to be not significant [24, 29].

- I. The *high entropy effect* proposes that the high configurational entropy promote the formation of solid solutions against intermetallic compounds.
- II. The *lattice distortion effect* originates from the high number of atom species, which make up the crystal and show different size.
- III. The *sluggish diffusion effect* states that diffusion kinetics in HEAs are intrinsically slower than those in conventional alloys due to locally varying bonding conditions.
- IV. The *cocktail effect* is not a hypothesis regarding physical properties, but describes that the alloy properties may emerge from a “cocktail” of multicomponent alloying with unexpected, synergistic response in a possibly non-linear manner.

2.2. Thermodynamics and diffusion of high entropy alloys

2.2.1. Entropic stabilisation

The high configurational entropy is one of the characteristic concepts of HEAs as defined by Yeh et al. [3]. It states that the increased configurational entropy in equimolar or near-equimolar alloys composed of a minimum of five elements is sufficiently high to stabilize solid solutions against the formation of intermetallic compounds [24]. The formation of phases in an alloy is controlled by the Gibbs free energy of mixing ΔG_{mix} , which can be expressed as shown in Eq. 1:

$$\Delta G_{mix} = \Delta H_{mix} - T\Delta S_{mix} \quad (1)$$

where ΔH_{mix} is the enthalpy of mixing, T the temperature and ΔS_{mix} the entropy of mixing [32, 34]. Other contributions to the entropy of mixing such as vibrational entropy, magnetic entropy or electronic entropy are often omitted. Therefore, the entropy of mixing of HEAs can be expressed by:

$$\Delta S_{mix} = -R \sum_i c_n \ln(c_n) \quad (2)$$

where R is the gas constant and c_n the mole fraction of the n-th element [24]. Similar to Eq. 1, the formation of intermetallic compounds can be described using Eq. 3:

$$\Delta G_f = \Delta H_f - T\Delta S_f \quad (3)$$

with ΔG_f , ΔH_f and ΔS_f as the corresponding values for the formation of intermetallic phases [2]. The phase, or the combination of several phases, with the lowest Gibbs free energy will be present at thermodynamic equilibrium. The situation becomes more complex by adding more constituents, as the number of possible phases increases according to Gibbs phase rule [2]. Yeh et al. [3] considered an ideal solution with random distribution of the atoms ($\Delta H_{mix} = 0$, Eq. 1) and a perfectly ordered intermetallic phase with $\Delta S_f = 0$ (Eq. 3). They concluded that the increased configurational entropy of mixing (ΔS_{mix}) in alloys with multi-principal elements stabilizes random solid solutions at the expense of intermetallic compounds. It is tempting to compare the entropy of mixing from Eq. 2 with the formation enthalpies of intermetallic compounds. For example, the configurational entropy of an equimolar five-component alloy is given with 1.61 times R, which is equal to 13.4 J/(mol*K). This value gives an idea for an upper limit of the entropic contribution. At e.g. 2000 K, the entropic contribution ($-T\Delta S_{mix}$) to the Gibbs free energy of mixing can be calculated to 26.7 kJ/mol. A comparison of these results with an evaluation of the formation enthalpies of more than 1000 intermetallic compounds

from Miracle et al. [24] shows that the entropic contribution is in the range of the formation enthalpy of intermetallics, where the median is reported to be -36 kJ/mol.

The entropic stabilization is fundamental to the design strategy of HEAs, however, recent reports revealed that the high configurational entropy does not have such an overachieving influence on the phase stability [29, 35-38]. Otto et al. [38] showed the limited influence of configurational entropy on the phase stability by substituting elements of the CrMnFeCoNi system with elements of comparable size, electronegativity and same crystal structure. They replaced one element at a time with a similar element according to the above mentioned parameters of the same concentration to keep the configurational entropy unchanged, e.g. Cu for Ni, Ti for Co, Mo for Cr or V for Fe. The chosen procedure maximised the chance of solubility according to the Hume-Rothery rules [39-41]. Decades ago, Hume-Rothery and co-workers contributed fundamentally to the understanding and prediction of the phase stability of solid solutions and compounds [39-41]. From this work, three general rules have been formulated that relate to the limits of solid solutions or the stability of certain intermediate phases. The Hume-Rothery rules can be briefly summarized as follows [39]:

- I. The atomic size mismatch of the elements forming an alloy should be lower than 14 - 15 %.
- II. The electronegativity difference (chemical affinity) of the constituents should be small.
- III. The valence electron number should not be very different.

However, despite following the Hume-Rothery rules, Otto et al. [38] reported that every case of substitution resulted in an alloy that was not stable as a single-phase solid solution. Consequently, the entropic contribution may not be the main factor responsible for the formed crystal structure. Hence, the configurational entropy cannot be used as a useful *a priori* predictor for thermodynamically stable single-phase HEAs. Even HEAs which are initially single-phase after solidification tend to decompose at temperatures below approx. 700 °C (see chapter 2.2.3) [2, 29, 38].

2.2.2. Phase stability models

According to the Hume-Rothery rules, numerous studies tried to relate the phase stability of HEAs to parameters such as atomic size mismatch, valence electron concentration, electronegativity or mixing enthalpy [5, 31, 34, 42-44]. In these studies, phase stability maps are constructed by empirical approaches. From these maps, threshold values for the respective

parameters can be estimated.

Following Zhang et al. [34, 44], two factors affect the formation of solid solutions, the atomic size mismatch and the chemical compatibility, i.e., the enthalpy of mixing. In this respect, the expected crystal structure can be shown as a function of the enthalpy of mixing and atomic size mismatch (Fig. 1). The atomic size mismatch parameter δ can be determined using Eq. 4:

$$\delta = \sqrt{\sum_{n=1}^N c_n (1 - r_n/\bar{r})^2} \quad (4)$$

with c_n the concentration of the n-th element in at.%, N the total number of elements, r_n the atomic radius and \bar{r} the average atomic radius with $\bar{r} = \sum_{n=1}^N c_n r_n$ [44].

Based on this, a quantitative criterion for the formation of random solid solutions (Fig. 1 blue zone) can be formulated. For the enthalpy of mixing being in the range from -15 to 5 kJ/mol and the atomic size mismatch δ being in the range up to 6 %, random solid solutions are expected [29, 34].

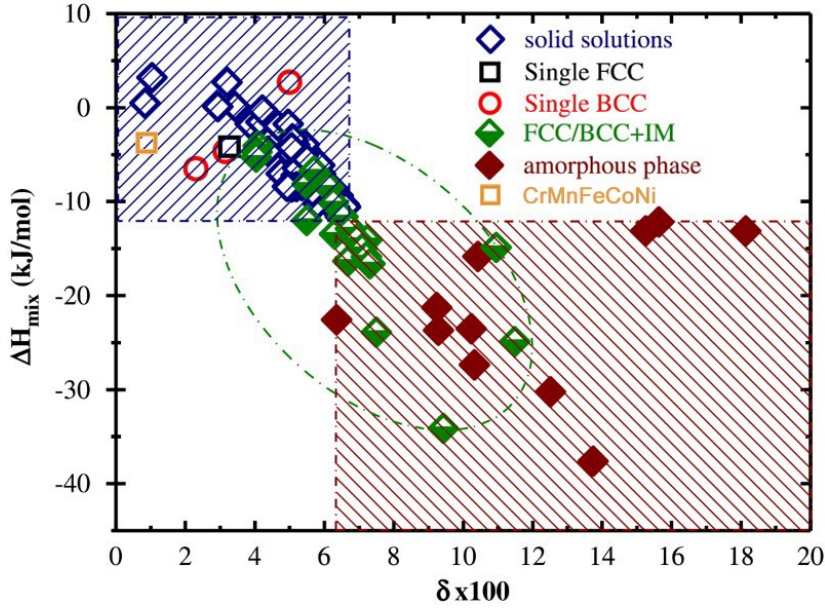


Fig. 1: Experimentally found phase formation map based on the relationship between the enthalpy of mixing ΔH_{mix} and atomic size mismatch δ for multi-component HEAs that form single-phase solid solutions (blue), that contain intermetallic phases (green) and that are amorphous (red) [45]. The CrMnFeCoNi Cantor is included in orange [46]. Adapted and reprinted with permission from Wang et al. [45], Copyright (2014), The Minerals, Metals & Materials Society, Springer Nature.

The effect of the equivalency of the alloying elements in the electron concentration is articulated in the Hume-Rothery rules (see chapter 2.2.1). Hence, it seems natural that another parametric approach for predicting the formation of solid solutions is the use of the valence electron concentration (VEC). In this context, Guo et al. [43] designed alloy series of $\text{Al}_x\text{CoCrCuFe}$,

$\text{Al}_x\text{CrCuFeNi}_2$ and $\text{Al}_x\text{CoCrCu}_{0.5}\text{FeNi}$ alloys, showing a correlation between VEC and the formed solid solution. Furthermore, numerous HEA systems taken from literature confirm the correlation between VEC and the formed solid solution (Fig. 2). Based on this empirical study, two threshold values can be defined for the formation of body-centered cubic (bcc) alloys ($\text{VEC} \leq 6.87$) or face-centered cubic (fcc) alloys ($\text{VEC} \geq 8.0$) [43]. Even though an empirical correlation could be shown, this does not necessarily imply causation. It is worth noting that several concerns arise when utilizing the VEC rules [42]. The proposed threshold values were defined using experimental results from cast alloys [42]. The applicability to other production routes has not been evaluated [42]. No distinction was made between disordered and ordered solid solutions and the formation of bcc or fcc does not imply the formation of a single phase [42]. For example, Otto et al. [38] has shown that the substitution of Ni with Cu results in the formation of a two-phase microstructure (both fcc), even if the Hume-Rothery rules are not violated. The VEC threshold values seems not to be consistent amongst different material systems or processing conditions and can vary within and between systems [47]. The determination of the microstructural state has been performed in many studies using X-ray diffraction (XRD) alone, although XRD is not able to detect small volume fractions of secondary phases [2]. Furthermore, a vast majority of the investigated HEAs have been found to be initially single-phase after solidification, but show decomposition tendencies during heat treatments [2, 29].

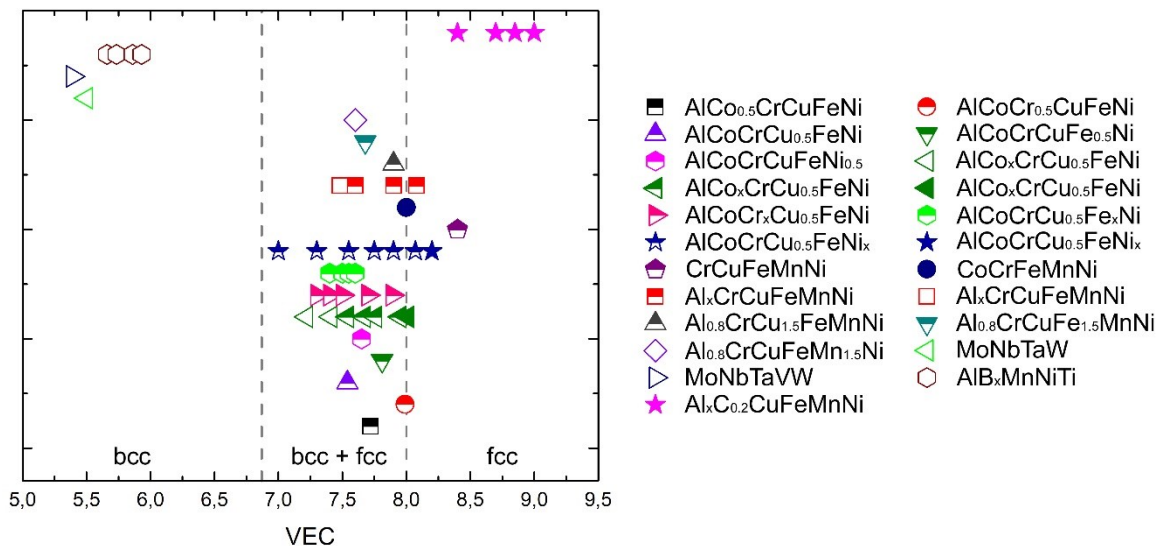


Fig. 2: Relationship between VEC and formed crystal structure. Fully open symbols represent sole bcc phases, fully closed symbols sole fcc phases half-closed symbols mixtures of bcc and fcc phases. Two threshold values separate into single-phase and two-phase regions. Data taken from Ref. [43].

2.2.3. Thermal stability

Even though a vast number of HEAs has been produced with a single-phase structure, which is often interpreted as a requirement for HEAs [24], it is still unclear which one is single-phase in the thermodynamic equilibrium or only being metastable [29, 48-50]. At present, the number of HEA systems showing a stable single solid solution at temperatures up to the melting point is very limited [29]. Contrary to initial assumptions, most HEAs are not thermodynamically stable, but kinetically stabilized in a metastable state [50].

The prominent CrMnFeCoNi Cantor alloy [4] is one of many examples, which was widely considered to be a HEA forming a single solid solution. However, recent reports reveal that temperature treatments below 700 °C cause the formation of various precipitates, depending on the microstructure and annealing time [30, 49-52]. For a coarse-grained material, annealing for 500 days at 500 °C results in the formation of NiMn, FeCo and Cr-rich phases, while at 700 °C a Cr-rich phase is observed [50]. Pickering et al. [50] annealed the coarse-grained Cantor alloy at 700 °C for times between 125 to 1000 h and showed that the Cr-rich σ -phase formed after 500 h of annealing. In addition, the volume fraction of the Cr-rich σ -phase increases with increasing annealing time. Schuh et al. [51] performed high pressure torsion (HPT) experiments on the Cantor alloy to produce a nanocrystalline (nc) microstructure with grain sizes in the range of 50 nm. After deformation, the alloy is single-phase down to atomic scale. However, the high defect density due to the increased dislocation and grain boundary density facilitates rapid diffusion and offers many nucleation sites in the system. As a consequence, precipitation formation occurs at annealing times as short as 5 minutes at temperatures of only 450 °C. After 5 minutes, NiMn and Cr-rich nano-scale phases were observed at grain boundaries and triple junctions. After longer annealing for 15 h, their volume fractions increased and a third FeCo phase was detected (Fig. 3).

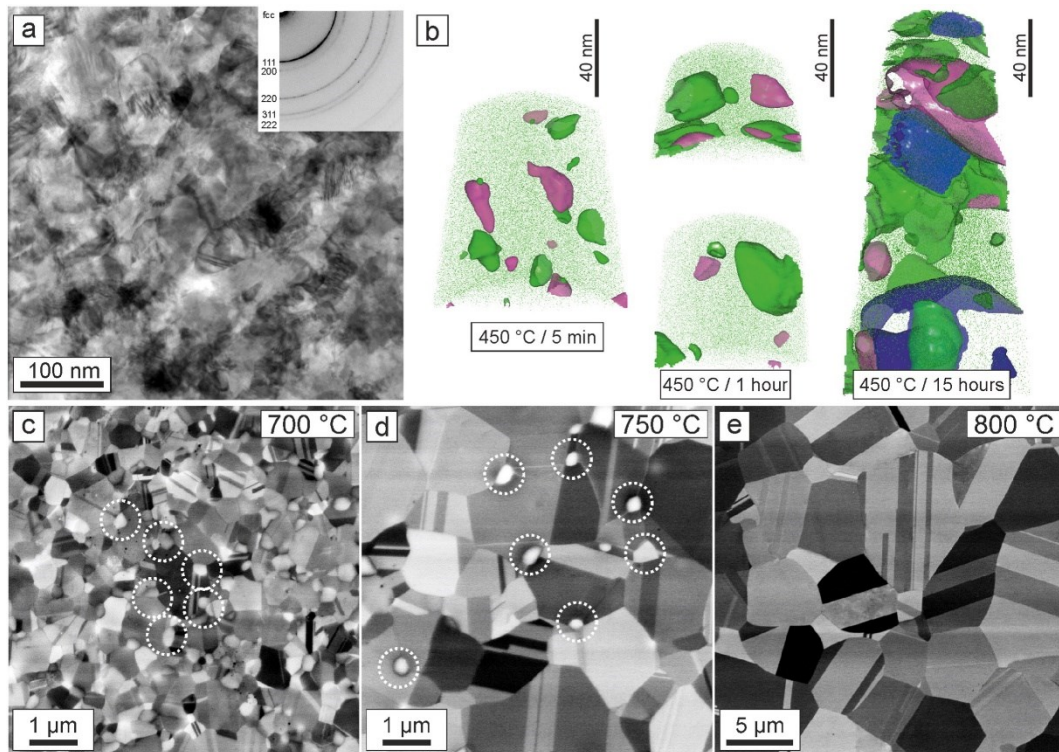


Fig. 3: Advanced microscopy results of the Cantor alloy after HPT deformation and subsequent annealing, a) transmission electron microscopy (TEM) image of the saturated nc state after deformation, b) atom probe tomography (APT) reconstructions of HPT deformed samples after different annealing conditions and c) – e) backscattered electron (BSE) images of the HPT samples after 1 h annealing at different temperatures (circles indicate the formation of intermetallic phases in c) and d). Reprinted with permission from Maier-Kiener et al. [53], Copyright (2017), Materials & Design, Elsevier.

Similar results are reported for the HEAs $\text{Al}_{0.5}\text{CoCrCuFeNi}$ [33, 37], AlCoFeMnNi [54], HfNbTaTiZr [55, 56] or HfNbTiVZr [57] as well as for ternary or quaternary alloys [58-61]. Knowledge of the decomposition tendencies in combination with an almost unlimited number of chemical compositions opens the possibility of proper controlling the microstructure and thus the mechanical properties by precipitation formation [24, 62-64]. Similar to conventional alloys, the type, volume fraction, shape and distribution of the precipitates is crucial for the resulting properties [62], which can be adjusted by composition and thermal treatment.

2.2.4. Diffusion

The concept of sluggish diffusion was proposed as one of the four core effects of HEAs by Yeh in 2006 [32] and has gained attention as it is of significant importance for possible high temperature applications [65]. As mentioned above, sluggish diffusion describes the intrinsically slower diffusion kinetics in HEAs due to locally varying bonding conditions.

First interdiffusion experiments using CrMnFeCoNi based alloys in a quasi-binary diffusion couple support this concept [66]. The observed reduction in diffusion kinetics is correlated to strong variations in the lattice potential energy and thus vacancy formation and migration enthalpies. Tsai et al. [66] concluded that the potential energy landscape in HEAs causes trapping of diffusing elements at energetically favourable positions. However, recent publications [65, 67, 68] critically addressed the analysis from Tsai et al. [66] and questioned the correctness of the interpretation and evaluation of the data.

In general, diffusion kinetics are studied using two different diffusion techniques, interdiffusion and tracer diffusion experiments [65, 67]. The two review articles from Dabrowa and Danielewski [65] and Divinski et al. [67] reveal a controversial discussion and different conclusions on sluggish diffusion.

In fact, the sluggish diffusion effect is only vaguely defined and was apparently suggested to comprise the effect of the simple increase in the number of constituents or configurational entropy [26, 69]. A straightforward correlation between decreasing diffusivity and increasing number of components is not evident, instead, the type of the added elements plays a decisive role with respect to the observed diffusivity [69-71]. Durant et al. [70] report a significant decrease in diffusivity by adding a third element to binary systems. However, diffusivity does not appear to decrease further when more elements are added. Moreover, Jin et al. [71] shows a faster diffusion in the quinary CrFeCoNiPd and CrFeCoNiMn systems than in the quaternary CrFeCoNi and even the ternary CrCoNi system at absolute temperatures. At homologous temperatures, Vaidya et al. [69] observed decelerated diffusion rates in HEAs when compared to alloys with a reduced number of containing elements. Using an absolute temperature scale, the tendency of decreasing diffusivities with higher number of principal elements cannot be confirmed [69].

2.3. Structure and defects in high entropy alloys

2.3.1. Lattice structure and short-range order

Due to the high entropy effect, no host matrix or dominant atom species is present in HEAs and each atom is surrounded by different kinds of species with different atomic sizes [42]. This causes a displacement from the mean lattice position, which results in an elastic distortion of the lattice (Fig. 4). The individual displacement at each lattice site and thus the elastic distortion depends on the chemical environment and are claimed to be more pronounced in HEAs than in dilute solid solutions [24]. These distortions affect several material properties like mechanical strength or hardness [32, 72-74], electrical and thermal conductivity [32, 75, 76] and the

thermodynamic stability [77].

The severe lattice distortion is one of the four proposed core effects of HEAs, however, the level of distortion in the benchmark CrMnFeCoNi HEA was shown to be not disproportionately larger than in other highly alloyed systems like Ni-33Cr or Ni-37.5Co-25Cr [78]. A combination of simulation and experiment revealed a rather small mean distortion in the Cantor system ($< 1\%$) [79]. For refractory bcc HEAs, Song et al. [80] found much more significant distortions compared to fcc 3d-transition metal HEAs. A study using density functional theory predicted localised strains in a bcc VNbMoTaW HEA of no more than $\pm 5\%$ of the lattice parameter, which is in the range of concentrated binary alloys. [29, 81]. While early studies [31, 33, 42, 82] predicted a severely distorted lattice for HEAs, more recent experiments and simulations [29, 78-81] do not measure significantly higher values compared to binary alloys. Likewise, the presence of elastic strain in the crystal lattice will lead to an increase in Gibb's free energy, which would counteract entropic stabilisation of the solid solution phases and makes the coexistence of thermodynamic stability and a severe lattice distortion effect questionable [29]. Consequently, this topic requires further investigation, which will provide significant contribution to the general understanding of HEAs [29].

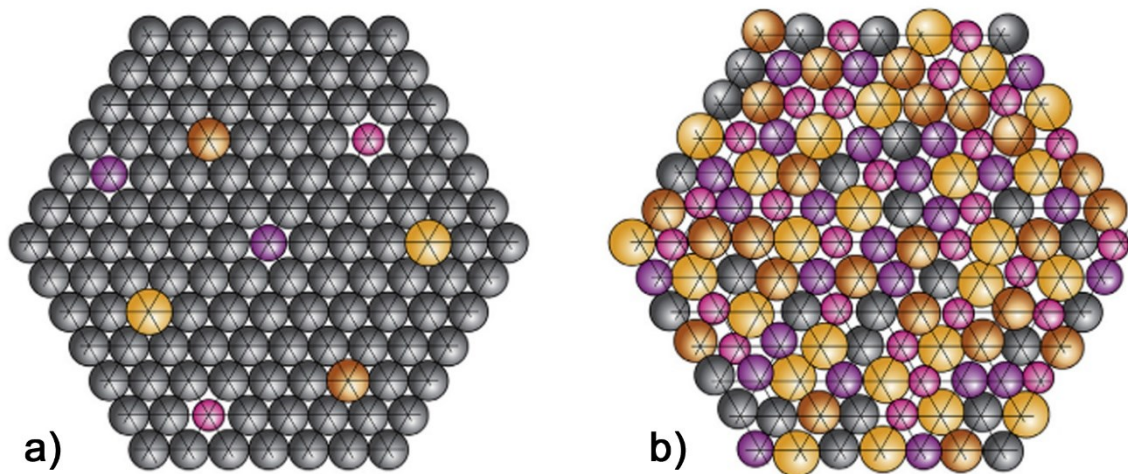


Fig. 4: Effect of atom size on the lattice position in a) a dilute solid solution with solutes surrounded by solvent atoms and b) a high entropy alloy with no dominant atom species [24]. Reprinted with permission from Miracle et al. [24], Copyright (2017), Acta Materialia, Elsevier.

While the severe lattice distortion effect is not evident in the Cantor system [79], it is still under debate if there is chemical short-range order (SRO) present in HEA's or not [51, 79, 83-97]. Several computer simulation studies reported chemical SRO in medium entropy alloys (MEAs) or high entropy alloys. Ding et al. [83] used density functional theory-based monte carlo simulations to predict chemical SRO in CrCoNi alloys in the vicinity of Cr atoms. Antillon et al. [84] found strong chemical ordering in a CoFeNiTi alloy between Fe and Ti. In this case, the

degree of chemical SRO changes with annealing in the way that it increases with decreasing annealing temperature. Tamm et al. [85] used monte carlo simulations combined with density functional theory calculations, revealing chemical SRO in the CrCoNi and CrFeCoNi systems. Besides the mentioned simulation results, Zhang et al. [86] experimentally studied chemical SRO in the CrCoNi system with the extended x-ray absorption fine structure technique. The results indicate ordering tendencies with preferential Cr – Ni and Cr – Co pairs. Concerning these results, Yin et al. [87] criticize that the interpretation of the data also relies on density-functional theory. Using TEM, Zhang et al. [88] observed diffusive superlattice peaks in the diffraction pattern of a CrCoNi alloy after annealing at 1000 °C (120 h) followed by slow furnace cooling. The authors have assigned these structural features to the presence of SRO [88]. However, there is also a large body of counter evidence present in literature. Most of the work is based on atom probe tomography (APT) investigations on medium- and high entropy alloys [51, 79, 93-97]. The APT studies revealed a randomly distributed solid solution down to the atomic scale. In 2020, Lee et al. [97] used electron diffraction, scanning transmission electron microscopy – energy dispersive x-ray spectroscopy (STEM-EDX) and APT on the equiatomic Cantor alloy and observed no chemical heterogeneity or ordered structures of sizes within the spatial resolution limit, which is in the range of 1 nm.

2.3.2. Dislocations

It is known that plastic deformation in crystalline solids occurs via motion of dislocations on closely packed slip planes with the slip direction corresponding to the closely spaced crystallographic direction [98, 99]. In fcc metals, slip typically takes place on {111} planes in $\langle 110 \rangle$ directions with dislocations having a Burgers vector b of the type $\frac{1}{2}\langle 110 \rangle$ [98]. It can be energetically more favourable for perfect dislocations to split up into $\frac{1}{6}\langle 121 \rangle$ Shockley partials, which is associated with slip and creates a stacking fault in between the two partials [98]. The dissociation width of the partials depends on the shear modulus, Burgers vector and the stacking fault energy (SFE) [98]. The resistance to dislocation sliding is caused by the periodicity of the crystal lattice and is called Peierls potential [98, 99]. To move a dislocation, this potential barrier needs to be overcome by the application of a critical stress (Peierls stress or Peierls - Nabarro stress) [98, 99].

Against this backdrop, the fundamental process for plastic deformation in HEAs is found to be similar to the one in conventional alloys, with dislocation glide on normal fcc slip systems and dissociation into Shockley partials [10, 13, 100]. One difference between HEAs and single element systems can be found in the dislocation line arrangement. In general, a dislocation

tends to minimize its energy [98, 101]. This is achieved in pure metals by being as short as possible (straight dislocation line) [98, 101]. In HEAs, however, when a dislocation glides over a certain distance, the dislocation is attracted by regions of favourable solute fluctuations and repelled by unfavourable ones [102, 103]. The dislocation can thus reduce its total energy by adopting a wavy configuration, even if it costs energy to create a longer dislocation line [102, 103]. Furthermore, large fluctuations in the SFE were observed in HEAs, depending on the local chemical composition [83, 104]. These fluctuations in SFE lead to local variations in the separation distance of Shockley partials, which further facilitates a wavy dislocation configuration [92, 104, 105]. In general, fcc HEAs show relatively low SFE values in the range of 30 mJ/m² and smaller [106-109]. Even though, these values are not particularly low compared to other binary fcc metals, the dissociation width can be relatively large because of its relatively large shear modulus [100]. In materials showing a low SFE or a large dissociation width between the partials, dislocation cross-slip or climb is hampered [108, 109]. As a consequence, these materials are more likely to deform by twinning, with increased dislocation storage capability and strain hardening through deformation induced twinning (dynamic Hall-Petch) [108, 109]. In case of HEAs, early literature stated a high average Peierls barrier, which impedes dislocation glide [13]. The strength of HEAs is, however, not based on a high average Peierls barrier but rather on the increased resistance against dislocations movement due the local chemical disorder, i.e., solid solution hardening (see chapter 2.4.1) [13, 110].

2.3.3. Structure evolution during severe plastic deformation

The production of ultrafine-grained (UFG) or nanocrystalline (nc) materials by means of severe plastic deformation (SPD) processes (top-down approach) has been subjected of intensive research for few decades due to the enhanced material properties [111, 112]. Among others, definitions of the microstructures are given by Valiev et al. [113] and Kumar et al. [114]. Accordingly, UFG materials show grain sizes in the range of 100 – 1000 nm and nc materials are defined as those with an average grain size smaller than 100 nm [113, 114].

In general, SPD processing is described as a process using high hydrostatic pressure to introduce very high strains into a bulk solid without significant change in the overall dimensions of the material [112]. Due to the retention of the shape of the sample, a high strain can be applied to the material, which is essential for introducing a very high dislocation density of at least 10¹⁴ m⁻² and thus achieving exceptional grain refinement well below 1 μm without fracture [112, 115]. The plastic strain introduced during the SPD process causes dislocation storage in the material. The dislocations introduced into the material by plastic deformation are not only

randomly distributed, but accumulated in dislocation cell walls or sub-grain boundaries [111, 116-119]. As the strain increases, the misorientation angle increases due to the storage of further dislocations followed by a decrease in boundary spacing. At very large strains, the average misorientation of neighboring elements increases and can reach values of $> 15^\circ$, which corresponds to a misorientation angle of high angle grain boundaries [111, 116-119]. Furthermore, homogeneous microstructures throughout the sample can be attained by HPT using very high strains [120, 121]. It has been found that a typical texture evolves during the HPT process in fcc metals [122]. Most fcc metals like pure Ni show a weak simple-shear texture after HPT deformation [123, 124]. This typical shear texture is also observed for the Cantor alloy to a low extent after HPT deformation [125, 126].

For metals processed by HPT, the grain size saturates to a material specific steady-state level at very large strains. In this stage, additional straining does not result in a further refinement of the microstructure [127, 128]. The minimal achievable grain size or saturation grain size d_s , as well as the strain necessary to reach the steady-state mainly depends on the composition (type of element, purity, alloying elements) [127, 129, 130] and the deformation temperature (higher d_s with increasing temperature) [131-133]. In contrast, the initial microstructure itself does not affect the saturation grain size [111, 127]. A shear strain of approx. 50 is sufficient to obtain the steady-state grain size of the equiatomic Cantor alloy, which is in the range of 50 nm [51]. Reaching the saturation grain size can be described by a process of counterbalanced elimination of dislocations by recovery or dynamic recrystallization and the production of new dislocation during continuous deformation [127, 133, 134]. From this point of view, it seems reasonable to assume that a material parameter like the SFE, which controls the dislocation mobility and dislocation storage, also affect the minimal achievable grain size. The SFE strongly influences the grain refinement rate, however, a direct correlation between saturation grain size and SFE could not be reported for various pure elements with strongly varying SFE [111] as well as different alloys [127, 129, 130]. Edalati et al. [127] propose that alloying, which affects the mobility of edge dislocations due to an atomic size and modulus mismatch of solutes, will also control the steady-state or saturation grain size. The authors concluded from the fact that the interaction of solutes with screw dislocations is much weaker compared to the interaction of solutes with edge dislocations, that the stronger interacting edge dislocations control the recovery and hence the saturation grain size [127]. The found empirical correlation between solid solution hardening (SSH) and saturation grain size has been observed for a variety of binary solutions, where the Labusch model [72, 73] is used to calculate the SSH contribution of fcc alloys (see chapter 2.4.1). Fig. 5 shows the correlation between normalized saturation grain size and SSH contribution for various binaries. It can be seen that a higher SSH

contributions causes a smaller saturation grain size. In this context, Bruder et al. [130] studied a series of binary Cu alloys which, compared to each other, show either comparable SFE or comparable SSH contributions. The results confirm the empirical correlation proposed by Edalati et al. [127], namely that the saturation grain size only correlates with SSH and not with the SFE.

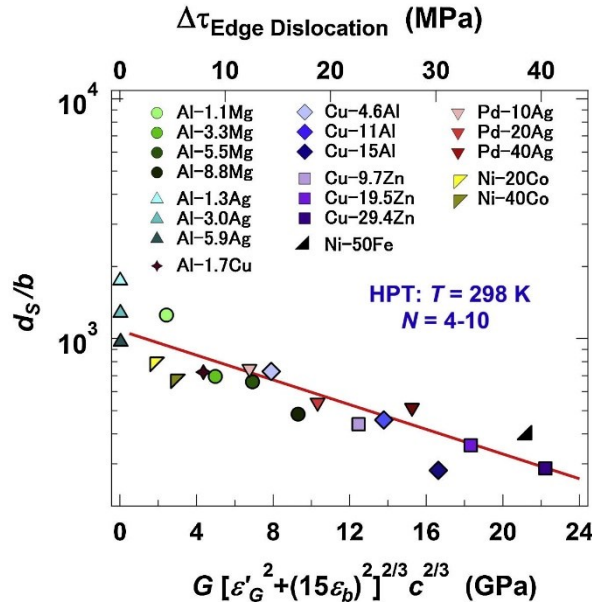


Fig. 5: Correlation between saturation grain size d_s normalized by the Burgers-vector b and the solid solution hardening contribution $\Delta\tau_{\text{Edge dislocation}}$ using Labusch's model, adapted from [127]. Reprinted with permission from Edalati et al. [127], Copyright (2014), Acta Materialia, Elsevier.

2.3.4. Grain boundary structure

For future alloy design, the grain boundary structure and the grain growth kinetics need to be understood. Since a stable microstructure and thus constant mechanical properties are essential for long-term use and structural applications, the microstructure is of significant importance [135]. In general, the driving force for grain growth or grain boundary motion is the reduction in excess energy either stored in the grain interior by dislocations (primary recrystallization) or in the grain boundary itself (secondary recrystallization or continuous grain growth) [39, 118]. During primary recrystallization, grain boundaries move across deformed regions with high dislocation densities, leaving behind significantly lower dislocation densities [39, 118]. A further driving force for grain boundary migration results from the energy stored in grain boundaries itself. A reduction of the stored energy can also be achieved by reducing the total grain boundary area [39, 118]. The initial microstructure has a decisive influence on the coarsening processes. Typically, no primary recrystallization is observed for nc or UFG materials processed by severe plastic deformation [118, 136-139]. Instead, strong recovery with

subsequent continuous recrystallization can be seen for severe plastic deformed metals [138-140].

The grain growth in fcc HEAs has been investigated intensively with reduced grain growth kinetics being frequently reported [52, 141-148]. Its origin is still a matter of debate and several explanations for the observed hindered grain growth kinetics emerged [52, 141-148]. Possible reasons that have been mentioned are an intrinsically reduced grain growth rate due to the distorted matrix [142]. Furthermore, the reduction in grain growth kinetics can be explained by sluggish diffusion and solute effects [141, 144, 148] or by the formation of secondary phases [145, 146]. Utt et al. [147] used atomistic computer simulations and a 4-component CuNiCoFe model system to address the question whether the microstructure is stabilized by solutes or if it is intrinsically more stable due to lattice distortions and local chemical fluctuations. They concluded that grain boundary migration is hindered by solute segregations to the grain boundaries and not by lattice distortions or local chemical fluctuations [147]. In this case, the specific grain boundary energy and thus the driving force for grain growth is lowered in the vicinity of solutes, resulting in a thermodynamic stabilization of the microstructure [118]. Li et al. [30] reported on the decisive role of high angle grain boundaries for segregation phenomena in the Cantor alloy, which trigger phase nucleation at grain boundaries. In this context, strong pinning due to secondary phases (Zener pinning [118]) has been observed in HEAs, stabilizing the microstructure in the nc or UFG regime [145, 146, 149, 150].

2.4. Deformation behaviour and hardening

The mechanical properties of alloys strongly depend on the composition, microstructure and processing conditions [13, 24]. Simultaneously, the HEA concept offers a vast compositional range and thus a huge number of (meta)stable compositions [13, 151]. Given the large number of possible alloy systems, a large amount of data regarding the mechanical properties of HEAs has been collected, which, however, cannot be directly compared with each other due to differences in element species and their concentrations, the way of thermomechanical processing and post-process heat treatment [13, 24]. Within a recent review article, George et al. [13] attempted to evaluate the mechanical property data of HEAs to address the questions of how special HEAs are with respect to their mechanical properties and whether they are potential candidates for structural applications. It has been shown that the fundamental processes for plastic deformation such as dislocation slip, twinning and grain boundary sliding present in conventional alloys are also seen in HEAs [13, 42]. As the fundamental deformation mechanisms appear to be similar to those of conventional alloys, the development of new HEAs

with promising mechanical properties can build on the prior metallurgical knowledge [13]. Not many HEAs have been found to possess superior properties compared to conventional alloys [13]. However, the current research effort in the field of HEAs remains valuable, as the compositional parameter space offers the possibility for new alloys in which multiple mechanisms work simultaneously or sequentially, which may lead to enhanced properties [13]. The Cr-Mn-Fe-Co-Ni alloy family and especially the equiatomic CrMnFeCoNi Cantor alloy are the most thoroughly investigated systems in literature, making the Cantor alloy the benchmark material and basis of the current knowledge of HEAs mechanical properties [13]. Wu et al. [12, 141] systematically investigated single-phase, equiatomic subsystems of the Cr-Mn-Fe-Co-Ni alloy family by macroscopic indentation and tensile testing. They revealed the individual effects of the different type of elements on the mechanical properties of the alloys. It has been shown that the tensile yield strength does not solely depend on the number of added elements, but rather on the nature of the elements, as the yield strength does not monotonically increase with the number of constituent [12]. In this context, the ternary CrCoNi alloy showed the highest strength, followed by two quaternary systems and then the five-component Cantor alloy [12]. These observations lead to the assumption that Cr is the most potent strengthening element in the present alloy family [12]. This behaviour was also observed by microhardness measurements on these alloys [141]. During the early stages of plasticity, the deformation mechanisms for CrCoNi are similar to the mechanisms observed in CrMnFeCoNi [152]. With increasing strain, nanotwinning occurs as an additional deformation mechanism in both systems [152]. The critical resolved shear stress for twinning is comparable for both alloys [152]. However, the twinning stress arises at lower strain values in the CrCoNi alloy, as the yield stress and the work hardening rate are higher compared to the Cantor alloy [152]. The higher yield stress can be explained by the solid solution hardening model proposed by Varvenne et al. [102, 103], where the mean shear modulus and the atomic size misfit volumes are taken into account. The increased work hardening rate for CrCoNi is related to the higher shear modulus of 87 GPa compared to 81 GPa of the Cantor alloy [152]. The activation of mechanical nanotwinning at lower strain results in a larger strain interval at which nanotwinning is activated, which in turn leads to enhanced mechanical properties (strength, ductility) [152].

2.4.1. Solid solution hardening and related models

High entropy alloys offer the opportunity for high solid solution hardening contributions due to their highly concentrated multi-element matrix [103]. However, the vast compositional

range cannot be easily studied systematically by means of experiments. Therefore, only a minor fraction of possible compositions has been explored so far [2, 13, 24]. Wu et al. [12, 141] changed the number of constituents of the equiatomic alloys in the Cr-Mn-Fe-Co-Ni alloy family and studied the effect on the mechanical properties. Laurent-Brocq et al. [27, 153] and Bracq et al. [28] investigated five-component subsystems of the Cantor alloy following the form $(ABCD)_{100-x}E_x$ and analysed the hardness and yield strength as a function of composition in the fcc phase region. Bracq et al. [28] selected 24 compositions to cover the fcc phase space and measured the hardness via nanoindentation (Fig. 6). The systematic study covers both higher and lower values of c_n with respect to the equiatomic composition ($c_n = 0.2$). If the alloy becomes more diluted ($c_n > 0.2$), Co or Ni additions result in an increase in hardness, while the hardness decreases with Cr, Fe or Mn additions. Lowering the concentration of the respective fifth element ($c_n < 0.2$) results in a constant hardness for Co, a significant increase for Fe and a decrease for Cr or Mn.

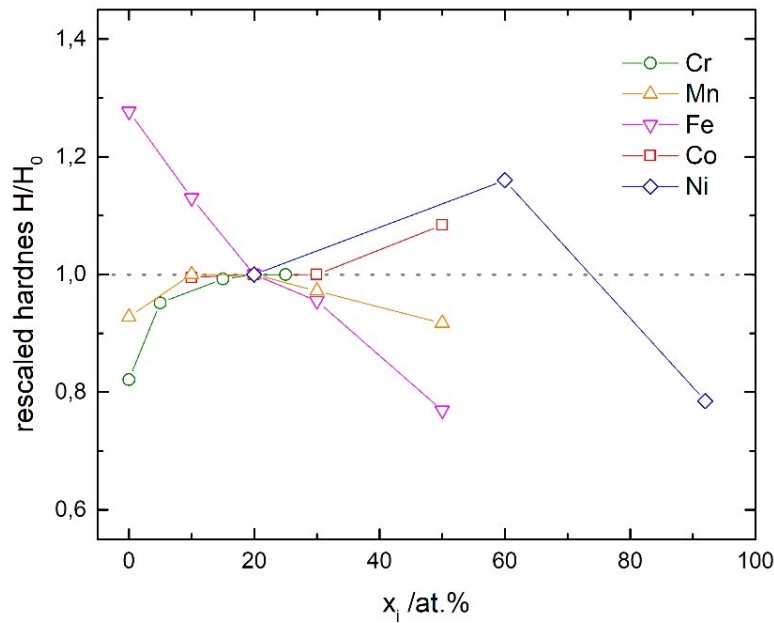


Fig. 6: Rescaled experimental nanoindentation hardness for the five isopleths of the CrMnFeCoNi Cantor alloy, which follow the form $(ABCD)_{100-x}E_x$, with E listed in the legend. All hardness values are normalized by the hardness of the equiatomic composition, which is given at $x_i = 20$ at.%. The investigated alloys are all single fcc solid solutions. The shown hardness values are averaged over an indentation depth interval from 350 – 400 nm, therefore size effects may affect the data. Data taken from Ref. [28]

The vast compositional range and the lack of experimental data reinforces the need for parameter free and predictive solid solution hardening models for fast exploration and serving as a basis and guidance for experiments.

Solid solution hardening is fairly well described for dilute solutions. Two different type of models are used, the strong-pinning models as described by Fleischer [74, 154] or Friedel [155]

or the weak-pinning models like the Labusch [72, 73] model. Fleischer [74, 154] and Friedel [155] describe hardening by dilute, strong obstacles, where the dislocation line is pinned at individual solutes at full interaction force or not at all. The dislocation line bows out under the influence of an applied stress, until the dislocation can overcome one obstacle and glide further. It is assumed that the predominant interaction is based on two elastic effects, a lattice parameter misfit and a shear modulus misfit. In contrast to the discrete obstacle model, Labusch provides a statistical description of a dislocation interacting with randomly distributed solutes. The Labusch model assumes concentrated, weak obstacles and a distribution of interaction forces. Trapping the dislocation line in energetically favored positions results in a reduced mobility of the dislocation and thus in a strengthening of the material as an additional force is required to move the dislocation further [39, 72-74, 154]. The solid solution hardening contribution according to the Labusch model can be calculated using Eq. 5:

$$\Delta\tau = \frac{G[\varepsilon_G'^2 + (15\varepsilon_b)^2]^{2/3} c^{2/3}}{550} \quad (5)$$

where G is the shear modulus, ε_G' the modulus mismatch parameter, ε_b the atomic size mismatch and c the concentration of the alloying element [127].

A comparison of the two assumptions – strong-pinning type / weak-pinning type – revealed that the Labusch-type models give a better description of the strengthening for solute concentrations relevant for engineering alloys [103, 156]. Nevertheless, the classical solid solution hardening models are based on well-defined solvent and solute species, where a base element (solvent) defines the host lattice and small amounts of alloying elements (solute) are introduced. This classical picture of clearly defined solvent and solute species is not valid for highly concentrated alloys and, moreover, breaks down for equiatomic compositions [103]. Even though the limitations of the Labusch model are known, some studies have applied it in modified forms to HEAs. Senkov et al. [157] applied the Labusch model in a modified form to the refractory TiZrNbHfTa bcc HEA to circumvent the problem of the host lattice definition. The HEA is assumed as a pseudo-binary system, pairing elements with similar properties in terms of atomic radius and shear modulus. This very rough analysis results in a moderate deviation between experiment and model of approx. 18 %. However, this approach cannot be applied in a generalized way for arbitrary compositions, especially not for compositions which cannot be treated as pseudo-binaries.

The solid solution hardening model proposed by Varvenne et al. [102, 158, 159], has attracted significant interest in recent years and is commonly used for predicting yield strength of random fcc HEAs [28, 87, 102, 158-163]. It describes the HEA as a homogeneous monoatomic matrix with average properties (grey matrix, see Fig. 7). Each element is considered as a solute

embedded into this effective matrix, causing local concentration fluctuations with respect to the average composition. The interaction between dislocation and the randomly distributed solutes (i.e. random local concentration fluctuations) in the effective matrix are responsible for the strengthening. The dislocation is attracted by energetically favorable solute fluctuations and is repelled by energetically unfavorable ones. This mechanism leads to a bowing of the dislocation line towards regions of favorable solute fluctuations, reaching a low-energy wavy configuration. For glide, the dislocation has to overcome an energy barrier, which arises from the energy cost to move from an energetically favored to an unfavorable potential energy.

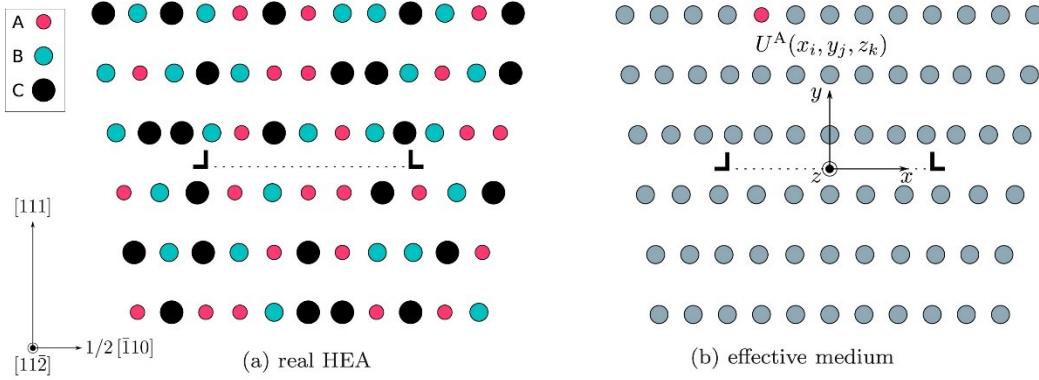


Fig. 7: Effective medium approach for dislocation-solute interactions of the Varvenne solid solution hardening model [102], a) fully random three-component alloy and b) effective matrix of the same alloy with one "A" solute embedded in the matrix, adapted from [102]. Reprinted with permission from Varvenne et al. [102], Copyright (2016), Acta Materialia, Elsevier.

As the full dislocation – solute interaction energies are not easily measurable or computable, Varvenne and co-workers [102] presented a reduced version of the theory. In the reduced and fully analytic theory, only the elastic contribution to the interaction energy is considered, which arise from the interactions of the dislocation stress field and the solute misfit volumes. The misfit volumes are representative for each solute and a key quantity in the theory. The zero-temperature flow stress τ_{y0} and the energy barrier ΔE_b can be written as Eq. 6 and Eq. 7 according to Ref. [159]:

$$\Delta\tau_{y0} = 0.01785\alpha^{-1/3}\bar{\mu}\left(\frac{1+\bar{\nu}}{1-\bar{\nu}}\right)^{4/3}\left[\frac{\sum_n c_n \Delta V_n^2}{b^6}\right]^{2/3} \quad (6)$$

$$\Delta E_b = 1.5618\alpha^{1/3}\bar{\mu}b^3\left(\frac{1+\bar{\nu}}{1-\bar{\nu}}\right)^{2/3}\left[\frac{\sum_n c_n \Delta V_n^2}{b^6}\right]^{1/3} \quad (7)$$

where α is a line tension parameter given as 0.123, $\bar{\mu}$ and $\bar{\nu}$ are the elastic constants shear modulus and Poisson's ratio of the random alloy, c_n is the mole fraction of component n, ΔV_n is the atomic size misfit volume of element n with $\Delta V_n = V_n - \bar{V}$ and b is the Burgers vector.

The input parameters are obtained from rule-of mixtures models following Varvenne et al. [159]:

$$\bar{\mu} = \sum_n c_n \mu_n, \quad \bar{E} = \sum_n c_n E_n, \quad \bar{\nu} = \frac{\bar{E}}{2\bar{\mu} - 1} \quad \text{and} \quad \bar{V} = \sum_n c_n V_n \quad (8)$$

At finite temperature, the thermally activated escape of a dislocation from a stress-dependent energy barrier follows an Arrhenius relationship, which relates strain rate, stress and temperature [164, 165]. From this, the flow stress τ_y can be written for ambient temperatures as:

$$\tau_y = \tau_{y0} \left[1 - \left(\frac{k_B T}{\Delta E_b} \ln \frac{\dot{\epsilon}_0}{\dot{\epsilon}} \right)^{\frac{2}{3}} \right] \quad (9)$$

where k_B is the Boltzmann-constant, $\dot{\epsilon}_0$ is a reference strain rate and $\dot{\epsilon}$ the strain rate [159]. The reference strain rate $\dot{\epsilon}_0$ is derived from the Orowan relationship, but is of minor importance due to its logarithmic contribution [102]. The flow stress can be converted into the yield stress σ_y using the Taylor factor M , which is 3.06 for polycrystalline fcc metals [102]:

$$\sigma_y = M \tau_y \quad (10)$$

2.4.2. Hall-Petch hardening

Applying an external mechanical stress greater than the Peierls stress results in slip of dislocations on the glide planes [98]. A direct transfer of slip across high angle grain boundaries is difficult, as glide planes typically rotate across grain boundaries [166]. Grain boundaries act as barriers to dislocation movement [166]. The Hall-Petch relation [167, 168] describes the correlation between the yield strength and the grain size of a material:

$$\sigma_y = \sigma_0 + k_y d^{-1/2} \quad (11)$$

with σ_y being the yield stress, σ_0 the grain size independent friction stress, k_y a material-dependent constant and d the grain size [166]. The Hall-Petch relation [167, 168] is based according to Cottrell [169] on dislocation pile-up at grain boundaries or according to Li [170, 171] on hardening due to grain boundary ledge dislocations. The theory of dislocation pile-up describes a pile-up of dislocations against grain boundaries, where the number of dislocations and thus the acting stress ahead of the dislocation pile-up depends on the length of the slip plane, i.e., on the grain size [166]. Therefore, the external stress required to induce dislocation

motion in the adjacent grain increases with decreasing grain size. In the non-pile-up theory, grain boundaries are assumed to act as dislocations sources, which cause enhanced dislocation accumulation in the presence of grain boundaries and thus hardening [170, 171].

Hardening of a material is feasible by reducing its grain size, where the Hall-Petch relationship predicts a linear dependence of the yield stress on the square root of the reciprocal grain size [39]. The Hall-Petch relation in the above shown form is only valid for recrystallized materials, which hardly contain other defects like dislocations [172, 173], hence, the studies regarding the Hall-Petch relationship are frequently based on plastically deformed and subsequently annealed samples. Investigations concerning the validity of the Hall-Petch relation in HEAs are therefore often limited to grain sizes in the micrometer range see e.g. Refs. [10, 141, 144, 174, 175]. At intermediate annealing temperatures, where reduced grain growth is expected, the formation of precipitates will take place (see chapter 2.2.3). Thus, the annealing process after deformation is limited to high temperatures, which is associated with enhanced grain growth. It has been shown that various equiatomic MEAs and HEAs, including the Cantor alloy, obey the classical Hall-Petch relationship, i.e., the hardness or yield strength was found to follow a linear relationship on the inverse square root of the grain size [10, 141, 144, 174, 175]. The Hall-Petch slope was found to be $494 \text{ MPa}\sqrt{\mu\text{m}}$ for the Cantor alloy [10] and $160 \text{ MPa}\sqrt{\mu\text{m}}$ for pure Ni [172].

2.4.3. Mechanical properties of nanocrystalline HEAs

HEAs show extraordinary structural refinement during SPD like HPT, which can lead to high strength of these materials [51, 55, 59]. For example, the tensile strength of the CrCoNi alloy can be increased dramatically from the coarse-grained state (several $100 \mu\text{m}$) with approx. 460 MPa to roughly 2000 MPa in the nc state after HPT [59]. A similar behavior can be seen for the CrMnFeCoNi alloy [51]. The bcc TiZrNbHfTa alloy already shows a yield strength of approx. 830 MPa in the coarse-grained state, which can be increased to approx. 1900 MPa by HPT processing [55]. It is known that the grain refinement to the nc or UFG regime leads to a significant loss in ductility, which can be attributed to the low strain hardening capability and hence the accompanying tendencies for localized deformation and plastic instabilities [176-178]. Interestingly, while the grain refinement leads to significant loss in ductility for the named fcc HEAs, the ductility is mostly retained for the bcc TiZrNbHfTa alloy (Fig. 8). This effect is unusual for nc materials, but was observed in literature for several materials and was termed by Valiev et al. [179, 180] as “*paradox of strength and ductility in SPD-processed metals*”. They argued, concerning the origin of this effect, that the introduction of a high density of high angle

grain boundaries will change the primary deformation mechanism from dislocation or twinning based plasticity to grain boundary mediated processes like grain boundary sliding and grain rotation [179, 180].

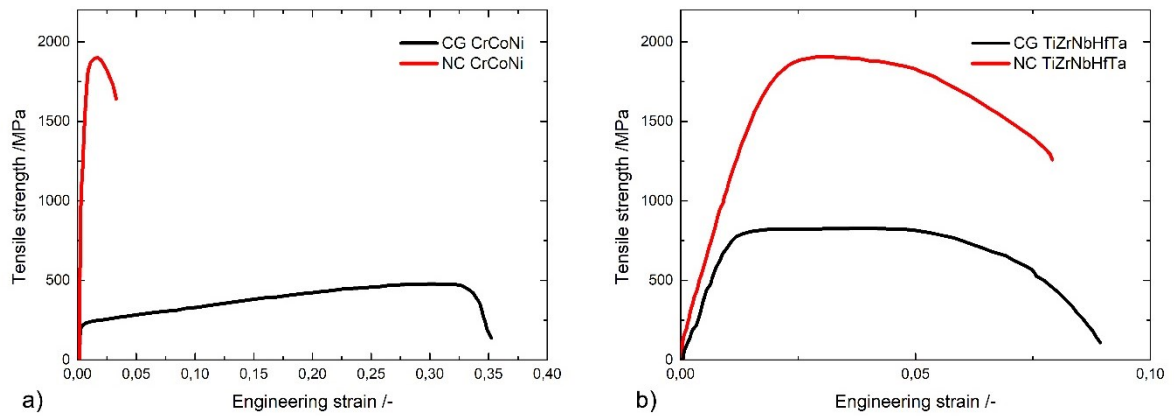


Fig. 8: Representative tensile stress vs. strain curves for the coarse-grained and nanocrystalline states of a) the fcc CrCoNi and b) the bcc TiZrNbHfTa alloys. Data taken from Refs. [55, 59].

3. Objective of the work

Based on the literature review in chapter 2, important scientific questions arise, which will be addressed throughout the synopsis of this thesis. The objective of the present work is to discuss and clarify fundamental questions concerning thermodynamic aspects and the mechanical properties of fcc HEAs. For this purpose, the prototypical CrMnFeCoNi alloy and its derivatives will be investigated to shed light on the following research questions:

- I. Are there composition-dependent structural discontinuities or significant changes in the properties of HEAs upon small variations in concentrations and do the specific alloy properties emerge from a “cocktail” of multicomponent alloying, which couples in a non-linear manner?
- II. Which characteristics of an alloying element are relevant for solid solution hardening in HEAs and how can it be described by means of a SSH model far from the picture of solute and solvent species?
- III. What is the role of solutes on the defect storage as well as the microstructural stability and what are the kinetics and thermodynamics of segregation and phase decomposition?

The present work contributes to the understanding of phase stability and solid solution hardening effects in fcc high entropy alloys and the questions outlined above will be addressed in the following chapters. A diffusion couple approach or discrete sample compositions are used to move away from equimolarity and to investigate the effects of composition or solutes on the microstructure and the respective properties. In this respect, emphasis is put on the multi-element matrix of HEAs and a possible classification of alloys into dilute solid solutions and high entropy-type compositions. The key findings are summarized in chapter 4 and presented and discussed in detail in chapter 5.

4. List of selected publications

The cumulative dissertation summarizes the fundamental scientific findings being reported in the following publications published with contributions as main-author in peer-reviewed journals. The full-text articles are attached in chapter “8.2 Selected reprints”.

Publication A:

Exploring the compositional parameter space of high-entropy alloys using a diffusion couple approach

Tom Keil, Enrico Bruder, Karsten Durst
Materials & Design, 176 (2019) p. 107816. DOI: 10.1016/j.matdes.2019.107816.

Diffusion couples were produced using the equiatomic fcc CrMnFeCoNi Cantor alloy and a commercial fcc CoNiCrMo (MP35N[®]) alloy with constituent and foreign elements in order to investigate the phase stability with respect to individual solubility limits or the formation of intermetallic phases. A combination of energy dispersive x-ray spectroscopy (EDX) and electron backscatter diffraction (EBSD) revealed the crystal structures present in the interdiffusion zones and the local composition at phase transition. The experimental procedure enables investigations of wide compositional ranges as well as a separation between phase transitions occurred during annealing and those occurred during quenching. No general correlation between atomic size mismatch and maximum solubility limit were found, whereas a correlation between valence electron concentration and formed crystal structure seems to exist for transitions between fcc and bcc.

Publication B:

Solid solution hardening in CrMnFeCoNi-based high entropy alloy systems studied by a combinatorial approach

Tom Keil, Daniel Utt, Enrico Bruder, Alexander Stukowski, Karsten Albe, Karsten Durst
Journal of Materials Research, 36 (2021) p. 2558. DOI: 10.1557/s43578-021-00205-6.

Solid solution hardening was studied in the fcc Cantor system using a diffusion couple approach with all alloying elements. The alloying content was varied continuously and the local nanoindentation hardness was directly correlated to the chemical composition. The hardness of the different solid solutions were analysed via a modified Labusch model and the more recent

Varvenne solid solution hardening model for HEAs. The Labusch model was used to fit the concentration dependent hardness data, suggesting Cr as the most potent strengthening element in the HEA. The Varvenne model on the other hand uses, among others, the shear modulus of the grey matrix as a material parameter to predict the concentration-dependent strength of the fcc solid solution. For comparison of experimental hardness and predicted strength, the composition-dependent work hardening behavior and the concept of representative indentation strain needs to be considered. Including these factors, a very good agreement between experiment and model is found for all diffusion couples.

Publication C:

From diluted solid solutions to high entropy alloys: Saturation grain size and mechanical properties after high pressure torsion

Tom Keil, Enrico Bruder, Mathilde Laurent-Brocq, Karsten Durst
Scripta Materialia, 192 (2021) p. 43. DOI: 10.1016/j.scriptamat.2020.09.046

The microstructural evolution of the equiatomic Cantor alloy and Ni-enriched variations ((CrMnFeCo)_xNi_{1-x}) with x=0.8, 0.4, 0.08 were investigated after high pressure torsion to elucidate the effect of solutes on the saturation grain size and the mechanical properties. The solid solution hardening contributions were determined using the conventional Labusch model and the more recent Varvenne model, which was specially developed for chemically complex fcc HEAs. The saturation grain size correlate with the SSH contribution, showing lower saturation grain size with higher solute content, i.e., higher SSH contribution. Here, the Varvenne model shows an accurate description of the saturation grain size development from a dilute solid solution to a chemically complex HEA. Hardness measurements on coarse-grained and HPT deformed states showed an increasing hardness with increasing solute content due to higher SSH and Hall-Petch contributions. Moreover, nanoindentation strain rate jump testing reveals a different transient behavior and similar strain rate sensitivities for all compositions in the nanocrystalline and ultra-fine grained regime.

Publication D:

Effects of solutes on thermal stability, microstructure and mechanical properties in CrMnFeCoNi based alloys after high pressure torsion

Tom Keil, Shabnam Taheriniya, Enrico Bruder, Gerhard Wilde, Karsten Durst
Acta Materialia, 227 (2022) p. 117689. DOI: 10.1016/j.actamat.2022.117689

This work focuses on the grain growth and decomposition tendencies of Ni-enriched subsystems of the Cantor alloy, with an emphasis on a transition from dilute solid solutions to high entropy alloys, revealing the influence of solutes on the microstructural stability and mechanical properties. Ni-enriched derivatives of the Cantor alloy in form of $(\text{CrMnFeCo})_x\text{Ni}_{1-x}$ with $x=0.8, 0.4, 0.08$ (Ni20, Ni60, Ni92 and Ni100) were used to investigate the effects of solutes on the microstructural stability, i.e., grain growth and decomposition tendencies, and the resulting mechanical properties after severe plastic deformation via high pressure torsion and subsequent isochronal annealing over a wide temperature range from room temperature to 900 °C. At intermediate annealing temperatures, the high entropy-type alloys exhibit decomposition tendencies in form of secondary phases (Ni20) or nanosized Cr-rich precipitates and Mn segregations to grain boundaries (Ni60), none of which is observed for the dilute solid solutions (Ni92, Ni100). All alloys exhibit a two-stage coarsening behavior with marginal grain growth below a certain temperature and typical diffusion driven growth above. The high entropy-type compositions show a higher transition temperature, which is attributed to the impact of solutes and partial decomposition on grain boundary mobility (solute drag and Zener pinning). Nanoindentation analyses are strongly affected by the pile-up behavior, which is very pronounced after annealing at intermediate temperatures due to the change in work hardening behavior (hardening by annealing and softening by deformation effect). The pile-up corrected data show that the hardness at room temperature of the high entropy-type compositions remains constant up to annealing at 450 °C (Ni60) or increases up to 500 °C (Ni20), whereas the dilute solid solutions already soften upon annealing above 300 °C. The modulus of the alloys is not affected by the heat treatment. Nanoindentation strain rate jump tests reveal differences in the transient behavior, which is discussed in terms of solute concentration and microstructural size.

5. Synopsis of publications

The following chapter provides an overview of the experimental approaches and main results of the published articles. The present work focuses on the phase stability and thermal stability as well as on solid solution hardening effects of fcc CrMnFeCoNi based systems using either a diffusion couple approach or discrete sample compositions.

In the first part, diffusion couples were produced to explore the wide compositional parameter space, offered by the alloying concept of HEAs, and to investigate solid solution hardening within chemical gradients in an effective manner. The maximum solubility limits of individual elements are identified and discussed within the context of various phase stability models. Additionally, the influence of different elements on the hardness and thus on the solid solution hardening behaviour is analysed within the fcc structure of the alloy using nanoindentation. Given that the Varvenne model, one of the most promising SSH models, has been derived from equiatomic compositions [102, 103, 159], the present work aims to prove the applicability of the model to a wide concentration range up to the phase boundary.

In the second part, discrete sample compositions were subjected to HPT deformation followed by isochronal annealing. The results of the diffusion couple approach revealed the presence of a single fcc structure for Ni-enriched compositions of the Cantor alloy up to pure Ni. This makes this material system a useful model system to study the transition behavior from a dilute solid solution to HEAs and to discuss and clarify the role of solutes on the microstructural stability and mechanical properties. It has been shown for Ni-enriched derivatives of the Cantor alloy that there is no continuous transition in properties from dilute solid solutions up the equiatomic composition. The observation of a breakpoint in lattice parameter evolution from Vegards law and the observed hardness trend [27, 28] indicates that alloys might be classified into dilute solid solutions and high entropy-type compositions. In this context, Ni-enriched derivatives of the CrMnFeCoNi Cantor alloy (Ni20, Ni60, Ni92 and Ni100) were used to investigate the effects of solutes on the microstructure and the mechanical properties. This includes the investigation of the saturation grain size after HPT deformation as well as after isochronal annealing over a wide temperature range, the analysis of the microstructural stability, i.e., grain growth and decomposition tendencies during annealing and the resulting mechanical properties.

5.1. Thermodynamic stability and solid solution hardening in single-phase HEAs

The results presented are published in:

Keil, T., Bruder, E. and Durst, K., *Exploring the compositional parameter space of high-entropy alloys using a diffusion couple approach*, *Materials & Design*, 176 (2019) p. 107816.

Keil, T., Utt, D., Bruder, E., Stukowski, A., Albe, K. and Durst, K., *Solid solution hardening in CrMnFeCoNi-based high entropy alloy systems studied by a combinatorial approach*, *Journal of Materials Research*, 36 (2021) p. 2558.

One main part of the present work is based on the production and analysis of diffusion couples to investigate the vast and widely unexplored compositional range of high entropy alloys. Therefore, diffusion couples were produced using the Cantor alloy with all constituent elements as diffusion partners to change the composition continuously starting from the equiatomic HEA. During the interdiffusion heat treatment, the constituents of the alloy diffuse towards the pure metal and vice versa, resulting in the formation of an interdiffusion zone. With the selected parameters, an interdiffusion zone width of approx. 200 μm was achieved. The combination of chemical and structural analysis using EDX and EBSD with a local resolution in the μm range was used to address phase stability aspects. By performing nanoindentation hardness mapping within the concentration gradients in the interdiffusion zone, the composition-dependent hardness can be used to analyse the role of solid solution hardening in HEAs with a spatial resolution down to a few microns.

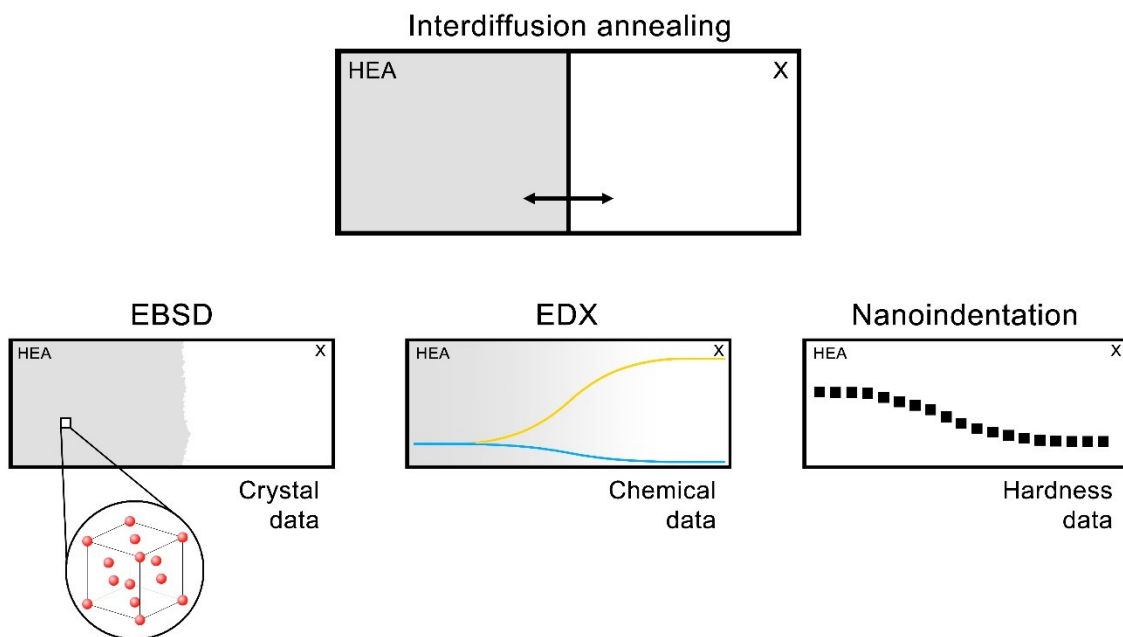


Fig. 9 Schematic illustration of the experimental procedure within the diffusion couple approach, including EBSD, EDX and nanoindentation.

5.1.1. Compositional parameter space

Using the chemical and structural information from EDX and EBSD, the phase stability of the Cantor alloy is investigated over wide concentration gradients in a continuous manner. In this respect, maximum solubility limits of individual elements or composition-dependent structural discontinuities in the matrix of the base alloy are observed in detail. Regarding the phase stability or phase formation rules of HEAs, it is worth to note that the terminology can be deceptive, as thermodynamic equilibrium and phase stability are not necessarily equivalent. As described in chapter 2.2.3, most HEAs, like the Cantor alloy, are not thermodynamically stable, but kinetically stabilized in their metastable state [50]. In case of the diffusion couple experiments, the samples were annealed at 1150 °C or 1000 °C and then quenched to room temperature. The phase stability is defined as states which are formed at annealing temperature and kept stable at room temperature, although being potentially metastable. In the second main part of this thesis, additional annealing steps at lower temperatures were applied to discrete compositions after HPT deformation to approach the thermodynamic equilibrium and to study decomposition tendencies.

After the interdiffusion heat treatment, three different cases are identified depending on the diffusion partner species (Fig. 10): a single fcc phase is present using Mn or Ni as diffusion partner elements (Fig. 10 a and b), a phase transition takes place from fcc to bcc (Fe) or to the hexagonal close-packed (hcp) structure (Co) within a smooth concentration gradient (Fig. 10 c and d) and a formation of an intermetallic phase can be seen using Cr as a diffusion partner element (Fig. 10 e). This transition to the intermetallic phase is characterised by abrupt changes in concentrations. While the concentration profiles show a distinct s-shape for the diffusion couples with Mn, Co and Fe, a strong interaction between Co and Mn can be observed for the diffusion couple Cantor+Ni (Fig. 10 a). The trajectory through the multi-dimensional phase space may even be more complex, such as when using Cr as a diffusion partner element. The formation of an intermetallic phase takes place at increased Cr concentrations, which can be indexed as a bcc structure. Prior to the intermetallic phase, the Cr as well as Ni concentration increases (uphill diffusion). For further evaluation of the phase stability, it should be taken into account that all element concentrations change simultaneously and do not necessarily remain in equiatomic ratio (Ni or Cr diffusion couple).

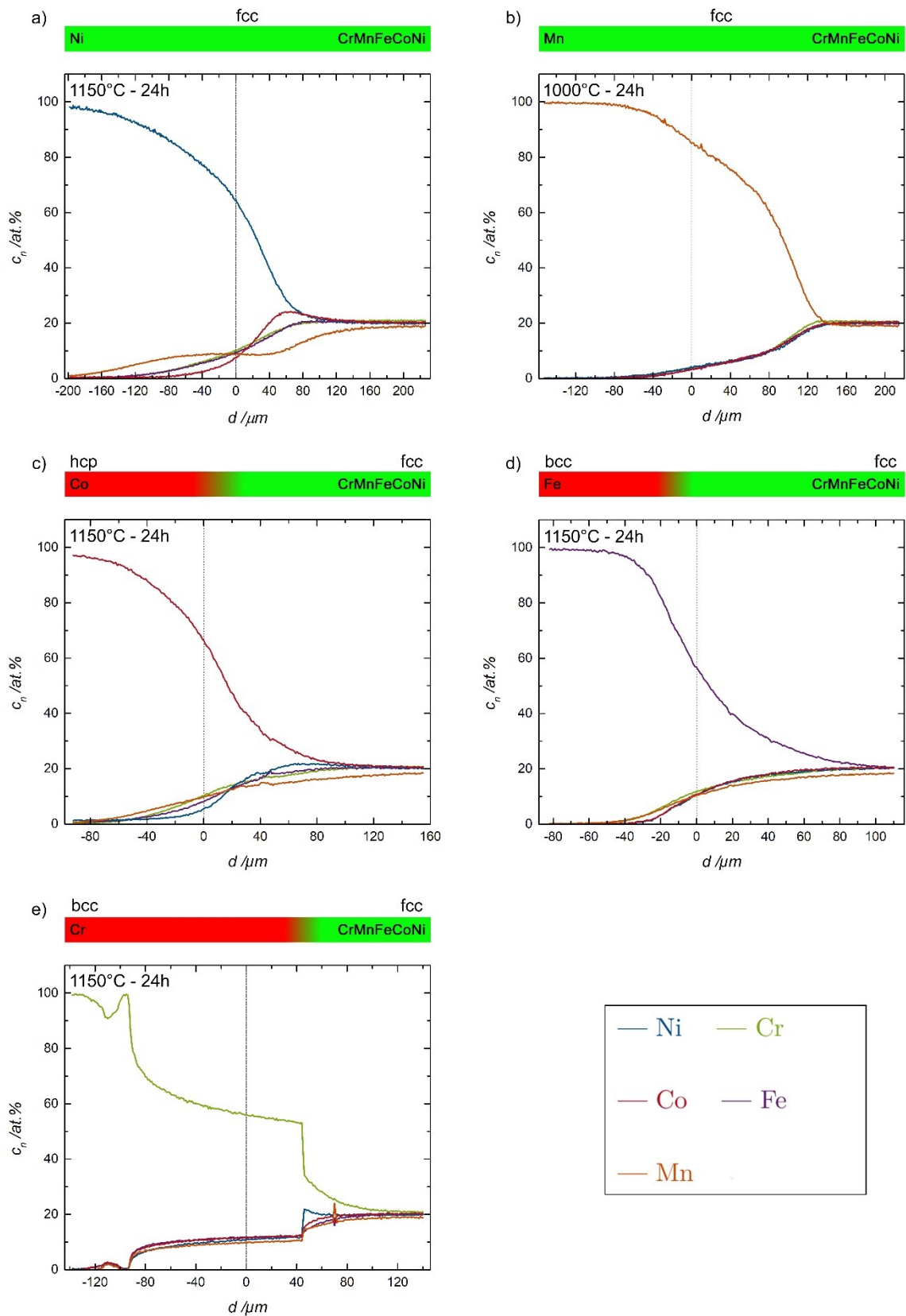


Fig. 10: Full concentration profiles for the different Cantor-*i* diffusion couples measured using EDX line scans. The initial boundary is found at $d = 0$ and marked by a dashed line. The coloured scale on top of each diagram represents the present phase. The diagram is categorized in three cases: a) – b) single phase, c) – d) phase transition and e) formation of an intermetallic phase.

The phase stability with respect to the local composition has been illustrated in spider web like diagrams (Fig. 11), where each column represents one single diffusion couple. Beside the three named cases (single fcc phase, phase transition and formation of intermetallic phases), it is also possible to separate between phase transitions, which were present during annealing and ones that occurred upon cooling.

Discontinuities and element accumulation prior to the phase boundary (uphill-diffusion) indicate that the phase transition was already present at annealing temperature. Compositions within the concentration interval of the discontinuity do not exist on a local scale and correspond to a two-phase region. The uphill diffusion of Ni prior to the intermetallic phase in the diffusion couple with Cr is related to its narrow concentration interval for the element Ni. Diffusion couples with Co and Fe on the other hand show smooth s-shaped concentration gradients within the interdiffusion zone. At annealing temperature (1150 °C), both Co and Fe are present in their fcc modifications, but transform to the hcp or bcc structure during quenching. Consequently, the phase transition must have formed during quenching, as such a phase transition would be associated with a multi-phase region and this in turn would result in discontinuities in the concentration gradient.

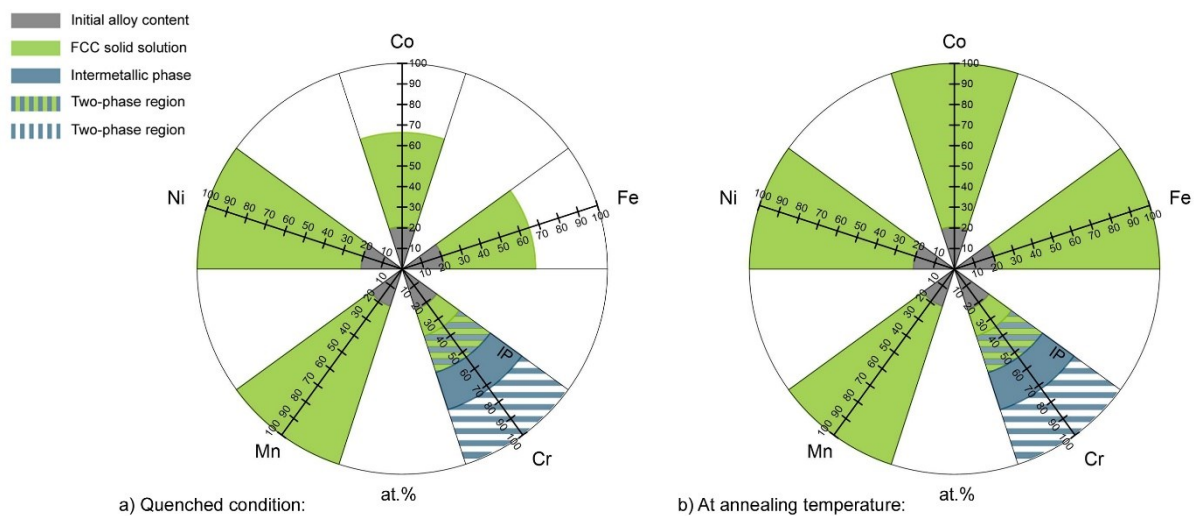


Fig. 11: Phase stability diagram for the Cantor+*i* diffusion couples in a) the quenched condition and b) at annealing temperature. The interdiffusion heat treatment was performed for 24 h at 1150 °C for Cr, Mn, Fe, Co and Ni and at 1000 °C for Mn. Each column represents one single diffusion couple experiment with the composition of the respective partner element displayed on the axis. Reprinted with permission from Keil et al. [48], Copyright (2019), Materials & Design, Elsevier.

Quenching of the samples results in a kinetic stabilisation of the metastable states at ambient temperatures, which is of importance for investigations regarding the mechanical properties and thus the solid solution hardening effects within the fcc structure of the HEA (see chapter 5.1.2). In case of Co or Fe, the concentrations of these elements can be increased substantially

up to the phase boundary to 66.4 at.% or 65.0 at.%, respectively. Due to the formation of an intermetallic phase in the Cantor+Cr diffusion couple, the concentration interval of Cr is limited to max. 34.3 at.% prior to the phase boundary. The phase stability ranges can now be used for comparison with existing results from Calphad (Calculation of Phase Diagrams) simulations [181]. The stability range of the fcc solid solution of the CrMnFeCoNi alloy was theoretically studied using the Calphad method and the TCHEA1 database by Bracq et al. [181] (Fig. 12).

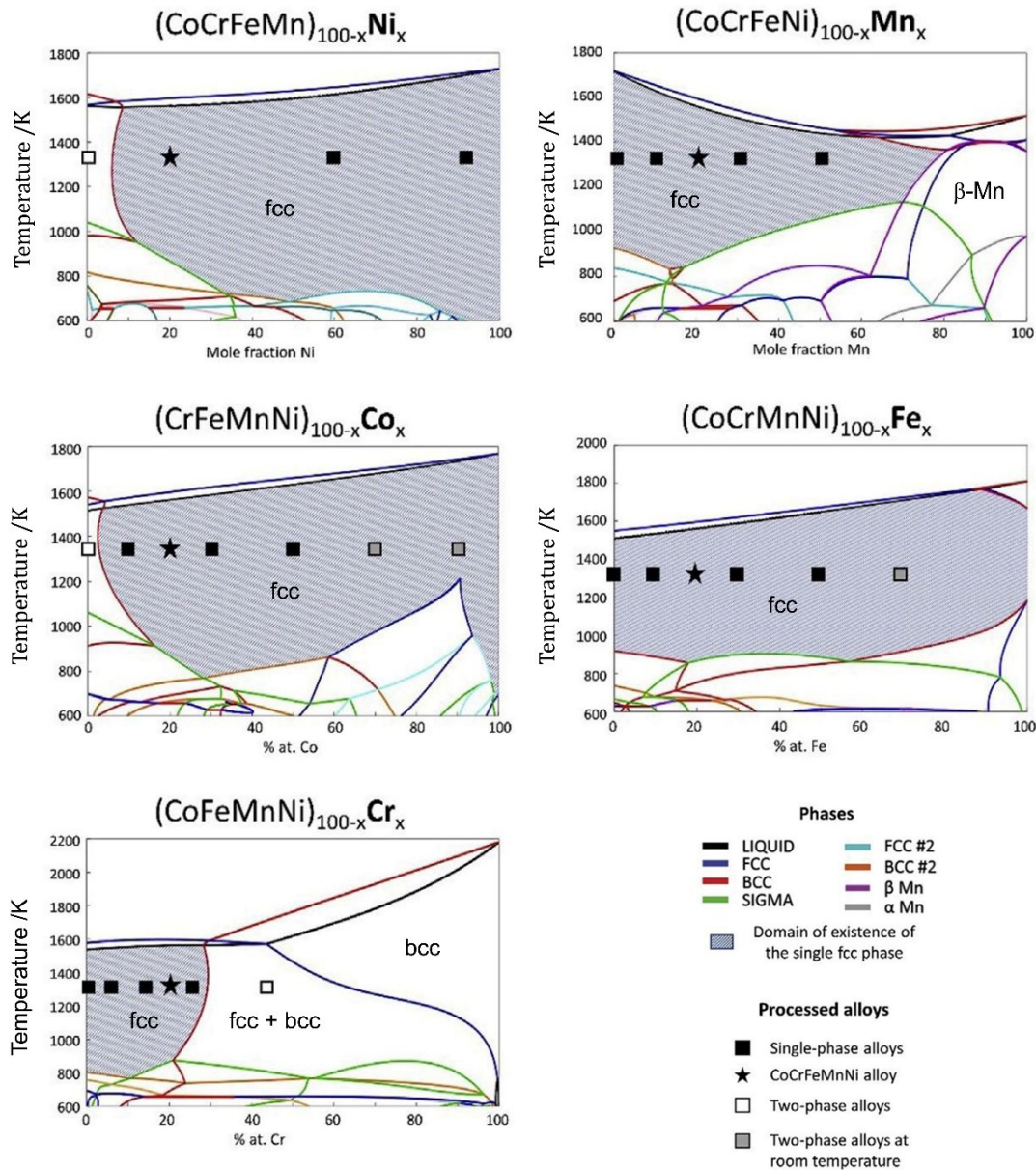


Fig. 12: Phase stability diagrams calculated using the Calphad method and the TCHEA-1 data base for CrMnFeCoNi based variants. Processed alloys are shown as symbols at homogenization temperature. Adapted from [28] and reprinted with permission from Bracq et al. [28], Copyright (2019), Acta Materialia, Elsevier.

At 1150 °C, experiment and simulation show the same results for an increase in Cr, Fe, Co or Ni. For the latter three, a complete miscibility (single fcc phase) between the equiatomic composition and the pure element can be seen for modelling and diffusion couples. The solubility limit of Cr in the fcc structure of the Cantor alloy was determined by Calphad to approx. 30 at.%, followed by a two-phase region in the concentration interval between 30 and 55 at.%. These concentration limits are also observed in the Cantor+Cr diffusion couple with minor differences in the absolute values. The small deviations could be related to the change in element ratios during diffusion, as in the simulation all other elements were kept in equimolar proportions. Bracq et al. [181] showed that Mn on the other hand destabilises the fcc solid solution, which is in contrast to the present results. However, the presence of a single fcc structure in the diffusion couple experiment with Mn cannot be explained at the moment, since pure Mn only shows the close-packed cubic structure at temperatures above 1095 °C.

The atomic size mismatch as well as the valence electron concentration can be used as a parameter to describe the phase stability of HEAs. Using the concentration gradients from the diffusion couple experiments, composition-dependent atomic size mismatch and VEC ranges can be determined within the interdiffusion zone. The atomic size mismatch is relatively small for Cr-Mn-Fe-Co-Ni based compositions and shows values below 1 for all possible compositions within the diffusion couple experiments using Eq. 4. Accordingly, the atomic size mismatch parameter does not indicate at which composition in the Cantor system a phase transition is present or expected. The VEC is another parameter, which directly affects the phase stability. Guo et al. [43] used the VEC to describe the phase formation of cubic solid solutions and defined two threshold values for the formation of bcc or fcc solid solutions based on an empirical study (Fig. 2). For the interpretation of the data, the following notes should be taken into account. First, the evaluation from Guo et al. [43] was based on cast alloys, the validity of the threshold values is not given for other processing routes. [42]. In the present study, the samples were annealed below the melting temperature and subsequently quenched in water, resulting in a different cooling rate. Second, no distinction was made between ordered and disordered solid solutions [42]. By forming an intermetallic phase showing an ordered bcc structure (Cantor+Cr), the proposed threshold values should be considered with care. Third, the different phase fields do not necessarily indicate that only one single solid solution is formed [42]. Especially after slow cooling rates or heat treatments at intermediate temperatures, several phases could be present in HEAs. Furthermore, the transition to an hcp structure (Cantor+Co) is not included in the proposed model. However, the VEC can be calculated using the measured concentration profiles. The equiatomic Cantor alloy shows a VEC of 8, the addition of Cr or Mn lowers of the VEC and an increase in Fe, Co or Ni results in constant (Fe) or higher (Co, Ni)

VECs of the resulting alloy. The diffusion couple Cantor+Ni remains single-phase fcc and shows VECs greater than 8, which is located in the fcc phase region according to Guo et al. [43]. Even though the VEC decreases towards 7 by adding Mn, which is located in the two phase region, the diffusion couples remains single-phase fcc. The phase transition from fcc to bcc in the Cantor+Fe diffusion couple takes place at a VEC of 7.9 and the fcc stability range of the diffusion couple with Cr is located between 8 and 7.75. Hence, the phase transition is close to the proposed threshold value for the fcc or fcc + bcc phase space. The VEC model from Guo et al. [43] provides a convenient way for HEA design and may be used as a guidance for alloy synthesis using mainly transition metals.

5.1.2. Solid solution hardening effects

Utilising the above discussed results on the different Cantor+i diffusion couple experiments with regard to the local chemical composition as well as the phase stability limits of the fcc solid solution, SSH can be studied in HEAs using nanoindentation and having access to a wide range of compositions. Nanoindentation offers the advantage of testing very small sample volumes to determine the mechanical properties of a material, which facilitates the study of SSH effects close to the solubility limit of the different constituents at the phase boundary. In Fig. 13, the local concentration and hardness profiles are shown up to the respective phase boundary of the fcc structure of the investigated HEA. As discussed in chapter 5.1.1, the Cantor+Mn diffusion couple shows a single fcc solid solution, but due to oxidation effects, the evaluation of SSH is limited to Mn concentrations below 55 at.%.

Starting with a hardness level of ≈ 2.2 GPa for the equiatomic composition of the Cantor alloy on the right, the hardness evolves within the interdiffusion zone as a function of concentration (solid lines) within the fcc structure of the alloy. The diffusion couple Cantor+Ni (a) shows a single fcc phase across the complete concentration gradient, which allows the investigation of SSH from a quasi-binary alloy to a HEA. The hardness remains almost constant up to a Ni concentration of 60 at.%, followed by a continuous decrease to the hardness level of pure Ni. This result suggests that a transition takes place from a dilute solid solution to HEA behaviour. The observation of a breakpoint in lattice parameter evolution [27] and hardness indicates a correlation between hardness and lattice parameter and that alloys might be classified into dilute solid solutions and high entropy-type alloys. The increase in Mn concentration to 55 at.% causes a hardening of the alloy to 2.5 GPa. Due to the phase boundary present in the interdiffusion zone of the Co, Fe or Cr diffusion couples, SSH is evaluated up to approx. 55 at.% Co or Fe and up to approx. 30 at.% Cr. While an increase in Co concentration shows nearly no

influence on the hardness, the addition of Fe results in a continuous softening of the alloy. Lastly, Cr shows a substantial hardening of the base alloy at concentrations below 30 at.%.

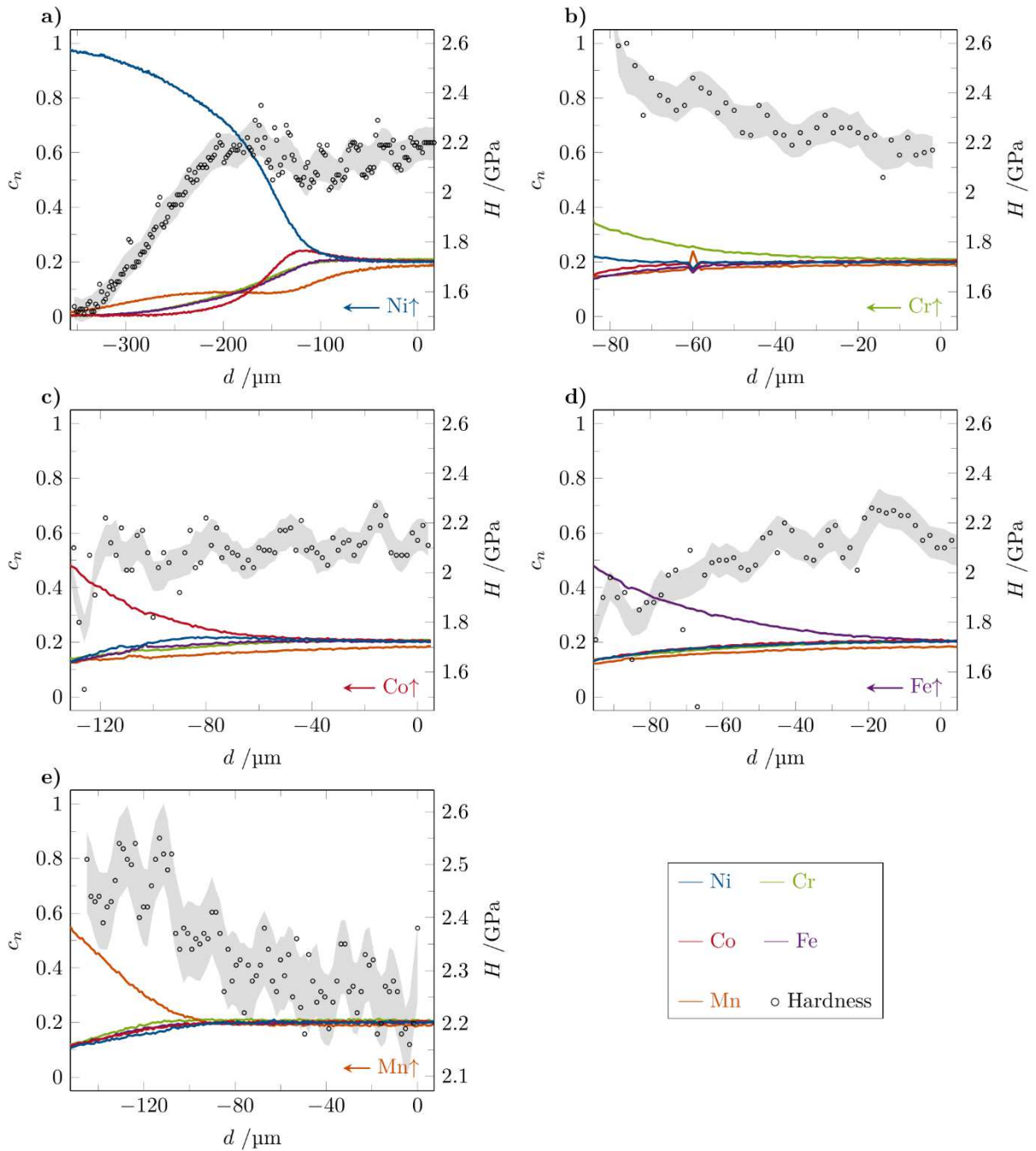


Fig. 13: Concentration and hardness profiles for the different Cantor+i diffusion couples within the single-phase fcc region. d represents the relative position in the interdiffusion zone starting from the equiatomic composition on the right. Solid lines show the concentration and each discrete data point represents the hardness of one indentation test. For further information on the indentation error bars (grey), please see the full text of publication B (chapter 8.2). Reprinted with permission from Keil et al. [182], Copyright (2021), Journal of Materials Research, Springer Nature.

Relating yield strength to hardness:

The direct correlation between chemical composition and nanoindentation hardness, as shown in Fig. 13, is used to investigate SSH in HEAs. However, when using nanoindentation testing to determine SSH effects in different compositions, some issues arise related to the testing method itself.

Instrumented nanoindentation is nowadays a highly automatized and standard technique to measure a materials hardness H and Young's modulus E . Thereby, the desired material properties are measured under load and can be recorded as a function of indentation depth. [183-187]. Therefore, the experimentally measured hardness is obtained at a specific representative plastic strain, which depends on the opening angle of the indenter tip [186, 188]. For geometrically self-similar indenters, like the three-sided Berkovich tip, the introduced strain remains constant, independently of the applied load or indentation depth, respectively. The three-sided Berkovich tip, which was used in the experiments, induces a representative strain of $\varepsilon_r \approx 8\%$ [186]. While nanoindentation determines the hardness at a given plastic strain, the aforementioned Varvenne SSH model (see chapter 2.4.1) predicts a yield strength at zero strain, both are not strictly equivalent to each other. Furthermore, nanoindentation on pure elements will always give finite hardness values [188, 189], the Varvenne SSH model on the other hand predicts a zero flow stress for monoatomic metals. Nonetheless, the hardness can be related to the representative strength σ_r at representative strain ε_r using Tabors equation [190, 191]:

$$H = C \sigma_r \quad (12)$$

where C is the constraint factor. C itself depends on the elastic/plastic work ratio and reaches a value of around 3 for materials showing a fully plastic behavior at representative strain [192].

Following Tabors equation (Eq. 12), the hardness can be understood as a measure of strength at representative strain (one discrete point on the stress-strain curve). Therefore, nanoindentation hardness measurements can be used to quantify SSH, as the difference in hardness between an alloy and its pure matrix element is representative for the strength change due to SSH. [188] But this relation only holds, if other contributions to nanoindentation hardness like strain hardening, indentation size effect (ISE), strain rate sensitivity and pile-up behavior do not change within the chemical gradients [188, 193]. It has been shown that pile-up and rate sensitivity can be neglected and the ISE is comparable for all investigated compositions [182]. However, the strain hardening behavior plays a major role during indentation [182], as a changing SFE is expected with changing composition, which in turn affects the local strain hardening behavior [107, 108]. Consequently, the two effects solid

solution hardening ($\Delta\sigma_{SSH}$) and strain hardening ($\Delta\sigma_{SH}$) contribute to the hardness difference between alloy composition and reference sample composition (Fig. 14). Therefore, both contributions needs to be taken into account for the hardness evaluation.

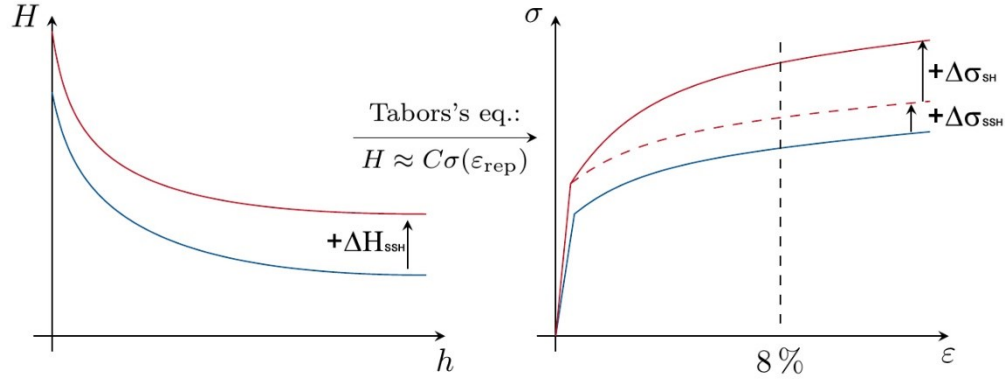


Fig. 14: Schematic representation of the relation between hardness and yield strength for two different compositions using Tabors equation, adapted from [182]. Reprinted with permission from Keil et al. [182], Copyright (2021), Journal of Materials Research, Springer Nature.

To analyse the hardness as a function of chemical composition, the concentration gradients from EDX are used as an input for the Labusch model [72, 73] and the state-of-the-art SSH model from Varvenne et al. [102, 103]. The calculated yield strength is then compared to experimental hardness using Tabors relation (Eq. 12).

Application of the Labusch model:

The Labusch SSH model describes the interaction of solutes and dislocations in dilute solid solutions, where the change in critical shear stress $\Delta\tau_{Labusch}$ is proportional to the solute concentration $c^{2/3}$ [72, 73]. The equation of the Labusch model is generalized to HEAs, assuming additive strengthening contributions for each constituent of the HEA:

$$\Delta\tau_{Labusch} = \sum_n k_n \Delta c_n^{2/3} \propto \Delta H \quad (13)$$

where k_n is the strengthening parameter for each element n . The following strengthening parameters are obtained from fitting the hardness data of the phase boundary composition and the equiatomic composition of the different diffusion couples using Eq. 13: $k_{Cr} = 0.0514$, $k_{Mn} = 0.0058$, $k_{Fe} = -0.0470$, $k_{Co} = -0.0109$, $k_{Ni} = -0.0342$, in units of $\text{GPa}/\text{at.\%}^{2/3}$. The above mentioned issues for relating hardness and yield strength are circumvented, since they get incorporated into the individual k_n values during fitting the hardness data. However, a change in strain hardening behaviour would affect the values of the individual k_n parameters.

The resulting hardness prediction is shown in Fig. 15 as solid lines and compared to the

experimental hardness (symbols) for the different diffusion couples. This approach works well for the Cr, Mn, Fe and Co diffusion couples, where a nearly linear regime can be seen. But it fails to describe the initial hardness plateau with subsequent hardness drop of the diffusion couple Cantor+Ni, where based on the breakpoint of lattice parameter [27] and hardness evolution (Fig. 13 a) a transition between dilute solid solutions and HEAs is expected.

Given the need for experimental data to be fitted, the modified Labusch model is not predictive. However, it sheds light on the hardening characteristics of the individual elements in the Cantor system. The sign and absolute value of the strengthening parameter determines the effect of a specific element on the strength of the system. A positive strengthening parameter indicates that this kind of solute increases the strength of the specific composition, whereas a negative parameter corresponds to a softening effect of the solute species. It can be seen from the obtained strengthening parameters that Cr is the most potent strengthening element, whereas Fe and Ni additions lead to a softening of the resulting alloys. Wu et al. [12] have already reported on the beneficial influence of Cr on the strength of a variety of equiatomic Cr-Mn-Fe-Co-Ni based alloys with different number of constituents. The authors attributed this effect to the modulus mismatch of Cr compared to the other constituents. Their assumption is based on the elastic constants of the elements in their ground states, while all tested alloys show an fcc structure, which could lead to inaccuracies or wrong implications.

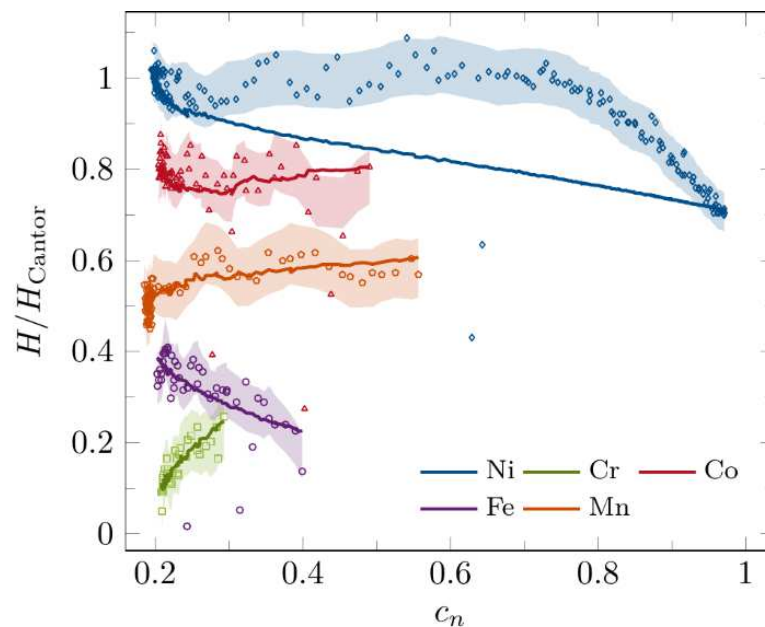


Fig. 15: Measured hardness (symbols) and best fit results of the modified Labusch model (solid lines) for the different diffusion couples over the stable fcc phase region. The composition of the respective diffusion partner element is scaled on the x-axis. Measured and calculated hardness is normalized by the hardness of the equimolar alloy H_{Cantor} . The different hardness series are shifted by a constant offset for better readability. Reprinted with permission from Keil et al. [182], Copyright (2021), Journal of Materials Research, Springer Nature.

Application of the Varvenne model:

As the strengthening parameter cannot be known *a priori* in the modified Labusch model, it can hardly be used for strength predictions of HEAs. The Varvenne model, on the other hand, remains parameter-free in its reduced elastic form (Eq. 6 to 9) and can thus be used as a predictive tool. The predicted critical shear stress will be converted into a macroscopic yield strength using the Taylor factor, which in turn is converted into a hardness using Tabors equation (Eq. 12). The Varvenne model cannot provide an absolute hardness value, therefore the composition-dependent hardness ($H(c_n)$) is normalized by the hardness level of the equiatomic alloy (H_{Cantor}). Strain hardening depends on the local composition and can change the relation between experimental hardness and the predicted SSH contribution by the model. Here, a strain hardening factor $f(c)$ is introduced to account for strain hardening during indentation. A concentration independent factor of $f = 2$ is initially assumed to take the strain hardening from 0 to 8 % plastic strain into account. Tensile tests show a hardening in this plastic regime of about 1.84 [10]. This initial assumption of a constant strain hardening factor of 2 leads to the results shown in Fig. 16 a). As the Varvenne model naturally describes a SSH contribution of 0 for pure Ni, but the macroscopic hardness of pure Ni will not converge to 0 [188], an indentation base hardness for pure Ni of 1.5 GPa is introduced to adjust the predicted hardness of the Ni series to the measured ones (dashed line). While good agreement is already found for the Fe, Co and Ni diffusion couples, especially the hardness plateau of the latter is well described, the hardness trends cannot be reproduced for all diffusion couples. Moreover, there is no physical reason for f to be constant within the concentration gradients. In this context, a linear dependency of the strain hardening factor on the concentration of the respective diffusion partner element is assumed and determined by fitting the existing hardness data (inset of Fig. 16 b). The introduction of a composition-dependent strain hardening behaviour strongly improves the agreement between SSH model and nanoindentation hardness. The hardness increase at higher Cr or Mn concentration can now be captured by the model, which is assumed to be caused by a stronger strain hardening behaviour during indentation.

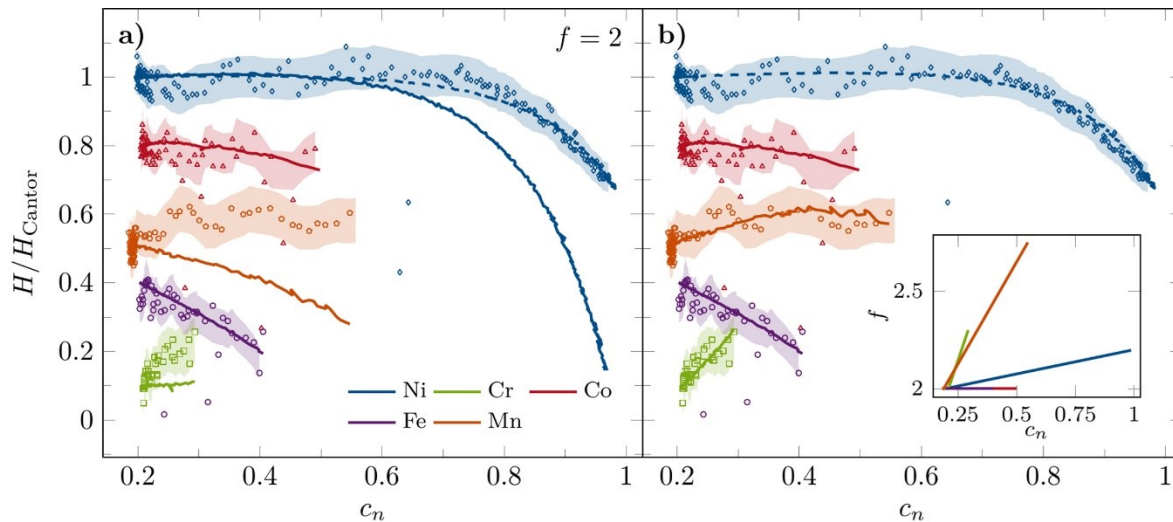


Fig. 16: Measured hardness (symbols), including coloured error bars for the indentation experiments, and predicted hardness (solid lines) for the different diffusion couples over the stable fcc phase region. The composition of the respective diffusion partner element is scaled on the x-axis. Measured and calculated hardness is normalized by the hardness of the equimolar alloy H_{Cantor} . a) shows the calculated hardness from the Varvenne model assuming a constant strain hardening behaviour in the investigated concentration gradients. b) shows the Varvenne fit assuming a concentration-dependent strain hardening factor f . The used f factors are shown in the inset. An indentation base hardness for pure Ni is additionally introduced for the Cantor+Ni diffusion couple (dashed lines). Reprinted with permission from Keil et al. [182]. Copyright (2021), Journal of Materials Research, SpringerNature.

In conclusion, the diffusion couple approach facilitates the investigation of HEAs to address phase stability aspects like maximum solubility limits of individual elements or the formation of intermetallic phases. By knowing the stability range of the fcc phase of the Cantor alloy, solid solution hardening effects can be investigated over wide concentration gradients up to the phase boundary. Thereby, going beyond previous results from discrete compositions [28]. The used SSH models can describe some hardness trends, but not all trends observed via experiment. After fitting the experimental data to introduce a correlation factor that takes the strain hardening behaviour into account, the Varvenne model represents the hardness trends well. But this is actually the crux as it is not possible to know in advance whether a model predicts the strength of a random system quite well or fails. It becomes more problematic if the SSH model is not predictive and requires strengthening parameters as input values from experiment (modified Labusch model). In consequence, the used SSH models are able to extrapolate from experimental data, but cannot be used independently. Yet this is the major endeavour for SSH models to explore the vast concentration range of HEAs without time consuming experiments. Additionally, small changes in the input parameter of the Varvenne model can cause significant changes in the predicted strength, as the model is based on a rule-of-mixtures.

5.2. Microstructural stability and mechanical properties after high pressure torsion

The results presented are published in:

Keil, T., Bruder, E., Laurent-Brocq, M. and Durst, K., *From diluted solid solutions to high entropy alloys: Saturation grain size and mechanical properties after high pressure torsion*, Scripta Materialia, 192 (2021) p. 43.

Keil, T., Taheriniya, S., Bruder, E., Wilde, G. and Durst, K., *Effects of solutes on thermal stability, microstructure and mechanical properties in CrMnFeCoNi based alloys after high pressure torsion*, Acta Materialia, 227 (2022) p. 117689.

The second main part of the thesis is based on severe plastic deformation of discrete Ni-enriched subsystems of the CrMnFeCoNi Cantor alloy. The alloy composition selection was based on the evolution of lattice parameter [27] and hardness [27, 182] with varying Ni content in form of $(\text{CrMnFeCo})_x\text{Ni}_{1-x}$. Laurent-Brocq et al. [27] found a deviation of the lattice parameter from Vegards law at Ni concentrations below 60 at.%. This breakpoint coincides with the hardness trend found in the diffusion couple experiment (Fig. 13 a), where the hardness first increases with increasing solute concentration, followed by a constant hardness level for Ni concentrations between 60 and 20 at.%. Finally, four compositions (Ni20, Ni60, Ni92 and Ni100) were subjected to severe plastic deformation by HPT and were subsequently annealed over a wide temperature range. The effects of solutes on the saturation grain size, solid solution hardening, thermal or microstructural stability and mechanical properties were investigated using a combination of electron microscopy and nanoindentation to further elucidate the presumed transition between conventional dilute solid solutions and HEAs.

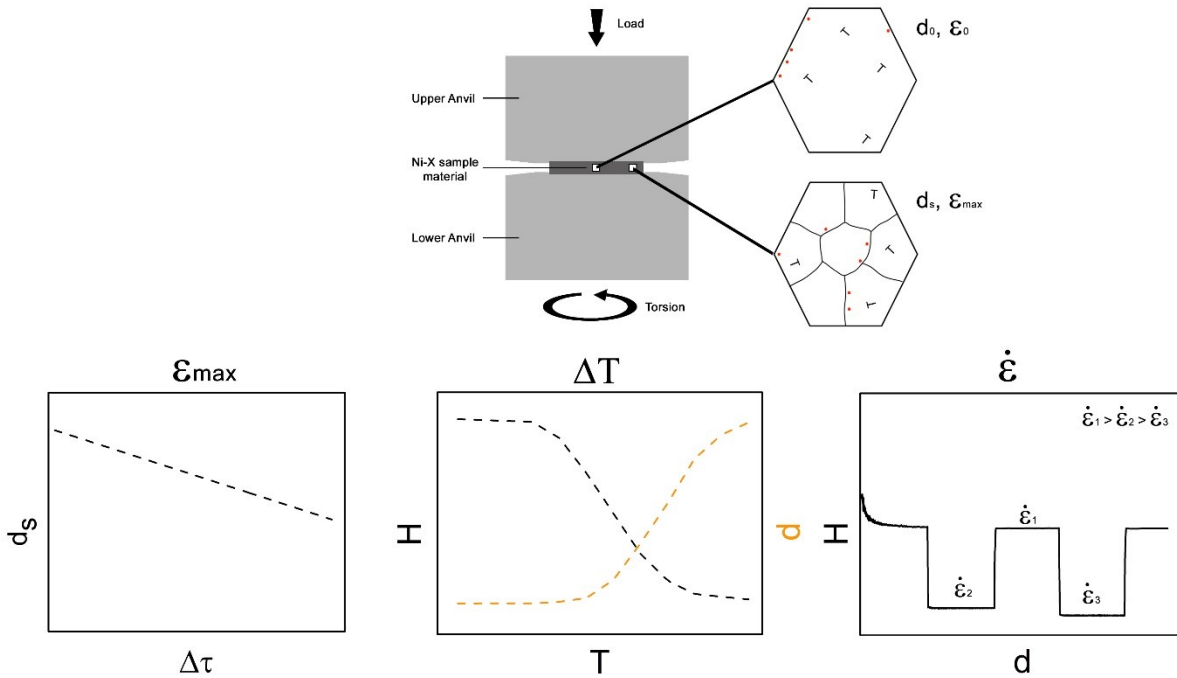


Fig. 17: Schematic illustration of the experimental procedure within the discrete sample composition approach, where the saturation grain size after deformation, the hardness change and grain growth upon annealing and the deformation behaviour at different strain rates will be analysed.

5.2.1. Steady-state microstructure after high pressure torsion

Both, SFE and SSH affect the grain refinement rate, but recent studies concerning the effect of SFE and SSH on the saturation grain size suggest that it is mainly controlled by SSH effects [111, 127, 130]. The found empirical correlation between saturation grain size and SSH contribution is explained by Edalati et al. [127] by a hindered dislocation motion necessary for dislocation recovery, grain boundary migration and recovery. Renk and Pippan [194] related the effects of alloying on d_s to a change in the grain boundary mobility. The gained knowledge from dilute solid solutions shall be used to gain further insights into SSH effects in HEAs, which are not yet fully understood. Therefore, the correlation between saturation grain size and SSH contribution predicted via different SSH models is investigated for the aforementioned compositions. Tab. 1 shows the alloy designation and composition, the different SSH contributions as well as the saturation grain size, determined by BSE images (Fig. 18). As the grain size measured in this work is in good agreement with literature values for Ni20 (50 nm [51]) and Ni100 (170 nm [195]), it is reasonable that no slip occurred during HPT deformation and all samples were strained to the saturation state. The resistance to edge dislocation motion of solute atoms is calculated using the classical Labusch model ($\Delta\tau_{Labusch}$) [72, 73, 127] and

the more recent model from Varvenne et al. [102, 103], which is specifically designed to describe SSH effects in fcc HEAs ($\Delta\tau_{\text{Varvenne}}$). While the Varvenne model assumes an effective matrix with average properties, where the solutes are embedded, the Labusch model demands a reference lattice. Even though it is not strictly valid for the equiatomic Cantor alloy, Ni is defined as the matrix element, where Cr, Mn, Fe and Co are embedded as solutes.

Tab. 1: Saturation grain size d_s and solid solution hardening contribution $\Delta\tau$ according to the Labusch and Varvenne model of the different compositions.

Alloy designation and composition	Saturation grain size d_s /nm	$\Delta\tau_{\text{Labusch}}$ /MPa	$\Delta\tau_{\text{Varvenne}}$ /MPa
Ni100	142 ± 57	0	0
Ni92 (Cr ₂ Mn ₂ Fe ₂ Co ₂ Ni ₉₂)	110 ± 45	11.10	11.03
Ni60 (Cr ₁₀ Mn ₁₀ Fe ₁₀ Co ₁₀ Ni ₆₀)	62 ± 23	33.13	40.45
Ni20 (Cr ₂₀ Mn ₂₀ Fe ₂₀ Co ₂₀ Ni ₂₀)	55 ± 17	53.87	41.36

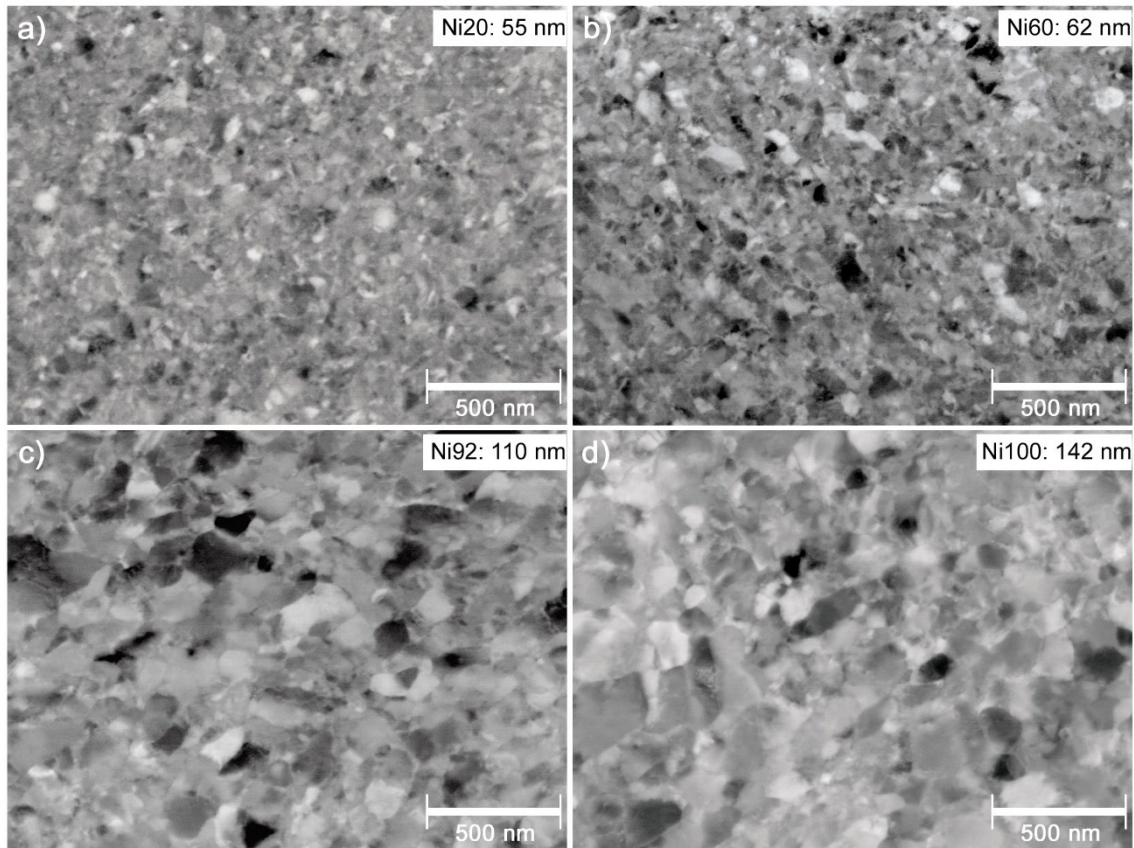


Fig. 18: Saturation microstructure of the different Ni-X alloys after HPT deformation using BSE contrast imaging: a) Ni20, b) Ni60, c) Ni92 and d) Ni100. The saturation grain size is measured using a line intercept method. Reprinted with permission from Keil et al. [129], Copyright (2021), Scripta Materialia, Elsevier.

From the BSE images shown in Fig. 18 it is apparent that the grain size after HPT deformation decreases with increasing solute concentration. The evaluation of the saturation grain size and SSH contribution according to Edalati et al. [127] reveals an inverse correlation between normalized saturation grain size (d_s/b) and $\Delta\tau$ for both SSH models (Fig. 19). The increase in solute content and thus an increase in SSH contribution leads to smaller achievable grain sizes from pure Ni to the equiatomic Cantor alloy, i.e., the higher $\Delta\tau$, the lower d_s . It is known for binary Ni alloys that solute additions increase the microstructural stability [196] and thus lower the grain boundary mobility. These differences in the grain boundary mobility due to SSH may explain the different saturation grain size after SPD.

Using the classical Labusch model, it is possible to describe the trend in normalized saturation grain size (d_s/b) using a linear fit, but its deviation increases as the solute concentration increases. It seems that the correlation found by Edalati et al. [127] using the Labusch SSH model breaks down for highly concentrated alloys. From Ni60 onwards to higher solute concentrations a plateau is more likely to form with a different slope (Fig. 19 dotted line). Despite a much higher $\Delta\tau_{Labusch}$ of Ni20 (≈ 54 MPa) compared to Ni60 (≈ 33 MPa), both show a comparable steady-state grain size. The Varvenne model on the other hand predicts similar SSH contribution for Ni20 (41.36 MPa) and Ni60 (40.45 MPa), which is in good agreement with the measured saturation grain size in combination with the correlation found by Edalati et al. [127]. Both alloys show a similar SSH contribution as well as a similar grain size, which indicates that the saturation grain size also correlates with the SSH contribution in chemically complex alloys. It seems that a transition between dilute solid solutions and high entropy-type compositions is also observable using the saturation grain size as an indicator. Both, the saturation grain size (Fig. 19) as well as the hardness (Fig. 13 a) depend on the SSH contribution, which in turn is based on the atomic size misfit or the solute misfit parameter ($\sum_n c_n \Delta V_n^2$). A direct comparison of the lattice constant, the solute misfit parameter, the SSH contribution calculated via the Varvenne model and the saturation grain size is given in Fig. 20 and reveals that a plateau is more likely to form at high solute or low Ni concentrations. This deviation from Vegards law at high solute concentrations may indicate a possible transition between conventional dilute solid solutions and HEAs.

Laurent-Brocq et al. [27] experimentally observed a deviation of the lattice parameter for the formerly discussed Ni-X samples from Vegards law (rules-of-mixtures), which is limited to pure element lattice parameters and extrapolates from dilute solid solutions. The increase in interatomic distances with increasing chemical complexity is less pronounced than predicted from Vegards law. The authors proposed that SRO could influence the evolution of lattice parameter, which may be present in HEAs (see chapter 2.3.1) [27]. The SSH model derived by Varvenne et al. [102] uses, among other material parameters, the solute misfit volume, which

is the key quantity in the theory for assessing SSH in HEAs. While it considers the atomic size misfit, shear modulus fluctuations are neglected and only the average shear modulus is taken into account (Eq. 6 & 7). The classical Labusch model on the other hand describes the interaction of obstacles and dislocations in dilute solid solutions and is based on two elastic interactions, the atomic size misfit as well as the modulus misfit [72, 73]. Satisfactory agreement between SSH contribution calculated using the Varvenne model and experimentally measured saturation grain size is found (Fig. 19), indicating that the consideration of both elastic interactions, like the Labusch model does, may not be valid for HEAs. It seems that a different strengthening mechanism plays a role, which is mainly based on the solute misfit rather than the shear modulus misfit. Even though a clear correlation has been found between experimentally observed saturation grain size and SSH contribution or solute misfit parameter, respectively, this result does not enable an extrapolation to other HEAs or element combinations nor predicts a comparable behavior for other systems.

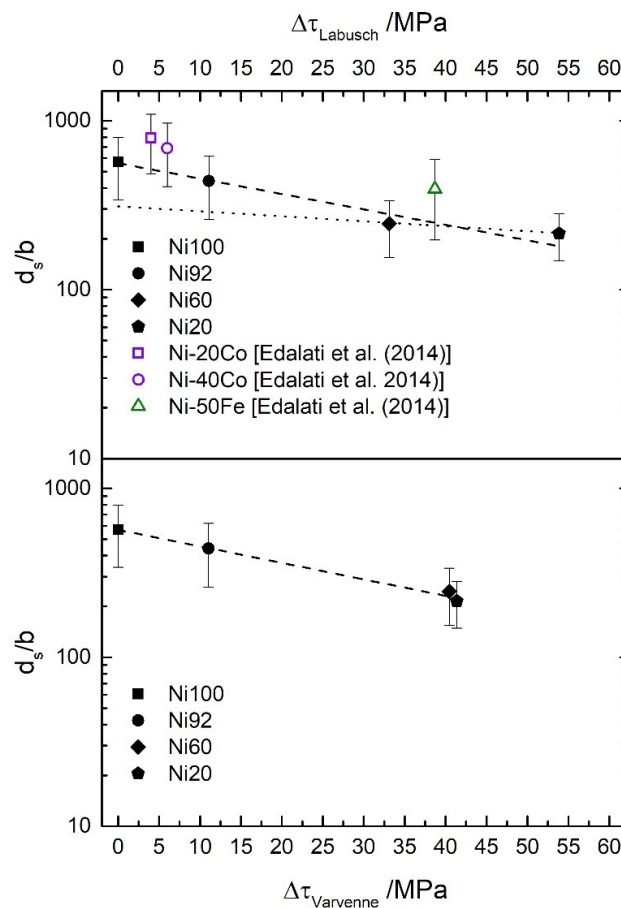


Fig. 19: Normalized saturation grain size (d_s/b) as a function of solid solution hardening contribution $\Delta\tau$ determined by the classical Labusch model (assuming Ni as the matrix element) and the Varvenne model. The dashed lines represent the linear fit of the Ni-X data, the dotted line shows the extrapolation of the Ni20 and Ni60 data. Reprinted with permission from Keil et al. [129], Copyright (2021), Scripta Materialia, Elsevier.

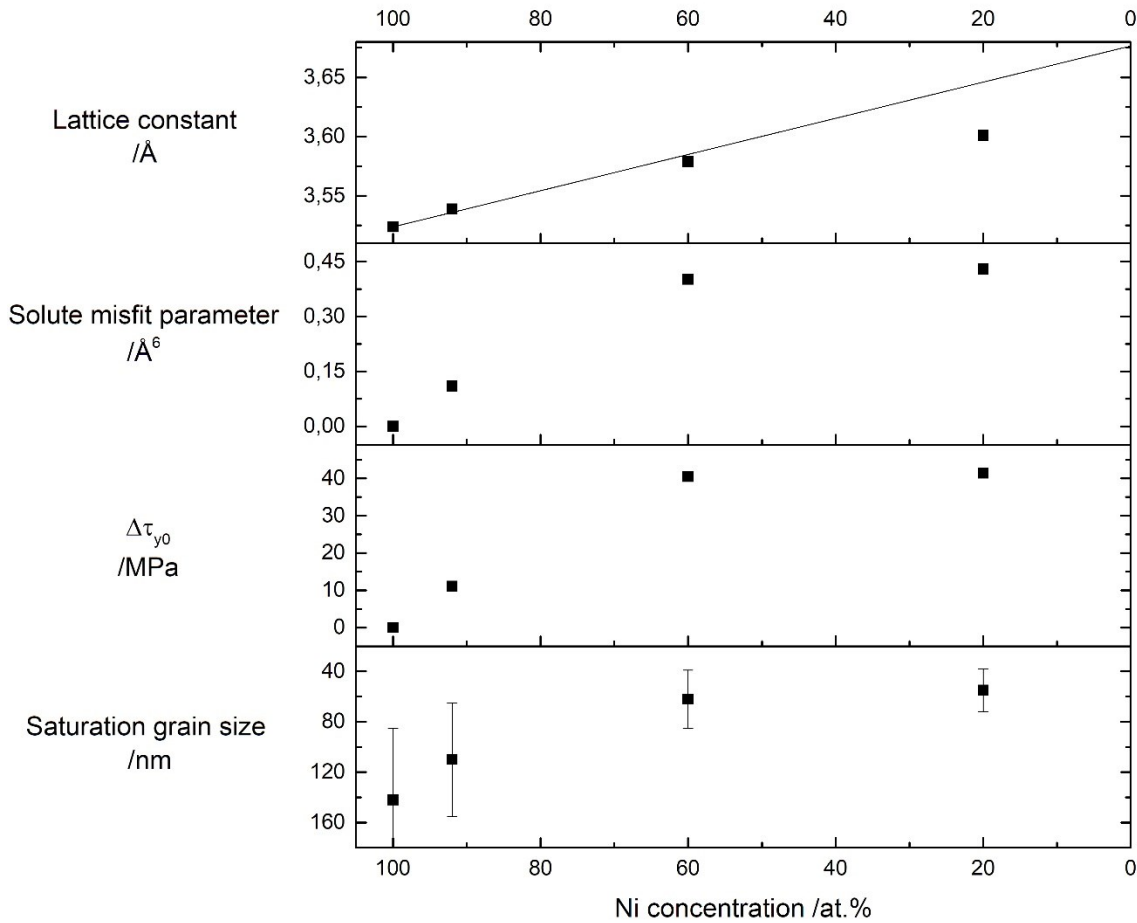


Fig. 20: Lattice constant (data taken from Ref. [27]), solute misfit parameter ($\sum_n c_n \Delta V_n^2$), SSH contribution calculated using the Varvenne model and saturation grain size as a function of Ni concentration. The solid line represents the lattice parameter evolution using Vegards law. The other constituents (Cr, Mn, Fe, Co) stay in equiatomic ratio.

5.2.2. Thermal stability and related properties

In the previous chapters, a transition in properties from dilute solid solutions to HEAs has already been shown (Fig. 20). As solutes influence the thermal stability of UFG binaries [196], the effect of solutes on the microstructure and mechanical properties is investigated via subsequent annealing of the HPT deformed Ni-X series. Annealing of the deformed states results in a coarsening of the microstructures of all compositions. The grain size is displayed as a function of annealing temperature in Fig. 21 a). It can be seen that the grain size does not change significantly after annealing at 300 °C for all compositions. The high entropy-type alloys, which show smaller saturation grain sizes compared to the dilute samples, exhibit almost no grain growth up to 500 °C annealing, where the Ni92 and Ni100 samples already start to coarsen significantly (insert Fig. 21 a). Nanostructured or UFG materials processed by severe

plastic deformation were shown to be stable against primary recrystallization, as strong recovery operates in the first stage of annealing, leading to a decrease in the dislocation density and thus in a decreasing driving force for primary recrystallization [136-139]. The occurrence of recovery in the Ni-X series is also found in form of a hardening by annealing effect and will be discussed later. A strong recovery at an early stage of annealing results in a variety of recrystallization nuclei that promote continuous or normal grain growth [138, 139]. Furthermore, Humphreys et al. [136, 137] showed in their theoretical analysis that materials, which contain a high amount of high angle grain boundaries are stable against discontinuous or abnormal grain growth. In this context the authors estimated a critical fraction of high angle grain boundaries to approx. 0.65 - 0.75, above which grain growth is continuous and below which it is discontinuous. Materials processed via HPT to the saturation state typically contain a fraction of high angle grain boundaries larger than the mentioned threshold value [121, 197]. This suggests that predominantly normal grain growth takes place in the investigated Ni-X alloy series, for which the driving force can be determined via the grain boundary curvature. The driving force for normal grain growth is inversely related to the curvature radius, which on the other hand directly correlates with the grain size [118]. Assuming that the specific grain boundary energy is constant, the driving force for normal grain growth can therefore be ordered according to the measured saturation grain size: Ni20 > Ni60 > Ni92 > Ni100. Hence, the grain growth kinetics do not seem to correlate with the stored energy (defect density) and can rather be attributed to a lower grain boundary mobility in the Ni20 and Ni60 alloys due to stronger pinning effects in the presence of higher amounts of solutes or secondary phases. As shown in chapter 2.3.4, solute segregation and secondary phase formation significantly inhibit grain boundary motion and thus coarsening of the microstructure [145-147, 149, 150]. At temperatures of 800 °C and above, strong grain growth takes place, resulting in coarse-grained, single-phase microstructures for the different compositions.

The grain growth kinetics are analysed by calculating the activation energy for grain growth Q according to Refs. [144, 174, 198] using Eq. 14:

$$\ln\left(\frac{d^n - d_0^n}{t}\right) \propto \left(-\frac{Q}{R}\right) * \frac{1}{T} \quad (14)$$

with d being the grain size, d_0 the initial grain size after HPT deformation, n the grain growth exponent, which was set to 3 for all compositions, t the annealing time, R the gas constant and T the annealing temperature. Fig. 21 b) indicates two regimes of activation energies with a transition at intermediate temperatures. The grain size remains almost constant at low temperatures, indicating that stress relaxation processes and rearrangement of unstable grain

boundary configurations take place, which is associated to low activation energies [199-201]. It is known that SPD modifies the atomic structure of grain boundaries due to the absorption of dislocations and accumulation of a high density of defects in the boundary-near region. However, only a fraction of the grain boundaries transform into a deformation-affected state [202-204]. Divinski et al. [205, 206] propose a picture of a composite structure of deformation-modified grain boundaries interspersed with non-modified areas (original or relaxed grain boundary structure) for severely deformed materials. This composite structure incorporates pinned regions of high stability against displacement, resulting in a stabilization of such grain boundary configurations against relaxation [205, 206].

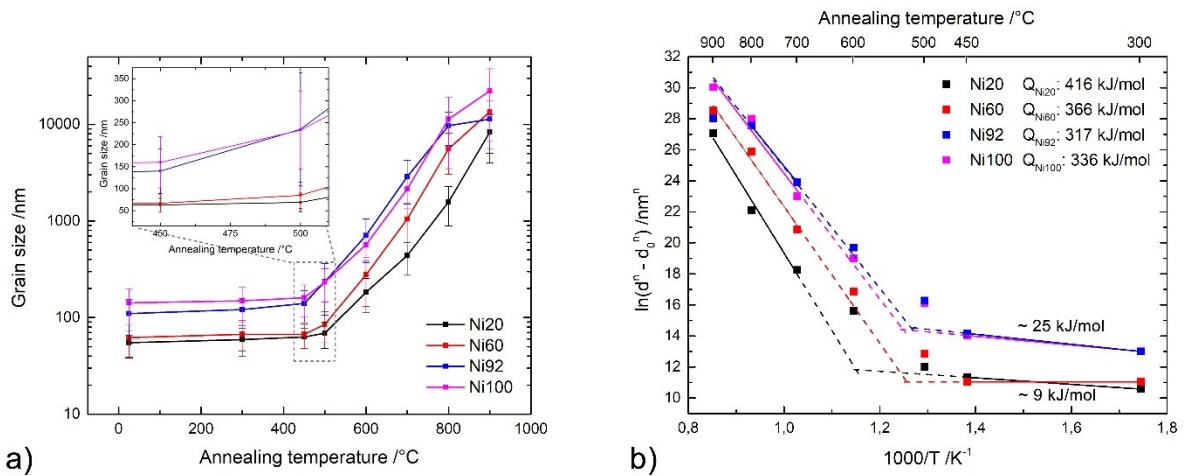


Fig. 21: a) grain size after 1h annealing at various temperatures for the different Ni-X compositions and b) arrhenius plot of $\ln(D^n - D_0^n)$ vs. $1000/T$. Reprinted with permission from Keil et al. [207], Copyright (2022), Acta Materialia, Elsevier.

At higher temperatures, the alloys start to coarsen significantly. The corresponding activation energies for grain growth (see Fig. 21 b) are similar to that of volume diffusion [208], hence, diffusion processes may be responsible for grain growth. The diffusion rates of the different alloys are known from tracer diffusion experiments [208] and can be ordered as $\text{Ni92} > \text{Ni100} > \text{Ni60} > \text{Ni20}$. A comparison with the calculated activation energies for grain growth shows a good qualitative agreement, indicating a correlation between diffusion coefficient D and activation energy Q for dilute solid solutions as well as for HEAs. The aforementioned high temperature regime with significant grain growth is shifted to higher temperatures in case of the more complex Ni20 and Ni60 alloys, indicating a higher thermal stability.

The grain growth kinetics are typically governed by the elemental distribution e.g. solute drag or Zener drag. As the decomposition tendencies of the Cantor alloy are thoroughly described elsewhere [50-52], the present studies regarding segregation or secondary phase formation

focus on the Ni60 and Ni92 alloys and aim at the aforementioned transition behaviour. While BSE contrast images do not show secondary phases in the Ni60 alloy after annealing at 700 °C (Fig. 22 b), a different picture emerges from scanning transmission electron microscope (STEM) analysis (Fig. 22 c). Cr-rich precipitates with an fcc crystal structure and an average size of approx. 40 nm can be seen at grain boundaries as well as inside the grains. While various secondary phases with significant volume fractions are expected after annealing of the equiatomic Cantor alloy at comparable temperature and exposure time (approx. 10 vol.% [51]), the volume fraction of the Cr-rich phase in the Ni60 alloy is very low and saturates at a value of about 1 vol.%, independent of the annealing time or temperature [207]. However, if the system has more time (10h or 100h), Mn segregations form at high angle grain boundaries in the Ni60 alloy as shown in Fig. 22 e), providing a further dragging force against grain boundary migration. Diffusion measurements on the specific alloy compositions used in this work revealed considerable differences in the elemental diffusivities, with Cr and Mn showing the highest diffusivities [26]. The Ni92 alloy on the other hand does not show any precipitates after annealing at 600 °C for 1h. Hence, the entropic contribution is not the main factor stabilizing a single-phase solid solution. Taking the precipitation formation as a further classification parameter into account, the investigated alloys show once more the same tendency of grouping into high entropy-type (Ni20 and Ni60) and dilute (Ni92 and Ni100) solid solutions. Here, the chemically complex alloys show decomposition, which is most pronounced for the Ni20 alloy (highest configurational entropy), indicating a limited effect of the configurational entropy on the thermal stability. The reduced number of secondary phases and their reduced volume fractions indicate a more stable structure for Ni60 showing similar coarsening tendencies compared to Ni20. Utt et al. [147] showed in their recent work that the grain boundary mobility is not intrinsically reduced in HEAs due to lattice distortions or local chemical fluctuations. Hence, the observed reduced grain growth of the high entropy-type alloys in comparison to the dilute solid solutions can be attributed to a kinetic stabilization facilitated by solute drag [118, 209] and Zener pinning [118, 149].

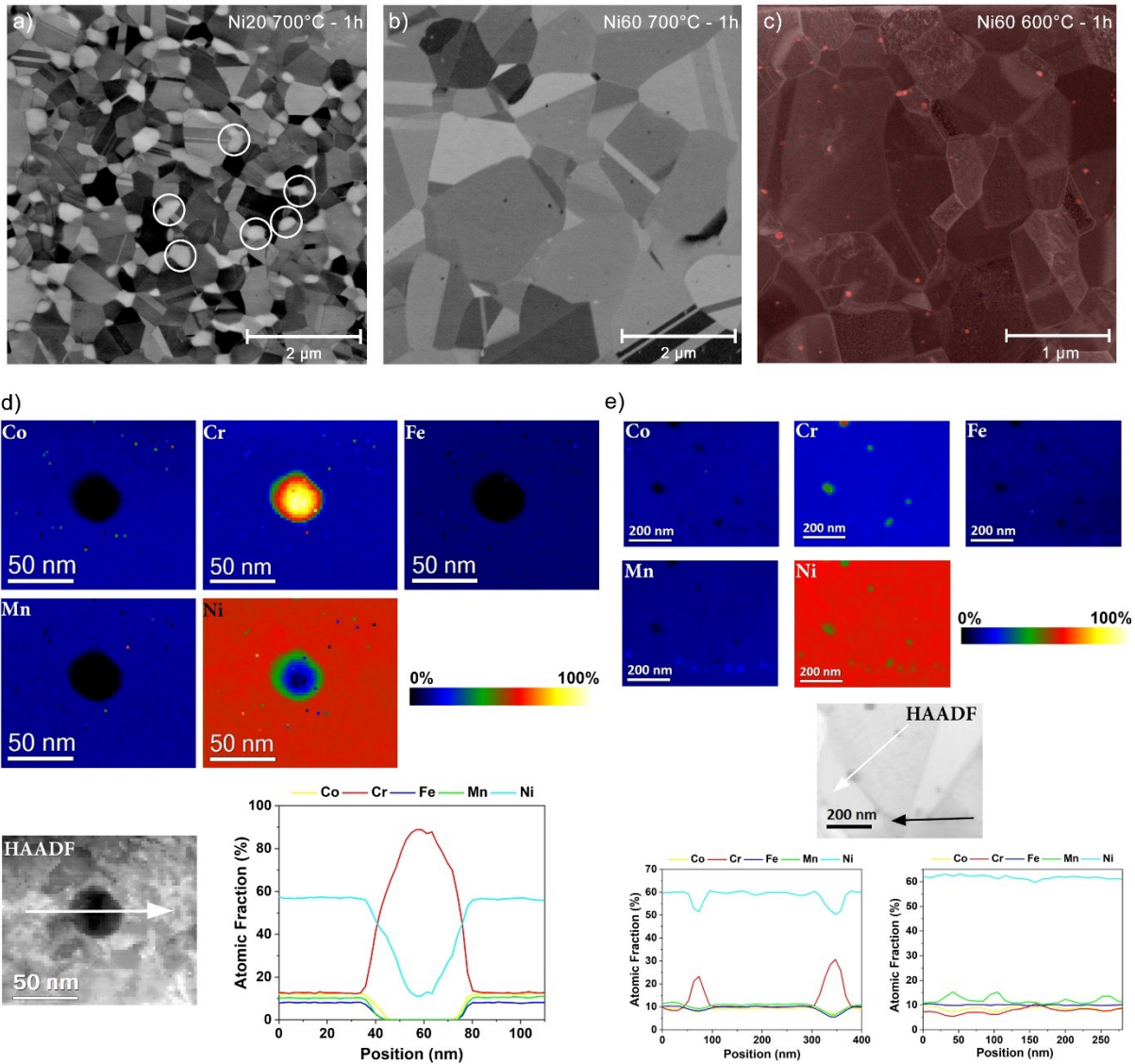


Fig. 22: Advanced microscopy results of Ni20 and Ni60 after HPT deformation and annealing. a) – b) BSE images showing the microstructure after annealing (1h) at 700 °C (secondary phases are indicated by circles). c) STEM high-angle annular dark-field (HAADF) micrograph with overlapping Cr elemental map showing precipitation formation of the Ni60 alloy after annealing at 600 °C for 1 h. Electron energy loss spectroscopy (EELS) high loss relative composition maps and the corresponding line profiles of the Ni60 alloy annealed at 600 °C for d) 1 h and e) 100 h. In e), the line scan over Cr-rich precipitates inside the grain (white arrow) is shown on the left and the line scan over Mn enrichments at a grain boundary (black arrow) is shown on the right. A higher annealing time triggers the formation of Mn segregations at grain boundaries, but results in no further change of the Cr-rich secondary phase. Adapted and reprinted with permission from Keil et al. [207], Copyright (2022), Acta Materialia, Elsevier.

The effects of solutes on the thermal stability can also be observed using the change in hardness after annealing. As it is known for dilute solid solutions, an addition of solutes increases the thermal stability, depending on the type of solutes (atomic size mismatch) and their amount [196, 210]. In the present study, nanoindentation testing is used to measure the effect of annealing on the microstructure and the mechanical properties to further elucidate the role of solutes in the CrMnFeCoNi system and its variants (Fig. 23).

The different compositions have shown significant material pile-up during indentation, depending on the annealing temperature or microstructure (UFG regime), respectively. This behaviour can be attributed to the low work hardening capability of the samples after SPD [211]. The pile-up formation changes during annealing, showing a peak in pile-up height at intermediate temperatures (see chapter 8.2. Publication D for a detailed description of the pile-up formation). Consequently, the evaluation of the indentation data using the Oliver-Pharr method [184] do not give proper values as only sink-in is considered in the method. The contact area obtained from the Oliver-Pharr method (A_{O-P}) has been corrected according to the procedure proposed by Kese et al. [212] and the corrected hardness and modulus values are shown in Fig. 23. In a previous work by Maier-Kiener et al. [53] from 2017, the pile-up behaviour was not considered, hence, the interpretation of the data was misleading.

In the as-deformed state, Ni20 and Ni60 show comparable hardness values of approx. 4.9 GPa, which is consistent to the similar SSH contribution and saturation grain size found for both alloys (Fig. 20). In addition, this hardness level is much higher than those of the dilute solid solutions. This is related to the higher SSH and Hall-Petch [167, 168] contributions. Low temperature annealing (300 °C) results in a slightly increased hardness for most of the compositions while keeping the grain size almost constant. This increase can be related to the hardening by annealing effect, where the number of free dislocations and dislocation sources is reduced without significant grain growth or recrystallization [213, 214]. After this short period of hardening, the hardness increases further to a peak value of 5.38 GPa for Ni20 at 500 °C, remains constant up to 450 °C for Ni60 or starts to decrease substantially for Ni92 and Ni100. The hardness increase for Ni20 may be an indicator for the formation of secondary phases, which takes place at intermediate temperatures in form of NiMn, FeCo or Cr-rich precipitates [50, 51, 215]. The constant hardness of the Ni60 alloy up to 450 °C correlates well with the measured grain size, which also remains nearly constant in the mentioned temperature range, indicating a high microstructural stability. Ni92 and Ni100 on the other hand already starts to soften at this temperature due to significant grain growth. Annealing at temperatures above 500 °C cause a decrease in hardness for all compositions due to grain coarsening as described by the Hall-Petch relation [167, 168]. In the coarse-grained state after annealing at 900 °C, where single-phase solid solutions are observable for all compositions, the hardness correlates with the alloying content, i.e., the higher the solute concentration and thus the higher the SSH contribution, the higher the hardness.

The indentation modulus shows similar trends for all compositions with a slightly decreased modulus for the as-deformed states followed by a small continuous increase towards the coarse-grained states after high temperature annealing. The lowered indentation modulus in the as-deformed state is presumably not attributed to the high grain boundary density after HPT, since

an effect of grain boundary density on the elastic properties is only expected at much smaller grain sizes [216]. Another hypothesis on the origin of the slightly reduced modulus refers to crystallographic texture present after shear deformation. However, texture analysis for Ni20 [125, 126] and Ni100 [123, 217] from literature and Ni60 and Ni92 from the present study [207] indicate that the reduced modulus is not caused by crystallographic texture or a change thereof due to annealing. Instead, samples showing pronounced material pile-up during indentation (preferably in the as-deformed state and annealed in the low and intermediate temperature range) also show reduced modulus values. Accordingly, the effect of a slightly reduced modulus could be attributed to small overestimations of the contact area, if not all of the piled-up material is in direct contact with the indenter tip. In literature [53], a significant modulus peak was observed for Ni20 after HPT and isochronal annealing (1h) at intermediate temperatures, which was attributed to secondary phase formation. This effect is also observable in the raw indentation data calculated by the Oliver-Pharr method, even for the compositions showing no precipitation formation [207]. As this peak in modulus is not apparent after contact area correction (Fig. 23 a), it may be concluded that this peak formation observed for the Ni20 alloy in literature [53] is caused by material pile-up and not by the limited amount of secondary phases (approx. 10 vol.% [51]).

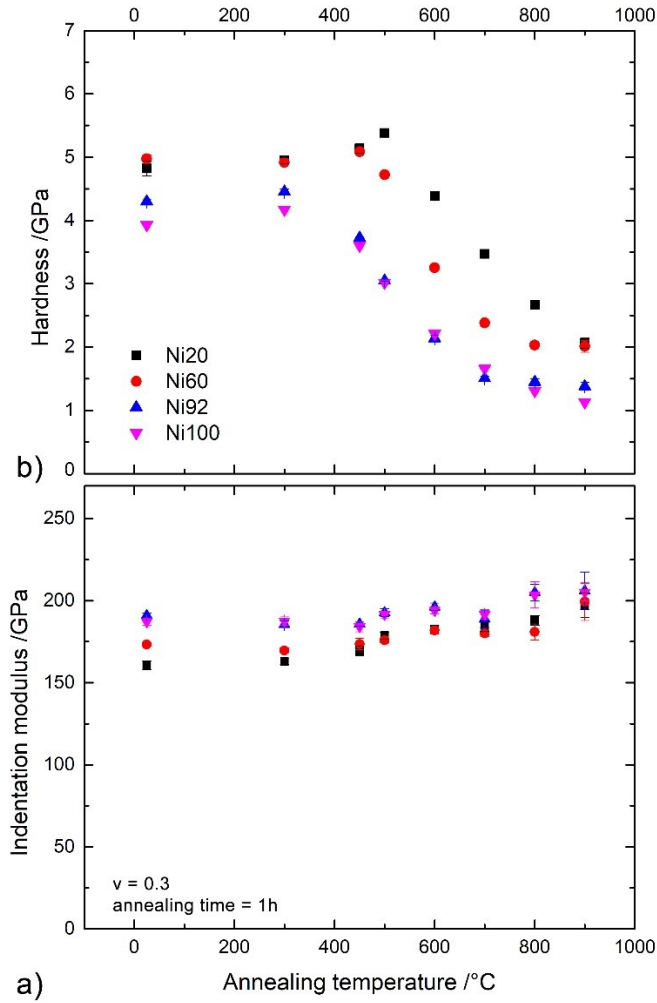


Fig. 23: Nanoindentation results of the HPT deformed Ni-X compositions after isochronal annealing at different temperatures (1h). a) indentation modulus and b) hardness measured at room temperature. Reprinted with permission from Keil et al. [207], Copyright (2022), Acta Materialia, Elsevier.

The strain rate sensitivity (SRS) and the derived activation volumes are measured using nanoindentation strain rate jump tests [218]. While samples with a nc or UFG microstructure in the low temperature regime show an almost depth independent hardness at higher indentation depth (> 1000 nm), the hardness needs to be corrected for the coarse-grained samples according to the Nix-Gao model [219]. A change in strain rate results in a change in hardness, where higher hardness values are found at higher strain rates. This change in hardness with changing strain rate is used to measure the strain rate sensitivity exponent m of the material, which is defined for nanoindentation according to Ref. [218] as:

$$m_{\text{nanoindentation}} = \frac{d(\ln H)}{d(\ln \dot{\epsilon})} \quad (15)$$

The corresponding apparent activation volume V^* can be written as [218]:

$$V^* = \frac{C\sqrt{3}k_B T}{mH} \quad (16)$$

with C the constraint factor, which is usually equal to 3 for metals [186], k_B the Boltzmann constant and T the test temperature of 25 °C. The activation volume for plastic deformation is related to the deformation mechanisms involved [220].

A different transient behaviour after the strain rate jump can be observed for the high entropy-type compositions (Ni20, Ni60) on the one hand and the dilute solid solutions (Ni92, Ni100) on the other hand as shown in Fig. 24 c). The high entropy-type alloys exhibit a yield point behaviour with softening after a strain rate jump, followed by a short section of strain hardening. This yield point behaviour is observable to the same extent after annealing at temperatures up to 600 °C. In this regime, a UFG microstructure is present for both compositions. The Ni92 and Ni100 samples exhibit the same yield point phenomenon in the as-deformed state, but less pronounced. Annealing at 300 °C results in a somewhat stronger strain hardening section. This phenomenon vanishes at temperatures above 300 °C.

It is known from stress reduction tests of nc Ni alloys [221, 222] that dislocation-based plasticity is suppressed after a stress drop due to temporarily pinning of mobile dislocations by solutes so that dynamic recovery by means of grain boundary processes get more prominent. Consequently, dynamic recovery of defects controls the strength by reducing the dislocation density while contributing to plastic strain. With further straining, hardening of the microstructure takes place, as mobile dislocations need to be generated, followed by a dynamic equilibrium of defect annihilation and generation. [221, 222] The observed transition behaviour of Ni20 and Ni60 can be described with the aforementioned processes and can thus be attributed to the high solute concentration in combination with a grain size in the nc and lower UFG regime, where grain boundary mediated processes are decisive [221]. The more pronounced yield point phenomena for Ni92 and Ni100 after annealing at 300 °C compared to the as-deformed state may be caused by the reduction of mobile dislocations during annealing [213, 214], while keeping the grain size almost constant in the lower UFG regime. The reduction in stress by reducing the strain rate in combination with the reduced number of mobile dislocations after annealing results in a suppressed forward glide of dislocations and recovery mechanisms start to dominate. As described above, further straining results in a short hardening section of the material due to dislocation nucleation.

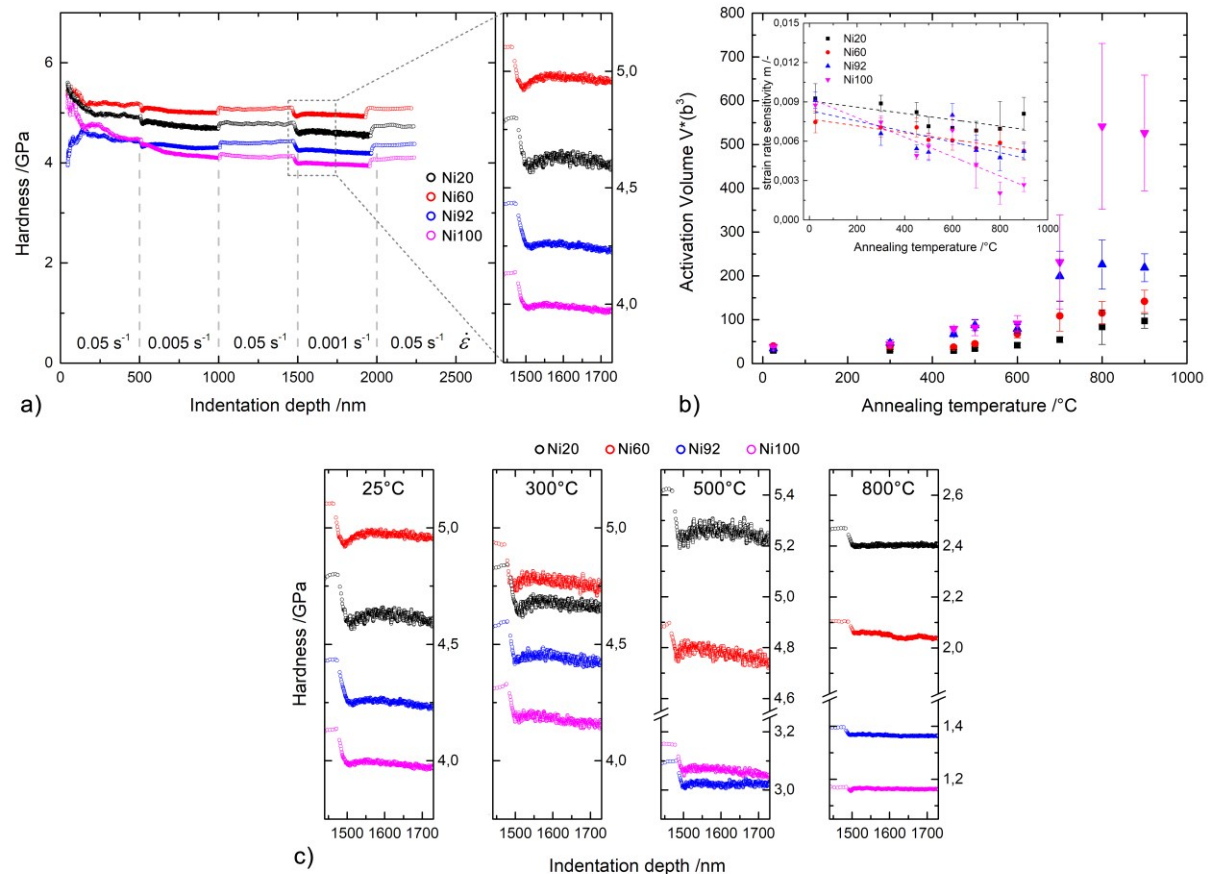


Fig. 24: a) hardness (pile-up corrected) vs. indentation depth for the Ni-X samples in the as-deformed state and b) activation volume and strain rate sensitivity vs. annealing temperature. The nanoindentation strain rate jump tests were performed at room temperature. Reprinted with permission from Keil et al. [207], Copyright (2022), Acta Materialia, Elsevier.

The strain rate sensitivity increases with decreasing grain size, as dislocation – grain boundary interactions getting more pronounced [218, 223, 224], the activation volume behaves inversely according to Eq. 16. In the as-deformed state, all compositions show nearly identical activation volumes in the range of 30 b³. This corresponds to dominating dislocation-glide based plasticity (dislocation cross-slip and/or dislocation nucleation), which acts in the range up to 100 b³. [225-227]. After high temperature annealing, alloys with a higher alloying content show lower activation volumes. Furthermore, Ni20, Ni60 as well as Ni92 show much smaller V* compared to Ni100. This behaviour may be attributed to the higher SSH contribution that have to be overcome thermally activated, similar to the Peierls mechanism in bcc alloys [53]. For Ni100, dislocation-dislocation interactions are expected in the coarse-grained states based on the V*, which is in the range of several hundred b³ [227].

The change in hardness after annealing and the differences in the transient behavior indicate that SSH strongly influence the microstructural stability, i.e., the grain boundary kinetics. For

samples showing higher solute content, a pronounced hardness plateau is observable at higher temperatures, referring to lower grain boundary mobilities and thus higher structural stabilities. The transient behavior after a strain rate jump indicate more stable microstructures for samples with higher SSH contributions. The lower mobility of the grain boundaries in turn explains the differences in grain refinement and thus the different saturation grain size.

6. Summary

The present thesis, which was carried out in the DFG framework “SPP2006: Compositionally Complex Alloys – High Entropy Alloys”, focuses on the phase stability and solid solution hardening effects of the single-phase fcc CrMnFeCoNi Cantor alloy and compositional deviations thereof using diffusion couples and discrete sample compositions.

Diffusion couples were used to explore the multi-component space of HEAs in terms of composition-dependent structural discontinuities and individual solubility limits. With respect to phase stability, three different scenarios were observed (single-phase, phase transition and formation of intermetallic phases) and the stability ranges were visualized in comprehensive phase stability diagrams. The maximum solubility limits of the different constituents were identified and different approaches for describing the phase stability have been discussed including the atomic size mismatch parameter or the valence electron concentration. In case of Cr-Mn-Fe-Co-Ni based compositions, the atomic size mismatch is relatively small. Hence this parameter gives no indication on the expected phase at a given composition. Guo et al. [43] utilized the VEC to describe the phase formation of cubic solid solutions, but some restrictions are associated to this model and thus the applicability to diffusion couples is only limited. Nevertheless, the observed fcc – bcc phase transitions are consistent with the predictions of the VEC model. Furthermore, SSH effects were investigated within the concentration gradients of the Cantor alloy up to the respective phase boundaries, as concentration-dependent SSH has been a topic of interest in HEA research [13, 24, 103]. While the Cantor alloy and several discrete subsystems have been characterized in terms of strength [28], this work focuses on SSH across continuous concentration gradients up to the phase boundary with an emphasis on the influence of different elements on the SSH behavior. The experimental hardness was analyzed using a modified Labusch and the Varvenne SSH model. The Labusch model was fitted to experimental data and Cr was shown to be the most potent strengthening element, which confirms previous suggestions from literature [12]. While the Labusch model is not predictive, the Varvenne model remains parameter-free in its simplified form and can therefore be used for strength predictions. After introducing a concentration-dependent strain hardening factor, the Varvenne model is able to describe the hardness trends up to the phase boundaries of all diffusion couples.

However, the used diffusion couple approach for studying the phase stability and SSH is also accompanied by some issues. First, a direct control of the local composition is not feasible, since all concentrations change simultaneously depending on the diffusion kinetics. Second, knowledge of the concentration-dependent strain hardening behavior during indentation is essential to relate the experimental hardness to strength predictions from SSH models.

Measuring the local strain hardening is linked to a high experimental effort. The flow behavior could be determined by means of a nanoindentation multiple sharp tip approach [228], by spherical indentation or by uniaxial micropillar compression tests [192].

Since Ni-enriched subsystems of the Cantor alloy show single-phase fcc structures throughout the concentration range, $(\text{CrMnFeCo})_x\text{Ni}_{1-x}$ material systems were used to study the transition from high entropy-type alloys to dilute solid solutions. The effects of solutes on the mechanical properties and microstructural evolution during deformation and annealing were comprehensively investigated using HPT, electron microscopy (SEM & TEM) and nanoindentation. An inverse correlation between d_s and SSH was found, i.e., higher SSH contributions cause smaller saturation grain sizes. Using the classical Labusch model, it is possible to describe the trend in grain size using a linear fit, however, the deviation increases at higher solute concentrations. The Varvenne model on the other hand predicts similar SSH contributions of the high entropy-type alloys (Ni20, Ni60), which is in good agreement with the measured grain size in combination with the Edalati correlation. The present results suggest that d_s correlates with SSH not only in binary systems but also in HEAs. Furthermore, the shown trend in saturation grain size indicates that the atomic size misfit may be the main contributor to SSH in fcc HEAs rather than fluctuations in the shear modulus, as agreement is only found for the Varvenne model and not for the Labusch model. It seems that another mechanism for SSH may operate in HEAs, indicating a transition between dilute solid solutions and HEAs.

Annealing of the Ni-X series results in grain growth and, if thermodynamically favourable, in segregation or secondary phase formation. While the decomposition tendencies of the Cantor alloy are already known in literature, see e.g. Ref. [51], the present study revealed Mn segregations at high angle grain boundaries and the formation of Cr-rich nanophases in the Ni60 alloy. Furthermore, the decomposition is limited to the high entropy-type alloys, as no segregations are observed for Ni92 after annealing. The grain coarsening behaviour was studied and a reduced grain boundary mobility was observed for the Ni20 and Ni60 alloys, which can be attributed to the kinetic stabilization due to pinning effects of solutes (solute drag) or the presence of secondary phases (Zener drag) and rather not to lattice distortions or local chemical fluctuations [145-147, 149]. The activation energy for grain growth was calculated for the alloys and two different temperature regimes have been found with significantly different activation energies. While at low temperatures stress relaxation processes and rearrangement of unstable grain boundary configurations dominate without significant grain growth, diffusion processes prevail at higher temperatures, resulting in grain coarsening. A comparison of the activation energies for grain growth Q and the diffusion coefficients D from tracer diffusion [208] reveals good qualitative agreement, indicating a correlation between Q and D .

The effect of solutes on the microstructural stability upon annealing was further studied by means of nanoindentation. The investigated compositions showed in the nc and UFG regime significant material pile-up during indentation, which changes with annealing temperature. In the as-deformed state, the hardness increases with increasing SSH contribution with its maximum for Ni60. This trend is caused by the higher SSH itself and the smaller saturation grain size, which in turn is also a consequence of the stronger SSH. Subsequent to a short period of hardening after annealing at 300 °C, different hardness trends evolve for the investigated compositions at intermediate temperatures. The high entropy-type alloys show a constant or increasing hardness up to 450 – 500 °C, where the grain size remains almost constant. The hardness of the dilute solid solutions already drops significantly after annealing in this temperature regime due to grain growth. However, the indentation modulus is not effected by the change in grain size or the formation of secondary phases at the given volume fraction. In this respect, nanoindentation hardness testing can be used to experimentally examine the composition-dependent thermal stability, indicating a higher microstructural stability for Ni20 and Ni60 even at smaller grain size (higher defect density). Nanoindentation strain rate jump tests revealed differences in the transient behaviour between the Ni20 and Ni60 high entropy-type alloys and the dilute Ni92 and Ni100 solid solutions, which can be attributed to the different amount of solutes. The determined strain rate sensitivity or activation volume for plastic deformation provided insights into the thermally activated deformation processes with dislocation-glide based plasticity in the as-deformed states and after annealing at temperatures up to 600 °C. The relatively small activation volumes of the Ni20, Ni60 and Ni92 alloy after high temperature annealing indicate that SSH needs to be overcome by thermal activation, which is comparable to the Peierls mechanism in bcc metals. In summary, the effects of solutes or SSH on the grain refinement, the thermal stability including grain growth and decomposition and on the mechanical properties have been investigated. Based on the evolution of the lattice parameter, Laurent-Brocq et al. [27] proposed a transition from dilute solid solutions to HEAs. The results of the present work points in the same direction. First, the hardness trend of the Cantor+Ni diffusion couple indicate a transition at approx. 60 at.% Ni (Fig. 13 a). Second, there is also a breakpoint in d_s and SSH contribution for the Ni-enriched derivatives of the Cantor alloy at the same Ni concentration (Fig. 20). Third, decomposition is limited to compositions with 60 at.% Ni and lower.

7. References

1. Gottstein, G., *Materialwissenschaft und Werkstofftechnik*. Vol. 4. 2014: SpringerVieweg ISBN: 978-3-642-36602-4.
2. George, E.P., Raabe, D., and Ritchie, R.O., *High-entropy alloys*. *Nature Reviews Materials*, 2019. **4**(8): p. 515-534 DOI: 10.1038/s41578-019-0121-4.
3. Yeh, J.-W., et al., *Nanostructured High-Entropy Alloys with Multiple Principal Elements Novel Alloy Design Concepts and Outcomes*. *Advanced Engineering Materials*, 2004: p. 299-303 DOI: 10.1002/adem.200300567.
4. Cantor, B., et al., *Microstructural development in equiatomic multicomponent alloys*. *Materials Science and Engineering: A*, 2004. **375-377**: p. 213-218 DOI: 10.1016/j.msea.2003.10.257.
5. Tsai, M.-H. and Yeh, J.-W., *High-Entropy Alloys: A Critical Review*. *Materials Research Letters*, 2014. **2**(3): p. 107-123 DOI: 10.1080/21663831.2014.912690.
6. Davis, J.R., *Alloying: understanding the basics*. 2001: ASM international ISBN: 1615030638.
7. Darolia, R., *Development of strong, oxidation and corrosion resistant nickel-based superalloys: critical review of challenges, progress and prospects*. *International Materials Reviews*, 2018. **64**(6): p. 355-380 DOI: 10.1080/09506608.2018.1516713.
8. Webler, R., et al., *Evolution of microstructure and mechanical properties of coated Co-base superalloys during heat treatment and thermal exposure*. *Materials Science and Engineering: A*, 2015. **628**: p. 374-381 DOI: 10.1016/j.msea.2015.01.060.
9. Gali, A. and George, E.P., *Tensile properties of high- and medium-entropy alloys*. *Intermetallics*, 2013. **39**: p. 74-78 DOI: 10.1016/j.intermet.2013.03.018.
10. Otto, F., et al., *The influences of temperature and microstructure on the tensile properties of a CoCrFeMnNi high-entropy alloy*. *Acta Materialia*, 2013. **61**(15): p. 5743-5755 DOI: 10.1016/j.actamat.2013.06.018.
11. Yeh, J.-W., *Physical Metallurgy of High-Entropy Alloys*. *Jom*, 2015. **67**(10): p. 2254-2261 DOI: 10.1007/s11837-015-1583-5.
12. Wu, Z., et al., *Temperature dependence of the mechanical properties of equiatomic solid solution alloys with face-centered cubic crystal structures*. *Acta Materialia*, 2014. **81**: p. 428-441 DOI: 10.1016/j.actamat.2014.08.026.
13. George, E.P., Curtin, W.A., and Tasan, C.C., *High entropy alloys: A focused review of mechanical properties and deformation mechanisms*. *Acta Materialia*, 2020. **188**: p. 435-474 DOI: 10.1016/j.actamat.2019.12.015.
14. Gludovatz, B., *A fracture-resistant high-entropy alloy for cryogenic applications*. *sciencemag*, 2014. **345** DOI: 10.1126/science.1254581.
15. Senkov, O.N., et al., *Mechanical properties of Nb₂₅Mo₂₅Ta₂₅W₂₅ and V₂₀Nb₂₀Mo₂₀Ta₂₀W₂₀ refractory high entropy alloys*. *Intermetallics*, 2011. **19**(5): p. 698-706 DOI: 10.1016/j.intermet.2011.01.004.
16. Senkov, O.N., et al., *Microstructure and elevated temperature properties of a refractory TaNbHfZrTi alloy*. *Journal of Materials Science*, 2012. **47**(9): p. 4062-4074 DOI: 10.1007/s10853-012-6260-2.
17. Gludovatz, B., George, E.P., and Ritchie, R.O., *Processing, Microstructure and Mechanical Properties of the CrMnFeCoNi High-Entropy Alloy*. *Jom*, 2015. **67**(10): p. 2262-2270 DOI: 10.1007/s11837-015-1589-z.
18. Shi, Y., Yang, B., and Liaw, P., *Corrosion-Resistant High-Entropy Alloys: A Review*. *Metals*, 2017. **7**(2) DOI: 10.3390/met7020043.
19. Qiu, X.-W., et al., *Microstructure and corrosion resistance of AlCrFeCuCo high entropy alloy*. *Journal of Alloys and Compounds*, 2013. **549**: p. 195-199 DOI: 10.1016/j.jallcom.2012.09.091.

20. Qiu, Y., et al., *Corrosion of high entropy alloys*. npj Materials Degradation, 2017. **1**(1) DOI: 10.1038/s41529-017-0009-y.
21. Gorr, B., et al., *Phase equilibria, microstructure, and high temperature oxidation resistance of novel refractory high-entropy alloys*. Journal of Alloys and Compounds, 2015. **624**: p. 270-278 DOI: 10.1016/j.jallcom.2014.11.012.
22. Butler, T.M. and Weaver, M.L., *Oxidation behavior of arc melted AlCoCrFeNi multi-component high-entropy alloys*. Journal of Alloys and Compounds, 2016. **674**: p. 229-244 DOI: 10.1016/j.jallcom.2016.02.257.
23. Steurer, W., *Single-phase high-entropy alloys – A critical update*. Materials Characterization, 2020. **162** DOI: 10.1016/j.matchar.2020.110179.
24. Miracle, D.B. and Senkov, O.N., *A critical review of high entropy alloys and related concepts*. Acta Materialia, 2017. **122**: p. 448-511 DOI: 10.1016/j.actamat.2016.08.081.
25. Laurent-Brocq, M., et al., *From high entropy alloys to diluted multi-component alloys: Range of existence of a solid-solution*. Materials & Design, 2016. **103**: p. 84-89 DOI: 10.1016/j.matdes.2016.04.046.
26. Kottke, J., et al., *Tracer diffusion in the Ni–CoCrFeMn system: Transition from a dilute solid solution to a high entropy alloy*. Scripta Materialia, 2019. **159**: p. 94-98 DOI: 10.1016/j.scriptamat.2018.09.011.
27. Laurent-Brocq, M., et al., *From diluted solid solutions to high entropy alloys: On the evolution of properties with composition of multi-components alloys*. Materials Science and Engineering: A, 2017. **696**: p. 228-235 DOI: 10.1016/j.msea.2017.04.079.
28. Bracq, G., et al., *Combining experiments and modelling to explore the solid solution strengthening of high and medium entropy alloys*. Acta Materialia, 2019 DOI: 10.1016/j.actamat.2019.06.050.
29. Pickering, E.J. and Jones, N.G., *High-entropy alloys: a critical assessment of their founding principles and future prospects*. International Materials Reviews, 2016. **61**(3): p. 183-202 DOI: 10.1080/09506608.2016.1180020.
30. Li, L., et al., *Segregation-driven grain boundary spinodal decomposition as a pathway for phase nucleation in a high-entropy alloy*. Acta Materialia, 2019. **178**: p. 1-9 DOI: 10.1016/j.actamat.2019.07.052.
31. Yeh, J.-W., *Alloy Design Strategies and Future Trends in High-Entropy Alloys*. Jom, 2013. **65**(12): p. 1759-1771 DOI: 10.1007/s11837-013-0761-6.
32. Yeh, J.-W., *Recent progress in high-entropy alloys*. Annales de Chimie Science des Matériaux, 2006. **31**(6): p. 633-648 DOI: 10.3166/acsm.31.633-648.
33. Yeh, J.-W., et al., *Formation of simple crystal structures in Cu-Co-Ni-Cr-Al-Fe-Ti-V alloys with multiprincipal metallic elements*. Metallurgical and Materials Transactions A, 2004. **35**(8): p. 2533-2536 DOI: 10.1007/s11661-006-0234-4.
34. Zhang, Y., et al., *Microstructures and properties of high-entropy alloys*. Progress in Materials Science, 2014. **61**: p. 1-93 DOI: 10.1016/j.pmatsci.2013.10.001.
35. Pradeep, K.G., et al., *Atomic-scale compositional characterization of a nanocrystalline AlCrCuFeNiZn high-entropy alloy using atom probe tomography*. Acta Materialia, 2013. **61**(12): p. 4696-4706 DOI: 10.1016/j.actamat.2013.04.059.
36. Praveen, S., Murty, B.S., and Kottada, R.S., *Alloying behavior in multi-component AlCoCrCuFe and NiCoCrCuFe high entropy alloys*. Materials Science and Engineering: A, 2012. **534**: p. 83-89 DOI: 10.1016/j.msea.2011.11.044.
37. Jones, N.G., et al., *On the entropic stabilisation of an Al_{0.5}CrFeCoNiCu high entropy alloy*. Intermetallics, 2014. **54**: p. 148-153 DOI: 10.1016/j.intermet.2014.06.004.
38. Otto, F., et al., *Relative effects of enthalpy and entropy on the phase stability of equiatomic high-entropy alloys*. Acta Materialia, 2013. **61**(7): p. 2628-2638 DOI: 10.1016/j.actamat.2013.01.042.
39. Cahn, R.W. and Haasen, P., *Physical metallurgy*. 4th, rev. and enhanced ed. 1996, Amsterdam: North Holland Elsevier Science B.V. ISBN: 9780080538945.

40. Hume-Rothery, W., *Elements of structural metallurgy*. 1961, London: The institute of Metals. Monograph and Report Series No. 26.
41. Hume-Rothery, W. and Raynor, G.V., *The Structure of Metals and Alloys*. Fourth edition ed. 1962, London: The institute of Metals. Monograph and Report Series No. I.
42. Gao, M.C., et al., *High-Entropy Alloys*. 2016, Switzerland: Springer-Verlag ISBN: 978-3-319-27011-1.
43. Guo, S., et al., *Effect of valence electron concentration on stability of fcc or bcc phase in high entropy alloys*. *Journal of Applied Physics*, 2011. **109**(10): p. 103505 DOI: 10.1063/1.3587228.
44. Zhang, Y., et al., *Solid-Solution Phase Formation Rules for Multi-component Alloys*. *Advanced Engineering Materials*, 2008. **10**(6): p. 534-538 DOI: 10.1002/adem.200700240.
45. Wang, Z., Guo, S., and Liu, C.T., *Phase Selection in High-Entropy Alloys: From Nonequilibrium to Equilibrium*. *Jom*, 2014. **66**(10): p. 1966-1972 DOI: 10.1007/s11837-014-0953-8.
46. Yang, X. and Zhang, Y., *Prediction of high-entropy stabilized solid-solution in multi-component alloys*. *Materials Chemistry and Physics*, 2012. **132**(2): p. 233-238 DOI: 10.1016/j.matchemphys.2011.11.021.
47. Kube, S.A., et al., *Phase selection motifs in High Entropy Alloys revealed through combinatorial methods: Large atomic size difference favors BCC over FCC*. *Acta Materialia*, 2019. **166**: p. 677-686 DOI: 10.1016/j.actamat.2019.01.023.
48. Keil, T., Bruder, E., and Durst, K., *Exploring the compositional parameter space of high-entropy alloys using a diffusion couple approach*. *Materials & Design*, 2019. **176** DOI: 10.1016/j.matdes.2019.107816.
49. Otto, F., et al., *Decomposition of the single-phase high-entropy alloy CrMnFeCoNi after prolonged anneals at intermediate temperatures*. *Acta Materialia*, 2016. **112**: p. 40-52 DOI: 10.1016/j.actamat.2016.04.005.
50. Pickering, E.J., et al., *Precipitation in the equiatomic high-entropy alloy CrMnFeCoNi*. *Scripta Materialia*, 2016. **113**: p. 106-109 DOI: 10.1016/j.scriptamat.2015.10.025.
51. Schuh, B., et al., *Mechanical properties, microstructure and thermal stability of a nanocrystalline CoCrFeMnNi high-entropy alloy after severe plastic deformation*. *Acta Materialia*, 2015. **96**: p. 258-268 DOI: 10.1016/j.actamat.2015.06.025.
52. Klimova, M.V., et al., *Effect of second phase particles on mechanical properties and grain growth in a CoCrFeMnNi high entropy alloy*. *Materials Science and Engineering: A*, 2019. **748**: p. 228-235 DOI: 10.1016/j.msea.2019.01.112.
53. Maier-Kiener, V., et al., *Nanoindentation testing as a powerful screening tool for assessing phase stability of nanocrystalline high-entropy alloys*. *Materials & Design*, 2017. **115**: p. 479-485 DOI: 10.1016/j.matdes.2016.11.055.
54. Karati, A., et al., *Thermal stability of AlCoFeMnNi high-entropy alloy*. *Scripta Materialia*, 2019. **162**: p. 465-467 DOI: 10.1016/j.scriptamat.2018.12.017.
55. Schuh, B., et al., *Thermodynamic instability of a nanocrystalline, single-phase TiZrNbHfTa alloy and its impact on the mechanical properties*. *Acta Materialia*, 2018. **142**: p. 201-212 DOI: 10.1016/j.actamat.2017.09.035.
56. Chen, S.Y., et al., *Phase transformations of HfNbTaTiZr high-entropy alloy at intermediate temperatures*. *Scripta Materialia*, 2019. **158**: p. 50-56 DOI: 10.1016/j.scriptamat.2018.08.032.
57. Pacheco, V., et al., *Thermal Stability of the HfNbTiVZr High-Entropy Alloy*. *Inorg Chem*, 2019. **58**(1): p. 811-820 DOI: 10.1021/acs.inorgchem.8b02957.
58. Schuh, B., et al., *Phase Decomposition of a Single-Phase AlTiVNb High-Entropy Alloy after Severe Plastic Deformation and Annealing* *Advanced Engineering Materials*, 2017. **19**(4): p. 1600674 DOI: 10.1002/adem.201600674.

59. Schuh, B., et al., *Influence of Annealing on Microstructure and Mechanical Properties of a Nanocrystalline CrCoNi Medium-Entropy Alloy*. Materials (Basel), 2018. **11**(5) DOI: 10.3390/ma11050662.
60. Li, Y.J., et al., *Phase decomposition in a nanocrystalline CrCoNi alloy*. Scripta Materialia, 2020. **188**: p. 259-263 DOI: 10.1016/j.scriptamat.2020.07.054.
61. Hung, P.T., et al., *Thermal stability of a nanocrystalline HfNbTiZr multi-principal element alloy processed by high-pressure torsion*. Materials Characterization, 2020. **168** DOI: 10.1016/j.matchar.2020.110550.
62. Liang, Y.J., et al., *High-content ductile coherent nanoprecipitates achieve ultrastrong high-entropy alloys*. Nat Commun, 2018. **9**(1): p. 4063 DOI: 10.1038/s41467-018-06600-8.
63. He, J.Y., et al., *A precipitation-hardened high-entropy alloy with outstanding tensile properties*. Acta Materialia, 2016. **102**: p. 187-196 DOI: 10.1016/j.actamat.2015.08.076.
64. Ren, B., et al., *Aging behavior of a CuCr2Fe2NiMn high-entropy alloy*. Materials & Design, 2012. **33**: p. 121-126 DOI: 10.1016/j.matdes.2011.07.005.
65. Dąbrowa, J. and Danielewski, M., *State-of-the-Art Diffusion Studies in the High Entropy Alloys*. Metals, 2020. **10**(3) DOI: 10.3390/met10030347.
66. Tsai, K.Y., Tsai, M.H., and Yeh, J.W., *Sluggish diffusion in Co–Cr–Fe–Mn–Ni high-entropy alloys*. Acta Materialia, 2013. **61**(13): p. 4887-4897 DOI: 10.1016/j.actamat.2013.04.058.
67. Divinski, S.V., et al., *A Mystery of "Sluggish Diffusion" in High-Entropy Alloys: The Truth or a Myth?* Diffusion Foundations, 2018. **17**: p. 69-104 DOI: 10.4028/www.scientific.net/DF.17.69.
68. Paul, A., *Comments on "Sluggish diffusion in Co–Cr–Fe–Mn–Ni high-entropy alloys" by K.Y. Tsai, M.H. Tsai and J.W. Yeh, Acta Materialia 61 (2013) 4887–4897*. Scripta Materialia, 2017. **135**: p. 153-157 DOI: 10.1016/j.scriptamat.2017.03.026.
69. Vaidya, M., et al., *Bulk tracer diffusion in CoCrFeNi and CoCrFeMnNi high entropy alloys*. Acta Materialia, 2018 DOI: 10.1016/j.actamat.2017.12.052.
70. Durand, A., et al., *Interdiffusion in Cr–Fe–Co–Ni medium-entropy alloys*. Intermetallics, 2020. **122** DOI: 10.1016/j.intermet.2020.106789.
71. Jin, K., et al., *Influence of compositional complexity on interdiffusion in Ni-containing concentrated solid-solution alloys*. Materials Research Letters, 2018. **6**(5): p. 293-299 DOI: 10.1080/21663831.2018.1446466.
72. Labusch, R., *Statistische Theorien der Mischkristallhärtung*. Acta Metallurgica, 1972. **20**: p. 917-927 DOI: 10.1016/0001-6160(72)90085-5.
73. Labusch, R., *A Statistical Theory of Solid Solution Hardening*. Phys. Stat. Sol., 1970. **41**: p. 659-669 DOI: 10.1002/pssb.19700410221.
74. Fleischer, R.L., *Solution Hardening*. Acta Metallurgica, 1961. **9**: p. 996-1000 DOI: 10.1016/0001-6160(61)90242-5.
75. Jin, K. and Bei, H., *Single-Phase Concentrated Solid-Solution Alloys: Bridging Intrinsic Transport Properties and Irradiation Resistance*. Frontiers in Materials, 2018. **5** DOI: 10.3389/fmats.2018.00026.
76. Kao, Y.-F., et al., *Electrical, magnetic, and Hall properties of Al_xCoCrFeNi high-entropy alloys*. Journal of Alloys and Compounds, 2011. **509**(5): p. 1607-1614 DOI: 10.1016/j.jallcom.2010.10.210.
77. Fèvre, M., et al., *Influence of atomic size mismatch on binary alloy phase diagrams*. Philosophical Magazine, 2013. **93**(13): p. 1563-1581 DOI: 10.1080/14786435.2012.748223.
78. Owen, L.R., et al., *An assessment of the lattice strain in the CrMnFeCoNi high-entropy alloy*. Acta Materialia, 2017. **122**: p. 11-18 DOI: 10.1016/j.actamat.2016.09.032.
79. Oh, H., et al., *Lattice Distortions in the FeCoNiCrMn High Entropy Alloy Studied by Theory and Experiment*. Entropy, 2016. **18**(9) DOI: 10.3390/e18090321.

80. Song, H., et al., *Local lattice distortion in high-entropy alloys*. Physical Review Materials, 2017. **1**(2) DOI: 10.1103/PhysRevMaterials.1.023404.
81. Toda-Caraballo, I., et al., *Interatomic spacing distribution in multicomponent alloys*. Acta Materialia, 2015. **97**: p. 156-169 DOI: 10.1016/j.actamat.2015.07.010.
82. Yeh, J.-W., et al., *Anomalous decrease in X-ray diffraction intensities of Cu–Ni–Al–Co–Cr–Fe–Si alloy systems with multi-principal elements*. Materials Chemistry and Physics, 2007. **103**(1): p. 41-46 DOI: 10.1016/j.matchemphys.2007.01.003.
83. Ding, J., et al., *Tunable stacking fault energies by tailoring local chemical order in CrCoNi medium-entropy alloys*. Proc Natl Acad Sci U S A, 2018. **115**(36): p. 8919-8924 DOI: 10.1073/pnas.1808660115.
84. Antillon, E., et al., *Chemical short range order strengthening in a model FCC high entropy alloy*. Acta Materialia, 2020. **190**: p. 29-42 DOI: <https://doi.org/10.1016/j.actamat.2020.02.041>.
85. Tamm, A., et al., *Atomic-scale properties of Ni-based FCC ternary, and quaternary alloys*. Acta Materialia, 2015. **99**: p. 307-312 DOI: 10.1016/j.actamat.2015.08.015.
86. Zhang, F.X., et al., *Local Structure and Short-Range Order in a NiCoCr Solid Solution Alloy*. Phys Rev Lett, 2017. **118**(20): p. 205501 DOI: 10.1103/PhysRevLett.118.205501.
87. Yin, B., et al., *Yield strength and misfit volumes of NiCoCr and implications for short-range-order*. Nat Commun, 2020. **11**(1): p. 2507 DOI: 10.1038/s41467-020-16083-1.
88. Zhang, R., et al., *Short-range order and its impact on the CrCoNi medium-entropy alloy*. Nature, 2020. **581**(7808): p. 283-287 DOI: 10.1038/s41586-020-2275-z.
89. He, Q.F., et al., *Understanding chemical short-range ordering/demixing coupled with lattice distortion in solid solution high entropy alloys*. Acta Materialia, 2021. **216**: p. 117140 DOI: <https://doi.org/10.1016/j.actamat.2021.117140>.
90. Jian, W.-R., et al., *Effects of lattice distortion and chemical short-range order on the mechanisms of deformation in medium entropy alloy CoCrNi*. Acta Materialia, 2020. **199**: p. 352-369 DOI: <https://doi.org/10.1016/j.actamat.2020.08.044>.
91. Ren, X.L., et al., *Effect of irradiation on randomness of element distribution in CoCrFeMnNi equiatomic high-entropy alloy*. Intermetallics, 2020. **126**: p. 106942 DOI: <https://doi.org/10.1016/j.intermet.2020.106942>.
92. Li, Q.J., Sheng, H., and Ma, E., *Strengthening in multi-principal element alloys with local-chemical-order roughened dislocation pathways*. Nat Commun, 2019. **10**(1): p. 3563 DOI: 10.1038/s41467-019-11464-7.
93. Laurent-Brocq, M., et al., *Insights into the phase diagram of the CrMnFeCoNi high entropy alloy*. Acta Materialia, 2015. **88**: p. 355-365 DOI: 10.1016/j.actamat.2015.01.068.
94. Wu, Z., Gao, Y.F., and Bei, H., *Single crystal plastic behavior of a single-phase, face-centered-cubic-structured, equiatomic FeNiCrCo alloy*. Scripta Materialia, 2015. **109**: p. 108-112 DOI: 10.1016/j.scriptamat.2015.07.031.
95. Tasan, C.C., et al., *Composition Dependence of Phase Stability, Deformation Mechanisms, and Mechanical Properties of the CoCrFeMnNi High-Entropy Alloy System*. Jom, 2014. **66**(10): p. 1993-2001 DOI: 10.1007/s11837-014-1133-6.
96. Li, Z., et al., *Metastable high-entropy dual-phase alloys overcome the strength-ductility trade-off*. Nature, 2016. **534**(7606): p. 227-30 DOI: 10.1038/nature17981.
97. Lee, S., et al., *Dislocation plasticity in FeCoCrMnNi high-entropy alloy: quantitative insights from in situ transmission electron microscopy deformation*. Materials Research Letters, 2020. **8**(6): p. 216-224 DOI: 10.1080/21663831.2020.1741469.
98. Hull, D. and Bacon, D.J., *Introduction to Dislocations*. Fifth Edition ed. 2011, Oxford: Butterworth-Heinemann ISBN: 978-0-08-096672-4.
99. Mughrabi, H., *Materials Science and Technology, Volume 6, Plastic Deformation and Fracture of Materials*. Materials Science and Technology, 1996. **6**: p. 710.

-
100. Okamoto, N.L., et al., *Size effect, critical resolved shear stress, stacking fault energy, and solid solution strengthening in the CrMnFeCoNi high-entropy alloy*. Sci Rep, 2016. **6**: p. 35863 DOI: 10.1038/srep35863.
 101. Weertman, J. and Wertmann, J.R., *Elementary dislocation theory*. 1992, New York ISBN: 0195069005.
 102. Varvenne, C., Luque, A., and Curtin, W.A., *Theory of strengthening in fcc high entropy alloys*. Acta Materialia, 2016. **118**: p. 164-176 DOI: 10.1016/j.actamat.2016.07.040.
 103. LaRosa, C.R., et al., *Solid solution strengthening theories of high-entropy alloys*. Materials Characterization, 2019. **151**: p. 310-317 DOI: 10.1016/j.matchar.2019.02.034.
 104. Pasianot, R. and Farkas, D., *Atomistic modeling of dislocations in a random quinary high-entropy alloy*. Computational Materials Science, 2020. **173** DOI: 10.1016/j.commatsci.2019.109366.
 105. Rao, S.I., et al., *Atomistic simulations of dislocation behavior in a model FCC multicomponent concentrated solid solution alloy*. Acta Materialia, 2017. **134**: p. 188-194 DOI: 10.1016/j.actamat.2017.05.071.
 106. Liu, S.F., et al., *Stacking fault energy of face-centered-cubic high entropy alloys*. Intermetallics, 2018. **93**: p. 269-273 DOI: <https://doi.org/10.1016/j.intermet.2017.10.004>.
 107. Zaddach, A.J., et al., *Mechanical Properties and Stacking Fault Energies of NiFeCrCoMn High-Entropy Alloy*. Jom, 2013. **65**(12): p. 1780-1789 DOI: 10.1007/s11837-013-0771-4.
 108. Zaddach, A.J., Scattergood, R.O., and Koch, C.C., *Tensile properties of low-stacking fault energy high-entropy alloys*. Materials Science and Engineering: A, 2015. **636**: p. 373-378 DOI: 10.1016/j.msea.2015.03.109.
 109. Huang, S., et al., *Temperature dependent stacking fault energy of FeCrCoNiMn high entropy alloy*. Scripta Materialia, 2015. **108**: p. 44-47 DOI: <https://doi.org/10.1016/j.scriptamat.2015.05.041>.
 110. Varvenne, C., et al., *Average-atom interatomic potential for random alloys*. Physical Review B, 2016. **93**(10) DOI: 10.1103/PhysRevB.93.104201.
 111. Pippan, R., et al., *Saturation of Fragmentation During Severe Plastic Deformation*. Annual Review of Materials Research, 2010. **40**(1): p. 319-343 DOI: 10.1146/annurev-matsci-070909-104445.
 112. Zhilyaev, A. and Langdon, T., *Using high-pressure torsion for metal processing: Fundamentals and applications*. Progress in Materials Science, 2008. **53**(6): p. 893-979 DOI: 10.1016/j.pmatsci.2008.03.002.
 113. Valiev, R.Z., et al., *Producing bulk ultrafine-grained materials by severe plastic deformation*. JOM, 2006. **58**(4): p. 33-39 DOI: 10.1007/s11837-006-0213-7.
 114. Kumar, K.S., Van Swygenhoven, H., and Suresh, S., *Mechanical behavior of nanocrystalline metals and alloys*. Acta Materialia, 2003. **51**(19): p. 5743-5774 DOI: 10.1016/j.actamat.2003.08.032.
 115. Valiev, R.Z., Islamgaliev, R.K., and Alexandrov, I.V., *Bulk nanostructured materials from severe plastic deformation*. Progress in materials science, 2000. **45**(2): p. 103-189 DOI: 10.1016/S0079-6425(99)00007-9.
 116. Hansen, N., Mehl, R.F., and Medalier, A., *New discoveries in deformed metals*. Metallurgical and Materials Transactions A, 2001. **32**(12): p. 2917-2935 DOI: 10.1007/s11661-001-0167-x.
 117. Hughes, D.A. and Hansen, N., *High angle boundaries formed by grain subdivision mechanisms*. Acta Materialia, 1997. **45**(9): p. 3871-3886 DOI: 10.1016/S1359-6454(97)00027-X.
 118. Humphreys, F.J. and Hatherly, M., *Recrystallization and related annealing phenomena*. 2nd Edition ed. 2004: Elsevier DOI: 10.1016/B978-0-08-044164-1.X5000-2 ISBN: 978-0-08-044164-1.

119. Hansen, N. and Kuhlmann-Wilsdorf, D., *Low energy dislocation structures due to unidirectional deformation at low temperatures*. *Materials Science and Engineering*, 1986. **81**: p. 141-161 DOI: 10.1016/0025-5416(86)90258-2.
120. Zhilyaev, A.P., et al., *Microstructural evolution in commercial purity aluminum during high-pressure torsion*. *Materials Science and Engineering: A*, 2005. **410-411**: p. 277-280 DOI: 10.1016/j.msea.2005.08.044.
121. Zhilyaev, A.P., et al., *Experimental parameters influencing grain refinement and microstructural evolution during high-pressure torsion*. *Acta Materialia*, 2003. **51**(3): p. 753-765 DOI: 10.1016/s1359-6454(02)00466-4.
122. Wei, P., et al., *A study on the texture evolution mechanism of nickel single crystal deformed by high pressure torsion*. *Materials Science and Engineering: A*, 2017. **684**: p. 239-248 DOI: 10.1016/j.msea.2016.11.098.
123. Hafok, M. and Pippan, R., *High-pressure torsion applied to nickel single crystals*. *Philosophical Magazine*, 2008. **88**(12): p. 1857-1877 DOI: 10.1080/14786430802337071.
124. Korznikova, E.A., et al., *Microstructural evolution and electro-resistivity in HPT nickel*. *Materials Science and Engineering: A*, 2012. **556**: p. 437-445 DOI: 10.1016/j.msea.2012.07.010.
125. Skrotzki, W., et al., *Microstructure, Texture, and Strength Development during High-Pressure Torsion of CrMnFeCoNi High-Entropy Alloy*. *Crystals*, 2020. **10**(4) DOI: 10.3390/cryst10040336.
126. Skrotzki, W., et al., *Microstructure and texture evolution during severe plastic deformation of CrMnFeCoNi high-entropy alloy*. *IOP Conference Series: Materials Science and Engineering*, 2017. **194** DOI: 10.1088/1757-899x/194/1/012028.
127. Edalati, K., et al., *Influence of dislocation–solute atom interactions and stacking fault energy on grain size of single-phase alloys after severe plastic deformation using high-pressure torsion*. *Acta Materialia*, 2014. **69**: p. 68-77 DOI: 10.1016/j.actamat.2014.01.036.
128. Edalati, K. and Horita, Z., *High-pressure torsion of pure metals: Influence of atomic bond parameters and stacking fault energy on grain size and correlation with hardness*. *Acta Materialia*, 2011. **59**(17): p. 6831-6836 DOI: 10.1016/j.actamat.2011.07.046.
129. Keil, T., et al., *From diluted solid solutions to high entropy alloys: Saturation grain size and mechanical properties after high pressure torsion*. *Scripta Materialia*, 2021. **192**: p. 43-48 DOI: 10.1016/j.scriptamat.2020.09.046.
130. Bruder, E., et al., *Influence of solute effects on the saturation grain size and rate sensitivity in Cu-X alloys*. *Scripta Materialia*, 2018. **144**: p. 5-8 DOI: 10.1016/j.scriptamat.2017.09.031.
131. Pippan, R., et al., *The Limits of Refinement by Severe Plastic Deformation*. *Advanced Engineering Materials*, 2006. **8**(11): p. 1046-1056 DOI: 10.1002/adem.200600133.
132. Rathmayr, G.B. and Pippan, R., *Influence of impurities and deformation temperature on the saturation microstructure and ductility of HPT-deformed nickel*. *Acta Mater*, 2011. **59**(19): p. 7228-7240 DOI: 10.1016/j.actamat.2011.08.023.
133. Bachmaier, A., Hafok, M., and Pippan, R., *Rate Independent and Rate Dependent Structural Evolution during Severe Plastic Deformation*. *Materials Transactions*, 2010. **51**(1): p. 8-13 DOI: 10.2320/matertrans.MB200912.
134. Hebesberger, T., et al., *Structure of Cu deformed by high pressure torsion*. *Acta Materialia*, 2005. **53**(2): p. 393-402 DOI: 10.1016/j.actamat.2004.09.043.
135. Penkalla, H.J., Wosik, J., and Czyrska-Filemonowicz, A., *Quantitative microstructural characterisation of Ni-base superalloys*. *Materials Chemistry and Physics*, 2003. **81**(2-3): p. 417-423 DOI: 10.1016/s0254-0584(03)00037-3.
136. Humphreys, F.J., et al., *Developing stable fine-grained microstructures by large strain deformation*. *Philosophical Transactions of the Royal Society of London. Series A:*

- Mathematical, Physical and Engineering Sciences, 1999. **357**(1756): p. 1663-1681 DOI: doi:10.1098/rsta.1999.0395.
137. Humphreys, F.J., *A unified theory of recovery, recrystallization and grain growth, based on the stability and growth of cellular microstructures—I. The basic model*. Acta Materialia, 1997. **45**(10): p. 4231-4240 DOI: 10.1016/S1359-6454(97)00070-0.
138. Belyakov, A., Kimura, Y., and Tsuzaki, K., *Recovery and recrystallization in ferritic stainless steel after large strain deformation*. Materials Science and Engineering: A, 2005. **403**(1): p. 249-259 DOI: <https://doi.org/10.1016/j.msea.2005.05.057>.
139. Belyakov, A., et al., *Continuous recrystallization in austenitic stainless steel after large strain deformation*. Acta Materialia, 2002. **50**(6): p. 1547-1557 DOI: [https://doi.org/10.1016/S1359-6454\(02\)00013-7](https://doi.org/10.1016/S1359-6454(02)00013-7).
140. Oscarsson, A., Ekström, H.E., and Hutchinson, W.B., *Transition from discontinuous to continuous recrystallization in strip-cast aluminium alloys*. Materials Science Forum, 1993. **113**: p. 177-182 DOI: 10.4028/www.scientific.net/MSF.113-115.177.
141. Wu, Z., et al., *Recovery, recrystallization, grain growth and phase stability of a family of FCC-structured multi-component equiatomic solid solution alloys*. Intermetallics, 2014. **46**: p. 131-140 DOI: 10.1016/j.intermet.2013.10.024.
142. Bhattacharjee, P.P., et al., *Microstructure and texture evolution during annealing of equiatomic CoCrFeMnNi high-entropy alloy*. Journal of Alloys and Compounds, 2014. **587**: p. 544-552 DOI: 10.1016/j.jallcom.2013.10.237.
143. Sathiaraj, G.D. and Bhattacharjee, P.P., *Effect of starting grain size on the evolution of microstructure and texture during thermo-mechanical processing of CoCrFeMnNi high entropy alloy*. Journal of Alloys and Compounds, 2015. **647**: p. 82-96 DOI: 10.1016/j.jallcom.2015.06.009.
144. Liu, W.H., et al., *Grain growth and the Hall–Petch relationship in a high-entropy FeCrNiCoMn alloy*. Scripta Materialia, 2013. **68**(7): p. 526-529 DOI: 10.1016/j.scriptamat.2012.12.002.
145. Sathiyamoorthi, P., et al., *Thermal stability and grain boundary strengthening in ultrafine-grained CoCrFeNi high entropy alloy composite*. Materials & Design, 2017. **134**: p. 426-433 DOI: 10.1016/j.matdes.2017.08.053.
146. Stepanov, N.D., et al., *Mechanical properties of a new high entropy alloy with a duplex ultra-fine grained structure*. Materials Science and Engineering: A, 2018. **728**: p. 54-62 DOI: 10.1016/j.msea.2018.04.118.
147. Utt, D., Stukowski, A., and Albe, K., *Grain boundary structure and mobility in high-entropy alloys: A comparative molecular dynamics study on a $\Sigma 11$ symmetrical tilt grain boundary in face-centered cubic CuNiCoFe*. Acta Materialia, 2020. **186**: p. 11-19 DOI: 10.1016/j.actamat.2019.12.031.
148. Otto, F., Hanold, N.L., and George, E.P., *Microstructural evolution after thermomechanical processing in an equiatomic, single-phase CoCrFeMnNi high-entropy alloy with special focus on twin boundaries*. Intermetallics, 2014. **54**: p. 39-48 DOI: 10.1016/j.intermet.2014.05.014.
149. Praveen, S., et al., *Exceptional resistance to grain growth in nanocrystalline CoCrFeNi high entropy alloy at high homologous temperatures*. Journal of Alloys and Compounds, 2016. **662**: p. 361-367 DOI: 10.1016/j.jallcom.2015.12.020.
150. Guo, L., et al., *Effects of carbon on the microstructures and mechanical properties of FeCoCrNiMn high entropy alloys*. Materials Science and Engineering: A, 2019. **746**: p. 356-362 DOI: 10.1016/j.msea.2019.01.050.
151. Kube, S.A. and Schroers, J., *Metastability in high entropy alloys*. Scripta Materialia, 2020. **186**: p. 392-400 DOI: 10.1016/j.scriptamat.2020.05.049.
152. Laplanche, G., et al., *Reasons for the superior mechanical properties of medium-entropy CrCoNi compared to high-entropy CrMnFeCoNi*. Acta Materialia, 2017. **128**: p. 292-303 DOI: 10.1016/j.actamat.2017.02.036.

153. Laurent-Brocq, M., et al., *Combining tensile tests and nanoindentation to explore the strengthening of high and medium entropy alloys*. *Materialia*, 2019. **7** DOI: 10.1016/j.mtla.2019.100404.
154. Fleischer, R.L., *Substitutional Solution Hardening*. *Acta Metallurgica*, 1963. **11**: p. 203-209 DOI: 10.1016/0001-6160(63)90213-X.
155. Friedel, J., *Dislocations*. International Series of Monographs on Solid State Physics. 1964: Pergamon. 512 ISBN: 9781483135922.
156. Leyson, G.P.M. and Curtin, W.A., *Friedel vs. Labusch: the strong/weak pinning transition in solute strengthened metals*. *Philosophical Magazine*, 2013. **93**(19): p. 2428-2444 DOI: 10.1080/14786435.2013.776718.
157. Senkov, O.N., et al., *Microstructure and room temperature properties of a high-entropy TaNbHfZrTi alloy*. *Journal of Alloys and Compounds*, 2011. **509**(20): p. 6043-6048 DOI: 10.1016/j.jallcom.2011.02.171.
158. Varvenne, C., et al., *Solute strengthening in random alloys*. *Acta Materialia*, 2017. **124**: p. 660-683 DOI: 10.1016/j.actamat.2016.09.046.
159. Varvenne, C. and Curtin, W.A., *Predicting yield strengths of noble metal high entropy alloys*. *Scripta Materialia*, 2018. **142**: p. 92-95 DOI: 10.1016/j.scriptamat.2017.08.030.
160. Yin, B. and Curtin, W.A., *First-principles-based prediction of yield strength in the RhIrPdPtNiCu high-entropy alloy*. *npj Computational Materials*, 2019. **5**(1) DOI: 10.1038/s41524-019-0151-x.
161. Varvenne, C. and Curtin, W.A., *Strengthening of high entropy alloys by dilute solute additions: CoCrFeNiAl_x and CoCrFeNiMnAl_x alloys*. *Scripta Materialia*, 2017. **138**: p. 92-95 DOI: 10.1016/j.scriptamat.2017.05.035.
162. Coury, F.G., et al., *High Throughput Discovery and Design of Strong Multicomponent Metallic Solid Solutions*. *Sci Rep*, 2018. **8**(1): p. 8600 DOI: 10.1038/s41598-018-26830-6.
163. Yin, B., Maresca, F., and Curtin, W.A., *Vanadium is an optimal element for strengthening in both fcc and bcc high-entropy alloys*. *Acta Materialia*, 2020. **188**: p. 486-491 DOI: 10.1016/j.actamat.2020.01.062.
164. Olmsted, D., Hectorjr, L., and Curtin, W., *Molecular dynamics study of solute strengthening in Al/Mg alloys*. *Journal of the Mechanics and Physics of Solids*, 2006. **54**(8): p. 1763-1788 DOI: 10.1016/j.jmps.2005.12.008.
165. Leyson, G.P., et al., *Quantitative prediction of solute strengthening in aluminium alloys*. *Nat Mater*, 2010. **9**(9): p. 750-5 DOI: 10.1038/nmat2813.
166. Hansen, N., *Polycrystalline strengthening*. *Metallurgical Transactions A*, 1985. **16**(12): p. 2167-2190 DOI: 10.1007/BF02670417.
167. Hall, E.O., *The Deformation and Ageing of Mild Steel: III Discussion of Results*. *Proceedings of the Physical Society. Section B*, 1951. **64**(9): p. 747-753 DOI: 10.1088/0370-1301/64/9/303.
168. Petch, N., *The cleavage strength of polycrystals*. *Journal of the Iron and Steel Institute*, 1953. **174**: p. 25-28.
169. Cottrell, A.H., *The mechanical properties of matter*. 1964, New York: Wiley.
170. Li, J.C.M. and Chou, Y.T., *The role of dislocations in the flow stress grain size relationships*. *Metallurgical and Materials Transactions B*, 1970. **1**(5): p. 1145 DOI: 10.1007/BF02900225.
171. Li, J.C., *Petch relation and grain boundary sources*. *Transactions of the Metallurgical Society of AIME*, 1963. **227**(1): p. 239.
172. Hansen, N., *Hall–Petch relation and boundary strengthening*. *Scripta Materialia*, 2004. **51**(8): p. 801-806 DOI: 10.1016/j.scriptamat.2004.06.002.
173. Valiev, R.Z., *Structure and mechanical properties of ultrafine-grained metals*. *Materials Science and Engineering: A*, 1997. **234-236**: p. 59-66 DOI: [https://doi.org/10.1016/S0921-5093\(97\)00183-4](https://doi.org/10.1016/S0921-5093(97)00183-4).

-
174. Huang, Y.C., et al., *A Study on the Hall-Petch Relationship and Grain Growth Kinetics in FCC-Structured High/Medium Entropy Alloys*. Entropy (Basel), 2019. **21**(3) DOI: 10.3390/e21030297.
 175. Yang, J., et al., *Revealing the Hall-Petch relationship of Al_{0.1}CoCrFeNi high-entropy alloy and its deformation mechanisms*. Journal of Alloys and Compounds, 2019. **795**: p. 269-274 DOI: <https://doi.org/10.1016/j.jallcom.2019.04.333>.
 176. Ma, E., *Instabilities and ductility of nanocrystalline and ultrafine-grained metals*. Scripta Materialia, 2003. **49**(7): p. 663-668 DOI: 10.1016/S1359-6462(03)00396-8.
 177. Valiev, R.Z., et al., *Fundamentals of Superior Properties in Bulk NanoSPD Materials*. Materials Research Letters, 2015. **4**(1): p. 1-21 DOI: 10.1080/21663831.2015.1060543.
 178. Koch, C.C., *Optimization of strength and ductility in nanocrystalline and ultrafine grained metals*. Scripta Materialia, 2003. **49**(7): p. 657-662 DOI: 10.1016/S1359-6462(03)00394-4.
 179. Valiev, R.Z., et al., *Paradox of Strength and Ductility in Metals Processed Bysevere Plastic Deformation*. Journal of Materials Research, 2002. **17**(1): p. 5-8 DOI: 10.1557/JMR.2002.0002.
 180. Valiev, R.Z. and Zhu, Y., *Recent Findings in Superior Strength and Ductility of Ultrafine-Grained Materials*. Transactions of the Materials Research Society of Japan, 2015. **40**(4): p. 309-318 DOI: 10.14723/tmrj.40.309.
 181. Bracq, G., et al., *The fcc solid solution stability in the Co-Cr-Fe-Mn-Ni multi-component system*. Acta Materialia, 2017. **128**: p. 327-336 DOI: 10.1016/j.actamat.2017.02.017.
 182. Keil, T., et al., *Solid solution hardening in CrMnFeCoNi-based high entropy alloy systems studied by a combinatorial approach*. Journal of Materials Research, 2021. **36**(12): p. 2558-2570 DOI: 10.1557/s43578-021-00205-6.
 183. Oliver, W.C. and Pharr, G.M., *Measurement of hardness and elastic modulus by instrumented indentation: Advances in understanding and refinements to methodology*. J. Mater. Res. 19 1, 2004: p. 3-20 DOI: 10.1557/jmr.2004.19.1.3.
 184. Oliver, W.C. and Pharr, G.M., *An improved technique for determining hardness and elastic modulus using load and displacement sensing indentation experiments*. Journal of Materials Research, 1992. **7**(06): p. 1564-1583 DOI: 10.1557/JMR.1992.1564.
 185. Pharr, G.M., Oliver, W.C., and Brotzen, F.R., *On the generality of the relationship among contact stiffness, contact area, and elastic modulus during indentation*. Journal of Materials Research, 1992. **7**(03): p. 613-617 DOI: 10.1557/jmr.1992.0613.
 186. Fischer-Cripps, A.C., *Nanoindentation*. Third ed. 2011: Springer New York ISBN: 978-1-4419-9871-2.
 187. Pethica, J.B. and Oliver, W.C., *Mechanical Properties of Nanometre Volumes of Material: Use of the Elastic Response of Small Area Indentations*. MRS Proceedings, 1988. **130** DOI: 10.1557/PROC-130-13.
 188. Durst, K., et al., *Indentation size effect in Ni-Fe solid solutions*. Acta Materialia, 2007. **55**(20): p. 6825-6833 DOI: 10.1016/j.actamat.2007.08.044.
 189. Pharr, G.M., Herbert, E.G., and Gao, Y., *The Indentation Size Effect: A Critical Examination of Experimental Observations and Mechanistic Interpretations*. Annual Review of Materials Research, 2010. **40**(1): p. 271-292 DOI: 10.1146/annurev-matsci-070909-104456.
 190. Tabor, D., *A simple theory of static and dynamic hardness*. Proceedings of the Royal Society of London. Series A. Mathematical and Physical Sciences, 1948. **192**(1029): p. 247-274 DOI: 10.1098/rspa.1948.0008.
 191. Tabor, D., *The hardness of metals* 1951, Oxford: Oxford university press ISBN: 0198507763.
 192. Leitner, A., Maier-Kiener, V., and Kiener, D., *Essential refinements of spherical nanoindentation protocols for the reliable determination of mechanical flow curves*. Materials & Design, 2018. **146**: p. 69-80 DOI: 10.1016/j.matdes.2018.03.003.

193. Franke, O., Durst, K., and Göken, M., *Nanoindentation investigations to study solid solution hardening in Ni-based diffusion couples*. Journal of Materials Research, 2009. **24**(03): p. 1127-1134 DOI: 10.1557/jmr.2009.0135.
194. Renk, O. and Pippan, R., *Saturation of Grain Refinement during Severe Plastic Deformation of Single Phase Materials: Reconsiderations, Current Status and Open Questions*. Materials Transactions, 2019. **60**(7): p. 1270-1282 DOI: 10.2320/matertrans.MF201918.
195. Zhilyaev, A.P., et al., *Microhardness and microstructural evolution in pure nickel during high-pressure torsion*. Scripta Materialia, 2001. **44**(12): p. 2753-2758 DOI: 10.1016/S1359-6462(01)00955-1.
196. Zhang, N., et al., *Influence of alloying elements on the thermal stability of ultra-fine-grained Ni alloys*. Journal of Materials Science, 2019. **54**(14): p. 10506-10515 DOI: 10.1007/s10853-019-03614-5.
197. Zhilyaev, A.P., et al., *Orientation imaging microscopy of ultrafine-grained nickel*. Scripta Materialia, 2002. **46**(8): p. 575-580 DOI: [https://doi.org/10.1016/S1359-6462\(02\)00018-0](https://doi.org/10.1016/S1359-6462(02)00018-0).
198. Liu, G., et al., *Solute segregation effect on grain boundary migration and Hall–Petch relationship in CrMnFeCoNi high-entropy alloy*. Materials Science and Technology, 2019: p. 1-9 DOI: 10.1080/02670836.2019.1570679.
199. Chauhan, M. and Mohamed, F.A., *Investigation of low temperature thermal stability in bulk nanocrystalline Ni*. Materials Science and Engineering: A, 2006. **427**(1): p. 7-15 DOI: 10.1016/j.msea.2005.10.039.
200. Klemm, R., et al., *Thermal stability of grain structure and defects in submicrocrystalline and nanocrystalline nickel*. Scripta Materialia, 2002. **46**(9): p. 685-690 DOI: 10.1016/S1359-6462(02)00054-4.
201. Hashemi-Sadraei, L., et al., *The Influence of Grain Size Determination Method on Grain Growth Kinetics Analysis*. Advanced Engineering Materials, 2015. **17**(11): p. 1598-1607 DOI: 10.1002/adem.201500057.
202. Wilde, G., et al., *Plasticity and Grain Boundary Diffusion at Small Grain Sizes*. Advanced Engineering Materials, 2010. **12**(8): p. 758-764 DOI: 10.1002/adem.200900333.
203. Sauvage, X., et al., *Grain boundaries in ultrafine grained materials processed by severe plastic deformation and related phenomena*. Materials Science and Engineering: A, 2012. **540**: p. 1-12 DOI: 10.1016/j.msea.2012.01.080.
204. Nazarov, A.A., Romanov, A.E., and Valiev, R.Z., *On the structure, stress fields and energy of nonequilibrium grain boundaries*. Acta Metallurgica et Materialia, 1993. **41**(4): p. 1033-1040 DOI: [https://doi.org/10.1016/0956-7151\(93\)90152-I](https://doi.org/10.1016/0956-7151(93)90152-I).
205. Divinski, S.V., et al., *Effect of heat treatment on diffusion, internal friction, microstructure and mechanical properties of ultra-fine-grained nickel severely deformed by equal-channel angular pressing*. Acta Materialia, 2015. **82**: p. 11-21 DOI: 10.1016/j.actamat.2014.08.064.
206. Wilde, G. and Divinski, S., *Grain Boundaries and Diffusion Phenomena in Severely Deformed Materials*. Materials Transactions, 2019. **60**(7): p. 1302-1315 DOI: 10.2320/matertrans.MF201934.
207. Keil, T., et al., *Effects of solutes on thermal stability, microstructure and mechanical properties in CrMnFeCoNi based alloys after high pressure torsion*. Acta Materialia, 2022. **227** DOI: 10.1016/j.actamat.2022.117689.
208. Kottke, J., et al., *Experimental and theoretical study of tracer diffusion in a series of (CoCrFeMn)_{100-x}Ni alloys*. Acta Materialia, 2020. **194**: p. 236-248 DOI: 10.1016/j.actamat.2020.05.037.
209. Cahn, J.W., *The impurity-drag effect in grain boundary motion*. Acta Metallurgica, 1962. **10**(9): p. 789-798 DOI: 10.1016/0001-6160(62)90092-5.

-
210. Zhang, H.W., et al., *Enhancement of strength and stability of nanostructured Ni by small amounts of solutes*. Scripta Materialia, 2011. **65**(6): p. 481-484 DOI: 10.1016/j.scriptamat.2011.06.003.
 211. Bolshakov, A. and Pharr, G.M., *Influences of pileup on the measurement of mechanical properties by load and depth sensing indentation techniques*. Journal of Materials Research, 1998. **13**(4): p. 1049-1058 DOI: 10.1557/JMR.1998.0146.
 212. Kese, K.O., Li, Z.C., and Bergman, B., *Method to account for true contact area in soda-lime glass during nanoindentation with the Berkovich tip*. Materials Science and Engineering: A, 2005. **404**(1-2): p. 1-8 DOI: 10.1016/j.msea.2005.06.006.
 213. Huang, X., Hansen, N., and Tsuji, N., *Hardening by Annealing and Softening by Deformation in Nanostructured Metals*. Science, 2006. **312**(5771): p. 249 DOI: 10.1126/science.1124268.
 214. Terada, D., Houda, H., and Tsuji, N., *Effect of strain on "hardening by annealing and softening by deformation" phenomena in ultra-fine grained aluminum*. Journal of Materials Science, 2008. **43**(23-24): p. 7331-7337 DOI: 10.1007/s10853-008-2809-5.
 215. Shahmir, H., et al., *Effect of annealing on mechanical properties of a nanocrystalline CoCrFeNiMn high-entropy alloy processed by high-pressure torsion*. Materials Science and Engineering: A, 2016. **676**: p. 294-303 DOI: 10.1016/j.msea.2016.08.118.
 216. *Bulk nanostructured materials*, M.J. Zehetbauer and Y.T. Zhu, Editors. 2009: Weinheim DOI: 10.1002/9783527626892.
 217. Zhilyaev, A.P., et al., *The microstructural characteristics of ultrafine-grained nickel*. Materials Science and Engineering: A, 2005. **391**(1-2): p. 377-389 DOI: 10.1016/j.msea.2004.09.030.
 218. Maier, V., et al., *Nanoindentation strain-rate jump tests for determining the local strain-rate sensitivity in nanocrystalline Ni and ultrafine-grained Al*. Journal of Materials Research, 2011. **26**(11): p. 1421-1430 DOI: 10.1557/jmr.2011.156.
 219. Nix, W. and Gao, H., *Indentation Size Effects In Crystalline Materials: A Law For Strain Gradient Plasticity*. J. Mech. Phys. Solids, 1998. **46**: p. 411-425.
 220. Lu, L., et al., *Nano-sized twins induce high rate sensitivity of flow stress in pure copper*. Acta Materialia, 2005. **53**(7): p. 2169-2179 DOI: 10.1016/j.actamat.2005.01.031.
 221. Sun, Z., et al., *Grain size and alloying effects on dynamic recovery in nanocrystalline metals*. Acta Materialia, 2016. **119**: p. 104-114 DOI: 10.1016/j.actamat.2016.08.019.
 222. Sun, Z., et al., *Dynamic recovery in nanocrystalline Ni*. Acta Materialia, 2015. **91**: p. 91-100 DOI: 10.1016/j.actamat.2015.03.033.
 223. Schwaiger, R., et al., *Some critical experiments on the strain-rate sensitivity of nanocrystalline nickel*. Acta Materialia, 2003. **51**(17): p. 5159-5172 DOI: 10.1016/s1359-6454(03)00365-3.
 224. Wei, Q., et al., *Effect of nanocrystalline and ultrafine grain sizes on the strain rate sensitivity and activation volume: fcc versus bcc metals*. Materials Science and Engineering: A, 2004. **381**(1-2): p. 71-79 DOI: 10.1016/j.msea.2004.03.064.
 225. Wehrs, J., et al., *Comparison of In Situ Micromechanical Strain-Rate Sensitivity Measurement Techniques*. Jom, 2015. **67**(8): p. 1684-1693 DOI: 10.1007/s11837-015-1447-z.
 226. Yang, X.-S., et al., *Time, stress, and temperature-dependent deformation in nanostructured copper: Stress relaxation tests and simulations*. Acta Materialia, 2016. **108**: p. 252-263 DOI: 10.1016/j.actamat.2016.02.021.
 227. Monclús, M.A. and Molina-Aldareguia, J.M., *High Temperature Nanomechanical Testing*, in *Handbook of Mechanics of Materials*. 2018. p. 1-29 ISBN: 978-981-10-6855-3.
 228. Leitner, A., Maier-Kiener, V., and Kiener, D., *Extraction of Flow Behavior and Hall-Petch Parameters Using a Nanoindentation Multiple Sharp Tip Approach* Advanced Engineering Materials, 2017. **19**(4) DOI: 10.1002/adem.201600669.

8. Cumulative part of the thesis

8.1. Statement of personal contribution – Credit¹ (Contributor Roles Taxonomy)

Publication A:



Tom Keil: Investigation, Data Curation, Formal Analysis, Validation, Visualization, Writing – Original Draft, Writing – Review & Editing. **Enrico Bruder:** Conceptualization, Methodology, Validation, Formal Analysis, Writing – Original Draft, Writing – Review & Editing, Project Administration. **Karsten Durst:** Conceptualization, Methodology, Writing – Review & Editing, Supervision, Project Administration, Funding Acquisition.

¹ Brand et al. (2015). Learned Publishing Vol. 28 (2). doi:10.1087/20150211

Publication B:



Journal of
MATERIALS RESEARCH

Article
DOI:10.1557/s43578-021-00205-6

ADVANCED NANOMECHANICAL TESTING

Check for updates

FOCUS ISSUE

Solid solution hardening in CrMnFeCoNi-based high entropy alloy systems studied by a combinatorial approach

Tom Keil^{1,a)}, Daniel Utt², Enrico Bruder¹, Alexander Stukowski², Karsten Albe², Karsten Durst¹

¹Technical University of Darmstadt, Materials Science, Physical Metallurgy, Alarich-Weiss-Str. 2, 64287 Darmstadt, Germany
²Technical University of Darmstadt, Materials Science, Materials Modelling, Otto-Berndt-Str. 3, 64287 Darmstadt, Germany
^{a)}Address all correspondence to this author. e-mail: t.keil@phm.tu-darmstadt.de

Received: 18 December 2020; accepted: 7 April 2021

Tom Keil: Investigation, Data Curation, Formal Analysis, Validation, Visualization, Writing – Original Draft, Writing – Review & Editing. **Daniel Utt:** Investigation, Data Curation, Formal Analysis, Software, Validation, Visualization, Writing – Original Draft, Writing – Review & Editing. **Enrico Bruder:** Conceptualization, Methodology, Validation, Formal Analysis, Writing – Review & Editing, Project Administration. **Alexander Stukowski:** Conceptualization, Methodology, Validation, Formal Analysis, Writing – Review & Editing, Project Administration. **Karsten Albe:** Conceptualization, Methodology, Writing – Review & Editing, Supervision, Project Administration, Funding Acquisition. **Karsten Durst:** Conceptualization, Methodology, Writing – Review & Editing, Supervision, Project Administration, Funding Acquisition.

Publication C:

Scripta Materialia 192 (2021) 43–48

Contents lists available at [ScienceDirect](#)

 **Scripta Materialia** 

journal homepage: www.elsevier.com/locate/scriptamat

From diluted solid solutions to high entropy alloys: Saturation grain size and mechanical properties after high pressure torsion 

Tom Keil^{a,*}, Enrico Bruder^a, Mathilde Laurent-Brocq^b, Karsten Durst^a

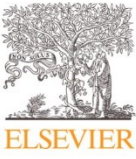
^a Technical University of Darmstadt, Materials Science, Physical Metallurgy, Alarich-Weiss-Str. 2, 64287 Darmstadt, Germany
^b Université Paris Est Créteil, CNRS, ICMPE, UMR 7182, Thiais, France

Tom Keil: Investigation, Data Curation, Formal Analysis, Validation, Visualization, Writing – Original Draft, Writing – Review & Editing. **Enrico Bruder:** Conceptualization, Methodology, Validation, Formal Analysis, Writing – Review & Editing, Project Administration. **Mathilde Laurent-Brocq:** Resources, Validation, Formal Analysis, Writing – Review & Editing. **Karsten Durst:** Conceptualization, Methodology, Writing – Review & Editing, Supervision, Project Administration, Funding Acquisition.

Publication D:

Acta Materialia 227 (2022) 117689

Contents lists available at ScienceDirect

 **Acta Materialia** 

journal homepage: www.elsevier.com/locate/actamat

Effects of solutes on thermal stability, microstructure and mechanical properties in CrMnFeCoNi based alloys after high pressure torsion 

Tom Keil^{a,*}, Shabnam Taheriniya^b, Enrico Bruder^a, Gerhard Wilde^b, Karsten Durst^a

^a Materials Science, Physical Metallurgy, Technical University of Darmstadt, Darmstadt, D-64287, Germany
^b Institute of Materials Physics, University of Münster, Münster D-48149, Germany

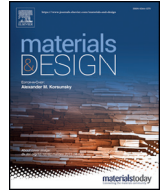
Tom Keil: Investigation, Data Curation, Formal Analysis, Validation, Visualization, Writing – Original Draft, Writing – Review & Editing. **Shabnam Taheriniya:** Investigation, Data Curation, Formal Analysis, Validation, Visualization, Writing – Original Draft, Writing – Review & Editing. **Enrico Bruder:** Conceptualization, Methodology, Validation, Formal Analysis, Writing – Review & Editing. **Gerhard Wilde:** Conceptualization, Methodology, Writing – Review & Editing, Supervision, Project Administration, Funding Acquisition. **Karsten Durst:** Conceptualization, Methodology, Writing – Review & Editing, Supervision, Project Administration, Funding Acquisition.

8.2. Selected reprints

Publication A

Reproduced full text article with permission from Elsevier Ltd.

Copyright (2019), Materials & Design.



Exploring the compositional parameter space of high-entropy alloys using a diffusion couple approach

Tom Keil*, Enrico Bruder, Karsten Durst

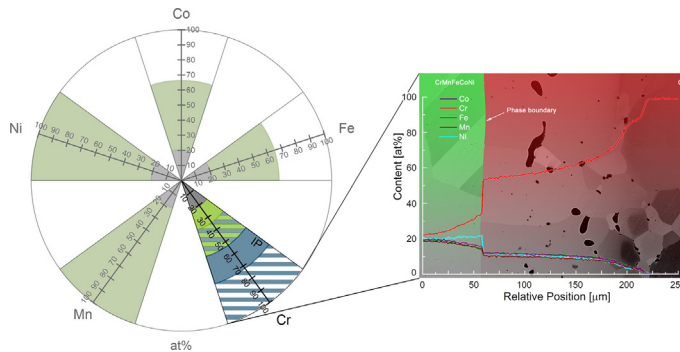
Physical Metallurgy, Materials Science Department, Technische Universität Darmstadt, Alarich-Weiss-Str. 2, 64287 Darmstadt, Germany



HIGHLIGHTS

- Continuous screening of the chemical composition space of high-entropy alloys based on diffusion couples
- Visualization of stability ranges for single phase solid solutions and intermetallic compounds in a comprehensive way
- Derivation of stability ranges for single phase solid solutions and intermetallic compounds
- Model of valence electron concentration for stable cubic solid solutions can be applied over large concentration intervals

GRAPHICAL ABSTRACT



ARTICLE INFO

Article history:

Received 20 February 2019
Received in revised form 15 April 2019
Accepted 25 April 2019
Available online 26 April 2019

Keywords:

High entropy alloy
Diffusion couple
Phase stability

ABSTRACT

In this paper the phase stability and solubility limits of high-entropy alloys are studied, using a diffusion couple approach. Diffusion couples have been fabricated using the established Cantor alloy (CrMnFeCoNi) and a commercial fcc CoNiCrMo alloy (MP35N®) with constituent or foreign elements as diffusion partners. Chemical gradients within the interdiffusion zone as well as the phase stability are quantified using EDX and EBSD. For comparability of the results, new phase stability diagrams are presented. The experimental results show no general correlation between maximum solubility of individual elements and atomic size mismatch, whereas the valence electron concentration model (VEC) seems to be a good approximation for fcc to bcc phase transitions for most of the investigated diffusion couples.

© 2019 The Authors. Published by Elsevier Ltd. This is an open access article under the CC BY-NC-ND license (<http://creativecommons.org/licenses/by-nc-nd/4.0/>).

1. Introduction

Over the last decade, the attention to a novel class of alloys called high-entropy alloys (HEA) has increased significantly. By definition, these alloys contain at least five principal elements, each with a concentration of minimum 5 to maximum 35 atomic percent (at.%). [1–3] Furthermore, a single-phase solid solution is often considered as another

mandatory criterion. The high-entropy alloys with five principal elements offer a huge parameter space for numerous alloys with potentially interesting properties. [4] Various alloys have already been developed and characterised from this vast compositional range, yet, it remains widely unexplored. [4,5]. So far, mainly equiatomic systems have been investigated in literature, which was driven by the idea of entropy maximisation [1,6]. One of these alloys is the prototypical equiatomic and nowadays well known CrMnFeCoNi alloy, which was first studied by Cantor et al. [7] and shows a single face-centered cubic (fcc) solid solution. Recent studies [8–11] on the thermal stability of

* Corresponding author.
E-mail address: t.keil@phm.tu-darmstadt.de (T. Keil).

the Cantor alloy have revealed the formation of precipitates at temperatures below 800 °C. Thus, even the Cantor alloy does not fulfil the single-phase criterion. However, information on the phase stability and the property range is hardly available in case of changing and non-equiatomic compositions. This understanding is essential for both alloy optimisation and fundamental scientific topics like solid solution strengthening or phase stability including the role of valence electron concentration and atomic size misfit. [12–16]

The diffusion couple technique or the modification to diffusion multiples are promising methods for investigating phase space, phase stability and mechanical properties over a wide range of compositions. [17,18] Franke et al. [17] investigated binary diffusion couples combining EDX with nanoindentation and discussed the results in terms of solid solution strengthening. Additionally, diffusion couples are used to study diffusion or diffusional interactions in high-entropy alloys and to discuss the phenomenon of “sluggish-diffusion”. [19,20] Using diffusion multiples, at least three components are placed in direct diffusional contact to each other. In this way, information about phase stability, mechanical properties and diffusion kinetics can be obtained for higher-order systems much faster than with conventionally produced alloys. The development of high-entropy alloys can be accelerated by using the resulting contour maps of composition, hardness and stability parameters of the quinary region. [21–24]

The objective of this work is to present possibilities and opportunities of the diffusion couple approach for investigation of the phase stability of high-entropy alloys over wide concentration intervals in a continuous manner. For this purpose, we developed a diffusion couple technique to explore in a continuous approach the chemical composition space of two different alloy systems. To investigate the phase stability of high-entropy alloys, we changed the chemical composition continuously starting from the base alloy. This allows to identify composition-dependent structural discontinuities and to screen the property range of the two different alloy systems. Phase stability is studied by a combination of energy dispersive X-ray spectroscopy (EDX) and electron backscatter diffraction (EBSD). The investigated diffusion couples are based on a commercial fcc CoNiCrMo alloy (MP35N®) and the established CrMnFeCoNi Cantor alloy. The CrMnFeCoNi alloy is the most well-known and investigated high-entropy alloy, but due to the higher total number of elements a more complex system. In addition, the four-component CoNiCrMo alloy provides further scenarios encouraging that this approach can be applied to subsets of high-entropy alloys to investigate entire compositional ranges of individual constituent elements and not only an increase compared to the nominal composition.

2. Experimental procedure

Diffusion couples of the homogenised $\text{Co}_{35.8}\text{Ni}_{35.3}\text{Cr}_{22.9}\text{Mo}_{6.0}$ medium-entropy alloy (MEA) and the $\text{Cr}_{20.7}\text{Mn}_{18.5}\text{Fe}_{20.2}\text{Co}_{20.5}\text{Ni}_{20.1}$ Cantor alloy were prepared with all constituent pure elements as well as Fe as foreign element in case of the CoNiCrMo alloy. The purity levels of the diffusion partner elements Cr, Mn, Fe, Co, Ni and Mo show purity

levels of 99.95%, 99.8%, 99.85%, 99.9%, 99.0% and 99.98%, respectively. The commercial CoNiCrMo alloy was used in a fully annealed condition and the Cantor alloy was synthesized by using an inductive furnace under inert atmosphere followed by a homogenization step as described in [25].

Fig. 1 schematically shows the experimental approach to generate diffusion couples. The contact areas of both the alloy and diffusion partner elements were polished down to $\frac{1}{4}\ \mu\text{m}$ diamond suspension. For the diffusion bonding step, the samples were mounted in a Mo sample holder and a load was applied by screws. Subsequently, a two-step heat treatment consisting of a diffusion bonding process and a high temperature interdiffusion heat treatment was performed. The diffusion welding process was carried out in a furnace under inert argon atmosphere at different temperatures between 1000 °C and 1250 °C for 1 h. In the next step, the welded specimen was sealed in quartz tubes at 0.3 bar argon atmosphere to perform the final heat treatment under inert conditions. In order to create a sufficiently large interdiffusion zone, a final heat treatment was carried out for 24 h at temperatures that were selected according to the material combination, followed by water quenching. Due to the low melting point of Mn, the CrMnFeCoNi + Mn diffusion couple was diffusion welded and heat treated at 1000 °C, all other diffusion couples were diffusion welded at 1250 °C and heat treated at 1150 °C. For chemical and structural investigations within the interdiffusion zone, cross sections were prepared and polished up to a mechano-chemical treatment with a colloidal silica suspension. The chemical and structural characterization was carried out at a scanning electron microscope (TESCAN Mira3). The concentration profiles within the interdiffusion zone were measured by EDX (energy dispersive x-ray spectroscopy) line scans using 20 kV acceleration voltage, a dwell-time of 200 ms, a step size of 1 μm and 32 to 64 frames. The phase analysis was performed using electron backscatter diffraction (EBSD).

3. Microstructural and chemical analysis

By combining the chemical analysis with the results of EBSD measurements, maximum solubility limits of individual elements in the matrix of the base alloys can be observed in detail. During the interdiffusion process, three different cases can be identified for both alloy systems. Fig. 2. gives examples for the single phase case (a.): CrMnFeCoNi + Ni), the formation of an intermetallic phase (b.): CrMnFeCoNi + Cr) and the occurrence of a phase transition from fcc to bcc (c.): CrMnFeCoNi + Fe). Table 1 and 2 provide an overview of the element concentrations at the phase transitions from the base alloys to the respective diffusion partner elements.

3.1. Single phase

If nickel is used as a diffusion partner element, the fcc crystal structure of both investigated alloys extends over the entire compositional range (Fig. 3 a.) - b.)). For the CoNiCrMo + Ni diffusion couple, the

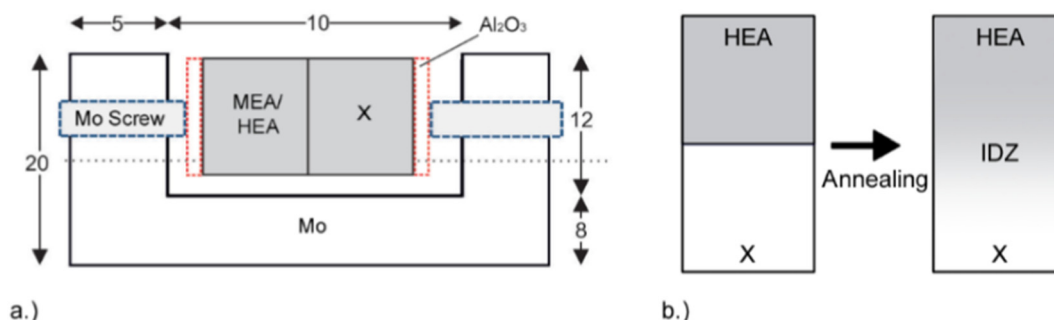


Fig. 1. Schematic diagram of a.) assembly of the diffusion couples (adapted from ur Rehman [26]), b.) formation of the interdiffusion zone (IDZ) during heat treatment.

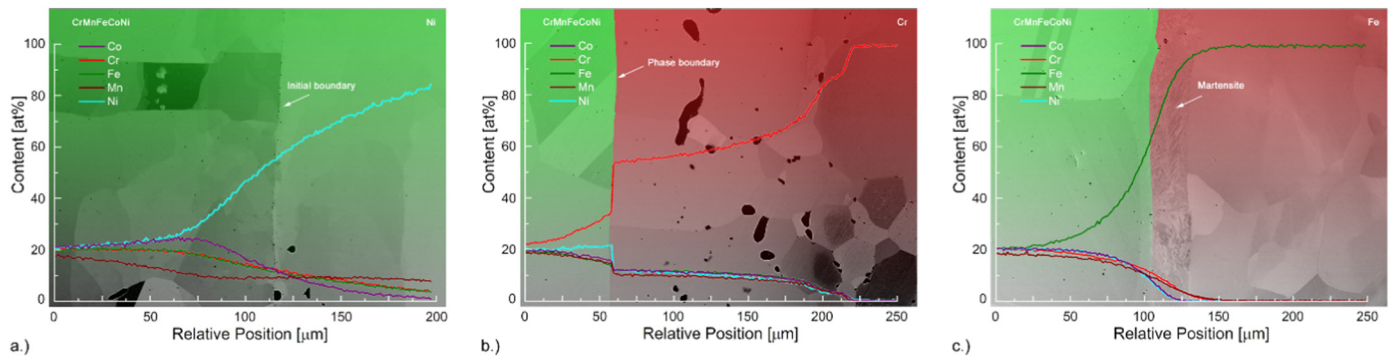


Fig. 2. BSE images with superimposed chemical and phase distribution of CrMnFeCoNi alloy (green) paired with a.) Ni, b.) Cr and c.) Fe.

concentration profile of Ni shows a distinct s-shape within the interdiffusion zone as it is expected for binary diffusion couples from literature (Grube-Jedele solution [27]). An increase in Ni content results in a continuous decrease of all other element concentrations. The changes in element concentrations extend over an interdiffusion zone width of approximately 130 μm . Starting from the equiatomic composition of the CrMnFeCoNi alloy, the Ni concentration shows an s-shaped increase. Up to a distance of approximately 67 μm to the interface, both Ni and Co show an equal concentration level of about 24 at.%. Up to this position the element concentrations of Cr and Fe are almost constant, while the Mn concentration has already dropped to 12.4 at.%. In this region an accumulation of the Co concentration takes place (uphill-diffusion). In the further course, the Mn concentration remains stable over a wide range and Co, Cr and Fe decrease in their concentrations. While the decrease in element concentration is most pronounced for Co, the concentrations of the elements Cr and Fe show a comparable course over the entire width of the diffusion couple.

In case of Mn as diffusion partner element for the CrMnFeCoNi alloy (Fig. 3 c.), the entire concentration profile shows an fcc structure. Accordingly, no phase transition is observed. This seems exceptional as pure Mn only appears above 1095 $^{\circ}\text{C}$ in the closest packed cubic structure [28]. The increase in Mn concentration leads to a decrease in the concentrations of all other constituent elements to the same extent, hence, the concentration profiles of the other constituent elements are similar over the entire concentration interval, which extends over approximately 210 μm .

3.2. Phase transition

In contrast to the results using Ni or Mn as diffusion partner elements, an increasing element concentration of Co or Fe causes a phase transition between the two base alloys and the pure element (Fig. 3 d.) – g.).

For CoNiCrMo, the element concentrations can be increased significantly up to approximately 62 at.% Co or 60 at.% Fe until a phase transition to the hcp structure of Co or to the bcc structure of Fe occurs. The

diffusion couple with Co (Fig. 3 d.) exhibits an interdiffusion zone width of approximately 108 μm . Within this compositional interval, Ni shows the strongest decrease in element concentration. An increase in Fe concentration (Fig. 3 e.) results in a collective decrease in all concentrations of the constituent elements. In this case, Ni and Co show a comparable chemical profile and a pronounced decrease in concentrations.

For the CrMnFeCoNi alloy, the chemical gradients also show an s-shaped concentration profile for the diffusion couples based on Co and Fe. The increase in Co content results in a collective decrease of the four other constituent elements. At first Ni exhibits a stable course, but decreases rapidly in the area of the initial interface. The increase in Co content leads to a phase transition of the fcc structure of the alloy to the hcp structure of Co at approximately 66 at.% Co. Due to the element exchange between the alloy and Fe, a phase transition from fcc to bcc can be observed at an Fe concentration of approximately 65 at.%. The increase in Fe results in a decrease of all element concentrations, whereby Co and Ni show a comparable chemical distribution within the interdiffusion zone.

3.3. Formation of intermetallic phases

Besides entire single phase and phase transition, a third case can be observed for both alloys, namely the formation of intermetallic phases. By using Cr as a diffusion partner element (Fig. 3 h.) and j.), the fcc phase extends up to approximately 41 at.% Cr for the CoNiCrMo alloy and up to 34 at.% for the CrMnFeCoNi alloy. A further increase results in the formation of intermetallic phases. In case of the CoNiCrMo alloy, the tetragonal sigma (CrFeMo) structure can be assigned to the intermetallic phase. The transition to the intermetallic phase is characterised by abrupt changes in concentrations of all elements. Within the fcc structure of the alloy, the increase in Cr leads to a decrease in Co and Mo content, Ni remains unaffected at a constant level of about 31 at.%. If the diffusion couple is based on the CrMnFeCoNi alloy, the formed intermetallic phase can be indexed as a bcc structure. In the area prior to the phase transition, the elements Co, Fe and Mn are substituted by Cr and Ni (uphill diffusion of Ni). The CoNiCrMo + Mo diffusion couple shows the formation of an intermetallic phase (Fig. 3 i.). Starting

Table 1

Element concentration at phase transition of the diffusion couples based on the CoNiCrMo alloy, entire single phase observed for the diffusion couple with Ni. The diffusion welding process was performed at 1250 $^{\circ}\text{C}$ for 1 h and the final heat treatment was carried out at 1150 $^{\circ}\text{C}$ for 24 h.

Concentration in at.%	Phase transition	Co	Cr	Mo	Ni
Base alloy		35.8	22.9	6.0	35.3
CoNiCrMo + Co	fcc/hcp	61.7	14.4	3.3	20.6
CoNiCrMo + Cr	fcc/sigma	24.8	41.2	3.3	30.7
CoNiCrMo + Fe	fcc/bcc	14.1	9.2	2.1	14.3
CoNiCrMo + Mo	fcc/IP ^a	27.4	19.5	16.0	37.1

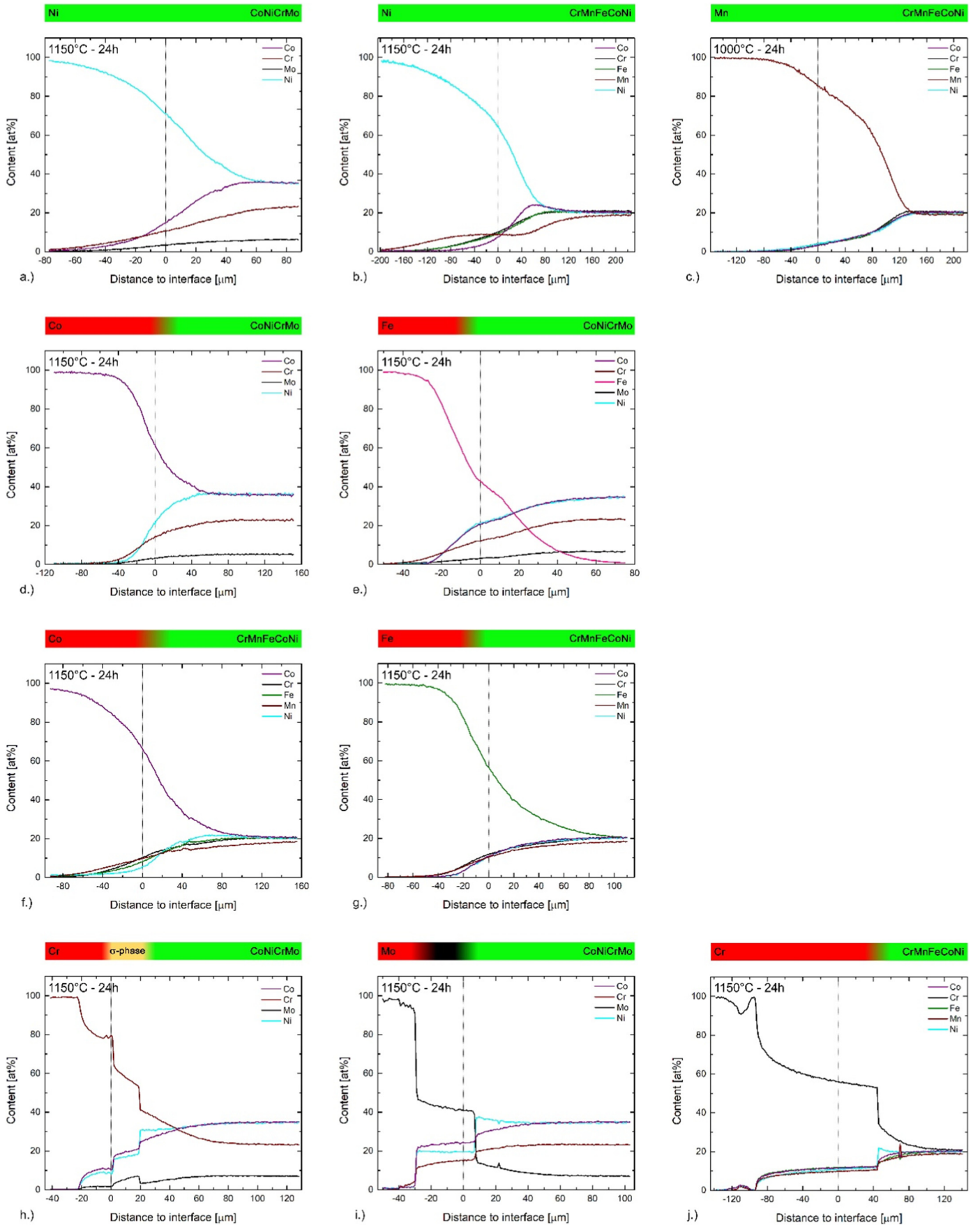
^a Unknown intermetallic phase, further investigations required.

Table 2

Element concentrations at phase transition of the diffusion couples based on the CrMnFeCoNi alloy, entire single phase observed for the diffusion couples with Mn and Ni. The diffusion welding process was performed at 1250 $^{\circ}\text{C}$ for 1 h and the final heat treatment was carried out at 1150 $^{\circ}\text{C}$ for 24 h.

Concentration in at.%	Phase transition	Co	Cr	Fe	Mn	Ni
Base alloy		20.5	20.7	20.2	18.5	20.1
CrMnFeCoNi + Co	fcc/hcp	66.4	10.2	8.1	9.8	5.5
CrMnFeCoNi + Cr	fcc/IP ^a	15.2	34.3	13.8	14.7	22.0
CrMnFeCoNi + Fe	fcc/bcc	8.3	10.0	65.0	8.8	7.9

^a Unknown intermetallic phase, further investigations required.



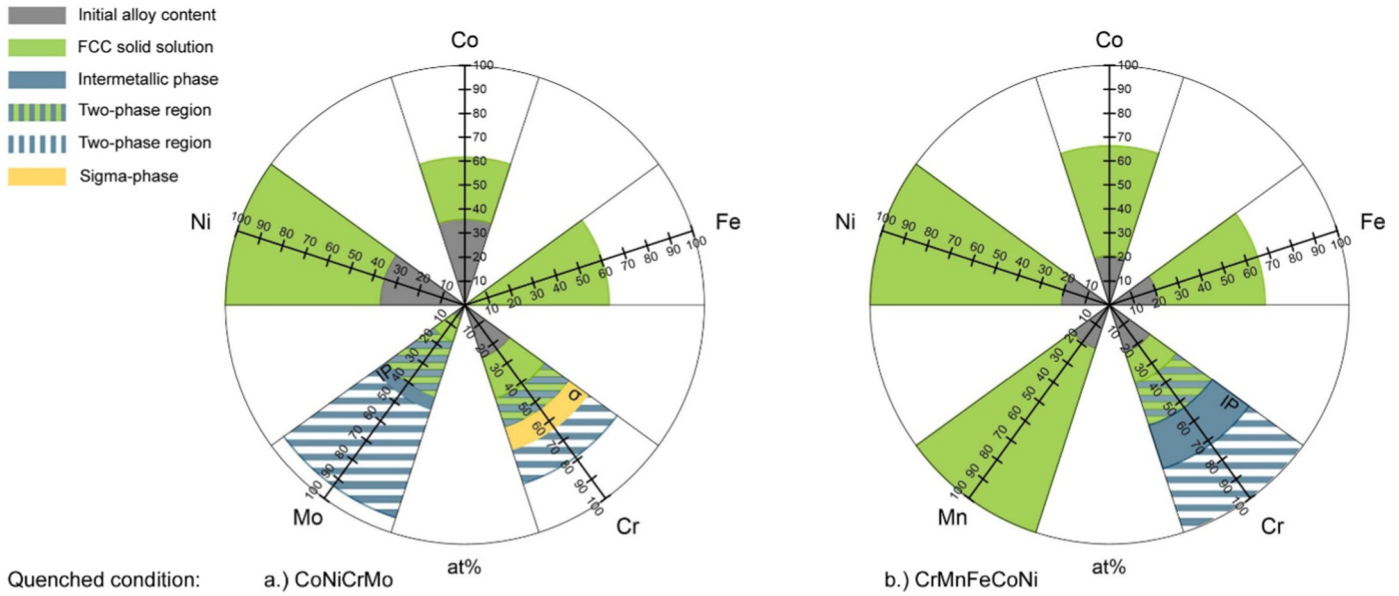


Fig. 4. Phase stability diagram of a.) CoNiCrMo and b.) CrMnFeCoNi alloy heat treated at 1150 °C (Cr, Mo, Fe, Co, Ni) or 1000 °C (Mn) and quenched to room temperature. The corresponding axis shows the element concentration of the respective diffusion partner element. The diffusion welding process was performed at 1250 °C for 1 h and the final heat treatment was carried out at 1150 °C for 24 h for all samples except CrMnFeCoNi + Mn, which was diffusion welded and heat treated at 1000 °C for 1 h and 24 h, respectively.

from the composition of the base alloy, the Mo content can be increased in the fcc structure up to maximum solubility of 16 at.%. A continuous increase in Mo results in a decrease in Co and Cr concentrations, whereas uphill-diffusion of Ni towards the phase boundary to approximately 37 at.% can be observed. The phase transition is characterised by abrupt changes in all element concentrations. The intermetallic phase shows a constant composition in a width of approximately 36 μm . In contrast to the diffusion couple with Cr, the formed intermetallic phase cannot be indexed as bcc, fcc or sigma phase.

In general, the investigated alloys show for all constituent elements (and Fe as a foreign element in case of CoNiCrMo) large concentration intervals, in which the fcc phase of the alloy remains stable, or metastable as discussed below. The results show a very insensitive response of the alloys to fluctuations in concentrations. In cases where an intermetallic phase is formed within the interdiffusion zone, the maximum amount of alloying element, which can be dissolved in the matrix of the alloy is substantially lower.

To illustrate the formation of secondary phases, BSE (backscattered electron) images with superimposed chemical distribution of the diffusion couples CrMnFeCoNi with Cr and Fe are shown in Fig. 2 b.) and c.) In case of Cr as a diffusion partner element, a grain orientation contrast shift is found at the abrupt change in composition between the fcc structure of the alloy and the intermetallic phase (Fig. 2 b.)). In contrast to this, a secondary phase can also be formed in smooth chemical concentration gradients. The BSE image clearly shows the formation of martensite in the range of higher alloying element concentrations in the bcc solid solution, which exhibits in a width of about 25 μm a different microstructure (Fig. 2 c.)). A change in material contrast is not observable. The position of the phase transition of the fcc structure measured by EBSD corresponds to the phase boundary with the secondary phase, which is visible in the BSE contrast.

There are several scenarios in a single diffusion couple experiments with regard to phase stability, including entire single phase, phase transition between solid solutions or the formation of intermetallic phases (Fig. 2). To visualize the sensitivity to compositional changes with regard to phase stability, the results of multiple diffusion couples can be combined in a spider web like diagram. Fig. 4 shows the dependence of the crystal structure on the chemical composition of the investigated alloys. Each branch represents a single diffusion couple experiment and the corresponding axis displays the composition of the respective diffusion partner element. The grey area indicates the initial content of the respective diffusion partner element in the base alloy. By the diffusive exchange with the pure partner element at annealing temperature, the concentration of this element increases, while all other elements decrease in their concentrations (Fig. 3), which is not shown here. Starting from the equiatomic composition of the Cantor alloy (Fig. 4 b.)), the Fe concentration can be increased up to 65 at.% with alloy remaining in the fcc structure (green area). A higher Fe concentration results in a phase transition from the fcc structure of the alloy to the bcc structure of Fe. In case of a Cr increase (Fig. 4 b.)), the phase of the base alloy remains stable up to 34 at.%. At this point there is a jump in the Cr concentration to 54 at.%, which indicates a two-phase region (green/blue shaded region). The EBSD analysis shows a bcc structure from 55 at.% Cr up to 100 at.%, yet, the shape of the profile with a nearly constant concentration over a certain width indicates an intermetallic phase (blue area). This was also proven by nanoindentation hardness measurements, that are part of an ongoing study, showing a high hardness level of approximately 11 GPa within the flat concentration interval. Considering the limitations of EBSD, further structural investigations are necessary, as the method is not appropriate to determine the crystal structure of an unknown intermetallic phase. The phase transition from the intermetallic phase to pure Cr is also characterised by a jump in concentrations, thus, exhibits

Fig. 3. EDX line profiles for the diffusion couples of CoNiCrMo and CrMnFeCoNi with Cr, Mn, Fe, Co, Ni and Mo. Based on the phase analysis, which is represented by a coloured scale on top of each diagram, the diffusion couples are categorised into the three cases single phase (a.) – c.)), phase transition (d.) – g.)) and formation of intermetallic phases (h.) – j.)). The initial interface is denoted by a dashed line. The diffusion welding process was performed at 1250 °C for 1 h and the final heat treatment was carried out at 1150 °C for 24 h for all samples except CrMnFeCoNi + Mn (c.)), which was diffusion welded and heat treated at 1000 °C for 1 h and 24 h, respectively.

a two-phase region that extends up to 99 at.% Cr beyond which the bcc structure of Cr becomes stable.

4. Discussion

4.1. Methodological aspects

Phase formation rules and phase stability are key aspects in the field of research on high-entropy alloys, yet, the terminology can be misleading as phase stability and thermodynamic equilibrium are often not equivalent. Even though numerous high-entropy alloys with a single phase solid solution at ambient temperature have been generated and investigated, it is still unclear whether any of them is actually in thermodynamic equilibrium or all being metastable. One example is the precipitation behaviour of the Cantor alloy, which is still the most common example for a single phase high-entropy alloy, despite being only metastable below 800 °C. [4,8–11] This aspect also affects the apparent phase stability ranges observed along the uniaxial concentration gradients in the diffusion couples, as presented in this work.

In principal, the experimental procedure allows different cooling conditions, such as freezing the condition at the annealing temperature via quenching or slow cooling to approach the thermodynamic equilibrium of the system. Low cooling rates or additional dwell times at lower temperatures would be the obvious choice for studies on thermodynamic equilibria and decomposition tendencies of high-entropy alloys. In this study, the specimen was quenched and phase stability is considered as states that can be kept stable at ambient temperature despite being potentially metastable. This approach would be a preferred choice for investigations of properties in single phase solid solutions over a wide compositional range such as solid solution hardening.

It is also possible to separate between phase transitions that already occurred during interdiffusion annealing and those that occurred upon cooling. During annealing, the system is in thermodynamic equilibrium with respect to local chemistry and there are no changes to local chemistry upon water quenching. Consequently, phase transitions that show discontinuities and accumulations in the concentration profile were already present during annealing and the discontinuities correspond to a two-phase region, where intermediate concentrations do not exist on a local scale (e.g. CoNiCrMo + Mo, CoNiCrMo + Cr and CrMnFeCoNi +

Cr). The accumulation in Ni concentration prior to the phase transition can be explained by a narrow concentration interval within the intermetallic phases. Phase transitions with a smooth concentration profile on the other hand must have formed during cooling. One example for a smooth concentration gradient is the CrMnFeCoNi + Fe diffusion couple. This diffusion couple exhibits an fcc structure over the entire concentration range at an annealing temperature of 1150 °C. Upon water quenching, Fe transforms to bcc structure for Fe concentrations above 65 at.%. This leads to the observation of a phase boundary at room temperature across a smooth diffusion gradient. Such a phase transition violates Gibbs phase rule and cannot exist in thermodynamic equilibrium at annealing temperature, but must have formed during water quenching. Based on this information, the phase stability diagram at annealing temperature is presented in Fig. 5 and discussed below.

While diffusion couples show a huge potential for providing a comprehensive view on phase stability ranges and phase transitions with limited experimental effort, there are also limitations to the method that have to be considered. An increase of the alloying or foreign element that is used in the diffusion couple not only results in a decrease of the other constituent elements but also changes their concentration ratios due to the different diffusivities of the elements involved. These deviations can be negligibly small such as in the CrMnFeCoNi + Mn case, where the diffusion couple resembles a quasi-binary phase diagram within the limitations discussed above (Fig. 3 c.). However, the trajectory through the multi-dimensional phase diagram of high-entropy alloys can also be more complex and far from linear in case of uphill diffusion (e.g. CrMnFeCoNi + Ni) or the occurrence of intermetallic phases during diffusion annealing (Fig. 3 b.).

Thus, the diffusion couple technique facilitates to analyse a wide range of concentrations, but a direct control of the composition is not feasible. The technique therefore is a good approach to screen the property range of medium- and high-entropy alloys over a wide compositional range, but it cannot replace the selective production of individual alloy compositions.

Furthermore, the concentration profiles as well as the phase stability ranges can be used for a comparison with existing results from Calphad simulations. Bracq et al. [29] have calculated the stability ranges in the Cantor alloy using the Calphad method and the TCHEA1 database by varying the concentration of each element in the Cantor system, while

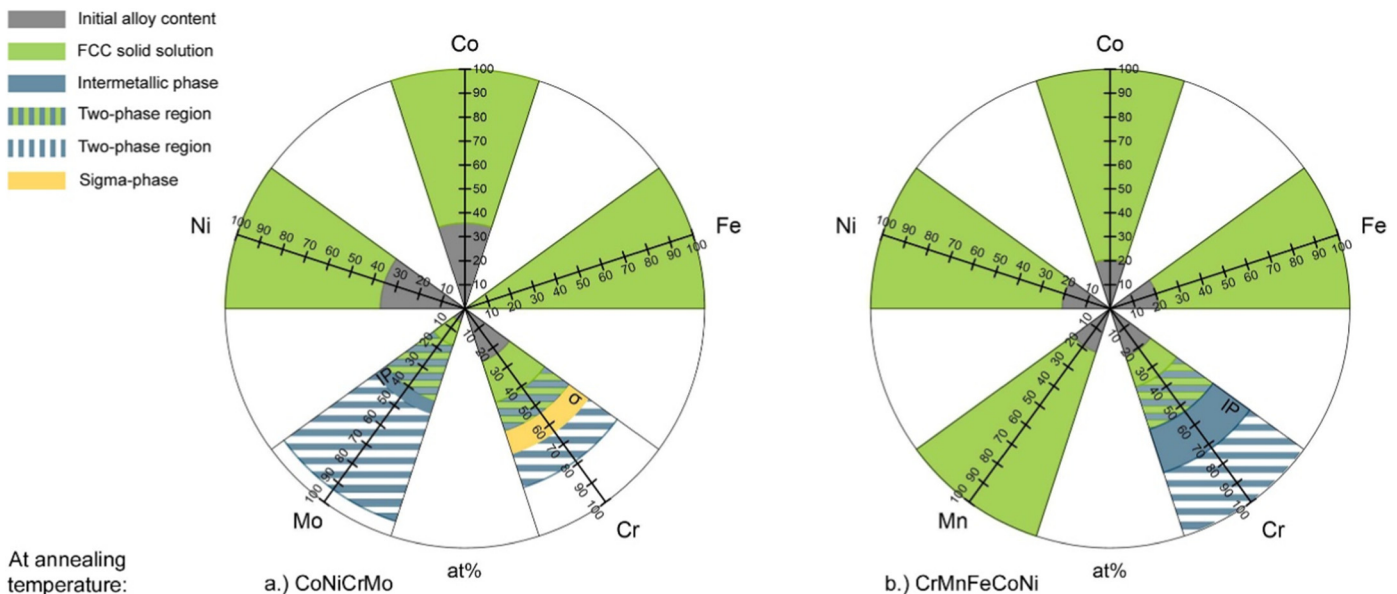


Fig. 5. Phase stability diagram of a.) CoNiCrMo and b.) CrMnFeCoNi alloy at annealing temperature, based on the shape of the concentration profiles. The diffusion couples with Cr, Mo, Fe, Co and Ni were heat treated at 1150 °C, the diffusion couple CrMnFeCoNi + Mn was heat treated at 1000 °C.

keeping all other elements in equimolar proportion. In case of an addition of Co, Fe and Ni the simulations show a complete miscibility (single phase fcc) between the pure element and the CrMnFeCoNi alloy at an annealing temperature of 1150 °C. This is confirmed by the present concentration profiles (Fig. 3), which exhibit no discontinuities for those diffusion couples, thus, indicating an entire single phase range at the annealing temperature (Fig. 5) as has been discussed above. The solubility limit of Cr in the fcc structure of the Cantor alloy at 1150 °C was determined by Calphad to approximately 30 at.%. The present work shows a maximum solubility of about 34 at.%. The small deviation could be attributed to the fact that not all elements change in the same ratio and an uphill diffusion of Ni occurs at the interface. Furthermore, the simulations show a two-phase region (fcc + bcc) in a Cr concentration interval from approximately 30 to 55 at.%. This corresponds well with the concentration interval of the discontinuity in the concentration profile (Fig. 3 j.) from approximately 34 to 53 at.% Cr, to which a two-phase region is assigned (Fig. 5 b.)

According to Bracq et al. [29], Mn destabilizes the fcc solid solution, however, the present results show a single fcc phase over the complete concentration interval. This behaviour cannot be explained at the moment and requires further investigations.

4.2. Application to phase stability

The well-defined concentration gradient within the interdiffusion zone of diffusion couples can be used to investigate fundamental scientific aspects such as the phase stability of high-entropy alloys over a wide concentration interval with limited experimental effort. By superimposing the chemical concentration gradients with phase distribution on a local scale, an insight into the phase stabilising factors can be obtained. One benefit of this method is that not only individual alloy compositions are considered, but also concentration intervals. Two parameters to describe the phase stability of high-entropy alloys are the atomic size mismatch parameter δ and the valence electron concentration (VEC). [13,14] The continuous measurement of the chemical concentration facilitates the determination of a composition-dependent atomic size mismatch and valence electron concentration distribution within the interdiffusion zone. In this way, the influence of these parameters on phase stability can be mapped.

4.3. Phase stability criteria: atomic size mismatch

The effect of the atomic size mismatch on the phase formation is not subjected to strict limits, it should be considered as a reference. The atomic size mismatch parameter δ can be determined according to Eq. 1 as a function of the chemical composition [13]:

$$\delta = \sqrt{\sum_{i=1}^N c_i (1 - r_i / \bar{r})^2} \quad (1)$$

where N is the total number of elements, c_i is the concentration in at.% of the i th element, $\bar{r} = (\sum_{i=1}^N c_i r_i)$ represents the average atomic radius and r_i is the atomic radius, which is obtained from literature [30]. The chemical compositions respectively the δ -intervals within the intermetallic phases (see Tables 3 and 4) can be used to complement the results of Zhang et al. [13]. The diffusion couples formed on the basis of the

Table 4
Atomic size mismatch of base alloy and intermetallic phase.

Diffusion couple	Atomic size mismatch		
	Base alloy	Phase transition	Intermetallic phase
CoNiCrMo + Cr	2.85	2.47	2.79
CoNiCrMo + Mo	2.85	3.77	5.38
CrMnFeCoNi + Cr	0.92	0.99	0.99

CoNiCrMo alloy are located in a δ -range in which both single phase solid solutions and ordered or intermetallic phases occur. Thus, the results of the CoNiCrMo alloy confirm the dependency of the crystal structure on the atomic size mismatch, which is shown in literature. Due to the very similar atomic radii of the constituent elements of the Cantor alloy, fluctuations in element concentrations do not affect the atomic size mismatch parameter.

4.4. Phase stability criteria: valence electron concentration

Another application of the diffusion couples that is related to phase stability is the interpretation of the results with regard to the valence electron concentration (VEC). Since the VEC directly affects the phase stability, Guo et al. [14] presented a statistical analysis (Fig. 6) to describe the phase formation of cubic solid solutions as a function of the valence electron concentration and adapted specific alloy compositions and calculated the valence electron concentrations. Since each composition must be produced individually, they vary in processing and are associated with much experimental effort. According to the observed crystal structures, they defined two threshold values for the formation of fcc and bcc solid solutions.

Based on the chemical gradients at phase transitions, valence electron concentration intervals can be calculated for the different diffusion couples. The CoNiCrMo and the CrMnFeCoNi base alloys show valence electron concentrations of 8.5 and 8, respectively. In case of the CoNiCrMo alloy, an increase in the concentrations of the bcc elements Cr, Mo and Fe results in a decrease of the VEC. The phase of the base alloy (green area) remains stable up to valence electron concentrations of 8.0 (+Cr), 8.3 (+Mo) and 8.2 (+Fe). Thus, the phase transition of the fcc medium-entropy alloy takes place at or before the mentioned threshold value of 8.0. Since the diffusion couples with Cr and Mo show the formation of intermetallic phases, a VEC interval can also be obtained for the compositions within these phases (blue area). No VEC is assigned to the concentration intervals within a discontinuity in the profile. The VEC at phase transitions of the CrMnFeCoNi alloy may provide information on the applicability of the model to five-component alloys. The concentrations within the fcc structure of the alloy show a VEC interval from 8.0 of the base alloy to 7.75 at phase transition when using Cr as diffusion partner. Therefore, the measured phase transition takes place in a VEC interval, in which a transition would be expected according to the model. In the same way, VEC intervals can be assigned to the intermetallic phase or to the phase of the diffusion partner element (grey area).

However, there are also limitations to the applicability of this model. The diffusion couple CrMnFeCoNi + Cr shows a transition from an

Table 3

Stability range of the intermetallic phases. The diffusion welding process was performed at 1250 °C for 1 h and the final heat treatment was carried out at 1150 °C for 24 h.

Concentration in at.%	Co	Cr	Fe	Mn	Mo	Ni
CoNiCrMo + Cr	21.0–17.1	53.8–63.9	–	–	7.0–3.2	18.2–15.8
CoNiCrMo + Mo	24.7–21.6	15.6–11.9	–	–	40.4–46.3	19.3–20.2
CrMnFeCoNi + Cr	12.1–7.7	53.6–71.3	12.1–8.2	10.4–6.5	–	11.8–6.26

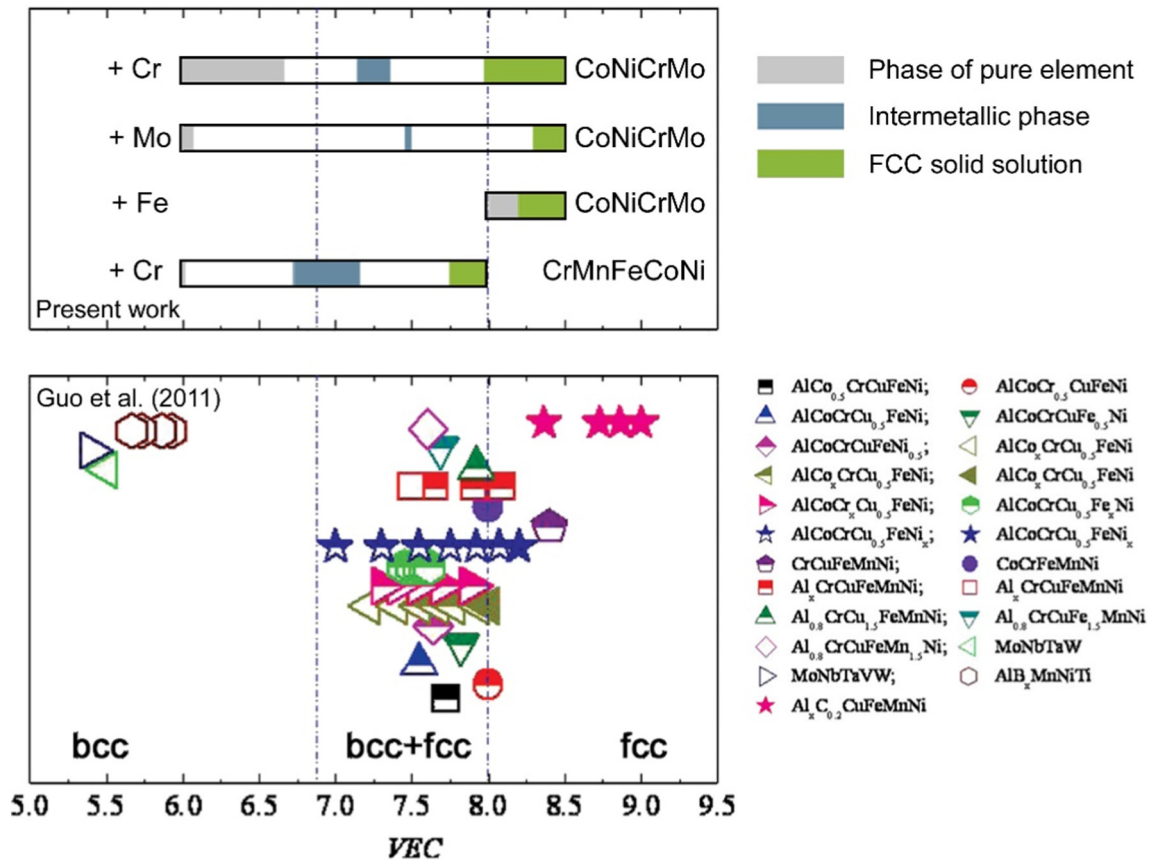


Fig. 6. Model of valence electron concentration for prediction of stable cubic phases. In addition to the statistical results of Guo et al. [14] (lower section of the figure), the measurements of this work are also shown for the CoNiCrMo and CrMnFeCoNi alloy systems (upper section of the figure).

ordered to a disordered bcc structure, which is not considered in the VEC model. The model also fails to predict the phase transition from fcc to bcc that is observed in the CrMnFeCoNi + Fe diffusion couple. Here, the VEC remains constant (8) over the entire interdiffusion zone due to the fact that the change in concentrations of Co and Ni (VEC > 8) is compensated by a change in concentration of Cr and Mn (VEC < 8). Furthermore, the threshold values mentioned in the work of Guo et al. [14] can only be considered as an estimate, given that they depend on the cooling rates [31]. The frequently used fast cooling rates in literature allow a comparability to the present results, where samples were also quenched. Yet, this implies that the stability ranges of the VEC model include metastable ranges, whereas the thermodynamic equilibrium at low temperatures may not be a single phase solid solution, as it has been demonstrated by the decomposition behaviour of the Cantor alloy. [8–10]

4.5. Further applications

Phase stability is a key aspect in research on high-entropy alloys, however several other aspects can be addressed using diffusion couples. One example is solid solution strengthening, which is still not fully understood for high-entropy alloys [4,5,16]. Here, diffusion couples provide the possibility to investigate the mechanical properties as a function of the chemical composition within the interdiffusion zone. The comparison of chemical composition and hardness distribution can reveal information about the solid solution strengthening behavior in chemically complex systems. Another application example could be related to diffusion properties of high-entropy alloys including the validation of modelling approaches for (inter)diffusion, which is beyond the scope of the current work.

5. Summary & conclusion

The aim of this work was to investigate the potential and limitations of a diffusion couple approach for high-entropy alloys as well as to apply this approach to address phase stability aspects of such alloys. Diffusion couples of the CoNiCrMo and CrMnFeCoNi alloys were prepared with constituent and foreign pure elements as diffusion partner. The uniaxial concentration gradients and the phase distribution within the interdiffusion zone were measured by a combination of EDX and EBSD.

- 1.) The diffusion couple approach enables investigations on phase stability over a wide compositional range with limited experimental effort. Since the samples were quenched, phase stability measurements consider potentially metastable phases, which can be kept stable at ambient temperatures.
- 2.) Three scenarios with respect to phase stability can be observed, including single phase, phase transition or the formation in intermetallic phases. A phase stability diagram is presented to visualize the solubility limits of individual elements in the investigated fcc high-entropy and medium-entropy alloys.
- 3.) Various approaches for predicting phase stability of high-entropy alloys have been discussed based on the atomic size mismatch or the valence electron concentration (VEC). While the atomic size mismatch describes the formation of intermetallic phases in the CoNiCrMo alloy, the prediction of the structure is insufficient for the CrMnFeCoNi alloy. The present results mostly validate the model of valence electron concentration for predicting stable cubic solid solutions. Hence, the threshold values defined by Guo et al. [14] provide an indication for describing the phase stability with the exception of the fcc to bcc transition with increasing Fe concentrations, which is not covered by the VEC model.

4.) Diffusion couples enable the study of quaternary and quinary intermetallic phases within the chemical composition space of high-entropy alloys. Intermetallic phases, which have already formed during annealing are represented by discontinuities in concentrations. The identification and characterization of these phases is important, as the experimental data on quaternary and quinary intermetallic phases currently still relatively limited.

CRedit authorship contribution statement

Tom Keil: Investigation, Data curation, Formal analysis, Validation, Visualization, Writing - original draft, Writing - review & editing. **Enrico Bruder:** Conceptualization, Methodology, Validation, Formal analysis, Writing - original draft, Writing - review & editing, Project administration. **Karsten Durst:** Conceptualization, Methodology, Writing - review & editing, Supervision, Project administration, Funding acquisition.

Acknowledgements

The authors gratefully acknowledge support by the German Research Foundation (DFG) under grant number DU-424/13-1. The authors also thank Heraeus Medical Components for providing the CoNiCrMo alloy and Dr. Sergiy Divinski (WWU Münster) for providing the Cantor alloy.

Conflicts of interest

The authors declare no conflict of interest.

Data availability

The raw/processed data required to reproduce these findings cannot be shared at this time as the data also forms part of an ongoing study.

Appendix A. Supplementary data

Supplementary data to this article can be found online at <https://doi.org/10.1016/j.matdes.2019.107816>.

References

- [1] J.-W. Yeh, et al., Nanostructured high-entropy alloys with multiple principal elements novel alloy design concepts and outcomes, *Adv. Eng. Mater.* (2004) 299–303.
- [2] J.-W. Yeh, Alloy design strategies and future trends in high-entropy alloys, *Jom* 65 (12) (2013) 1759–1771.
- [3] M.C. Gao, et al., *High-Entropy Alloys*, Springer-Verlag, Switzerland, 2016.
- [4] D.B. Miracle, O.N. Senkov, A critical review of high entropy alloys and related concepts, *Acta Mater.* 122 (2017) 448–511.
- [5] Y. Zhang, et al., Microstructures and properties of high-entropy alloys, *Prog. Mater. Sci.* 61 (2014) 1–93.
- [6] J.-W. Yeh, et al., Formation of simple crystal structures in Cu-Co-Ni-Cr-Al-Fe-Ti-V alloys with multiprincipal metallic elements, *Metall. Mater. Trans. A* 35 (8) (2004) 2533–2536.
- [7] B. Cantor, et al., Microstructural development in equiatomic multicomponent alloys, *Mater. Sci. Eng. A* 375–377 (2004) 213–218.
- [8] B. Schuh, et al., Mechanical properties, microstructure and thermal stability of a nanocrystalline CoCrFeMnNi high-entropy alloy after severe plastic deformation, *Acta Mater.* 96 (2015) 258–268.
- [9] J.Y. He, et al., Steady state flow of the FeCoNiCrMn high entropy alloy at elevated temperatures, *Intermetallics* 55 (2014) 9–14.
- [10] E.J. Pickering, et al., Precipitation in the equiatomic high-entropy alloy CrMnFeCoNi, *Scr. Mater.* 113 (2016) 106–109.
- [11] M.V. Klimova, et al., Effect of second phase particles on mechanical properties and grain growth in a CoCrFeMnNi high entropy alloy, *Mater. Sci. Eng. A* 748 (2019) 228–235.
- [12] Y. Zhang, et al., Guidelines in predicting phase formation of high-entropy alloys, *MRS Communications* 4 (02) (2014) 57–62.
- [13] Y. Zhang, et al., Solid-solution phase formation rules for multi-component alloys, *Adv. Eng. Mater.* 10 (6) (2008) 534–538.
- [14] S. Guo, et al., Effect of valence electron concentration on stability of fcc or bcc phase in high entropy alloys, *J. Appl. Phys.* 109 (10) (2011), 103505.
- [15] O.N. Senkov, et al., Microstructure and room temperature properties of a high-entropy TaNbHfZrTi alloy, *J. Alloys Compd.* 509 (20) (2011) 6043–6048.
- [16] Z. Wu, et al., Temperature dependence of the mechanical properties of equiatomic solid solution alloys with face-centered cubic crystal structures, *Acta Mater.* 81 (2014) 428–441.
- [17] O. Franke, K. Durst, M. Göken, Nanoindentation investigations to study solid solution hardening in Ni-based diffusion couples, *J. Mater. Res.* 24 (03) (2011) 1127–1134.
- [18] A.A. Kodentsov, G.F. Bastin, F.J.J. van Loo, The diffusion couple technique in phase diagram determination, *J. Alloys Compd.* 320 (2001) 207–217.
- [19] K.Y. Tsai, M.H. Tsai, J.W. Yeh, Sluggish diffusion in Co–Cr–Fe–Mn–Ni high-entropy alloys, *Acta Mater.* 61 (13) (2013) 4887–4897.
- [20] V. Verma, A. Tripathi, K.N. Kulkarni, On interdiffusion in FeNiCoCrMn high entropy alloy, *J. Phase Equilib. Diffus.* 38 (4) (2017) 445–456.
- [21] P. Wilson, R. Field, M. Kaufman, The use of diffusion multiples to examine the compositional dependence of phase stability and hardness of the Co-Cr-Fe-Mn-Ni high entropy alloy system, *Intermetallics* 75 (2016) 15–24.
- [22] Zhao, J.C., Reliability of the diffusion-multiple approach for phase diagram mapping, *J. Mater. Sci.*, 2004, 39(12): p. pp 3913 - 3925.
- [23] J.C. Zhao, et al., A diffusion-multiple approach for mapping phase diagrams, hardness, and elastic modulus, *JOM* 54 (7) (2002) 42–45.
- [24] W. Chen, L. Zhang, High-throughput determination of interdiffusion coefficients for Co-Cr-Fe-Mn-Ni high-entropy alloys, *J. Phase Equilib. Diffus.* 38 (4) (2017) 457–465.
- [25] J. Kottke, et al., Tracer diffusion in the Ni-CoCrFeMn system: transition from a dilute solid solution to a high entropy alloy, *Scr. Mater.* 159 (2019) 94–98.
- [26] H.u. Rehman, *Solid Solution Strengthening and Diffusion in Nickel- and Cobalt-Based Superalloys*, Friedrich-Alexander-Universität Erlangen-Nürnberg: FAU University Press, 2016.
- [27] H. Mehrer, *Diffusion in Solids*, vol. 17, Springer Berlin Heidelberg, 2007.
- [28] W. Martienssen, H. Warlimont, *Springer Handbook of Condensed Matter and Materials Data*, Springer, Berlin Heidelberg, 2005.
- [29] G. Bracq, et al., The fcc solid solution stability in the Co-Cr-Fe-Mn-Ni multi-component system, *Acta Mater.* 128 (2017) 327–336.
- [30] C. Kittel, *Einführung in die Festkörperphysik*, 14th ed, 2006 (München).
- [31] S. Singh, et al., Decomposition in multi-component AlCoCrCuFeNi high-entropy alloy, *Acta Mater.* 59 (1) (2011) 182–190.

Publication B

Reproduced full text article with permission from Springer Nature.

Copyright (2021), Journal of Materials Research.



Solid solution hardening in CrMnFeCoNi-based high entropy alloy systems studied by a combinatorial approach

Tom Keil^{1,a)}, Daniel Utt², Enrico Bruder¹, Alexander Stukowski², Karsten Albe², Karsten Durst¹

¹Technical University of Darmstadt, Materials Science, Physical Metallurgy, Alarich-Weiss-Str. 2, 64287 Darmstadt, Germany

²Technical University of Darmstadt, Materials Science, Materials Modelling, Otto-Berndt-Str. 3, 64287 Darmstadt, Germany

^{a)}Address all correspondence to this author. e-mail: t.keil@phm.tu-darmstadt.de

Received: 18 December 2020; accepted: 7 April 2021; published online: 21 April 2021

Solid solution hardening in high entropy alloys was studied for the Cantor alloy using diffusion couples and nanoindentation. We study a continuous variation of the alloying content and directly correlate the nanoindentation hardness to the local composition up to the phase boundary. The composition dependent hardness is analysed using the Labusch model and the more recent Varvenne model. The Labusch model has been fitted to experimental data and confirms Cr as the most potent strengthening element. For comparison of the experimental hardness and the predicted yield strength of the Varvenne model, a concentration-dependent strain-hardening factor is introduced to account for strain hardening during indentation, which leads to a very good agreement between experiment and model. A study of the input parameters of the Varvenne model, performed by atomistic computer simulations, shows no significant effect of fluctuations in the atomic size misfit volumes or in the local shear modulus to the computed yield strength.

Introduction

The role of solid solution hardening (SSH) in chemically complex alloys e.g. high entropy alloys (HEAs) [1] has been subject of substantial attention in the past few years [2–6]. However, a generalised and validated model for the prediction of solid solution hardening in HEAs is still needed [2, 7]. The conventional Labusch SSH model [8, 9] describes the interaction of obstacles and dislocations in dilute solid solution alloys based on a combination of two elastic effects (namely size and modulus misfits). In the Labusch model solid solution hardening is described as the change in critical shear stress $\Delta\tau_{\text{Labusch}} \propto \Delta c^{2/3}$ required for dislocation motion, where Δc is the change in concentration of the solute. This conventional SSH model requires a clearly defined differentiation of solute and solvent species [8, 9]. The issue applying the Labusch model to HEAs is that no atomic species can be taken as solute or solvent as all elements are present in similar fractions in the alloy.

An early approach for modelling SSH in HEAs was proposed by Senkov [4] using the Labusch model. In this case, the

TiZrNbHfTa body-centered cubic (BCC) alloy was modelled as pseudo-binary in terms of atomic size misfit and modulus misfit, which resulted in a yield strength difference of 18% between model and experiment. This approach, however has not been generalized for all HEAs, especially for alloys which cannot be split into pseudo-binaries.

A more recent approach for modelling SSH in highly concentrated face-centered cubic (FCC) HEAs was proposed by Varvenne [10, 11]. The Varvenne model describes a HEA as a homogeneous monoatomic matrix with average mechanical properties, in which the different constituents of the HEA are embedded. These randomly distributed solutes are responsible for the observed strengthening. Therefore, a dislocation moving through a HEA sees this homogeneous background matrix and the influence of the different solutes. The strain fields of the solutes interact with the dislocation line, exhibiting an interaction force [10–12]. Whereas in the classical SSH models local fluctuations in the shear modulus ($\Delta\mu$) are assumed to influence the magnitude of this interaction force [8, 9], the Varvenne

model only considers an atomic size misfit (ΔV), neglects these fluctuations, and depends on an average shear modulus. Nevertheless, satisfactory agreement between experimental and predicted strength was obtained in previous studies of Cantor alloy subsystems [5, 6, 13].

In this paper, we study diffusion couples of the Cantor (CrMnFeCoNi) alloy [14] with its pure constituent elements to determine nanoindentation hardness as a function of local composition in a continuous manner. This approach allows us to study SSH in HEAs having access to a wide range of chemical compositions up to the solubility limit of each constituent element. Concentrations up to the phase boundary can thereby be accessed, which would be impossible using samples prepared with discrete concentrations (compare Refs. [5, 6]). We use this unique data set to correlate hardness and local composition to test the two SSH models and isolate the individual strength contributions of the different solutes in the Cantor alloy system.

Results

Nanoindentation hardness measurements

Figure 1a shows the hardness as a function of indentation depth h of pure Ni and Cantor ($H-h$ curves of the other diffusion couples are shown in the Appendix). The indentation size effect (ISE) causes a decreasing hardness with increasing indentation depth until a depth independent macroscopic H is reached [15]. To minimize the contributions from the indentation size effect and also to ensure a high lateral resolution, the hardness is averaged over an indentation depth interval from 900 to 1000 nm. Indentations to higher depth (2500 nm) on discrete Ni-diluted

Cantor subsystems (Ni20, Ni60, Ni92) have shown a concentration independent internal length scale ($h^* \approx 0.4$) and thus a comparable ISE in the FCC solid solution of the Cantor alloy [16]. Since the ISE is expected to be comparable for all compositions investigated, the averaged hardness from 900 to 1000 nm indentation depth can be used to evaluate the SSH. Furthermore, indentation strain rate jump tests on the aforementioned discrete Ni-diluted Cantor subsystems revealed a negligible strain rate sensitivity in the range of 0.004 (pure Ni) to 0.009 (Cantor). Furthermore, all indentation experiments are performed at a constant strain rate, no effects on the evaluation of SSH are expected due to strain rate sensitivity. The pile-up behavior was measured and no significant pile-up could be detected for all investigations up the phase boundary. From these results, a composition independent pile-up behavior and strain rate sensitivity is assumed for these samples, thus, the used Tabor's equation holds true and no effects on the evaluation of solid solution hardening is expected.

The effect of SSH in the CrMnFeCoNi alloy can be clearly seen in the indentation data in Fig. 1a as the hardness increases upon addition of Cr, Mn, Fe, and Co to Ni. The indentation modulus E is constant for each indentation but shows a concentration dependency, as can be seen for Ni and Cantor. A mean indentation modulus of 198.3 ± 7.9 GPa is obtained for the Cantor alloy and 221.4 ± 2.4 GPa for Ni, both being in good agreement with literature data of single phase materials [17, 18].

Concentration and hardness profiles

The local concentration, crystal structure and hardness were measured over the whole interdiffusion zone using a diffusion

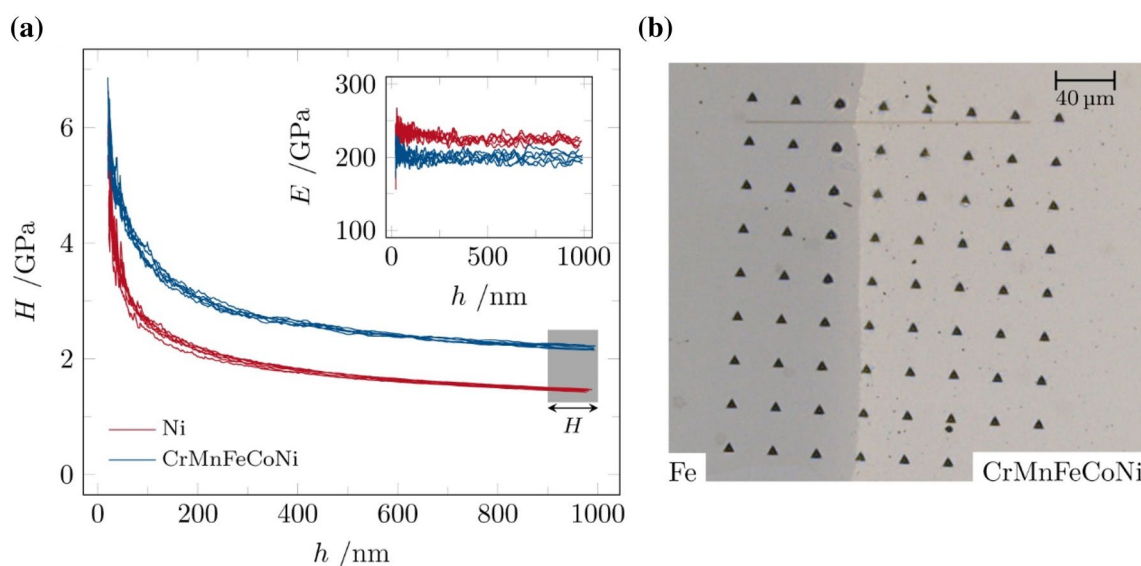


Figure 1: (a) Typical measurement of nanoindentation hardness H and indentation modulus E as function of indentation depth h for Cantor and Ni. (b) Light microscopy image of the indentation field across the interdiffusion zone of the diffusion couple CrMnFeCoNi + Fe.

couple approach; here only the FCC single-phase region is shown. For more details on the microstructure and a detailed discussion of the different diffusion profiles and the stability ranges of other phases see Ref. [19]. A light microscopy image of a representative indentation field across the complete interdiffusion zone between Cantor and Fe is shown in Fig. 1b. We can assume that the composition within the plastic zone beneath the indenter is nearly uniform, as we limited the penetration depth to 1000 nm. Due to the large grain size of $\approx 100 \mu\text{m}$, grain boundary strengthening effects can be neglected, as each indent probes only a single grain. Furthermore, we do not observe a gradient in grain size along the interdiffusion zone. For the evaluation of SSH, only indents with a minimum distance of the plastic zone's diameter from the phase boundary were considered.

Figure 2 shows the hardness as a function of varying concentrations (solid lines) of the FCC structure in the interdiffusion zone (IDZ) starting from the equiatomic composition of the Cantor alloy with a hardness level of $\approx 2.2 \text{ GPa}$ on the right. The coefficient of variation (ratio of the standard deviation to the mean value), caused by the nanoindentation testing setup, is shaded in gray. The maximum coefficient of variation was determined by reference measurements in the equiatomic Cantor alloy as well as in the pure elements and is assumed as being constant within the concentration gradients (max. $\pm 3\%$). On the x-axis, the relative position in the IDZ is shown, while the concentrations of the constituents are given by colored lines. Figure 2a shows the diffusion couple CrMnFeCoNi + Ni, with a single FCC phase over the entire compositional gradient, thus, the complete hardness profile can be used to analyse the effect of SSH starting from a constant and equiatomic composition. Up to a Ni concentration of 70 at.%, the hardness remains almost constant at a hardness level of about 2.2 GPa and decreases with further increase in Ni. The hardness decreases to the hardness of pure Ni as the Ni concentration approaches 1.

If a phase transition takes place within the interdiffusion zone (Fig. 2b–d), only the FCC phase region will be considered in the further analysis. The concentrations of the respective diffusion partner elements Co or Fe can be increased substantially up to $\approx 65 \text{ at.}\%$ until a phase transition takes place [19], it is possible to evaluate SSH up to $\approx 55 \text{ at.}\%$. As Co and Fe increase in concentration, all other constituent elements show a decreasing concentration. The diffusion couple CrMnFeCoNi + Co (Fig. 2c) shows nearly no influence of changing concentrations on the hardness level. An increase in Fe (Fig. 2d) results in a continuously decreasing hardness. The diffusion couple CrMnFeCoNi + Cr shows the formation of an intermetallic phase above $\approx 35 \text{ at.}\%$. The relatively small increase in Cr prior to the formation of an intermetallic phase leads to a hardness increase of 0.3 GPa up to 29 at.% Cr.

Due to oxidation and other surface defects in the CrMnFeCoNi + Mn diffusion couple (evident from the scattering of the nanoindentation data), the evaluation of the hardness is limited to Mn concentrations below 55 at.%. The hardness increases in this concentration interval with increasing Mn content from 2.2 to 2.5 GPa.

Discussion

The direct correlation between hardness and chemical gradients allows to draw conclusions about solid solution hardening. The measured concentration profiles are used as an input for the Labusch model [8, 9] and alternatively the Varvenne model [10, 11]. Both applied models will then be validated against the experimentally measured hardness. By adding each constituent species to the equiatomic composition, the respective influence can be investigated over the complete compositional ranges for all five diffusion couples, where the FCC structure of the Cantor alloy is (meta-)stable.

Application of the Labusch model

To apply the Labusch model to highly concentrated multi component alloys—including HEAs, we generalize the model introducing a different strengthening parameter k_n for each element n leading to the following formulation of the Labusch strengthening model (Eq. 1). Here it is assumed that $\Delta\tau_{\text{Labusch}}$ contributions are additive per constituent of the alloy:

$$\Delta\tau_{\text{Labusch}} = \sum_n k_n \Delta c_n^{2/3} \propto \Delta H \quad (1)$$

Equation 1 is used to fit the modified Labusch model to the experimental hardness data. The individual k_n parameters are found using the change in hardness (ΔH) and the change in concentration (Δc) for the two boundary phases (equiatomic Cantor alloy and composition at phase boundary) for all five diffusion couples simultaneously and solving the resulting system of linear equations. The following strengthening parameters in units of $\text{GPa/at.}\%^{2/3}$ were obtained: $k_{\text{Cr}} = 0.0514$, $k_{\text{Mn}} = 0.0058$, $k_{\text{Fe}} = -0.0470$, $k_{\text{Co}} = -0.0109$, $k_{\text{Ni}} = -0.0342$. The absolute value and sign of the strengthening parameter determine the effect of a changing concentration of the specific element on the strength of the equiatomic Cantor alloy. Based on these k -values and the measured concentration profiles, the concentration dependent hardness is modelled and compared to experimental results. The measured and calculated hardness values normalised by the hardness of the Cantor alloy are shown in Fig. 3. Discrete points denote our measurements, while solid lines give the Labusch solution. Please note, that the different data series are shifted by a constant offset to improve readability. The modified Labusch model is able to accurately

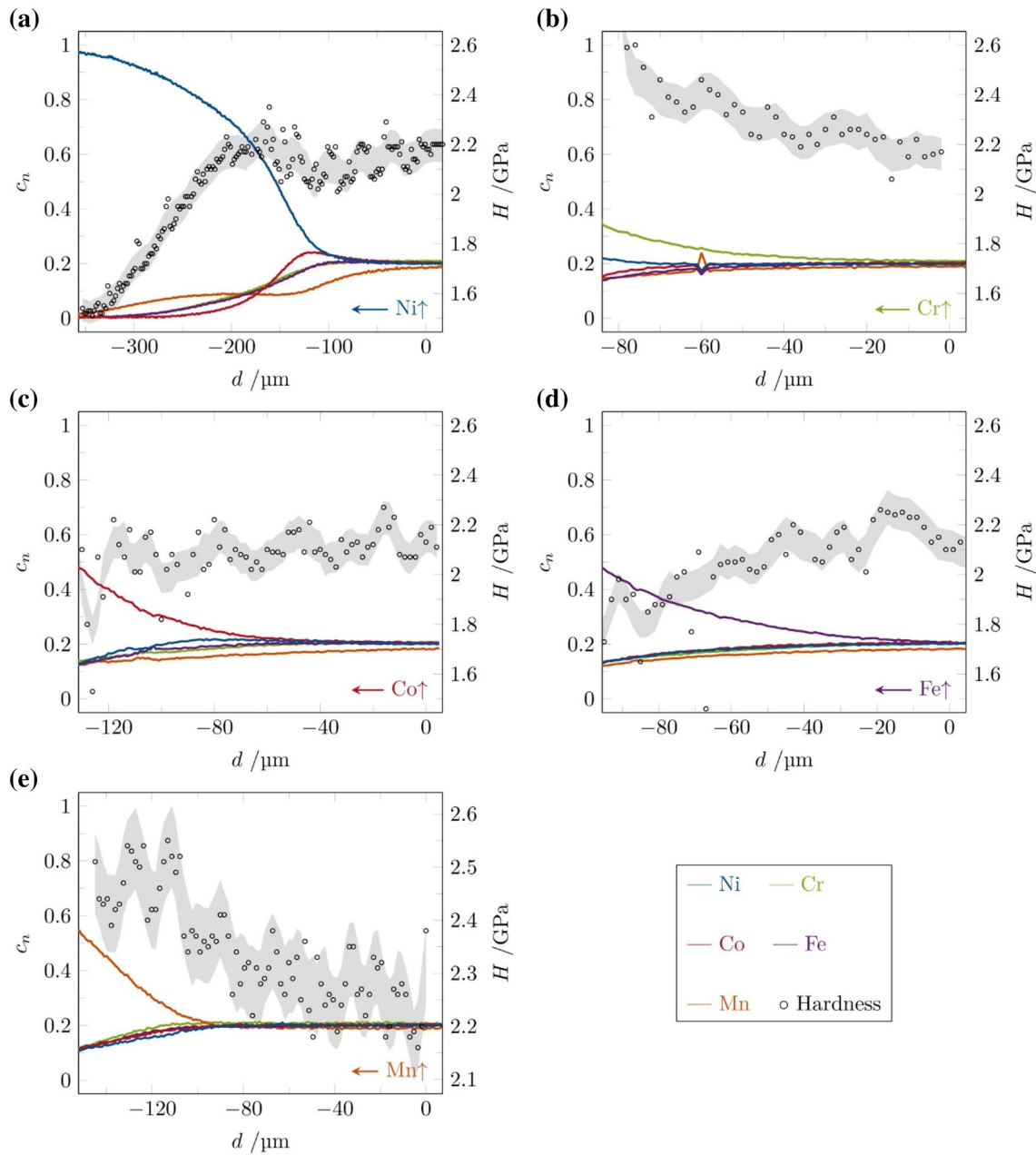


Figure 2: Concentration profiles for the different Cantor + i diffusion couples measured using EDX. d is the relative position within the IDZ starting from the Cantor alloy on the right. The respective diffusion partner is Ni, Cr, Co, Fe, and Mn going from (a) to (e). Only the single-phase FCC region for each sample is shown. Due to oxidation effects of Mn (e), the evaluation of the hardness is limited to the Mn concentration interval from 20 to 55 at. %. The full concentration profiles can be found in Ref. [19]. The nanoindentation hardness is scaled on the secondary y-axis. For further details regarding the error bars (grey), please see the full text.

describe the measured hardness for Cr, Mn, Co, and Fe. For Ni on the other hand, the hardness plateau up to ≈ 70 at. % Ni is not captured by this model. It predicts a continuously decreasing hardness in the Cantor + Ni sample.

As outlined in “Relating yield stress to hardness” section, the conversion between changes in the hardness of a material and

its yield strength is not straight forward. Fitting Eq. (1) however, allows us to circumvent these uncertainties as they are incorporated in the different k_n values. Therefore, the apparent deviation of the Ni hardness series from the prediction cannot be explained by concentration dependent strain hardening or the ISE.

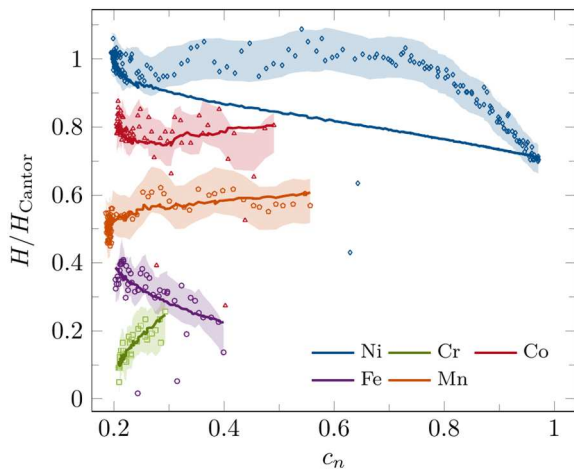


Figure 3: Measured hardness as function of the concentration of the Cantor alloy partner in each diffusion couple (symbols). The fit results from the modified Labusch model (Eq. (1)) are given by solid lines. For clarity, each sample has been shifted along the ordinate. The coloured bars represent the error of the indentation experiments.

Even though, the modified Labusch model is not predictive (the strengthening parameters k_n cannot be known a priori) it provides important insights into the strengthening characteristics of the Cantor system. Note that we have not only used the narrow concentration gradient towards the phase boundary of the diffusion couple Cantor + Cr but we also solved the linear system of equations using all five diffusion couples simultaneously. Based on the obtained strengthening parameters, Cr (positive k_n) seems to be the most potent strengthening element. This observation is consistent with results from Wu et al. [3], where Cr was identified as the element with the strongest impact on strength, which they attributed to modulus mismatch effects. They suggest that the effect is caused by the different shear modulus of Cr compared to the other constituents, based on the assumption of the elastic constants of the elements in their ground state. But it should still be considered, that the Cantor alloy shows a well-defined shear modulus distribution (Fig. 6), which raise the question how the shear modulus misfit needs to be taken into account.

Fe on the other hand shows a contrary effect as it leads to a decrease in hardness, which has already been observed by Bracq et al. [5] for discrete compositions. This behavior is expressed by a negative strengthening parameter.

Application of the Varvenne model

The Labusch model can be used to describe the measured hardness data, but given its large number of tunable parameters it can hardly be used to predict the concentration dependent strength of a HEA. The Varvenne model in its simplified elastic form given by Eqs. (2)–(4) (see methodology “[Varvenne solid solution-hardening model](#)” section), on

the other hand, remains parameter-free and can therefore be used as a predictive tool. However, the Varvenne model cannot provide the absolute hardness measured by nanoindentation, as it describes only a concentration dependent critical shear stress at zero strain. Therefore, we rescaled the experimental and predicted hardness by the Cantor hardness level: $\Delta\sigma_{SS} \propto H(c_n)/H_{Cantor} \propto fCM\Delta\tau_{Varvenne}$ and the ratio between the composition of the equiatomic Cantor alloy on the one side and the local composition at the phase boundary on the other side. This ratio ($H(c_n)/H_{Cantor}$) is considered in Fig. 4. This approach is similar to the normalisation chosen in Refs. [5, 6]. Additionally, a *strain hardening factor* $f(c)$ is introduced, which includes concentration dependent strain hardening and other effects during indentation. The normalization H/H_{Cantor} cancels out errors in the conversion from H to σ_y for the Cantor alloy. Concentrations far away from equimolarity have different strain hardening contributions and this effect can be compensated by the strain hardening factor. Initially, a concentration independent strain hardening was assumed using a constant f parameter of 2 (≈ 1.84 found in tensile tests [20]), which leads to the results shown in Fig. 4a, where the predicted and measured hardness ratios over the concentration of the main element in the diffusion couple are shown. Here the solid lines corresponds to the yield strength obtained from the Varvenne model at 300 K. The required pure metal material constants were taken from Refs. [21, 22], model specific parameters e.g. α and ΔV_n were taken from Ref. [11] and are summarized in Table 2.

The Varvenne model is able to describe the hardness gradients for the increase in Co and Fe, but it fails to predict the hardening behavior for Cr or Mn, or the softening for Ni accurately. In case of the CrMnFeCoNi + Ni couple, the model predicts a decreasing hardness down to 0 GPa for pure Ni. This behavior is caused by the fact that for pure elements, the atomic size misfit in Eq. (2) becomes zero and consequently the predicted critical shear stress is zero. In order to take the indentation base hardness of Ni (1.5 GPa) into account, we shifted the predicted hardness by this constant hardness level: $H(c) = H_{Ni} + fCM\tau_{Varvenne}$. The superposition of the Ni base hardness and the Varvenne model is now represented by a dashed line in Fig. 4a and good agreement is found. Moreover, the Varvenne model is able to capture the plateau in hardness upon addition of Ni. Since we are not able to describe all diffusion couples sufficiently well with the model, the question arises whether this is due to the basic assumptions of the Varvenne model (grey matrix, fixed misfit volumes) or due to the comparison between computed yield strength at zero strain and nanoindentation hardness. To address the first issue, we have determined the standard deviation of the atomic misfit volumes using atomistic computer simulations (Appendix C.2.: [Misfit volumes](#)) and integrated these into Eqs. (2) and (3) according to Ref. [11]. Here ΔV_n^2 is replaced by $(\Delta \bar{V}_n^2 + \sigma_{\Delta V_n}^2)$, where $\Delta \bar{V}_n$ is the mean

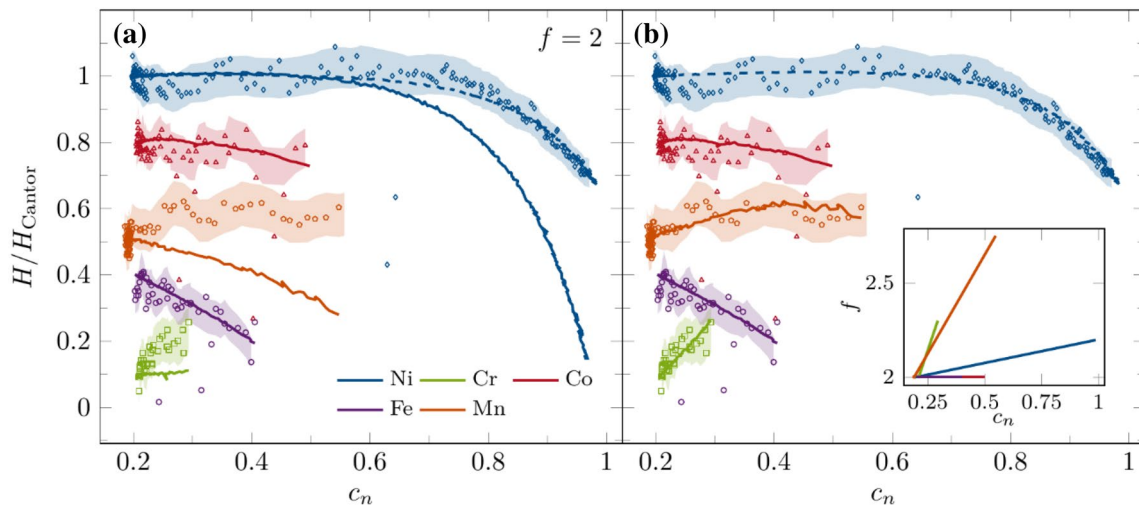


Figure 4: Predicted (solid lines) and measured hardness (symbols) normalized by H_{Cantor} as function of the concentration of the Cantor alloy partner in each diffusion couple. (a) shows the calculated results from the Varvenne model (Eqs. (2)–(4)). (b) shows the Varvenne fit results with a concentration dependent f factor for Cr, Fe, Mn and Ni. The respective f factors are shown in the inset. For Co and Fe a constant f of 2 is assumed as it describes the measured hardness data well. For Cantor + Ni a constant hardness value was introduced to describe the indentation base hardness of pure Ni (dashed lines). The coloured bars represent the error of the indentation experiments.

misfit volume and σ denotes its standard deviation. The respective standard deviations of the solutes are determined to: $\sigma_{\Delta V_{Cr}}^2 = 0.0887\text{\AA}^3$, $\sigma_{\Delta V_{Mn}}^2 = 0.0900\text{\AA}^3$, $\sigma_{\Delta V_{Fe}}^2 = 0.0754\text{\AA}^3$, $\sigma_{\Delta V_{Co}}^2 = 0.0773\text{\AA}^3$, $\sigma_{\Delta V_{Ni}}^2 = 0.0673\text{\AA}^3$. Furthermore, we determined the distribution of the local shear modulus (Appendix C.1: Local shear modulus) and implemented the standard deviation of the local shear modulus (6.246 GPa) as additive strengthening contribution into the aforementioned equations ($\bar{\mu}$ is changed to $\bar{\mu} + \sigma_{\mu}$). Inserting both standard deviations ($\sigma_{\Delta V_n}$ and σ_{μ}) is only physically meaningful, if there is a correlation between the atomic size misfit and the local shear modulus in the HEA-matrix. Even though simulations could not show a correlation, it serves as an upper limit for yield strength predictions of the Varvenne model. Including the standard deviations, a maximum increase in yield strength of roughly 13% can be observed for the equiatomic Cantor alloy, which is mostly attributed to the variation in shear modulus. Nevertheless, the absolute nanoindentation hardness is not provided.

Despite the consideration of the standard deviations, some hardness trends (Cr and Mn) cannot be described by the model. Therefore, a concentration-dependent strain-hardening behavior has now been introduced. Figure 4b shows the fit using a concentration dependent f factor for describing the nanoindentation hardness evolution for all diffusion couples. Substantial concentration changes are found within the IDZ and as a consequence, parameters such as the stacking fault energy (SFE) will change, which in turn affects the local strain hardening behavior and thus the parameter f . The concentration dependent parameter f was fitted based on the measured hardness to account for the strain hardening of changing compositions within the

interdiffusion zone. Since we do not have access to all required experimental data for the direct derivation of the concentration-dependent f factor for all diffusion couples, in the following we will assume a linear dependency. As it can be seen in Fig. 4b, a linearly increasing hardening behavior from 2.0 for Cantor to 2.3 for Cr rich compositions and to 2.75 for Mn rich compositions describes the increasing hardness with increasing Cr or Mn concentration well. The introduction of a concentration dependent f factor leads to good agreement using the Varvenne SSS model and nanoindentation hardness mapping, whereas fluctuations in the local shear modulus and atomic size misfit volumes show negligible effects on the predicted hardness.

Bracq et al. [5] tested 24 discrete compositions based on the Cantor alloy with four elements staying in equiatomic ratio, while the respective fifth element is varied in concentration within the FCC phase space. Using discrete compositions gives better statistics for the mechanical characterisation on each sample, but the investigation of the vast compositional range of HEAs is strongly limited due to a high experimental effort. The diffusion couple approach on the other hand can be considered as a high-throughput screening method investigating broad concentration ranges up to the phase boundary. A quantitative comparison of the nanoindentation hardness values seems to be not appropriate, as the evaluation of hardness took place at different indentation depth. Furthermore, the equiatomic ratio of the other elements can not be kept while adding the respective fifth element during interdiffusion heat treatment. However, a qualitative comparison shows similarities for the addition of Co, Fe, Ni and differences for Cr, Mn. While Bracq et al. [5] could not notice any effect of Mn or Cr increase on hardness,

we observe an increase in hardness especially by adding Cr up to the FCC phase boundary. This observation is consistent with the results from Wu et al. [3], where Cr was also identified as the most potent strengthener element.

Summary and conclusion

The diffusion couple approach enables the investigation of multicomponent alloys over wide compositional intervals regarding phase stability or solid solution strengthening. In this work, the superposition of EDX and nanoindentation hardness measurements was used to investigate SSH as a function of the chemical composition up to the phase boundary of the FCC phase of the Cantor alloy system. It has been shown that nanoindentation hardness mapping can be used for fast exploration of SSH of various chemical compositions. Moreover, the experimentally measured hardness was compared to the hardness predicted by a modified Labusch model and the more recent Varvenne model.

1. The Labusch model can be modified and fit to experimental nanoindentation data. Trends and effects for different constituent elements and solute additions (Co, Cr, Fe) are described well, but the model fails to describe trends for the large compositional range to pure Ni. According to this model, Cr seems to be the most potent strengthening element due to its highest strengthening parameter.
2. The Varvenne model qualitatively describes the trends in most diffusion couples over the whole compositional range in the FCC structure. A concentration dependent correlation factor was introduced to consider changing strain hardening behavior and to fit the Varvenne model to experimental nanoindentation results, leading to good quantitative agreement.
3. Considerable fluctuations in the local shear modulus as well as in the atomic size misfit volumes were calculated

by atomistic computer simulations, which in turn have no significant effect on the yield strength predictions of the Varvenne model and could be neglected.

Methodology

Varvenne solid solution-hardening model

The Varvenne solid solution model specifically designed to describe highly concentrated FCC alloys based on the assumption of a homogeneous average background matrix. There are various notations for the Varvenne model, which contain different prefactors. The notation we will be using follows Ref. [23] and is valid for FCC samples:

$$\Delta\tau_{y0} = 0.01785\alpha^{-1/3}\bar{\mu}\left(\frac{1+\bar{\nu}}{1-\bar{\nu}}\right)^{4/3}\left[\frac{\sum_n c_n\Delta V_n^2}{b^6}\right]^{2/3} \quad (2)$$

$$\Delta E_b = 1.5618\alpha^{1/3}\bar{\mu}b^3\left(\frac{1+\bar{\nu}}{1-\bar{\nu}}\right)^{2/3}\left[\frac{\sum_n c_n\Delta V_n^2}{b^6}\right]^{1/3} \quad (3)$$

$$\tau_y = \tau_{y0}\left[1 - \left(\frac{k_B T}{\Delta E_b} \ln \frac{\dot{\epsilon}_0}{\dot{\epsilon}}\right)^{\frac{2}{3}}\right] \quad (4)$$

Parameters of the model are the mean shear modulus $\bar{\mu}$ and Poisson's ratio $\bar{\nu}$ of the alloy, the length of the Burgers vector b , the concentration of each constituent c_n and the corresponding misfit volume ΔV_n . The temperature T can then be used to calculate the critical shear stress τ_y at finite temperatures. Further parameters and their derivation are explained in Ref. [11]. The mean properties of the HEA are commonly obtained from a rule-of-mixture, $\bar{\xi} = \sum_n c_n \xi_n$, where ξ is the physical property of interest [23]. The misfit volumes of the Cantor system are taken from Ref. [11]. The flow stress is linked to the predicted shear stress (cf. Eq. (4)) by the Taylor factor M (equal to 3.06 for

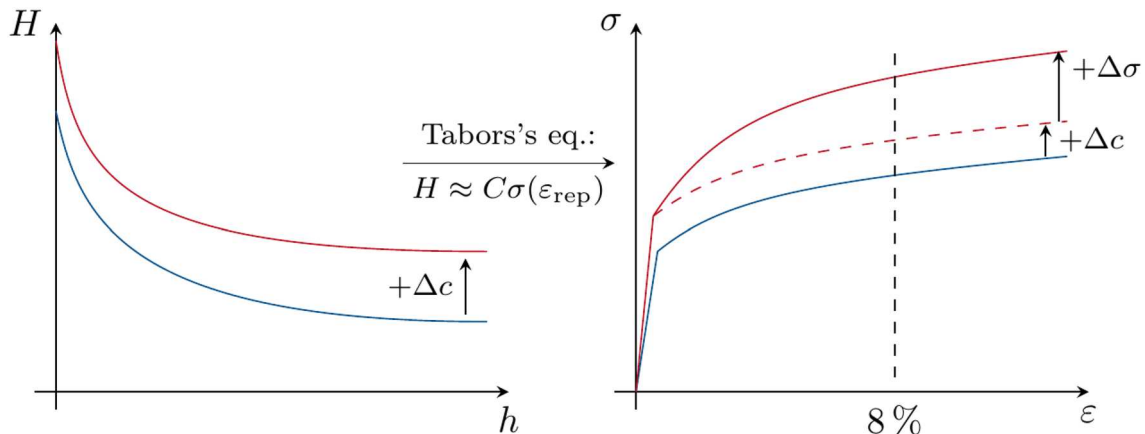


Figure 5: Relation between depth and concentration-dependent hardness $H(h, c)$ and the yield strength σ_y as function of the concentration change Δc using Tabors eq. Knowledge of the strain hardening σ_{strain} is required to extrapolate from the experimentally measured hardness to the yield strength.

polycrystalline FCC samples) [11]. The Varvenne model only considers a mean shear modulus and the respective atomic size misfit volumes ΔV_n , whereas Labusch describes the strengthening based on the addition of two elastic contributions: atomic size and shear modulus mismatch [8, 9].

Experimental procedure

Diffusion couples were prepared from a homogenized $\text{Cr}_{20.7}\text{Mn}_{18.5}\text{Fe}_{20.2}\text{Co}_{20.5}\text{Ni}_{20.1}$ Cantor alloy and its constituent pure elements. The purity levels of the diffusion partner elements (> 99.0%), sample preparation, heat treatment and quenching conditions can be found in Ref. [19]. The used heat treatment procedure avoids decomposition and retains the FCC phase stable of the Cantor alloy at ambient temperatures despite being potentially metastable. Cross sections of the diffusion couples were prepared by a mechano-chemical polishing down to colloidal silica to prepare deformation free and smooth surfaces, required for chemical, structural and mechanical investigations within the interdiffusion zone. The mechanical properties were investigated by nanoindentation testing, using a G200 nanoindentation system (KLA) equipped with a diamond Berkovich tip (Synton-MDP). The local mechanical properties were measured with a continuous stiffness measurement (CSM) [24, 25], with an oscillation frequency of 45 Hz and a harmonic displacement of 2 nm. An input strain rate ($\dot{\epsilon} = \frac{\dot{p}}{p}$) of 0.05 was chosen. The maximum indentation depth was set to 1000 nm and the hardness is averaged over an indentation range of 900–1000 nm. The pile-up behavior around the indent was measured via a Laser Scanning Microscope (Olympus Lext OLS 4100). A scanning electron microscope (TESCAN Mira3) was used to investigate the chemical and phase distribution within the interdiffusion zone by energy dispersive X-ray spectroscopy (EDX) and electron backscatter diffraction (EBSD).

Relating yield stress to hardness

With SSS models, the contribution of individual alloying elements onto the yield stress are determined, whereas these models do not quantify possible changes in the defect storage, annihilation and thus work hardening behaviour of the alloys. The experimentally determined hardness H however comprises different factors besides solid solution strengthening, for example work hardening in presence of the indentation strain gradient needs to be considered. Hence, the difference in hardness between an alloy and the pure matrix element (referred to as unalloyed) is used to quantify solid solution strengthening using nanoindentation:

$\Delta\sigma_{\text{SSH}} \propto \Delta H_{\text{SSH}} = H_{\text{alloy}} - H_{\text{unalloyed}}$ [26]. Figure 5 schematically depicts an approach to relate the depth h and concentration dependent indentation hardness $H(h)$ to the concentration dependent yield strength $\sigma_y(x_i)$. The hardness can be related to the flow stress σ at representative strain using Tabor's equation [27]: $H \approx C\sigma(\epsilon_{\text{rep}})$, where C represents the constraint factor $C=3$ [28] and ϵ_{rep} is the representative strain. The dependency of the constraint factor on the elastic/plastic work ratio according to Leitner et al. [29] was used and a fully plastic behavior was observed for all compositions up to the phase boundary and we do not expect any influence for the further model analysis. For the used Berkovich tip, a representative strain of $\epsilon_{\text{rep}} \approx 8\%$ [28] is found. Tabor's eq. only holds true if other contributions to the experimental hardness, like strain hardening, indentation size effect (ISE), pile-up behavior and strain rate sensitivity, are independent of concentration [26, 30]. For the tested material systems pile-up and rate sensitivity can be neglected, and the ISE is considered to be comparable for all compositions (as shown for Cantor and pure Ni in Fig. 1). However, knowledge of the strain hardening behavior $\sigma = \sigma_0\epsilon^n$ where the work hardening exponent n depends on the composition is essential for a correlation between flow stress at representative strain and the yield strength σ_y at zero strain. In particular, the stacking fault energy (SFE) will change with composition and thus affect the local strain-hardening behavior ($+\Delta\sigma$, see Fig. 5) [31, 32]. Finally, the yield strength can be related to a hardness value and thus nanoindentation hardness mapping as function of the concentration c allows us to investigate solid solution strengthening in a continuous manner. Bracq et al. [5] also compared the indentation hardness of various FCC HEAs based on the Cantor alloy with a calculated yield strength using Tabor's eq. and assumed a 20% uncertainty.

Acknowledgments

The authors would like to thank the German Research Foundation (DFG) for financial support through its priority program SPP2006 under Grant Numbers DU 424/13-1 and STU 611/2-1 and Dr. Sergiy Divinski (WWU Münster) for providing the Cantor alloy. Calculations for this research were conducted on the Lichtenberg high performance computer of TU Darmstadt.

Funding

Open Access funding enabled and organized by Projekt DEAL.

Data availability

The data is available upon request from the corresponding author (T.K.).

Declarations

Conflict of interest The authors declare no conflict of interest.

Open Access

This article is licensed under a Creative Commons Attribution 4.0 International License, which permits use, sharing, adaptation, distribution and reproduction in any medium or format, as long as you give appropriate credit to the original author(s) and the source, provide a link to the Creative Commons licence, and indicate if changes were made. The images or other third party material in this article are included in the article's Creative Commons licence, unless indicated otherwise in a credit line to the material. If material is not included in the article's Creative Commons licence and your intended use is not permitted by statutory regulation or exceeds the permitted use, you will need to obtain permission directly from the copyright holder. To view a copy of this licence, visit <http://creativecommons.org/licenses/by/4.0/>.

Appendix A: List of symbols

See Table 1.

TABLE 1: List of symbols.

τ_{crit}	Critical shear stress
k_n	Strengthening parameter of element n
c_n	Concentration of each constituent
α	Line tension parameter
$\bar{\mu}$	Mean shear modulus
$\bar{\nu}$	Mean Poisson's ration
b	Burgers vector
ΔV_n	Misfit volume of element n
T	Temperature
ΔE_b	Energy barrier
$\dot{\epsilon}_0$	Experimental strain rate
τ_{y0}	Zero temperature critical shear stress
τ_y	Critical shear stress
C	Constraint factor
σ_y	Yield strength
\dot{p}	Loading rate
P	Load
a	Lattice constant

Appendix B: Material parameter

See Table 2.

TABLE 2: Material parameters used as input for the yield strength calculations based on the Varvenne model [11, 21, 22].

Element	a/pm	μ/GPa	ν	E/GPa	b/pm	$\Delta V_n \text{ \AA}^3$
Cr	288.46	115.3	0.21	279	249.81	12.27
Mn	386.24	79.5	0.24	191	273.11	12.60
Fe	364.68	81.6	0.29	208	257.87	12.09
Co	354.45	82	0.32	211	250.63	11.12
Ni	352.38	76	0.31	199	249.17	10.94

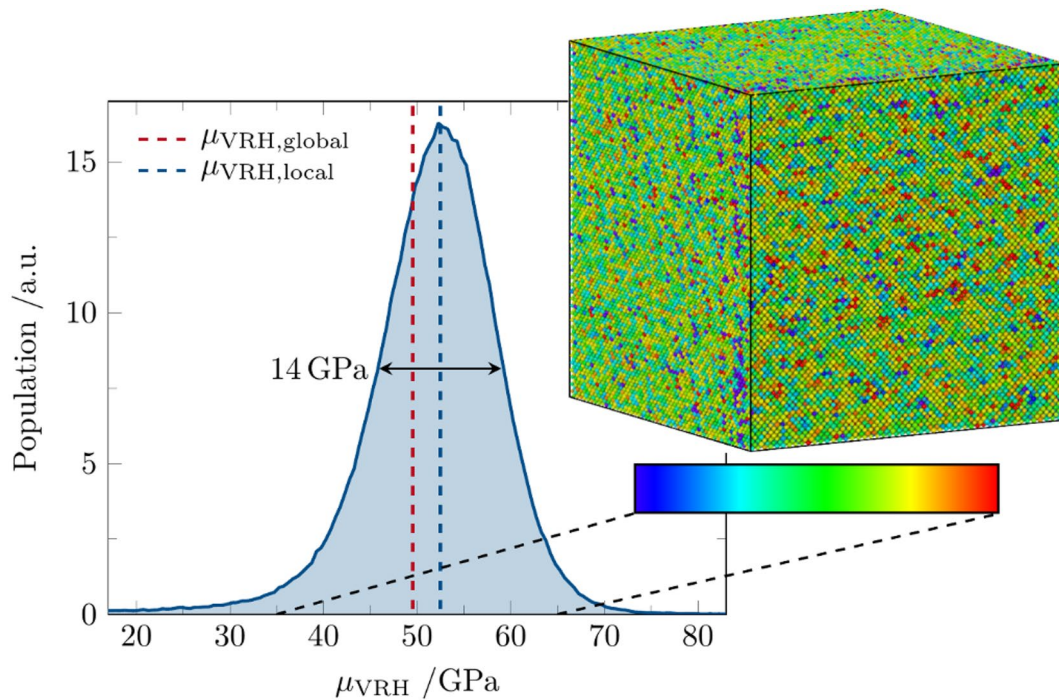


Figure 6: Distribution of the local VRH shear modulus ($\mu_{\text{VRH,local}}$) in the equimolar Cantor alloy. For comparison the VRH shear modulus for the same alloy determined from Hooke's law is given ($\mu_{\text{VRH,global}}$). The inset shows a snapshot of the sample with atoms color-coded based on their local shear modulus.

Appendix C: Atomistic computer simulations

C.1: Local shear modulus

The Varvenne model is based on the assumption of an average background matrix, into which solutes are embedded [10, 11]. This average matrix has an average shear modulus $\bar{\mu}$, which is taken as homogeneous over the whole sample. The interaction of the dislocation with the local chemical fluctuations of the HEA are included by means of the volume misfit term ΔV , which accounts for the size difference of the elements. Atomistic computer simulations are used to investigate whether the HEA matrix can be seen as an average matrix with a homogeneous shear modulus or if there are strong local fluctuations which need to be treated individually (Fig. 6).

To answer this question, we calculate the local stiffness tensor for each atom in a Cantor alloy sample using the computational approach presented in Ref. [33]. Calculations were performed using LAMMPS [34] and the equimolar CrMnFeCoNi HEA was described by the 2-nearest neighbor modified embedded atom method (MEAM) interatomic potential [35] parametrized by Choi et al. [36]. The single crystalline FCC sample was prepared using ATOMSK [37] and contained 5×10^5 lattice sites occupied by randomly distributed Cr, Mn, Fe, Co, and Ni atoms. We determined the macroscopic elastic constants from

finite deformations of the simulation cell using Hooke's law. Post processing and visualization were performed in OVITO [38].

From this data the Voigt–Reuss–Hill (VRH) [39] averaged local shear modulus can be obtained for each atom. Fig. 6 shows a histogram of the local shear modulus ($\mu_{\text{VRH,local}}$) compared to

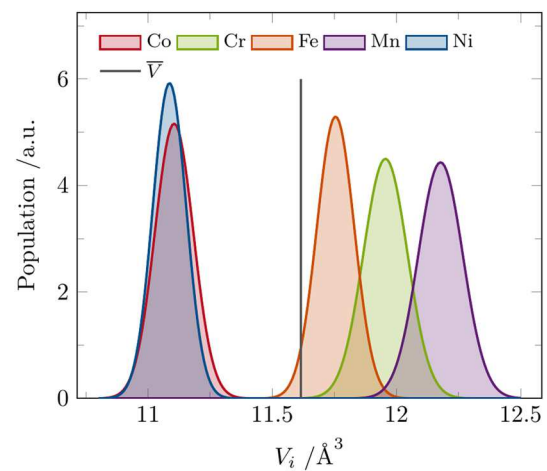


Figure 7: Distribution of the static atomic volume V_i for each atomic species in the CrMnFeCoNi HEA determined by polydisperse Voronoi tessellation at 0 K. The average atomic volume \bar{V} is indicated as well.

the VRH shear moduli obtained from Hooke's law for the whole simulation cell ($\mu_{VRH,global}$). The inset shows a snapshot of the simulated sample with the atoms color-coded based on their local shear modulus.

The mean of the local shear modulus distribution is located at 52 GPa which is lower than the one reported by Wu et al. [3] 80 GPa. Nevertheless, the atomic shear modulus shows a broad distribution with a full width a standard deviation of 6.25 GPa and a full width at half maximum of 14 GPa. The inset shows no significant clustering of low (high) shear modulus atoms forming subvolumes of locally decreased (increased) stiffness. Given that the strain field of the dislocation is farther reaching than multiple interatomic distances [40] and with the activation volume for dislocation glide in the Cantor alloy being about 70–360 b^3 [41], it remains unclear whether these short ranged fluctuations of the shear modulus need to be included in a SSH model.

C.2.: Misfit volumes

The misfit volume is a key quantity strongly influencing the yield strength predicted by the Varvenne model. It can be obtained from experiments on binary subsystems of the HEA [11], the rule-of-mixtures [23], or from atomistic computer simulations of the full HEA [12]. In the following, we determine the misfit volume of the different constituents in the Cantor alloy using atomistic computer simulations based on the approach developed by Yin and Curtin [12].

Similar to the local shear modulus, the local atomic volume in a HEA is not a single number, but varies locally depending on the chemical environment. We use poly-disperse Voronoi tessellation as implemented in OVITO [38] to determine the volume associated to each atomic species in the HEA. We used the sample prepared in sec. Appendix C.1 as it contained a sufficiently large number of atoms to achieve representative results. The elemental Goldschmidt radii are used as input for the tessellation and the resulting atomic volume distribution V_i is shown in Fig. 7. Additionally, the average atomic volume $\bar{V}_{CrMnFeCoNi}$ is indicated. The five constituent elements show differences between their element specific Voronoi volume and the average atomic volume of the matrix \bar{V} in the range of 0.14–0.56 \AA^3 . The Voronoi volumes confirm that the atomic volume in the HEA is not a single number, but follows a normal distribution with standard deviations in the range of 0.0674 \AA^3 for Ni to 0.0909 \AA^3 for Mn. If the atomic volumes in a HEA show a finite width distribution, the corresponding misfit volumes need to have a similar distribution. While the finite width of the misfit volume distribution is included as $\sigma_{\Delta V_n}$ in the original equations of the Varvenne SSH model (see Ref. [11] Eqs. 15 and 16) this value is usually set to 0 (e.g. Refs. [11, 12, 23]).

Appendix D: Nanoindentation hardness data

See Fig. 8.

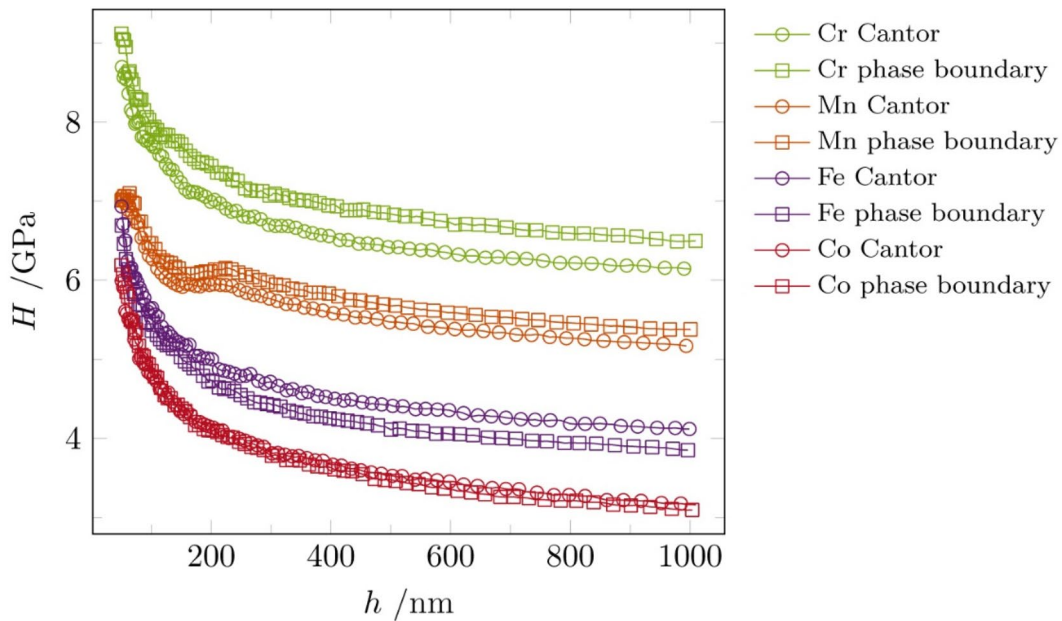


Figure 8: Nanoindentation hardness as a function of indentation depth for the equiatomic composition (named as Cantor) and the composition at phase boundary for the respective diffusion partner element (named as phase boundary). Please note here, only indents with a minimum distance of the plastic zone's diameter from the phase boundary were considered. For clarity, not all data points are displayed and each sample has been shifted along the ordinate.

References

1. J.-W. Yeh et al., Nanostructured high-entropy alloys with multiple principal elements novel alloy design concepts and outcomes. *Adv. Eng. Mater.* **6**, 299–303 (2004)
2. D.B. Miracle, O.N. Senkov, A critical review of high entropy alloys and related concepts. *Acta Mater.* **122**, 448–511 (2017)
3. Z. Wu et al., Temperature dependence of the mechanical properties of equiatomic solid solution alloys with face-centered cubic crystal structures. *Acta Mater.* **81**, 428–441 (2014)
4. O.N. Senkov et al., Microstructure and room temperature properties of a high-entropy TaNbHfZrTi alloy. *J. Alloys Compd.* **509**(20), 6043–6048 (2011)
5. G. Bracq et al., Combining experiments and modelling to explore the solid solution strengthening of high and medium entropy alloys. *Acta Mater.* **177**, 266–279 (2019)
6. M. Laurent-Brocq et al., From diluted solid solutions to high entropy alloys: on the evolution of properties with composition of multi-components alloys. *Mater. Sci. Eng., A* **696**, 228–235 (2017)
7. F. Thiel et al., Breakdown of Varvenne scaling in (AuNiPdPt)_{1-x}Cu high-entropy alloys. *Scr. Mater.* **181**, 15–18 (2020)
8. R. Labusch, A statistical theory of solid solution hardening. *Phys. Stat. Sol.* **41**, 659–669 (1970)
9. R. Labusch, Statistische Theorien der Mischkristallhärtung. *Acta Metall.* **20**, 917–927 (1972)
10. C.R. LaRosa et al., Solid solution strengthening theories of high-entropy alloys. *Mater. Charact.* **151**, 310–317 (2019)
11. C. Varvenne, A. Luque, W.A. Curtin, Theory of strengthening in fcc high entropy alloys. *Acta Mater.* **118**, 164–176 (2016)
12. B. Yin, W.A. Curtin, First-principles-based prediction of yield strength in the RhIrPdPtNiCu high-entropy alloy. *NPJ Comput. Mater.* **5**(1), 1–7 (2019)
13. C. Varvenne et al., Solute strengthening in random alloys. *Acta Mater.* **124**, 660–683 (2017)
14. B. Cantor et al., Microstructural development in equiatomic multicomponent alloys. *Mater. Sci. Eng., A* **375–377**, 213–218 (2004)
15. W. Nix, H. Gao, Indentation size effects in crystalline materials: a law for strain gradient plasticity. *J. Mech. Phys. Solids* **46**, 411–425 (1998)
16. T. Keil et al., From diluted solid solutions to high entropy alloys: saturation grain size and mechanical properties after high pressure torsion. *Scr. Mater.* **192**, 43–48 (2021)
17. M. Laurent-Brocq et al., Combining tensile tests and nanoindentation to explore the strengthening of high and medium entropy alloys. *Materialia* **7**, 100404 (2019)
18. V. Maier et al., Nanoindentation strain-rate jump tests for determining the local strain-rate sensitivity in nanocrystalline Ni and ultrafine-grained Al. *J. Mater. Res.* **26**(11), 1421–1430 (2011)
19. T. Keil, E. Bruder, K. Durst, Exploring the compositional parameter space of high-entropy alloys using a diffusion couple approach. *Mater. Des.* **176**, 107816 (2019)
20. F. Otto et al., The influences of temperature and microstructure on the tensile properties of a CoCrFeMnNi high-entropy alloy. *Acta Mater.* **61**(15), 5743–5755 (2013)
21. W. Martienssen, H. Warlimont, *Springer Handbook of Condensed Matter and Materials Data* (Springer, Berlin, 2005)
22. F. Cardarelli, *Materials Handbook*, vol. 2 (Springer, London, 2008)
23. C. Varvenne, W.A. Curtin, Predicting yield strengths of noble metal high entropy alloys. *Scr. Mater.* **142**, 92–95 (2018)
24. J.B. Pethica, W.C. Oliver, *Mechanical Properties of Nanometre Volumes of Material: Use of the Elastic Response of Small Area Indentations*. MRS Proceedings. 130 (1988)
25. W.C. Oliver, G.M. Pharr, An improved technique for determining hardness and elastic modulus using load and displacement sensing indentation experiments. *J. Mater. Res.* **7**(06), 1564–1583 (1992)
26. K. Durst et al., Indentation size effect in Ni–Fe solid solutions. *Acta Mater.* **55**(20), 6825–6833 (2007)
27. D. Tabor, A simple theory of static and dynamic hardness. *Proc. R. Soc. Lond. Ser. A. Math. Phys. Sci.* **192**(1029), 247–274 (1948)
28. A.C. Fischer-Cripps, *Nanoindentation*, 3rd edn. (Springer, New York, 2011)
29. A. Leitner, V. Maier-Kiener, D. Kiener, Essential refinements of spherical nanoindentation protocols for the reliable determination of mechanical flow curves. *Mater. Des.* **146**, 69–80 (2018)
30. O. Franke, K. Durst, M. Göken, Nanoindentation investigations to study solid solution hardening in Ni-based diffusion couples. *J. Mater. Res.* **24**(03), 1127–1134 (2009)
31. G.J.L. van der Wegen, P.M. Bronsveld, J.T.M. de Hosson, A comparison between different theories predicting the stacking fault energy from extended nodes. *Scr. Metall.* **14**(2), 285–288 (1980)
32. R.W. Cahn, P. Haasen, *Physical Metallurgy*. 4th, rev. and enhanced ed. ed. 1996, Amsterdam u.a
33. T. Brink, L. Koch, K. Albe, Structural origins of the boson peak in metals: from high-entropy alloys to metallic glasses. *Phys. Rev. B* **94**(22), 224203 (2016)
34. S. Plimpton, Fast parallel algorithms for short-range molecular dynamics. *J. Comput. Phys.* **117**(1), 1–19 (1995)
35. B.-J. Lee, M.I. Baskes, Second nearest-neighbor modified embedded-atom-method potential. *Phys. Rev. B* **62**(13), 8564–8567 (2000)
36. W.-M. Choi et al., Understanding the physical metallurgy of the CoCrFeMnNi high-entropy alloy: an atomistic simulation study. *NPJ Comput. Mater.* **4**(1), 1–9 (2018)
37. P. Hirel, Atomsk: a tool for manipulating and converting atomic data files. *Comput. Phys. Commun.* **197**, 212–219 (2015)

38. A. Stukowski, Visualization and analysis of atomistic simulation data with OVITO—the Open Visualization Tool. *Model. Simul. Mater. Sci. Eng.* **18**(1), 015012 (2010)
39. R. Hill, The elastic behaviour of a crystalline aggregate. *Proc. Phys. Soc. Sect. A* **65**(5), 349–354 (1952)
40. J.P. Hirth, J. Lothe, Theory of dislocations, in *A Wiley-Interscience Publication*. New York (1982)
41. G. Laplanche et al., Thermal activation parameters of plastic flow reveal deformation mechanisms in the CrMnFeCoNi high-entropy alloy. *Acta Mater.* **143**, 257–264 (2018)

Publication C

Reproduced full text article with permission from Elsevier Ltd.

Copyright (2021), Scripta Materialia.



From diluted solid solutions to high entropy alloys: Saturation grain size and mechanical properties after high pressure torsion

Tom Keil^{a,*}, Enrico Bruder^a, Mathilde Laurent-Brocq^b, Karsten Durst^a

^a Technical University of Darmstadt, Materials Science, Physical Metallurgy, Alarich-Weiss-Str. 2, 64287 Darmstadt, Germany

^b Université Paris Est Créteil, CNRS, ICMPE, UMR 7182, Thiais, France

ARTICLE INFO

Article history:

Received 10 August 2020

Revised 24 September 2020

Accepted 30 September 2020

Keywords:

High Entropy Alloy
High pressure torsion
Nanoindentation
Microstructure

ABSTRACT

Effects of solutes on saturation grain size and mechanical properties are investigated for the Cantor alloy and Ni-enriched variations ((CrMnFeCo)_xNi_{1-x}) with $x=0.8, 0.4, 0.08$ and 0. Indentation on coarse-grained and severely deformed states shows increasing hardness with increasing alloying content due to higher solid solution strengthening and Hall-Petch contributions. Nanoindentation strain rate jump tests reveal similar rate sensitivities of the deformed states without pronounced transient regimes. All compositions exhibit a history dependent softening indicating an unstable microstructure. The saturation grain size d_s after HPT deformation inversely correlates with the solid solution strengthening contribution, i.e. the higher $\Delta\tau$ the lower d_s .

© 2020 Acta Materialia Inc. Published by Elsevier Ltd. All rights reserved.

Single-phase high entropy alloys (HEAs), such as the five component equiatomic CrMnFeCoNi Cantor alloy [1] have attracted a wide research interest in recent years. The concept of HEAs opens up a high number of possible alloys, with compositions placed in the centre of the multicomponent phase diagram. Given the large number of possible alloy systems, only a few alloys form a single-phase solid solution [2–4] and the Cantor alloy is one of them. However, it is still unclear how the properties change, starting from diluted solid solutions to a HEA [5]. Therefore, Laurent-Brocq et al. [5,6] have studied diluted subsystems of the Cantor alloy along various isopleths and discovered a breakpoint of the lattice parameter and hardness evolution for Ni-enriched alloys at 40 at.% solute concentration, where a transition between diluted systems and high entropy alloy takes place.

The Ni-diluted Cantor systems are therefore nicely suited to study the influence of solid solution strengthening effects on the grain refinement during severe plastic deformation and the resulting properties of the ultrafine-grained (UFG) or nanocrystalline (NC) HEA. We use diluted subsystems of the Cantor alloy – starting from pure Ni to the five-component Cantor alloy – to understand the transition from conventional alloys to HEAs in terms of solid solution strengthening effects and mechanical properties (i.e. effect of grain boundaries, strain rate sensitivity).

One common method to achieve high defect densities in the microstructure and to reduce the grain size to the UFG or NC regime is high pressure torsion (HPT) [7], which has already been applied to the Cantor system [8,9]. Even though severe plastic deformation processes have been used for many years, the principle mechanisms of grain refinement and saturation grain size d_s (minimum achievable grain size at large strain) are still under debate. The stacking fault energy (SFE) affects the dislocation cell formation and refinement rate, but its influence on the saturation grain size d_s is not evident. [10–12] A comparison of pure metals (Ni, Cu, Ag) with strongly different SFEs reveals no difference in d_s after HPT deformation at given homologous temperature [10]. Recent studies on the influence of SFE and solid solution strengthening (SSS) on d_s suggest that it is mainly controlled by the SSS contribution in the alloy system rather than the SFE [11,12]. Edalati et al. [11] found an empirical correlation between SSS contribution determined by the Labusch model and the minimum achievable grain size for different binary alloys, which can be explained by stronger localized stress fields hindering necessary dislocation motion and thus dislocation recovery, grain boundary migration or recrystallization. The resulting dislocation accumulation due to a lower mobility of edge dislocations causes smaller steady-state grain sizes in face-centered cubic (FCC) alloys. This knowledge about defect storage vs. recovery and deformation behavior can now be transferred to chemically complex systems to shed light on SSS processes in HEAs, which have not yet been fully understood. A correlation of the saturation grain size and predicted solid SSS contributions from

* Corresponding author.

E-mail address: t.keil@phm.tu-darmstadt.de (T. Keil).

different strengthening models can be used to investigate these effects in HEAs.

In this work, the influence of solute strengthening on saturation grain size d_s , hardness and rate sensitivity is investigated for three selected alloys with the nominal compositions $\text{Cr}_{2.5}\text{Mn}_{2.4}\text{Fe}_{2.6}\text{Co}_{2.9}\text{Ni}_{92}$ (further referred to as Ni92), $\text{Cr}_{10}\text{Mn}_{10}\text{Fe}_{10}\text{Co}_{10}\text{Ni}_{60}$ (Ni60), the equiatomic $\text{Cr}_{20}\text{Mn}_{20}\text{Fe}_{20}\text{Co}_{20}\text{Ni}_{20}$ (Ni20) Cantor alloy as well as for pure Ni (Ni100) as a reference material with minor solute strengthening effects. The Ni reference sample has a purity of 99.6%. After homogenization, Ni92, Ni60 and Ni20 exhibit compositions of $\text{Cr}_{2.5}\text{Mn}_{2.4}\text{Fe}_{2.6}\text{Co}_{2.9}\text{Ni}_{99.6}$, $\text{Cr}_{10.5}\text{Mn}_{9.9}\text{Fe}_{10.3}\text{Co}_{10.6}\text{Ni}_{58.7}$ and $\text{Cr}_{20.6}\text{Mn}_{19.3}\text{Fe}_{19.9}\text{Co}_{20.1}\text{Ni}_{20.1}$. The purity levels of the used elements are at least 99.9% and the production routes are described elsewhere [13,14].

Due to the chemical complexity and the absence of a main matrix element in high entropy systems, the Varvenne model [15,16], which is specifically designed for FCC HEAs, is used to calculate the shear stress $\Delta\tau_{\text{Varvenne}}$ induced by solid solution strengthening. The calculated SSS contribution can also be linked to the predicted yield strength from Varvenne et al. [15] using the Taylor factor of 3.06 for FCC polycrystals. The required material parameters are obtained from Refs. [17,18] using the rule-of-mixtures, the atomic size misfit volumes are taken from Ref. [15], respectively. Here, the calculated shear stress due to SSS differ strongly from 0 MPa for pure Ni up to 41.4 MPa for the Cantor alloy.

Discs with an initial height of 2 mm were deformed to 10 revolutions at a rate of 1.0 rpm with an applied contact pressure of 5.0 GPa using active water-cooling. Subsequently, the HPT samples were annealed at 900°C for 1h to achieve a coarse-grained state (CG) of the alloys. Flat sections of the HPT discs were prepared by grinding and polishing down to colloidal silica, hence the loading direction of the nanoindentation system and the viewing direction for microstructural analysis is parallel to the loading direction of the HPT process. Nanoindentation testing was then performed on the CG and the deformed HPT states using a G200 nanoindentation system (KLA) with a diamond Berkovich tip (Synton-MDP) on the outer radius of the samples, 1 mm away from the edge of the sample. The indentation modulus and hardness were measured using a continuous stiffness measurement method (CSM) at an input strain rate of 0.05 s^{-1} and the rate sensitivity of the different states was investigated by strain rate jump tests (SRJ), where every 500 nm indentation depth the applied strain rate was varied between 0.05 s^{-1} , 0.005 s^{-1} and 0.001 s^{-1} . The saturation grain size d_s was analyzed using a high-resolution scanning electron microscope (TESCAN Mira3) in backscattered electron (BSE) contrast imaging mode using a line intercept method. The microstructural characterization was carried out at a distance of 1 mm from the outer edge of the samples to ensure a homogeneous deformation.

Fig. 1 a) shows the hardness as a function of the indentation depth for the CG states. Here, the hardness decreases with higher indentation depth, which is caused by the indentation size effect (ISE) and can be described well by the Nix-Gao model [19] (dashed lines). According to the Nix-Gao model, the macroscopic hardness H_0 can be extracted from nanoindentation data: $H_0, \text{Ni}_{20} = 1.91 \pm 0.11$, $H_0, \text{Ni}_{60} = 1.88 \pm 0.11$, $H_0, \text{Ni}_{92} = 1.41 \pm 0.16$, $H_0, \text{Ni}_{100} = 1.08 \pm 0.10$. The macroscopic hardness is only slightly smaller compared to the averaged hardness in the indentation depth interval from 2000 – 2200 nm (see Tab. 1), thus the hardness has already reached a depth independent plateau. In order to minimize the influence of the ISE, the hardness and indentation modulus are averaged over an indentation depth interval from 2000 – 2200 nm for further analysis. Furthermore, the internal length scale h^* is determined, which describes the dislocation storage capability (sensitivity to strain gradients) of a material [20]. An increasing alloying element content starting from pure Ni to Ni92 decreases h^* sub-

stantial, a further addition shows only a minor effect on h^* from Ni92 to the equiatomic Cantor alloy (Fig. 1b)).

Nanoindentation of the CG states shows an increasing hardness with increasing alloying content due to stronger SSS and Hall-Petch contributions starting from pure Ni up to the equiatomic Cantor alloy (Ni20) (Fig. 1c)). This superposition is due to the fact that the microstructure is different for the four compositions, which result in deviations of the Hall-Petch contributions (Ni100: $22.3 \pm 15.5 \text{ }\mu\text{m}$, Ni92: $11.4 \pm 6.3 \text{ }\mu\text{m}$, Ni60: $13.5 \pm 7.9 \text{ }\mu\text{m}$ and Ni20: $8.3 \pm 4.2 \text{ }\mu\text{m}$). Therefore, the hardness increase from Ni100 to Ni20 is caused by an increase of SSS and Hall-Petch contributions, hence, the SSS contribution cannot be derived from the hardness data. Due to the annealing of the CG states, we expect no differences in the dislocation densities and nearly dislocation-free microstructures for the different compositions as it was shown in Ref. [21] for the Cantor alloy. The present nanoindentation results of the CG states are in good agreement with Laurent-Brocq et al. [5,6] in terms of hardness and modulus, considering a different grain size and indentation depth. The saturated HPT states show the trend of an increasing hardness with increasing alloying content with its maximum for Ni60, for which the SSS contribution is in the range of Ni20 at approximately 40 MPa. Although Ni20 shows a slightly higher SSS contribution and smaller grain size, Ni60 has the highest hardness. In literature, higher dislocation densities after HPT deformation are found for the Cantor alloy (Ni20 in the order of 10^{16} m^{-2} [22]), in comparison to pure Ni (Ni100 10^{15} m^{-2} [23]). The higher dislocation density for Ni20 could also contribute to the increase in hardness from Ni100 to Ni20. Furthermore, the HPT states show significantly higher hardness ($\approx 6 \text{ GPa}$) compared to the CG states ($\approx 2 \text{ GPa}$). The indentation modulus is similar for both microstructural states and thus unaffected by the grain size (Tab. 1).

The strain rate sensitivity, i.e. thermally activated deformation processes of the different alloy systems in the HPT states are investigated using nanoindentation strain rate jump tests (Fig. 2). Whereas in the CG states the hardness decreases with increasing indentation depth (caused by indentation size effect – ISE), the HPT specimens show a nearly depth independent hardness at indentation depths greater than 500 nm (Fig. 2) at a strain rate of 0.05 s^{-1} . The strain rate sensitivity is determined using the strain rate jumps at 1500 nm indentation depth from 0.05 s^{-1} to 0.001 s^{-1} (inset in Fig. 2). Higher strain rates cause higher hardness values for both, the diluted solutions (Ni92, Ni100) as well as the chemically complex alloys (Ni20, Ni60). Additionally, the rate sensitivity in the HPT states ($m \approx 0.01$) is similar for all compositions. The corresponding activation volumes V ($V = C * \sqrt{3} k_B * T/mH$), with C : constraint factor of 3, k_B : Boltzmann constant and T : room temperature of 25°C, are in the same range of $19 - 23 \text{ V} * b^3$ for the different compositions and confirm the results from Maier-Kiener et al. on NC-Ni ($14 \text{ V} * b^3$) [24] and NC Cantor ($16 \text{ V} * b^3$) [25]. The indentation modulus is not affected by changes in the strain rate, but show stronger scattering in intervals with lower strain rate due to the higher number of data points (Appendix A1), which was previously observed in literature [25].

In FCC materials, the strain rate sensitivity is more pronounced for decreasing grain sizes, as thermally activated dislocation – grain boundary interactions become more dominant due to the higher number of grain boundaries. [26,27]. After HPT, the different compositions show similar strain rate sensitivities in the range of 0.01. This implies that the strain rate sensitivity is compositionally independent and is also not affected by grain size differences in the NC or UFG regime, as the different compositions show grain sizes in an interval from approx. 50 nm (Ni20) to 150 nm (Ni100).

The present SRJ tests reveal an unstable microstructure of the different alloy systems, as the hardness shows a history dependent behavior [26,27]. The hardness plateaus at a strain rate of 0.05 s^{-1} ,

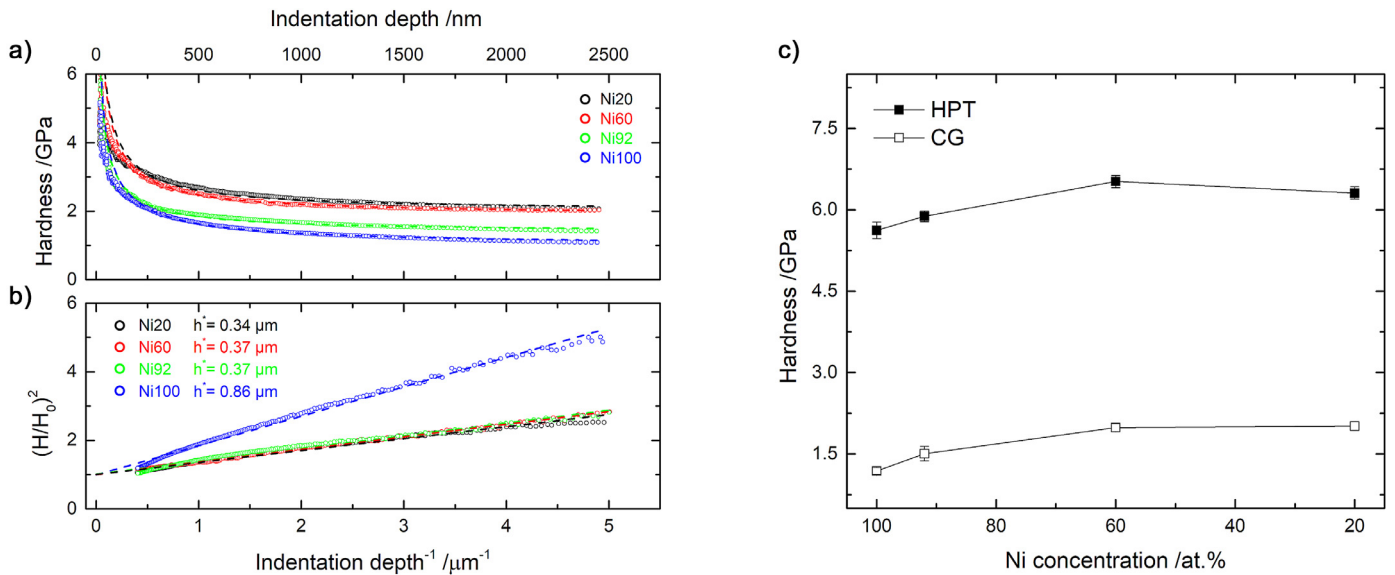


Fig. 1. a) nanoindentation testing of the annealed CG samples (1h at 900°C) at constant strain rate of 0.05 s^{-1} , the dashed lines represent the hardness calculated by the Nix-Gao model, b) Nix-Gao analysis of the CG sample data and c) indentation hardness as a function of composition for the CG and HPT states. Nanoindentation testing data of the HPT samples are shown in [Appendix A2](#).

Table 1

Hardness H , indentation modulus E , strain rate sensitivity m , activation volume V , solid solution strengthening contribution $\Delta\tau$ according to the Labusch and the Varvenne model and saturation grain size d_s of the different alloy compositions.

Alloy composition /at.%	H /GPa		E /GPa		SRJ		$\Delta\tau_{\text{varvenne}} / \text{MPa}$	$\Delta\tau_{\text{Labusch}} / \text{MPa}$	d_s / nm
	CG	HPT	CG	HPT	m	$V \cdot b^3$			
Ni100	1.19 ± 0.1	5.62 ± 0.2	214.2 ± 8.3	235.9 ± 3.0	0.012 ± 0.001	21	0	0	142 ± 57
Ni92	1.51 ± 0.1	5.88 ± 0.1	216.4 ± 13.1	233.9 ± 2.5	0.011 ± 0.0014	22	11.03	11.10	110 ± 45
Ni60	1.98 ± 0.1	6.52 ± 0.1	193.1 ± 8.2	206.5 ± 3.9	0.009 ± 0.0008	23	40.45	33.13	62 ± 23
Ni20	2.01 ± 0.1	6.31 ± 0.1	190.7 ± 8.3	192.5 ± 3.0	0.011 ± 0.0013	19	41.36	53.87	55 ± 17

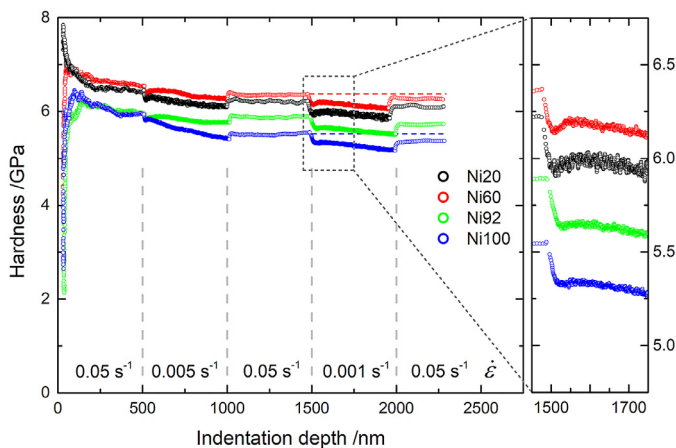


Fig. 2. Nanoindentation strain rate jump tests on Ni-X alloys deformed by HPT.

which are interrupted by a strain rate segment of 0.001 s^{-1} show a history dependent softening of approx. 1.3 – 2.0 %. This softening is discussed on being linked to grain coarsening processes [12].

Differences in the transient behavior can be observed for the investigated compositions in the enlarged section of [Fig. 2](#) at a strain rate change from 0.05 s^{-1} to 0.001 s^{-1} . The hardness changes

abruptly for all compositions, with a continuous softening for Ni100, whereas Ni20 and Ni60 show after the strain rate jump a short period of strain hardening. This phenomenon has been observed before for the nanocrystalline Cantor alloy [25], and also the more diluted Ni60 composition shows the same effect. This yield point effect is limited to the more concentrated Ni20 and Ni60 HEA-type alloys and is almost not observable for Ni92. Moreover, only Ni20 with the lowest grain size of $55 \pm 17 \text{ nm}$ shows serrations in the hardness in the strain rate segment of 0.001 s^{-1} , which is commonly related to dynamic dislocation pinning and break-away during plastic deformation [21]. For nanomechanical testing, the activation volume represents the number of atoms, which are involved in the thermally activated deformation [28]. In NC materials with low activation volumes, the deformation mechanisms are related to thermally activated diffusion processes at grain boundaries [24], which can be associated to the observed serration behavior at low strain rates.

The saturation grain sizes determined by BSE ([Fig. 3](#)) are in good agreement to grain size reference values from literature for Ni20 (50 nm [8]) and Ni100 (170 nm [23]). The evaluation of the minimal achievable grain size (see [Tab. 1](#)) reveals that an increasing alloying content and thus a stronger SSS contribution leads to smaller saturation grain sizes from $142 \pm 57 \text{ nm}$ (Ni₁₀₀) to $55 \pm 17 \text{ nm}$ (Ni₂₀). We do not expect any significant influence by the presence of impurities in the ingredient elements on the saturation grain size, as changes in the purity level of Ni between 99.5% and 99.967% result only in slight changes of the microstructure [29].

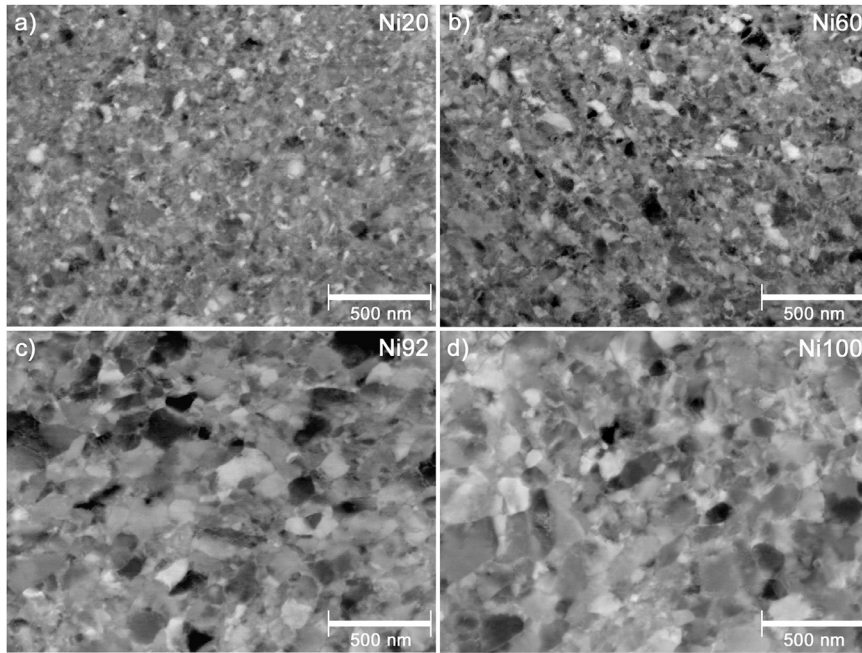


Fig. 3. BSE images of the different alloy systems after HPT deformation: a) Ni20, b) Ni60, c) Ni92 and d) Ni100.

The SSS contribution τ_{Labusch} is calculated using the equations proposed by Edalati [11] and for the τ_{Varvenne} calculation the notation from Ref. [30] is used. Fig. 4 shows the correlation between the SSS contribution (Labusch, Varvenne SSS models) and the normalized saturation grain size (d_s/b), with b as the Burgers-vector.

The correlation found by Edalati et al. [11] for binary solutions breaks down for the highly concentrated solid solutions (see Fig. 4). Despite a higher SSS contribution of Ni 20 compared to Ni60 (Labusch), both alloys exhibit nearly the same grain size.

For conventional alloys, the correlation between saturation grain size and SSS contribution can be attributed to stronger localized stress fields and hindered dislocation motion, dislocation recovery and grain boundary migration or recrystallization. Thus, smaller steady-state grain sizes can be achieved [11]. The same processes seem to influence the saturation grain size in FCC medium and high entropy alloys, as the same dependency of saturation grain size on SSS contribution is obtained using the Varvenne SSS model (all data points lie on a single line in a semi-log scale (see Fig. 4)). The Varvenne model predicts the same SSS contribution for Ni20 and Ni60, which is in good agreement with the experimentally observed saturation grain size and hardness that are in the same range for both alloys (see Tab. 1). This is also confirmed by literature, showing a breakpoint in lattice parameter evolution at 60 at.% Ni, which leads to similar lattice constants for Ni20 and Ni60 [5].

Extrapolating d_s using the Labusch model and the saturation grain sizes of Ni, Ni92, Ni60, would lead to a saturation grain size of Cantor of approx. 37 nm. This is still within the experimental scatter bar, however the Varvenne model seems to give a better description.

While we do see a correlation with SSS, we still don't know what the exact mechanism is. However, segregation phenomena (phase decomposition, inhomogeneities or clusters of solutes) due to HPT deformation appear to be unlikely to play a role given that they do not exist in the extreme cases (Ni20 [8] and Ni100) and presumably also not within the entire concentration range even though this remains to be proven experimentally.

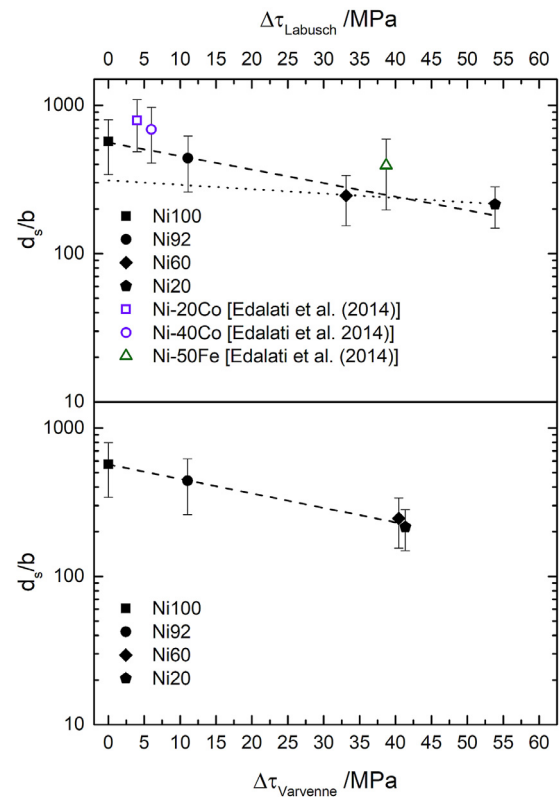


Fig. 4. Normalized grain size d_s/b as a function of the solid solution strengthening contribution $\Delta\tau$, determined by the Labusch model and Varvenne model. The dashed lines fit only the Ni-X values, while the dotted line represents the extrapolation of Ni20 and Ni60.

In summary, the Cantor alloy and Ni-diluted subsystems were investigated with respect to saturation grain size, hardness and strain rate sensitivity to elucidate the evolution of these properties with composition from a pure element over a diluted solid solution up to the equiatomic HEA. For several mechanical properties like ISE and strain rate sensitivity no differences between HEA and diluted solid solutions were observed. All compositions exhibit a history dependent hardness in the SRJ tests, with Ni20 and Ni60 additionally showing yielding phenomena after the strain rate change to 0.001 s^{-1} . The saturation grain size follows the empirical law proposed for binary solid solutions. Compositions with higher alloying content show higher SSS contributions according to the Labusch and Varvenne strengthening models and simultaneously smaller achievable saturation grain sizes by HPT deformation, thus, indicating a correlation between d_s and $\Delta\tau$.

It is not mandatory to reach the equiatomic composition for an optimum of the mechanical properties. Ni60 exhibits approximately the same SSS contribution, same low saturation grain size and thus the same hardness compared to the equiatomic alloy (Ni20). Therefore, chemically complex systems beside the equiatomic composition and the transition from diluted systems to HEAs should be further investigated with respect to effects of solutes on dislocation dynamics.

Data availability

The raw/processed data required to reproduce these findings cannot be shared at this time as the data also forms part of an ongoing study.

Declaration of Competing Interest

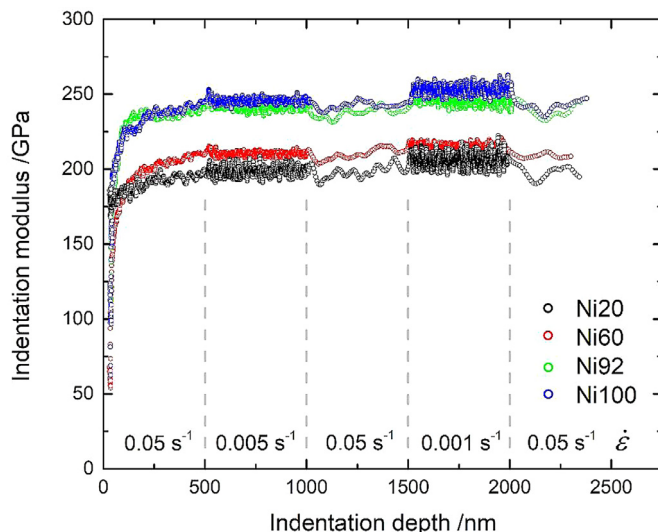
The authors declare no conflict of interest.

Acknowledgements

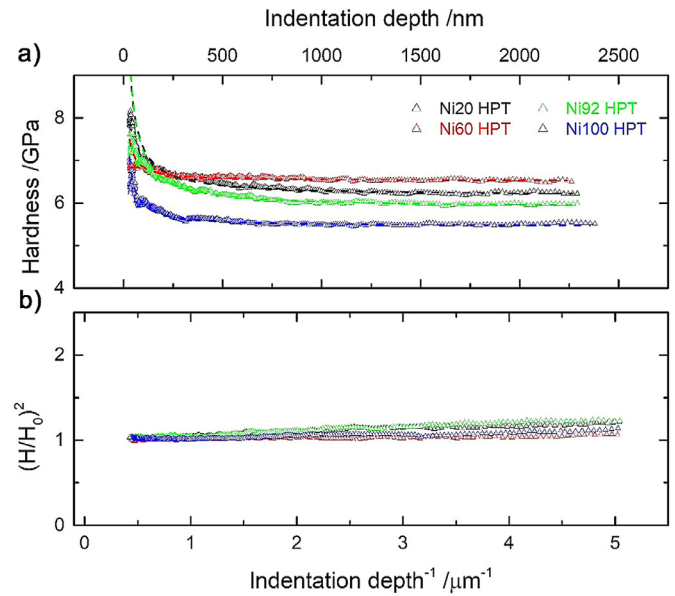
The authors gratefully acknowledge support by the German Research Foundation (DFG) under grant number [DU-424/13-1](#).

Appendix

Appendix.



Appendix A1. Indentation modulus as a function of indentation depth for different strain rates of the deformed Ni-X HPT samples.



Appendix A2. Hardness as a function of indentation depth for the HPT samples at constant strain rate (0.05 s^{-1}); the dashed lines represent the hardness calculated by the Nix-Gao model.

References

- [1] B. Cantor, et al., Microstructural development in equiatomic multicomponent alloys, *Materials Science and Engineering: A* 375-377 (2004) 213–218.
- [2] D.B. Miracle, O.N. Senkov, A critical review of high entropy alloys and related concepts, *Acta Materialia* 122 (2017) 448–511.
- [3] J.-W. Yeh, Alloy Design Strategies and Future Trends in High-Entropy Alloys, *Jom* 65 (12) (2013) 1759–1771.
- [4] J.-W. Yeh, et al., Nanostructured High-Entropy Alloys with Multiple Principal Elements Novel Alloy Design Concepts and Outcomes, *Advanced Engineering Materials* (2004) 299–303.
- [5] M. Laurent-Brocq, et al., From diluted solid solutions to high entropy alloys: On the evolution of properties with composition of multi-components alloys, *Materials Science and Engineering: A* 696 (2017) 228–235.
- [6] G. Bracq, et al., Combining experiments and modelling to explore the solid solution strengthening of high and medium entropy alloys, *Acta Materialia* (2019).
- [7] R.Z. Valiev, et al., Producing bulk ultrafine-grained materials by severe plastic deformation, *JOM* 58 (4) (2006) 33–39.
- [8] B. Schuh, et al., Mechanical properties, microstructure and thermal stability of a nanocrystalline CoCrFeMnNi high-entropy alloy after severe plastic deformation, *Acta Materialia* 96 (2015) 258–268.
- [9] C.C. Koch, Optimization of strength and ductility in nanocrystalline and ultrafine grained metals, *Scripta Materialia* 49 (7) (2003) 657–662.
- [10] R. Pippin, et al., Saturation of Fragmentation During Severe Plastic Deformation, *Annual Review of Materials Research* 40 (1) (2010) 319–343.
- [11] K. Edalati, et al., Influence of dislocation-solute atom interactions and stacking fault energy on grain size of single-phase alloys after severe plastic deformation using high-pressure torsion, *Acta Materialia* 69 (2014) 68–77.
- [12] E. Bruder, et al., Influence of solute effects on the saturation grain size and rate sensitivity in Cu-X alloys, *Scripta Materialia* 144 (2018) 5–8.
- [13] J. Kottke, et al., Tracer diffusion in the Ni-CoCrFeMn system: Transition from a dilute solid solution to a high entropy alloy, *Scripta Materialia* 159 (2019) 94–98.
- [14] M. Glienke, et al., Grain boundary diffusion in CoCrFeMnNi high entropy alloy: Kinetic hints towards a phase decomposition, *Acta Materialia* 195 (2020) 304–316.
- [15] C. Varvenne, A. Luque, W.A. Curtin, Theory of strengthening in fcc high entropy alloys, *Acta Materialia* 118 (2016) 164–176.
- [16] C.R. LaRosa, et al., Solid solution strengthening theories of high-entropy alloys, *Materials Characterization* 151 (2019) 310–317.
- [17] F. Cardarelli, *Materials Handbook*, 2, Springer, London, 2008.
- [18] W. Martienssen, H. Warlimont, *Springer Handbook of Condensed Matter and Materials Data*, Springer, Berlin Heidelberg, 2005.
- [19] W. Nix, H. Gao, Indentation Size Effects In Crystalline Materials: A Law For Strain Gradient Plasticity, *J. Mech. Phys. Solids* 46 (1998) 411–425.
- [20] B. Backes, et al., The correlation between the internal material length scale and the microstructure in nanoindentation experiments and simulations using the conventional mechanism-based strain gradient plasticity theory, *Journal of Materials Research* 24 (3) (2009) 1197–1207.

- [21] F. Otto, et al., The influences of temperature and microstructure on the tensile properties of a CoCrFeMnNi high-entropy alloy, *Acta Materialia* 61 (15) (2013) 5743–5755.
- [22] W. Skrotzki, et al., Microstructure, Texture, and Strength Development during High-Pressure Torsion of CrMnFeCoNi High-Entropy Alloy, *Crystals* 10 (4) (2020).
- [23] A.P. Zhilyaev, et al., Microhardness and microstructural evolution in pure nickel during high-pressure torsion, *Scripta Materialia* 44 (12) (2001) 2753–2758.
- [24] V. Maier, et al., Nanoindentation strain-rate jump tests for determining the local strain-rate sensitivity in nanocrystalline Ni and ultrafine-grained Al, *Journal of Materials Research* 26 (11) (2011) 1421–1430.
- [25] V. Maier-Kiener, et al., Nanoindentation testing as a powerful screening tool for assessing phase stability of nanocrystalline high-entropy alloys, *Materials & Design* 115 (2017) 479–485.
- [26] R. Schwaiger, et al., Some critical experiments on the strain-rate sensitivity of nanocrystalline nickel, *Acta Materialia* 51 (17) (2003) 5159–5172.
- [27] Q. Wei, et al., Effect of nanocrystalline and ultrafine grain sizes on the strain rate sensitivity and activation volume: fcc versus bcc metals, *Materials Science and Engineering: A* 381 (1–2) (2004) 71–79.
- [28] M.A. Monclús, J.M. Molina-Aldareguia, in: *Handbook of Mechanics of Materials*, 2018, pp. 1–29.
- [29] H.W. Zhang, et al., Thermal behavior of Ni (99.967% and 99.5% purity) deformed to an ultra-high strain by high pressure torsion, *Acta Materialia* 58 (5) (2010) 1698–1707.
- [30] C. Varvenne, W.A. Curtin, Predicting yield strengths of noble metal high entropy alloys, *Scripta Materialia* 142 (2018) 92–95.

Publication D

Reproduced full text article with permission from Elsevier Ltd.

Copyright (2022), Acta Materialia.



Effects of solutes on thermal stability, microstructure and mechanical properties in CrMnFeCoNi based alloys after high pressure torsion



Tom Keil^{a,*}, Shabnam Taheriniya^b, Enrico Bruder^a, Gerhard Wilde^b, Karsten Durst^a

^a Materials Science, Physical Metallurgy, Technical University of Darmstadt, Darmstadt, D-64287, Germany

^b Institute of Materials Physics, University of Münster, Münster D-48149, Germany

ARTICLE INFO

Article history:

Received 23 December 2021

Revised 19 January 2022

Accepted 27 January 2022

Available online 28 January 2022

Keywords:

High entropy alloys

Phase stability

High pressure torsion

Nanoindentation

TEM

ABSTRACT

The equiatomic Cantor alloy and Ni-enriched derivatives of it ((CrMnFeCo)_xNi_{1-x} with $x = 0.8, 0.4, 0.08$ and 0) were deformed by high pressure torsion to the saturation regime and subsequently annealed in a wide temperature range. The microstructural stability of the alloys was investigated in terms of grain growth and decomposition tendencies with an emphasis on Ni92 and Ni60 that are marking a transition from dilute solid solutions to HEA alloys. Ni92 and Ni100 show a larger grain size after HPT than the HEA type alloys Ni20 and Ni60, yet, they do exhibit a lower resistance to grain growth. Both HEA type alloys exhibit decomposition tendencies in the form of secondary phases (Ni20) or nanosized Cr-rich precipitates and Mn segregations to grain boundaries (Ni60), that reduce the grain boundary mobility. A comparison of the activation energies for grain growth and diffusion coefficients of the alloys shows a good qualitative agreement. The differences in microstructural stability are also reflected by the mechanical properties. All alloys show a small amount of hardening after annealing, followed by a softening for higher temperatures in case of dilute solid solutions. In contrast, the hardness of the HEA type alloys remains constant up to 450 °C (Ni60) or even increases up to 500 °C (Ni20) followed by a softening at higher annealing temperatures. The second phase formation with limited volume fractions has no effect on the modulus.

© 2022 Acta Materialia Inc. Published by Elsevier Ltd. All rights reserved.

1. Introduction

The equiatomic CrMnFeCoNi Cantor system [1] is one of the most investigated high entropy alloys (HEAs) and is widely considered to crystallize in a single face-centered cubic (FCC) phase. Many HEAs have been produced with a single-phase structure, yet, it is still unclear whether one of them is in thermodynamic equilibrium at ambient temperature or only metastable. In this context, recent reports revealed the precipitate formation for the equiatomic CrMnFeCoNi Cantor alloy below 700 °C [2–4]. This precipitate formation can be shifted to shorter annealing times by introducing high thermodynamic driving forces and grain boundaries acting as fast diffusion pathways [3–5]. Li and co-workers [6] reported that high angle grain boundaries play a decisive role for segregation phenomena in the Cantor alloy, which act as precursor states for phase nucleation at grain boundaries. In this context, grain boundary wetting by a second solid phase has been observed in various primarily homogeneous HEAs after annealing at intermediate temperatures [7]. This phenomenon can be used to alter the properties of HEAs, as the nature of the grain boundaries

strongly affect the properties of the material (e.g. the grain growth kinetics), especially for nanocrystalline (NC) materials [8]. It is well known that the grain boundary motion in metals is strongly influenced by impurities [9–14]. On the one hand, small additions of certain elements can substantially accelerate the grain boundary mobility by forming a liquid-like solute layer at the grain boundaries [9–11]. On the other hand, grain boundary motion can significantly be lowered in the vicinity of solutes by reducing the driving force for grain growth [14].

The high degree of deformation introduced by severe plastic deformation (SPD) methods like high pressure torsion (HPT) results in a reduction in grain size to the ultrafine-grained (UFG) or NC regime, which makes grain boundary interactions more decisive for the resulting properties of the material. HPT experiments on the Cantor alloy have shown that relatively small equivalent strains of $\epsilon_{eq} \approx 44$ (2 rotations) are required to obtain the minimal achievable grain size or the saturation grain size of approx. 40 nm [15]. The resulting grain refinement leads to a significant increase in strength, yet, it is also accompanied by a loss of ductility in many materials including the Cantor system [3,16,17]. This behavior is related to the change in the dominant deformation mechanism, with grain boundary mediated mechanisms being decisive in NC and UFG FCC materials [17–19]. Here, the adjustment of strength and ductil-

* Corresponding author.

E-mail address: t.keil@phm.tu-darmstadt.de (T. Keil).

ity by a subsequent annealing step after deformation can be problematic as segregation and precipitation formation at intermediate annealing temperatures is expected for many HEAs including the Cantor alloy, see for instance Refs. [2–4,20–24]. However, solute segregations to grain boundaries are also considered to inhibit grain boundary migration during annealing, resulting in a stabilization of the microstructure [25], which is getting more prominent for samples showing high grain boundary densities (NC and UFG materials).

Driven by the concept of entropy maximization, there has been an emphasis on using equiatomic compositions in the HEA literature. However, at least for the CrMnFeCoNi system, the equiatomic Cantor alloy does not stand out in terms of its properties when compared to some other compositions or even subsets [26–28]. Investigations on various diluted subsystems of the Cantor alloy show a transition in behavior from that of dilute solid solutions to high entropy alloys, where a breakpoint of lattice parameter evolution, hardness and saturation grain size evolution is found for Ni-enriched alloys at 40 at.% solute concentration [26,27,29–31]. Additionally, by using discrete Ni-diluted Cantor subsystems, Laurent-Brocq et al. [27,30] showed that it is not necessary to reach an equiatomic concentration to obtain maximum strength. The (CrMnFeCo)₄₀Ni₆₀ alloy shows the same solid solution hardening (SSH) contribution according to the Varvenne model [32,33], the same mechanical properties for grain sizes in the micrometer regime as well as the same saturation grain size and higher hardness in the HPT state compared to the equiatomic Cantor alloy (Ni20) [29].

Chemically complex compositions far away from the equiatomic one may not only offer superior mechanical properties, they could also be thermodynamically more stable, showing either no decomposition tendencies or at least broader windows for thermal treatments. This would open up the chance to more easily tune favored properties such as strength or ductility via plastic deformation with subsequent annealing. Whether this adjustment of specific mechanical properties is possible for chemically complex but non-equiatomic alloys is investigated in this work using Ni-diluted subsystems of the CrMnFeCoNi Cantor alloy. Starting from pure Ni over diluted solid solutions up to the equiatomic HEA, the transition behavior in terms of thermal stability and mechanical properties is investigated. The alloys are processed by HPT to reach the minimal achievable grain size (saturation grain size d_s) and subsequently annealed isochronally (1h) at temperatures between 300 and 900 °C. To analyze structural instabilities, the different states are mechanically and structurally characterized by nanoindentation, scanning and transmission electron microscopy (SEM & TEM).

2. Experimental procedure

The thermal stability and grain coarsening processes are investigated for pure Ni (99.6% purity level), for homogenized Ni-diluted subsystems of the Cantor alloy with the compositions Cr_{2.5}Mn_{2.4}Fe_{2.6}Co_{2.9}Ni_{89.6} (nominal Ni92), Cr_{10.5}Mn_{9.9}Fe_{10.3}Co_{10.6}Ni_{58.7} (Ni60) as well as for the equiatomic Cr_{20.6}Mn_{19.3}Fe_{19.9}Co_{20.1}Ni_{20.1} Cantor alloy (Ni20). The elemental precursors show purity levels of at least 99.9%. The production routes are described in Refs. [34,35].

Samples with a height of 2 mm were deformed by HPT to 10 revolutions at 1.0 rpm using 5.0 GPa contact pressure and active water-cooling of the anvils. The deformed samples were used for isochronal annealing at various temperatures from 300 to 900 °C for 1h in inert Ar- atmosphere. Additionally, 10 and 100 h heat treatments at 600 °C were performed for the Ni60 alloy. For subsequent characterization, flat sections of the HPT discs were prepared by grinding and polishing with SiC paper, diamond suspension and finally with colloidal silica. The mechanical and mi-

crostructural analyses were performed on the outer radius of the samples parallel to the rotational axis of the HPT process. The microstructures after annealing were analyzed via backscattered electron (BSE) contrast imaging and electron backscatter diffraction (EBSD) either in conventional or transmission mode (Transmission Kikuchi Diffraction – TKD [36]) in a high-resolution scanning electron microscope (SEM - TESCAN Mira3). The grain size was measured via BSE images using a line intercept method. The crystallographic texture was analyzed via EBSD measurements for the Ni60 and Ni100 samples in the as-deformed state as well as after annealing at 700 °C. The Ni60 and Ni92 samples were used for further analysis in a transmission electron microscope (TEM - Thermo Fisher Scientific FEI Themis 300 G3). The microscope was equipped with a high brightness field emission gun (X-FEG), a quadrupole EDX (energy dispersive x-ray spectroscopy) system and a high angle annular dark field detector (HAADF - Fischione Model 3000). The TEM samples were prepared using the focused ion beam method (FIB - ZEISS Crossbeam 340) to cut lamellae out of the sample disks. To obtain a better spatial resolution of the elements and elemental distribution in the vicinity of Cr-rich precipitates and high angle grain boundaries (HAGBs), electron energy loss spectroscopy (EELS - Gatan Quantum 965 ER imaging filter (GIF)) was applied at 300 kV and the selected area for EELS spectra was examined for the presence of Co, Cr, Fe, Mn and Ni L-edges as well as the thickness homogeneity. The structure of the Cr-rich precipitates in the grain matrix was studied by means of nano-beam diffraction (NBD) in the scanning transmission electron microscopy (STEM) mode with a probe size of 1 nm and a step size of 5 nm in x- and y-directions. The diffraction mapping was carried out by acquiring a full set of nano-beam diffraction patterns (NBDPs) at every position during STEM imaging from which arbitrary virtual dark-field images and phase maps were reconstructed. The data processing was done using a custom code written in Digital Micrograph [37,38].

Nanoindentation testing was conducted using a G200 nanoindentation system (KLA) equipped with a diamond Berkovich tip (Synton-MDP). The hardness and indentation modulus were measured using a continuous stiffness measurement method (CSM) [39,40] with an input strain rate of 0.05 over an indentation depth interval from 2000 to 2200 nm. The strain rate sensitivity was investigated by means of indentation strain rate jump tests (SRJ), where the applied strain rate was varied between 0.05 s⁻¹, 0.005 s⁻¹ and 0.001 s⁻¹ every 500 nm of indentation depth. The strain rate jumps from 0.05 s⁻¹ to 0.001 s⁻¹ at an indentation depth of 1500 nm were used to evaluate the strain rate sensitivity and the activation volume according to Ref. [41]. A laser scanning microscope (Olympus Lext OLS 4100) was used to measure the pile-up formation around the indents. For samples showing pile-up behavior, the contact depth and thus the contact area was corrected according to the method proposed by Kese et al. [42].

3. Results and discussion

3.1. Thermal stability and precipitation formation

The grain growth behavior is evaluated as a function of chemical composition and annealing temperature from pure Ni up to the equiatomic Cantor alloy. BSE images of the different alloys are exemplarily shown for the as-deformed state and after annealing at 500 °C, revealing the different grain growth kinetics (Fig. 1). Starting from pure Ni, a higher alloying content generally results in a smaller saturation grain size after severe plastic deformation. However, Ni60 shows a similar grain size compared to that of the Ni20 alloy, despite a substantially lower alloying content, whereas Ni92 and Ni100 are much coarser. A correlation between saturation grain size and SSH contribution was first reported by

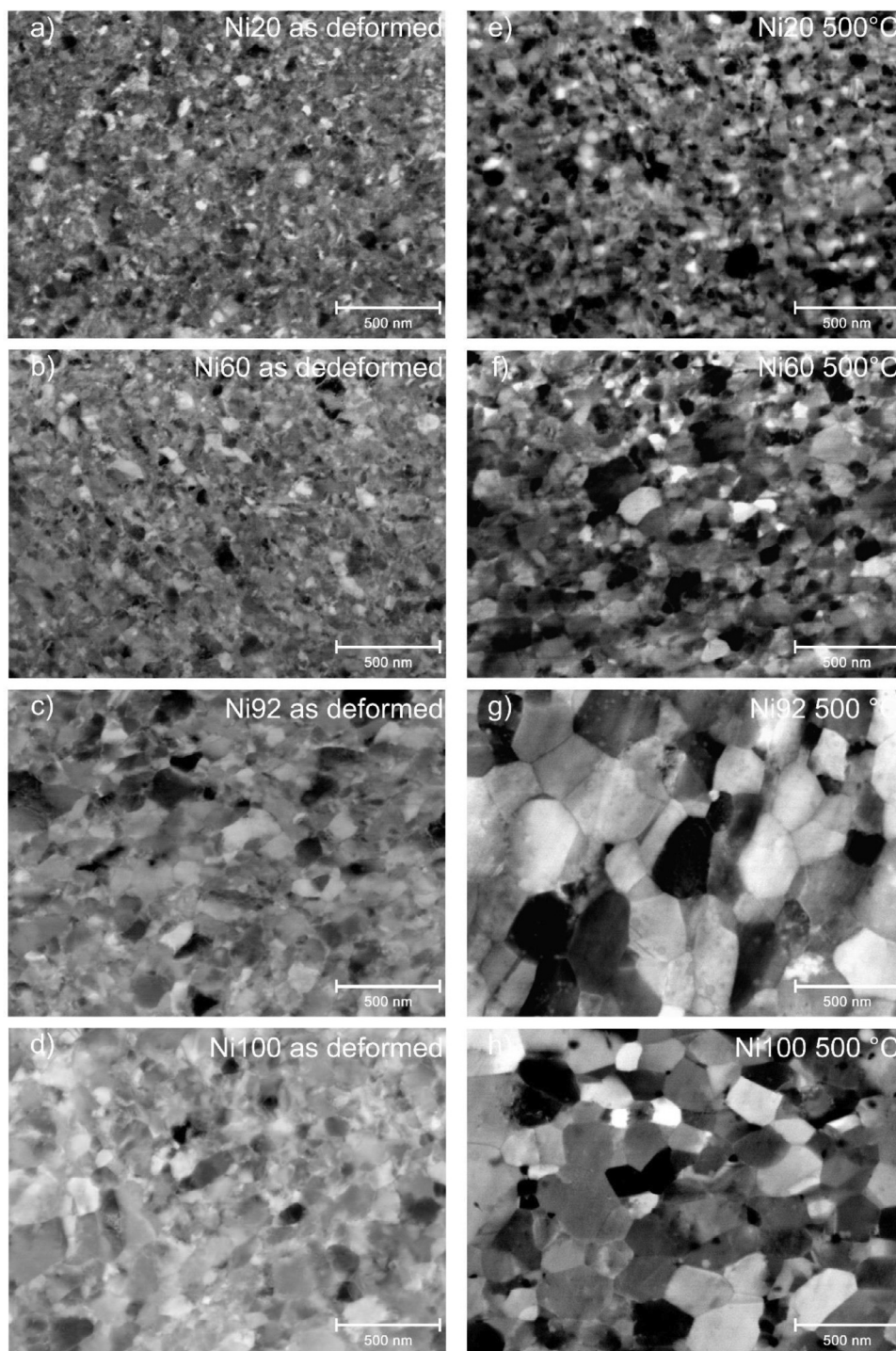


Fig. 1. BSE images of the HPT states (a)–(d) and the 500°C annealed states (e)–(h)) of the Ni-X samples.

Edalati et al.[43] for binaries and was later adapted by Keil et al. [29] for the Ni-X series using the Varvenne SSH model for FCC HEAs [32,33]. It has been found that both Ni20 and Ni60 show similar SSH contributions and similar saturation grain size. The saturation grain size can be found in Table 1 for all compositions.

Annealing of the severely deformed microstructures results in an increasing grain size for all compositions. (Fig. 2 a) shows the grain size of the different alloys in the as deformed condition and after isochronal annealing at various temperatures. The Ni20 and Ni60 alloys are more stable against grain coarsening than Ni92 and Ni100, as the HEA-like alloys show no grain coarsening

at intermediate temperatures (up to 500 °C), whereas the dilute solid solutions (Ni92, Ni100) exhibit a more pronounced coarsening (see Table 1). This indicates that there is no correlation between the stored energy (defect density) and the growth kinetics in the present systems, as the defect density is much higher for the HEA-type solid solutions. Isochronal annealing at 800 and 900 °C leads to recrystallization and single-phase microstructures in the micrometer range for all compositions. After annealing at 800 °C, the trend of a decreasing grain size can be observed with increasing alloying content i.e., the equiatomic Cantor alloy shows the smallest grain size. At 900°C, in turn, Ni20, Ni60 and Ni92 show

Table 1
Grain size of the different alloy compositions after deformation and isochronal annealing for 1 h.

Alloy designation	Grain size							
	HPT/nm	300°C/nm	450°C/nm	500°C/nm	600°C/nm	700°C/nm	800°C/ μm	900°C/ μm
Ni100	142 \pm 57	149 \pm 56	160 \pm 58	233 \pm 88	568 \pm 181	2139 \pm 803	11.4 \pm 7.9	22.3 \pm 15.5
Ni92	110 \pm 45	121 \pm 38	140 \pm 51	235 \pm 129	711 \pm 342	2882 \pm 1380	9.7 \pm 3.7	11.4 \pm 6.3
Ni60	62 \pm 23	67 \pm 22	67 \pm 19	85 \pm 30	277 \pm 146	1048 \pm 492	5.5 \pm 2.5	13.5 \pm 7.9
Ni20	55 \pm 17	59 \pm 19	63 \pm 15	69 \pm 21	183 \pm 71	439 \pm 164	1.6 \pm 0.7	8.3 \pm 4.2

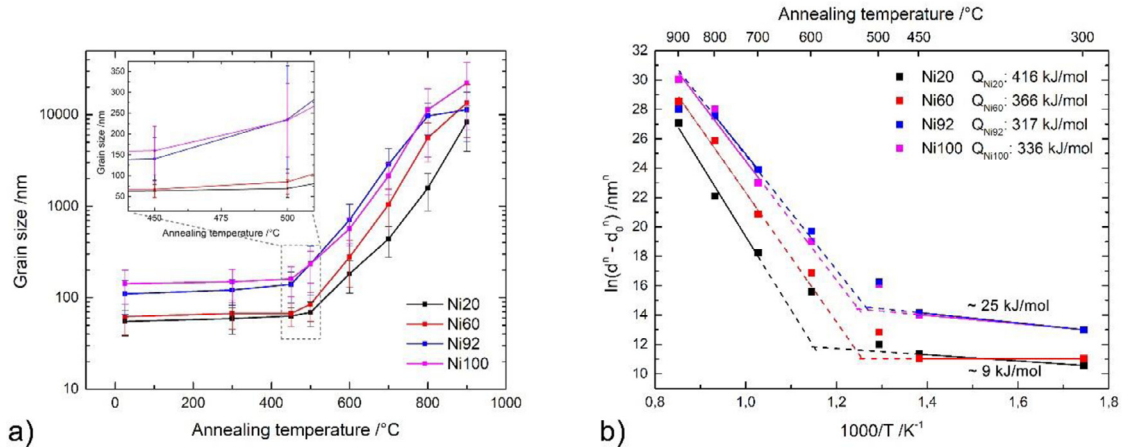


Fig. 2. (a) Grain size as a function of annealing temperature (1h) and (b) Arrhenius plot of $\ln(D^n - D_0^n)$ vs. $1000/T$ to estimate the activation energy for grain growth Q of the Ni-X samples. For better readability, the error bars are only shown in (a).

similar grain sizes, with only pure Ni having a significantly larger grain size. Thus, in this temperature range, a small addition of alloying elements to a Ni matrix seems to have the same effect in terms of impeding grain growth as an equiatomic composition.

The grain growth kinetics can be deduced by analyzing the grain size after annealing and calculating the activation energy for grain growth Q using Eq. (1) [25,44,45]:

$$\ln\left(\frac{D^n - D_0^n}{t}\right) \propto \left(-\frac{Q}{R}\right) * \frac{1}{T} \quad (1)$$

with D being the grain size, D_0 the initial grain size, n the grain growth exponent, R the gas constant and T the temperature. In theory, the grain growth exponent n should approach a value of 2 for pure metals [14,45,46] at temperatures near the melting point. At intermediate annealing temperatures, the grain boundary mobility is often lowered due to solute drag effects, which results in values well above 2 [14,45,46]. According to literature values for the equiatomic Cantor alloy [25,44,47] and commercial Ni [48,49], the grain growth exponent was set to 3 for all four compositions in this study. Furthermore, an isothermal annealing series of Ni60 at 600 °C reveals an approx. n value of 2.9.

(Fig. 2 b) indicates two temperature regimes with significantly different activation energies dominated by different mechanisms. In the low temperature regime, the very low activation energy probably corresponds to stress relaxation processes associated with a rearrangement of unstable grain boundary configurations without significant grain growth. [50–52]. As indicated in literature, severe plastic deformation can lead to modifications of the atomic structure of internal interfaces due to the interaction of lattice dislocations with grain boundaries [53]. Such grain boundaries that are in a deformation-affected state have been shown to have higher diffusivities along the grain boundary and are also characterized by pronounced strain fields in their vicinity. Compared to random high angle grain boundaries in a relaxed state, the width of those strain fields is higher by a factor of approx. 3 [54]. It has also been shown that only a fraction of the grain boundaries is

transformed into such a deformation-affected state. Moreover, dedicated analyses of the volume- and grain boundary diffusion and the thermal stability of the deformation-affected state have indicated that the state of such grain boundaries after severe plastic deformation can be described as a composite structure. These structures exhibit different properties along the boundary plane, with locked regions of high stability against displacement of the interface, explaining also the remarkable stability of such grain boundary configurations [55].

In the high temperature regime, the activation energies for grain growth are similar to that of volume diffusion for the four different compositions [56], indicating that diffusion processes are responsible for grain growth. Huang et al. [45] showed a correlation between diffusion coefficient D and the activation energy for grain growth resulting in decreasing Q values with increasing D for various ternary, quaternary and quinary alloys. From tracer diffusion experiments [56] the diffusion rates are known for the investigated alloys and can be ordered as $\text{Ni92} > \text{Ni100} > \text{Ni60} > \text{Ni20}$. The qualitative comparison shows a good agreement between the diffusion coefficients [56] and the calculated activation energy for grain growth (Fig. 2 b), indicating a correlation between D and Q for both, dilute solid solutions and HEAs. Furthermore, (Fig. 2 b) indicates a higher thermal stability for the more complex Ni20 and Ni60 alloys, as the high temperature regime with significant grain growth is shifted to higher temperatures (parallel shift of the linear fit). For Ni20 and Ni60, we observe a substantial change in grain growth kinetics between 500 and 600 °C (see Fig. 2). In this temperature regime, the formation of second phases or solute segregations to grain boundaries takes place. This effect could be related to the change in grain growth kinetics, as additions of solute may accelerate the grain boundary mobility by forming a liquid-like solute layer at grain boundaries [9–11]. However, Ni92 and Ni100 show the same trend in grain growth kinetics (only shifted to lower temperatures), both being single phase without any observable solute segregations to grain boundaries (see Appendix A2 for Ni92). Against this backdrop, it seems unlikely

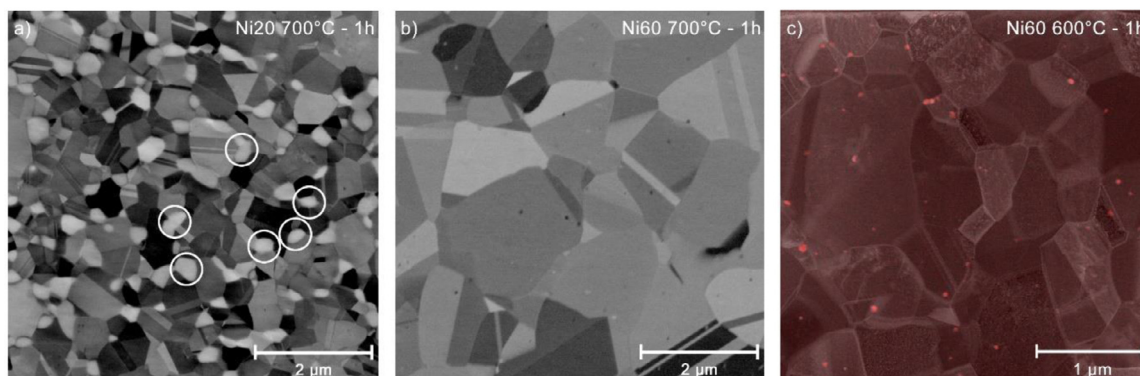


Fig. 3. Advanced microscopy results of the Ni20 and Ni60 alloys after HPT deformation and annealing. (a)–(b) BSE images of the Ni20 and Ni60 alloys after annealing at 700°C (1h) showing precipitation formation (circles) for Ni20 and a supposedly single FCC phase for Ni60. (c) STEM HAADF micrograph with the Cr elemental map overlapping showing Cr-rich precipitates (red) for the Ni60 alloy annealed at 600°C for 1 h. (For interpretation of the references to colour in this figure legend, the reader is referred to the web version of this article.)

that the enhancement of the grain boundary mobility is primarily attributed to grain boundary wetting phenomena, even though, we cannot exclude such effects on the grain growth kinetics in case of Ni20 and Ni60. An accelerated grain growth due to grain boundary wetting may be overcompensated by strong pinning effects from second phase particles or solutes, as the enhancement of the grain boundary mobility by grain boundary wetting seems to be less pronounced in the presence of further impurities [57].

The resistance to grain growth in alloys is typically related to the elemental distribution, e.g. the presence or absence of segregations (solute drag) or second phase particles (Zener drag). According to literature, the Cantor alloy shows a homogeneous element distribution with no segregation or secondary phases after HPT deformation [3], which we also confirmed by TEM analysis for the Ni60 alloy (Appendix A1). As it is well known that the Cantor alloy exhibits decomposition tendencies [2–4], we focus in the present work on the more dilute Ni60 and Ni92 alloys to complement existing data and to investigate a possible transition from a HEA to a dilute solid solution in terms of decomposition.

Diffusion measurements on high-entropy alloys as well as on compositionally complex alloys and their variants, specifically in the Cantor alloy family, have shown that diffusion cannot be described as sluggish, as suggested in literature [58,59]. Concerning the specific alloys that have been investigated in this work, radiotracer diffusion measurements of the tracer self-diffusion of all constituents have shown that considerable differences in the specific diffusivities of the constituents exist, with Mn and Cr being the fastest diffusors [35]. The variations in diffusivity have been explained by local heterogeneities of the atomic configurations around a vacancy that cause element-specific correlation effects [35]. The BSE image in (Fig. 3 b) shows a supposedly single face-centered cubic (FCC) phase for Ni60 after annealing at 700°C. Using TEM (Fig. 3 c), a different picture emerges with Cr-rich precipitates in the nanometer regime at grain boundaries as well as inside the grains in the HPT processed Ni60 sample annealed for 1 h at 600 °C. The observed Cr-rich second phase shows an FCC crystal structure with an average diameter of approx. 40 nm. A NiMn-rich phase, which is reported for the equiatomic Cantor alloy [2], is not detected for the Ni60 alloy, neither in the as-deformed nor in the annealed states. Ni92 on the other hand, shows a single-phase structure in the as-deformed state as well as after annealing (Appendix A3). Consequently, the TEM analysis also confirms the classification of the investigated alloys into HEA-type alloys (Ni20 and Ni60) and dilute solid solutions (Ni92 and Ni100) based on the thermodynamic instability. To relate the experimental results for the Ni60 alloy composition with theoretical predictions on phase

stability, CALPHAD simulations were performed using the TCHEA-3 database (Appendix A4). A single FCC crystal structure is expected down to 430 °C, whereas at lower temperatures a coexistence of two FCC structures is predicted. This finding is consistent with the experimental results, although the temperature range appears to be shifted to lower temperatures in the calculations. However, this does not necessarily prove that the predicted transition temperature is nominally wrong. The simulations neglect the role of defects such as grain boundaries or triple junctions and may therefore deviate from the experimental reality, especially for severely deformed conditions. It has been shown that those conditions can promote the formation of phases despite nominally positive formation enthalpies [60,61]. In addition, a BCC B2 phase is predicted with minor phase fraction beside the FCC structures at temperatures below approx. 370°C, that has not been observed experimentally. The absence of BCC precipitates could be related to the annealing time of 1 h being too short to facilitate diffusion-driven formation of second phases at 300°C, as a decomposition of single-phase metastable HEAs is kinetically suppressed in this regime [62].

To shed some more light on the decomposition behavior, we performed additional heat treatments on the HPT processed Ni60 alloy at 500 °C and 600 °C for 10 h and 100h, respectively. Increasing the annealing time by a factor of 10 leads to an approximate doubling of the grain size at 500 °C (85 ± 30 nm for 1h, 150 ± 52 nm for 10 h and 345 ± 145 nm for 100 h) as well as at 600 °C (277 ± 146 nm for 1 h, 654 ± 300 nm for 10 h and 1114 ± 488 for 100 h). The overlay of STEM HAADF micrograph and Cr elemental map (Fig. 4) shows Cr-rich precipitates in the Ni60 samples subjected to HPT processing and subsequent annealing at 500°C for 10 and 100 h as well as 600 °C for 10 and 100 h, respectively. The formation of the Cr-rich phase triggered by the heat treatment starts in the temperature range of approx. 450 °C (Appendix A5 and A6). If the system is given more time at this temperature, the number of precipitates increases but does not yet reach a saturation state after 100 h. A different picture emerges after annealing at 600 °C, where the volume fraction of the Cr-rich phase already saturates after just 1 h (approx. 0.8 vol.%). A further increase in annealing time to 10 or 100 h shows the evolution of Mn enrichment at HAGBs into precipitates can be observed after 100 h of annealing using EELS (Fig. 5 b). According to the STEM EDS maps heat treatment at a temperature of 450°C does not lead to the formation of Cr-rich precipitates, but a slight enrichment of Mn at HAGBs is observed which transforms into Mn rich precipitates after 100 h of annealing at 600°C (Appendix A6). The Mn segregation to the HAGBs is independent from that of Cr as also apparent from

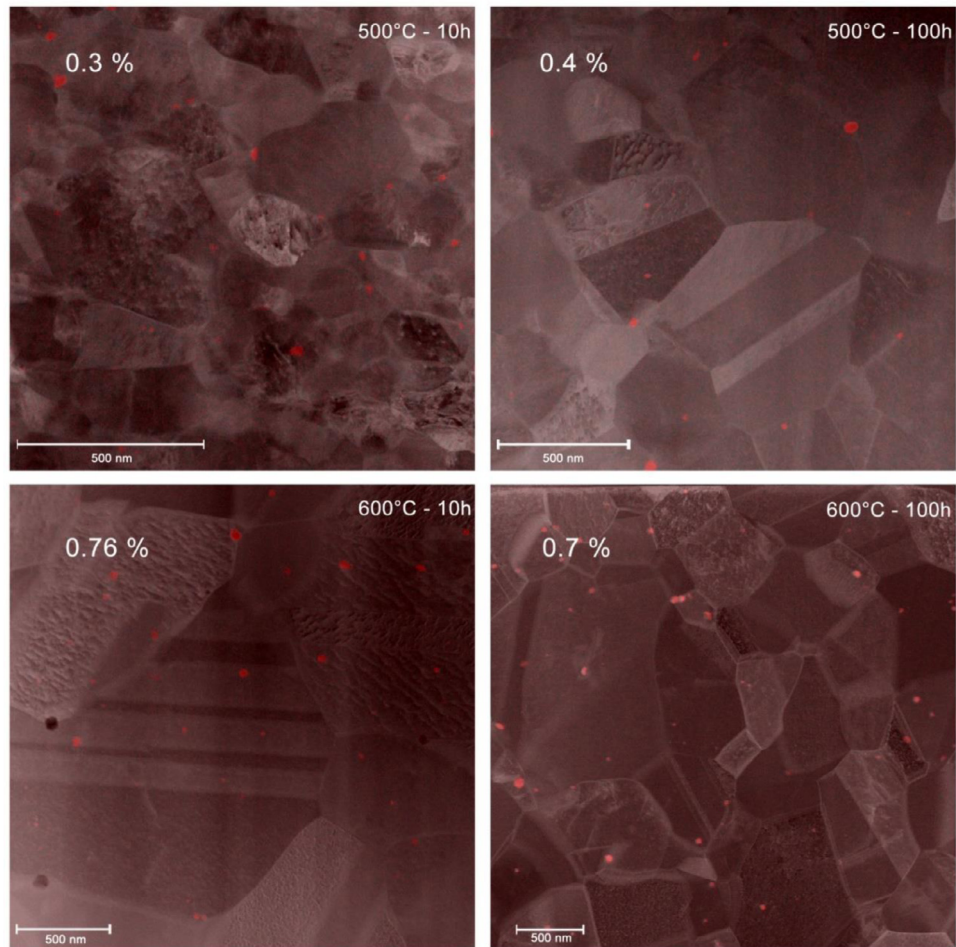


Fig. 4. The STEM HAADF micrograph and the Cr elemental map overlays showing the Cr-rich precipitates (red) of the Ni60 alloy annealed at 500 and 600°C for 10 and 100 h. Included is the approx. volume fraction of the precipitates. (For interpretation of the references to colour in this figure legend, the reader is referred to the web version of this article.)

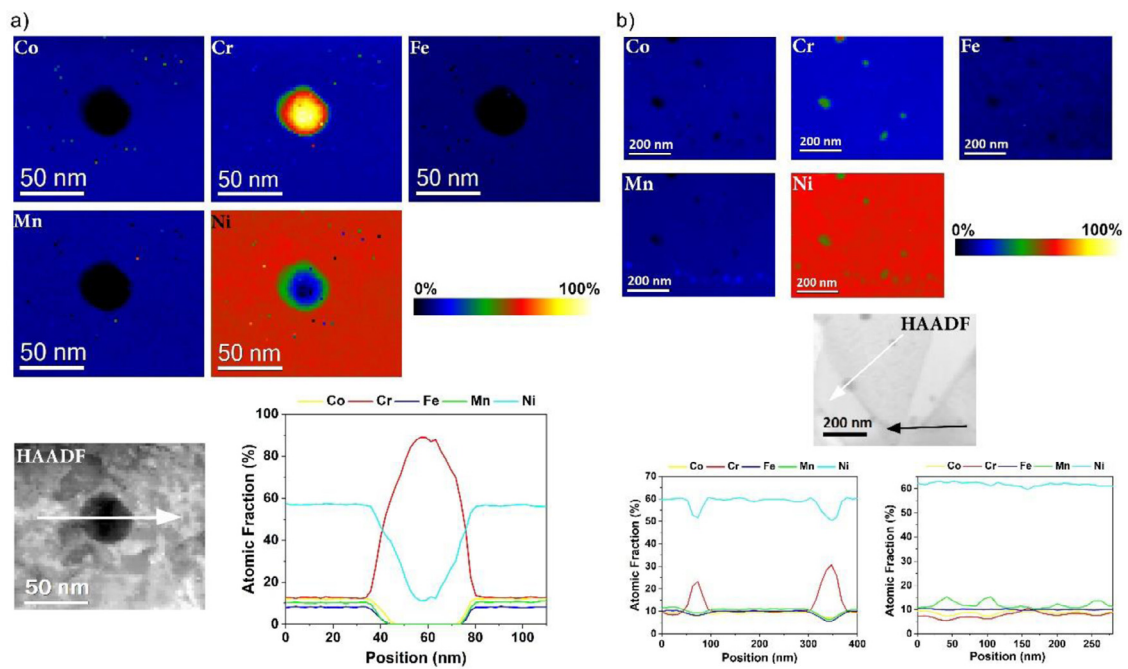


Fig. 5. (a) EELS high loss relative composition maps of the HPT deformed Ni60 annealed for 1 h at 600°C and the corresponding L-edge relative composition line scan profile of the corresponding elements. (b) EELS high loss L edge elemental maps and relative composition line scan profiles of the HPT processed Ni60 annealed at 600°C for 100 h. The line scan over Cr-rich precipitates inside the grain (white arrow - left) and the line scan over Mn enrichments at high angle grain boundary (black arrow - right) show that an increased annealing time results in no further change in the Cr-rich precipitates but rather triggers a Mn segregation to grain boundaries.

the line scans in Fig. A5 which associate the enrichment of one element to the depletion of all other elements. This segregation to HAGBs provides a dragging force for grain boundary migration, thus adding a stabilizing factor to the system. This can eventually also lead to a phase separation at grain boundaries given the right conditions in terms of annealing time and temperature.

Assessing the thermal stability against grain coarsening is complicated Ni20 and Ni60, both of which start to decompose in the intermediate temperature interval, where we expect the onset of coarsening. It should be noted that Ni20 and Ni60 show a comparable coarsening behavior, but Ni20 decomposes to a much higher degree (approx. 10 Vol.% for Ni20 [3] compared to < 1 vol.% for Ni60). The reduced number of second phases in the Ni60 alloy and the comparable grain coarsening rate may indicate that the microstructure of Ni60 alloy is thermodynamically more stable compared to the equiatomic HEA (Ni20). Here, the chemically more complex Ni20 and Ni60 alloys are thermally more stable in terms of grain coarsening than Ni92 and Ni100. Both HEA-type alloys just start to decompose but do not coarsen significantly at intermediate temperatures (up to 500 °C), whereas the more dilute solid solutions (Ni92, Ni100) coarsen significantly (doubling of the grain size, see Table 1). As an intrinsically reduced grain boundary mobility caused by lattice distortions or local chemical fluctuations does not seem to be present in HEAs [63], the observed coarsening behavior could be attributed to the reduction of the grain boundary mobility due to a kinetic stabilization by pinning effects of solute species or the presence of second phases, both of which can strongly inhibit grain boundary motion [63–67].

3.2. Mechanical properties

3.2.1. Hardness and indentation modulus

The effect of annealing on the microstructure and thus on the mechanical properties is further investigated using nanoindentation. As the knowledge of the true contact area is crucial for correct indentation data, and material pile-up is expected for samples with low hardening capability [68], the residual impressions are measured via confocal laser scanning microscopy to avoid overestimations of hardness and modulus using the Oliver-Pharr method. The measured pile-up heights are shown as a function of annealing temperature in Fig. 6. Interestingly, all compositions show a peak in pile-up heights at intermediate temperatures. According to Bolshakov and Pharr [68], the modulus-to-hardness ratio as well as the work hardening capability are crucial for the formation of material pile-up during indentation. However, for ma-

terials showing a moderate amount of work hardening, pile-up is not a significant factor and the indentation data analysis according to Oliver-Pharr [40] provides proper values [68]. The effect of annealing on the pile-up behavior is exemplary shown for Ni100 in Fig. 7. The severely work-hardened as-deformed samples show pronounced pile-up formation (Fig. 7a), as the plastic zone is confined and the material also deforms to the free surface [69]. In contrast, samples in a recrystallized state are able to work harden further during indentation, which inhibits pile-up formation [68] (Fig. 7 c). The peak in pile-up height at intermediate temperatures (Fig. 6) may be related to the change in work hardening behavior, as the modulus-to-hardness (also h_f/h_{max}) ratio changes only marginally to higher values with increasing annealing temperature up to 600°C. During annealing at intermediate temperatures, the number of mobile dislocations will be reduced, while keeping the grain size in the range of the UFG regime, resulting in a hardening of the bulk sample (hardening by annealing) [70,71]. In consequence, the plastic strain that has to be sustained by the material during indentation results in the introduction of free dislocations and dislocation sources in the material around the indenter tip, which facilitates further plastic deformation (softening by deformation) [70,71]. The high mechanical resistance from the bulk material surrounding the softer plastic zone could force the deformation towards the free surface and further enhances pile-up formation.

The correction method proposed by Kese et al. [42] is used to account for pile-up and to evaluate the mechanical properties (Fig. 8). For further information regarding the pile-up correction procedure, please see Appendix B. Since the specimens that show increased pile-up also have a slightly reduced modulus, it can be assumed that the contact area is marginally overestimated. This could be attributed to the fact that not all of the piled-up material is in contact with the indenter tip and thus the contact area is overestimated by the methods described in Appendix B.

After HPT deformation, Ni20 and Ni60 show a comparable hardness level of approx. 4.9 GPa, which is in good agreement with the similar saturation grain size of both alloys as well as similar SSH contributions of approx. 40 MPa calculated using the Varvenne model [32,33]. In terms of strength, it seems that it is not mandatory to aim for an equiatomic composition or entropy maximization to achieve the highest hardness within a material system. The more dilute Ni92 and Ni100 exhibit a lower hardness, which is related to the lower SSH and Hall-Petch contributions [44,72]. After annealing at 300°C, hardening can be observed for most of the investigated alloy compositions. This slight increase in hardness can be related to the elimination of free dislocations and dislocation sources without significant grain growth or recrystallization (hardening by annealing) [70,71]. For Ni20, the hardness even further increases with annealing temperature to a peak value of 5.38 GPa at 500°C, which could be caused by the presence of secondary phases, see (Fig. 3 a) and Ref. [3]. The main difference between Ni20 and Ni60 can be seen for the samples annealed at 500°C. While Ni60 shows a small drop in hardness, Ni20 reaches its maximum value at this temperature. The formation of NiMn, FeCo and Cr-rich precipitates at moderate temperatures is well described in literature for the Cantor alloy [3,4,73] and is also found here after annealing at 700°C (Fig. 3 a). Ni60 shows a nearly constant hardness level of approx. 5 GPa up to 450°C annealing. This finding is in good agreement with the measured grain size, which is almost constant up to this temperature, indicating a high microstructural stability. Annealing at temperatures above 500°C then results in a continuously decreasing hardness to approx. 2 GPa after 900°C annealing for both compositions, Ni20 and Ni60, which can be attributed to grain coarsening processes [44,72] and the dissolution of the precipitates at temperatures above 800°C.

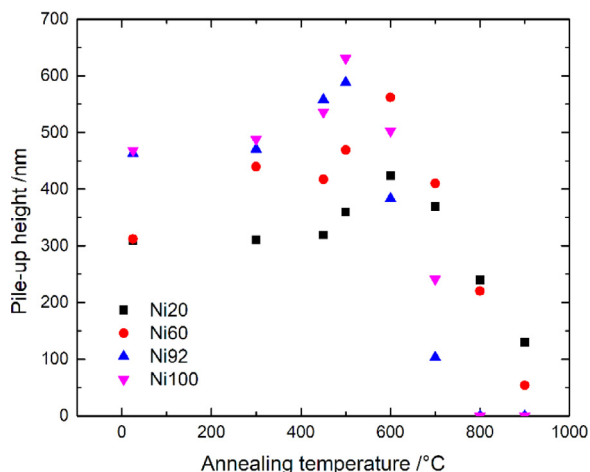


Fig. 6. Maximum pile-up heights of the deformed Ni-X samples after isochronal annealing (1 h).

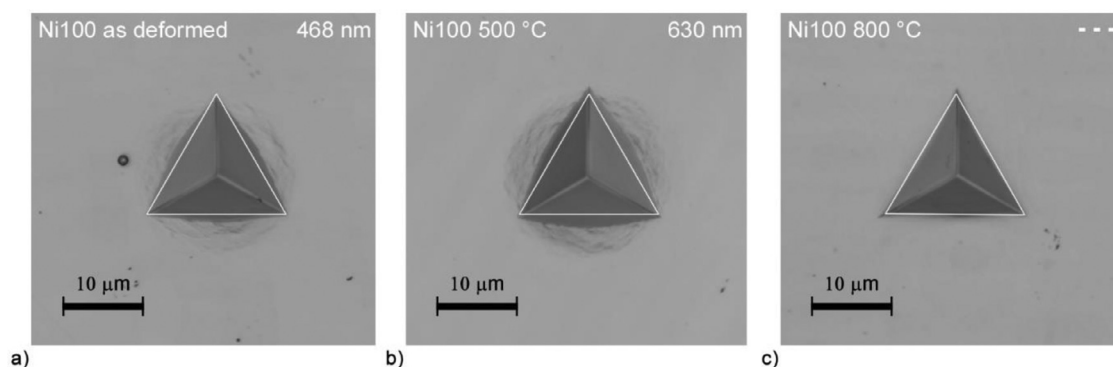


Fig. 7. Laser scanning microscope images of the residual nanoindentation impressions of the Ni100 sample after different annealing treatment: (a) as deformed, (b) 500 °C and (c) 800 °C. The white triangle represents the theoretical projected contact area assuming a perfect Berkovich tip.

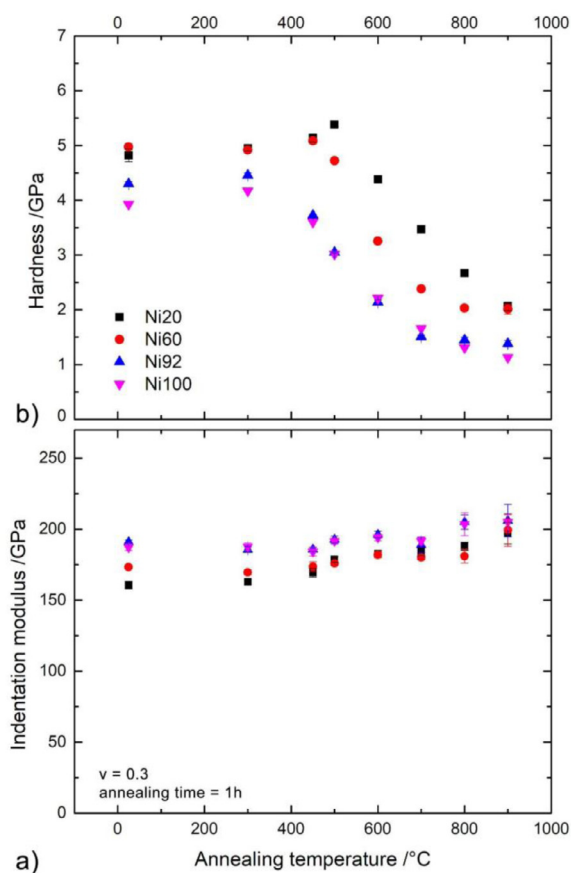


Fig. 8. (a) Indentation modulus and (b) hardness of the deformed Ni-X series after isochronal heat treatment (1 h).

The hardness of Ni92 and Ni100 on the other hand decreases continuously for all temperatures above 300°C due to pronounced grain coarsening. In the coarse-grained state, the hardness correlates with alloying content i.e., the higher the solute concentration, the higher the hardness.

The indentation modulus increases marginally for all compositions with increasing annealing temperature and increasing grain size, respectively, showing no peak formation at intermediate temperatures. Although severe plastic deformation significantly increases the grain boundary density, the elastic properties of UFG and NC materials are insensitive to the grain size in the grain size range larger than 30 nm [74,75]. Hence, the slightly reduced modulus after deformation could either be caused by a crystallo-

graphic texture, which may be present after shear deformation, or by a deviation between assumed and actual contact area. Given the elastic anisotropy of the alloys being used [76,77], the slightly reduced modulus after deformation (see Fig. 8 a) could be caused by a crystallographic texture, which may be present after shear deformation. For Ni20, the texture formation during HPT deformation is already reported in literature [78,79], showing a weak shear texture developed by slip and mechanical twinning. Therefore, we investigated the Ni60 and Ni100 samples as one example for a chemically complex and one for a dilute solid solution. In the as-deformed state, both, the Ni60 and Ni100 alloy show only marginal texture components, which do not change significantly after annealing at 700°C, indicating that the reduced modulus for samples annealed at low temperatures is not caused by texture or rather a change thereof. Accordingly, it is assumed that the calculated contact area is slightly overestimated for specimens showing significant pile-up. In literature [3,80], significant peaks in hardness and modulus were found after annealing at 600°C for the Ni20 composition, which were attributed to the formation of secondary phases. Similarly, the raw indentation data calculated by the Oliver-Pharr method [40] for Ni20 and Ni60 also show a pronounced peak in hardness and modulus, yet, it is caused by the significant amount of material pile-up (Appendix B1). The formation of secondary phases with their low volume fractions does not lead to a significant increase in indentation modulus of the Cantor alloy. This observation is also supported by TEM analysis of the Ni60 samples. For this composition, we also observe a pronounced peak in the Oliver-Pharr analysis of the indentation modulus (see Appendix B2). However, the small volume fraction of second phase particles (less than 1 vol.%) can not cause such a change. The reported modulus and hardness peak for Ni20 is thus caused by material pile-up around the indentation, which is not considered in the Oliver-Pharr analysis, leading to an underestimation of the contact area and corresponding apparent increase in modulus and hardness.

3.2.2. Strain rate sensitivity and activation volume

The strain rate sensitivity (SRS) for the different microstructural states of the alloys and the activation volumes derived from them are investigated by means of nanoindentation strain rate jump tests according to Ref. [41]. In the NC and UFG regime, the materials show a nearly depth independent hardness at indentation depths larger than 1000 nm (Fig. 9 a), whereas the indentation size effect is more pronounced for the coarse-grained microstructures. In this case, the hardness data was corrected according to the Nix-Gao model [81]. The as-deformed states show the trend of an increasing hardness with increasing solute content with its maximum for Ni60 (Ni20 and Ni60 show comparable SSH contributions according to the Varvenne SSH model [32,33]) followed by Ni20,

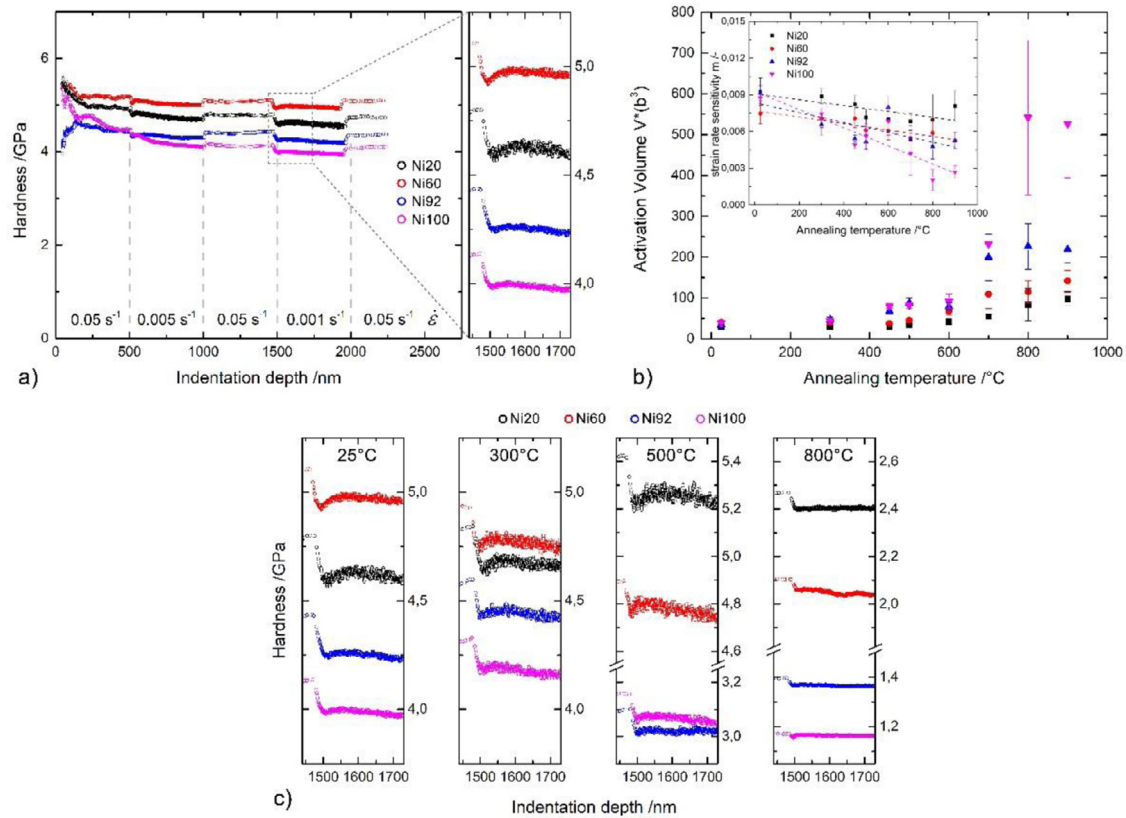


Fig. 9. (a) pile-up corrected hardness vs. indentation depth of the as-deformed Ni-X samples, (b) activation volume and strain rate sensitivity as a function of annealing temperature and (c) enlarged section from (a) for different annealing temperatures.

Ni92 and Ni100. By changing the strain rate, a change in hardness is found, where higher strain rates cause higher hardness values. The different alloys show a distinctively different transient behavior during strain rate change (see Fig. 9 c). After a strain rate jump to a lower strain rate, Ni20 and Ni60 show a period of softening, followed by a short strain hardening section. This yield point phenomenon, which is very distinct for Ni20 and Ni60 is barely observable for Ni92 and Ni100 in their as-deformed HPT state. This behavior changes slightly with annealing. Whereas Ni20 and Ni60 show this yield point phenomena to the same extent up to intermediate annealing temperatures, the strain hardening section is rather more pronounced for the Ni92 and Ni100 sample after 300°C annealing, but vanishes at higher temperatures (Fig. 9 c).

The reduction of strain rate in a nanoindentation strain rate jump experiment is accompanied by a reduction of stress. As shown in stress reduction tests of NC Ni alloys [82,83] two competing deformation mechanisms – dislocation-based (storage and annihilation) and grain boundary mediated deformation – take place, depending on the magnitude of the stress drop, the grain size and the composition. It was shown for a NC Ni₅₀Fe₅₀ alloy that dislocation-based plasticity is suppressed after a stress drop as solutes diffuse to mobile dislocations and temporarily pin them. As a result, dynamic recovery caused by grain boundary processes become more prominent, contribute to plastic strain and control the strength by reducing the dislocation density [83]. With further plastic strain, mobile dislocations need to be generated and the material hardens while approaching a steady state of dislocation nucleation and annihilation.

In case of Ni20 and Ni60 the presence of these yield point phenomena can be related to the high solute content and thus SSH contributions in combination with a UFG or NC microstructure. If this effect is solely based on solute – dislocation interactions, it

should also be observable for the coarse-grained microstructures after annealing. However, for heat treatments performed above 600°C, the yield point effects vanish, hence, this effect is limited to NC and UFG microstructures, where grain boundary mediated mechanisms are decisive. The Ni92 and Ni100 sample show in the as-deformed state the mentioned yield point phenomena after a strain rate jump to a lower strain rate to a much lesser extent, but it increases slightly after annealing at 300°C. In this case, the number of mobile dislocations in the grain interior was reduced during annealing [70,71], resulting in a short strain hardening section after the strain rate reduction due to the generation of a sufficient number of mobile dislocations for plastic strain.

(Fig. 9 b) shows the analysis of the strain rate sensitivity m and the apparent activation volume V^* . The strain rate sensitivity m ($m = \frac{d(\ln H)}{d(\ln \dot{\epsilon})}$) decreases with increasing grain size, whereas the corresponding activation volumes ($V^* = \frac{C \cdot \sqrt{3} \cdot k_B \cdot T}{m \cdot H}$ with C : constraint factor of 3, k_B : Boltzmann constant, T : ambient temperature of 25°C) behaves inversely for all compositions. Although this is a common testing procedure, it should be noted that the microstructure in the plastic zone may be unstable during indentation [84]. Furthermore, it is not possible to infer if the change in hardness with varying strain rate is caused by a change in dislocation density, dislocation velocity or a combination of both [18,85]. In NC and UFG FCC materials, the increased SRS can be attributed by dislocation – grain boundary interactions, which get more prominent due to the high grain boundary density present after HPT [17,80,86]. The present study reveals nearly identical activation volumes of approx. 30 b³ for all the different compositions after HPT. This corresponds to dislocation-glide based plasticity (dislocation nucleation or/and dislocation cross-slip), acting in a range from several b³ to 100 b³ [18,87–89]. Up to an annealing temperature

of 600°C, the activation volumes of all compositions are below this limit of 100 b³.

It is worth noting that after annealing Ni20, Ni60 and Ni92 show relatively small activation volumes compared to Ni100, which could indicate that solid solution hardening needs to be thermally overcome for plasticity, similar to the Peierls mechanism in BCC metals [80]. Ni100 exhibits a much larger activation volume in the coarse-grained state, indicating dislocation-dislocation interactions [88].

4. Conclusions

A series of Ni-diluted solid solutions were severely deformed by HPT to a single-phase FCC, ultrafine-grained or nanocrystalline state, reaching the saturation state. Subsequent isochronal annealing was performed to shed light on the thermal stability of room-temperature mechanical properties (hardness, modulus) as well as microstructural stability and precipitation behavior, with an emphasis on a transition from dilute solid solutions to HEAs.

1. In terms of thermal stability, the present work reveals similar behavior for Ni20 and Ni60 (HEA-type solid solutions) on the one hand and Ni92 and Ni100 (dilute solid solution) on the other hand, which indicates a transition from conventional solid solutions to HEAs.
2. While the decomposition tendencies of Ni20 have recently been shown in literature, the Cr-rich nanophases ($\varnothing \approx 40$ nm) with an FCC structure and Mn segregations to grain boundaries were detected in the Ni60 alloy using TEM in this work. The Ni92 alloy shows a single-phase solid solution, which is consistent with the higher thermodynamic stability expected for dilute solid solutions.
3. The investigated alloys exhibit a two stage coarsening behavior, with almost no grain growth at $T < 450^\circ\text{C}$ and diffusion driven grain growth above 500°C. Reduced grain growth can be observed up to 500°C for the higher concentrated compositions (Ni20 and Ni60), where Ni92 and Ni100 show significantly larger grain sizes. The hindered coarsening behavior of the HEA type alloys may be attributed to pinning effects by solutes and second phases. The activation energies for grain growth are calculated and a qualitative comparison reveals a correlation between Q and the volume diffusion coefficients D . After annealing in the range of the recrystallization temperature at 900°C, all compositions show a single-phase microstructure in the micrometer range, with Ni100 showing a grain size twice as big as the other alloys.
4. Significant material pile-up takes place during indentation for the NC and UFG microstructures, showing peak values in the intermediate annealing temperatures. The increase in pile-up formation is related to a change in work hardening behavior, i.e., to the hardening by annealing phenomenon, facilitating plastic flow of constrained material towards the free surface in the vicinity of the contact (softening by deformation). Pile-up ef-

fects around the indentation can also lead to misinterpretation of hardness and modulus, applying the OP method. Without correction, physically meaningless peaks in modulus and hardness are found, whereas after correction, only slight hardening by annealing is observed for all compositions

5. The nanoindentation hardness trends show a higher thermal stability for the HEA-type alloys. Whereas the hardness of Ni92 and Ni100 already starts to decrease at temperatures above 300°C due to grain growth, Ni60 shows a constant hardness up to an annealing temperature of 450°C and Ni20 exhibit a hardness peak in the intermediate temperature interval (450 – 600°C). The hardness peak after annealing of Ni20 may be attributed to the formation of second phases, a modulus peak is not observable after contact area correction. The nanoindentation SRJ tests show a different transient behavior for dilute solid solutions and HEA-type alloys and indicate dislocation-glide based plasticity acting in the UFG regime.

Data availability

The raw/processed data required to reproduce these findings cannot be shared at this time as the data also forms part of an ongoing study. [Appendix A](#)

Declaration of Competing Interest

The authors declare that they have no known competing financial interests or personal relationships that could have appeared to influence the work reported in this paper.

CRediT authorship contribution statement

Tom Keil: Methodology, Investigation, Data curation, Formal analysis, Visualization, Writing – original draft, Writing – review & editing. **Shabnam Taheriniya:** Investigation, Data curation, Formal analysis, Validation, Visualization, Writing – original draft, Writing – review & editing. **Enrico Bruder:** Conceptualization, Methodology, Validation, Formal analysis, Writing – review & editing. **Gerhard Wilde:** Conceptualization, Methodology, Writing – review & editing, Supervision, Project administration, Funding acquisition. **Karsten Durst:** Conceptualization, Methodology, Writing – review & editing, Supervision, Project administration, Funding acquisition.

Acknowledgments

This work was funded by the German Research Foundation (DFG) within the priority programme “Compositionally Complex Alloys - High Entropy Alloys (CCA-HEA)” (SPP2006) under Grant Nos. DU 424/13-2 and WI 1899/32-2. The authors thank Dr. Mathilde Laurent-Brocq for providing the different alloy systems.

Appendix A. Thermal stability and precipitation formation

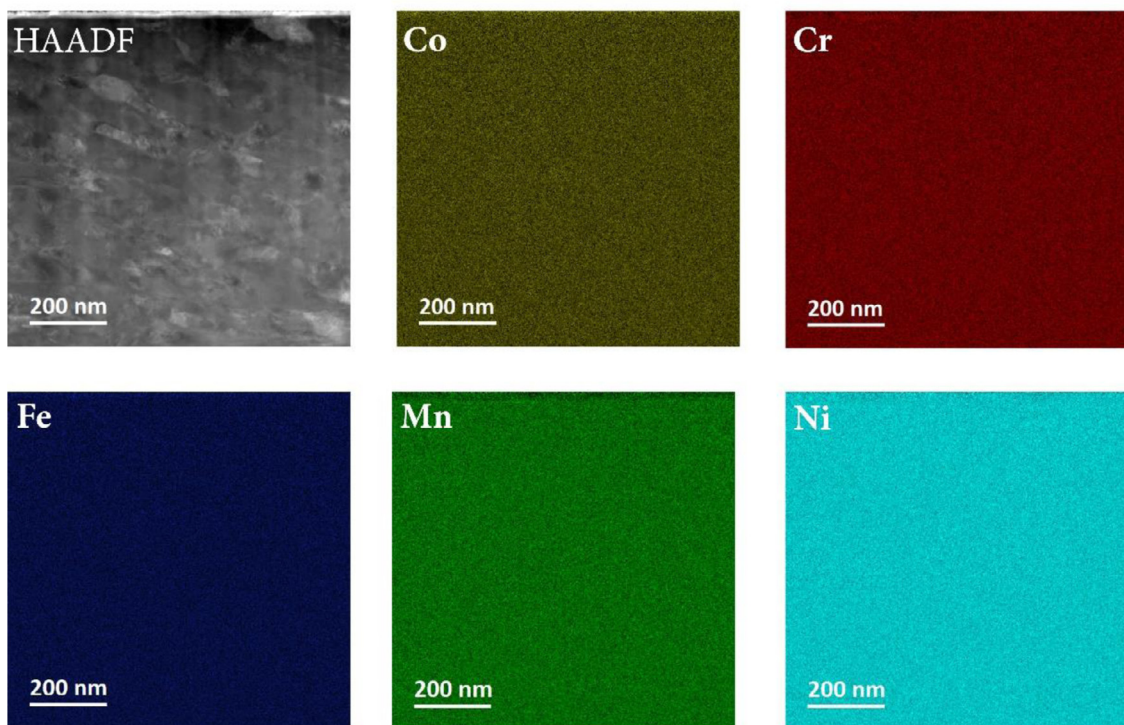


Fig. A1. The STEM HAADF micrograph showing a close-up view of the grain and the corresponding elemental maps of the Ni60 alloy after HPT deformation.

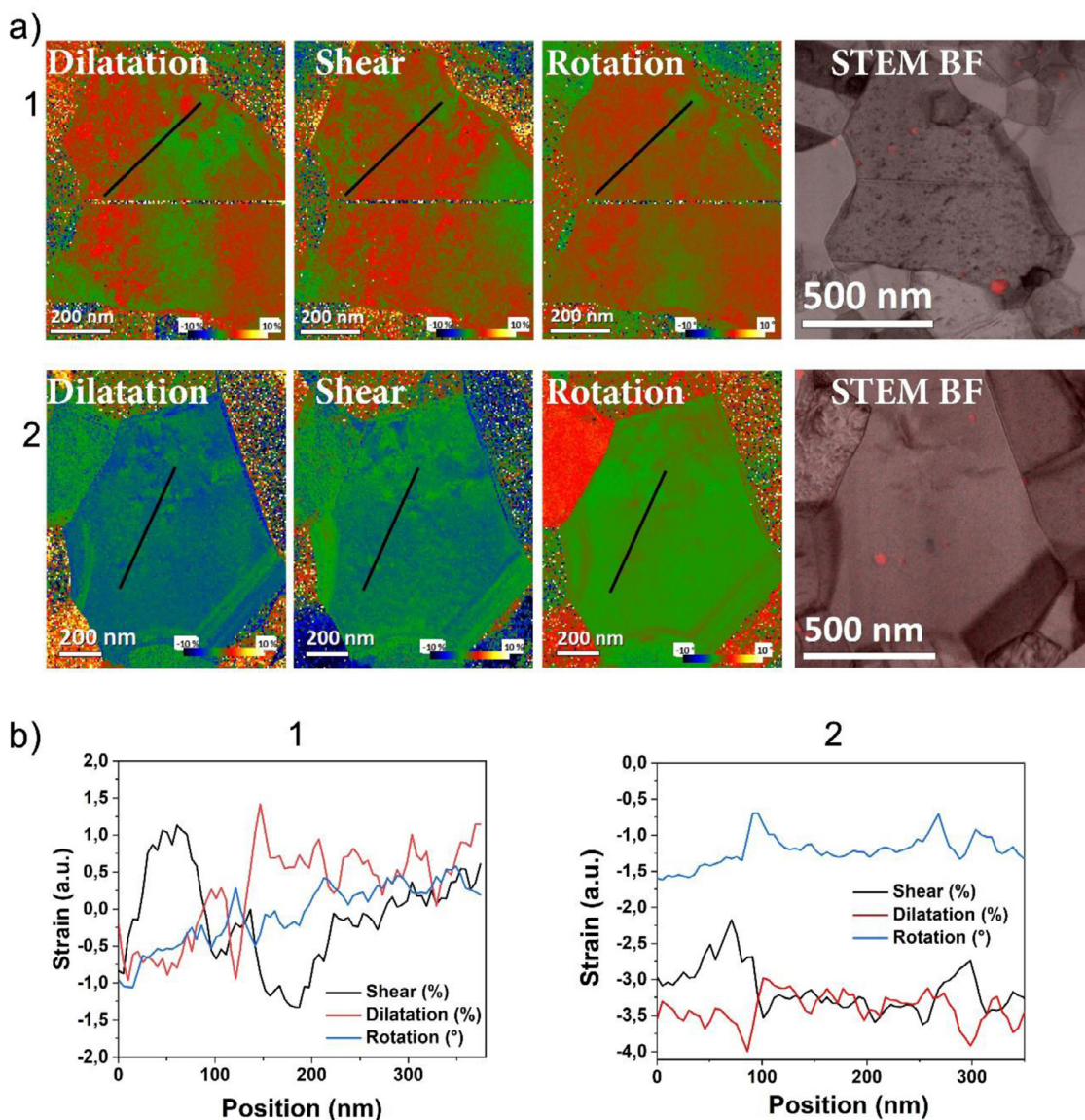


Fig. A2. Strain map reconstructed from the nanobeam diffraction series using a custom code written in Digital Micrograph of the Ni60 sample annealed at 600°C for 1 h (line 1) and 100 h (line 2). The Cr-rich precipitates are characterized as a part of the matrix which was reconstructed using a virtual aperture on the resulting FCC diffraction patterns. The line profile (white arrow) over the shear strain as well as the rotational strain maps show a strain buildup of 2% and rotation of -0.9° respectively behind the Cr-rich precipitate.

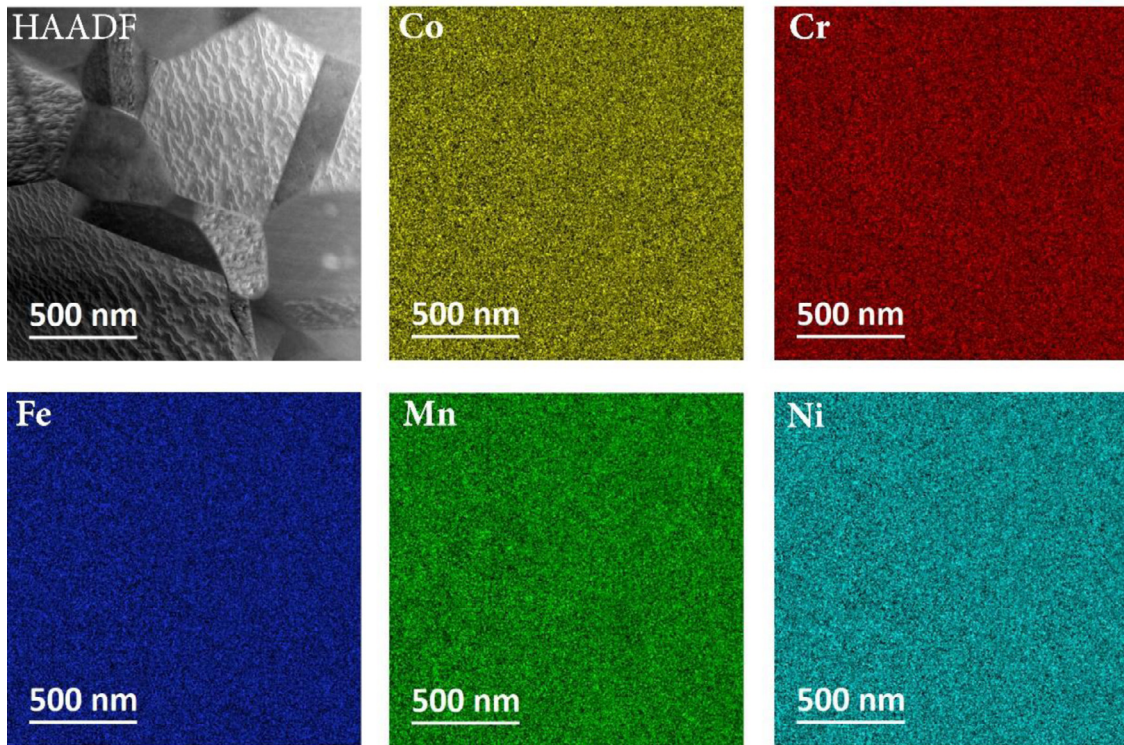


Fig. A3. The STEM HAADF micrograph showing a close-up view of the grain and the corresponding elemental maps of the Ni92 alloy after 600 °C annealing for 1 h.

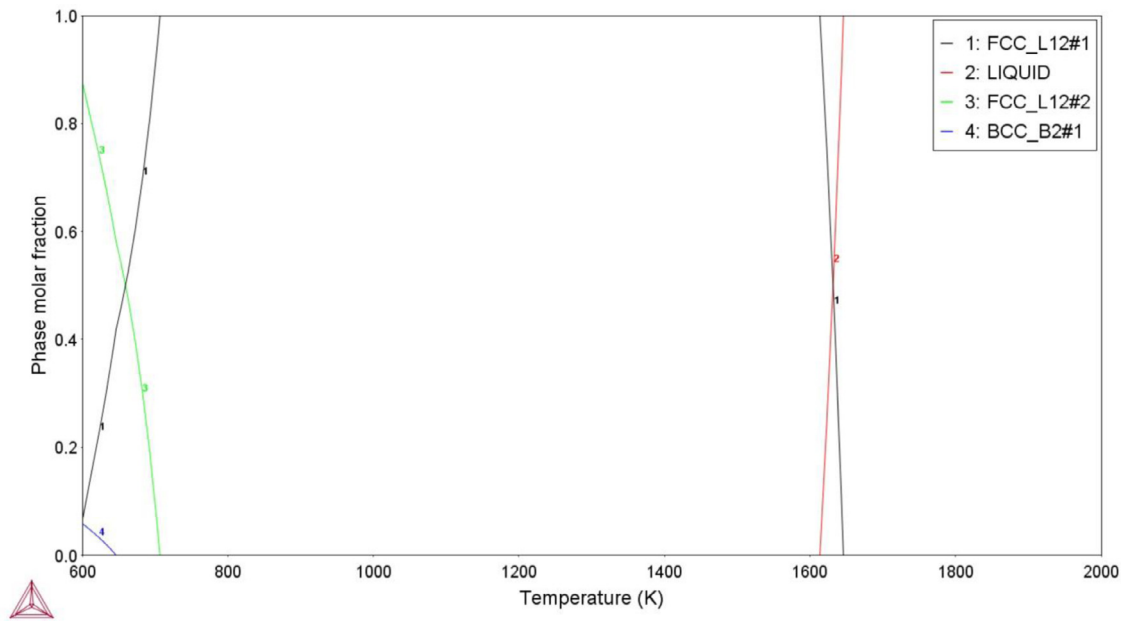


Fig. A4. Calculated equilibrium phase fractions for Ni60 ($\text{Cr}_{10}\text{Mn}_{10}\text{Fe}_{10}\text{Co}_{10}\text{Ni}_{60}$) using the TCHEA3 database.

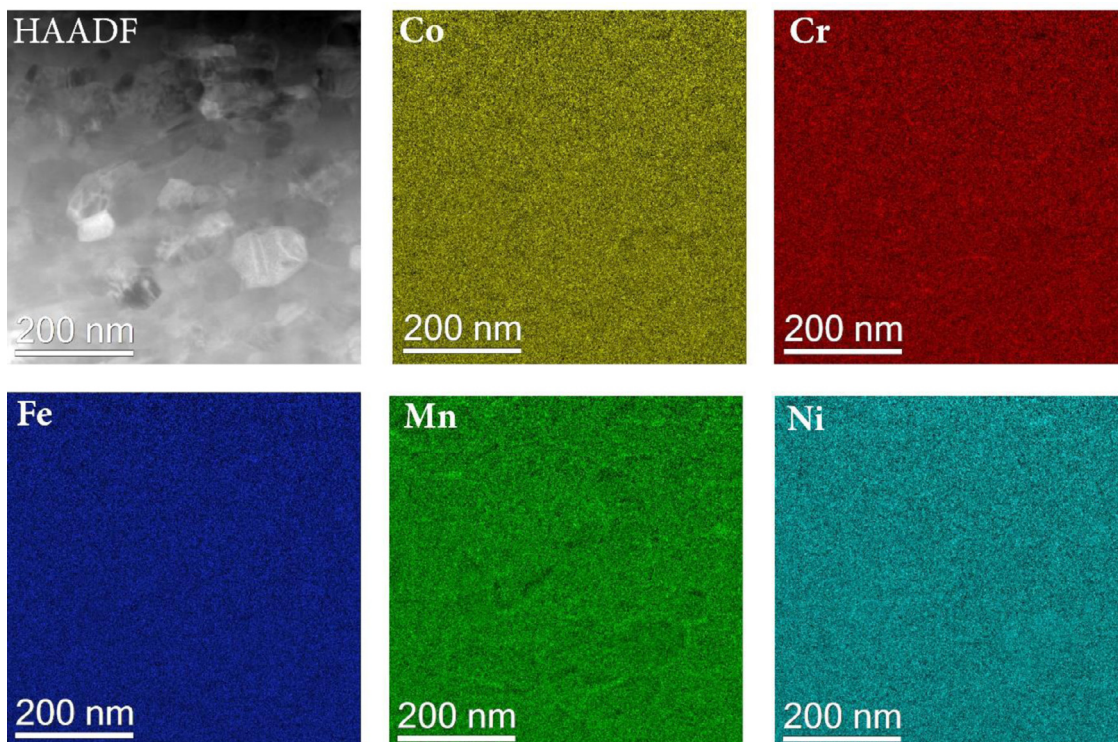


Fig. A5. The STEM HAADF micrograph showing a close-up view of the grains and the corresponding elemental maps of the HPT deformed Ni60 alloy after 1 h of annealing at 450°C.

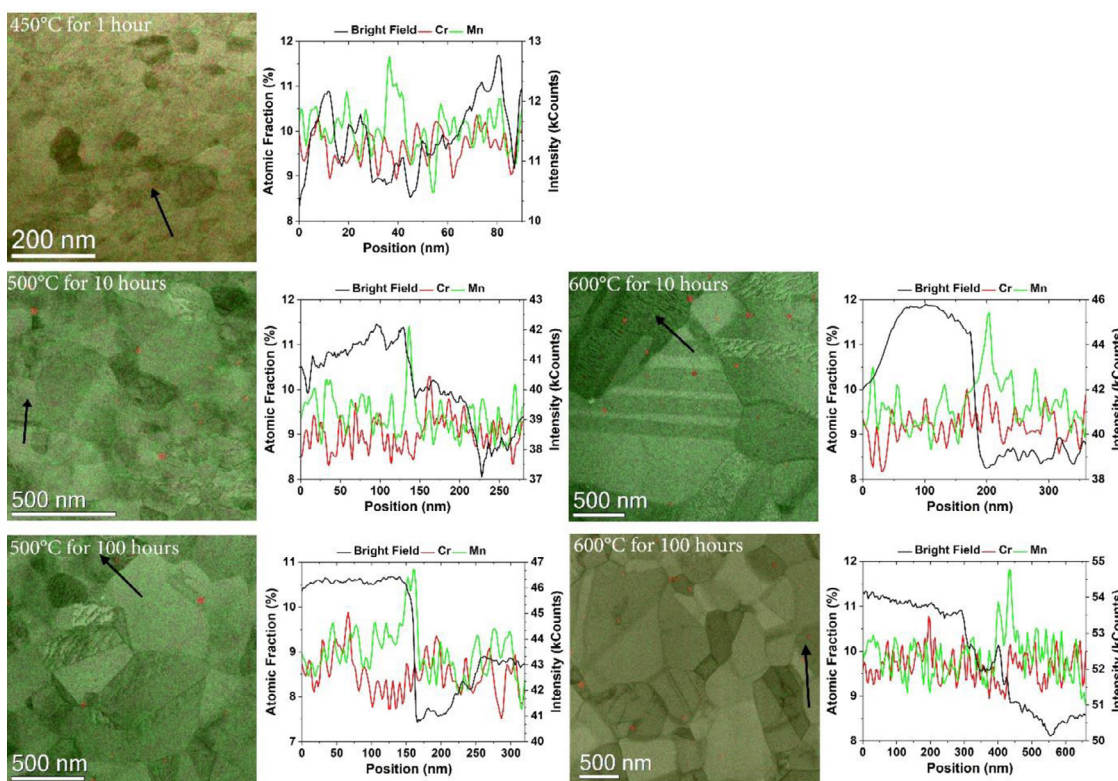


Fig. A6. The overlay of STEM BF micrograph, Cr and Mn elemental maps as well as the corresponding line scans showing an enrichment of Mn at HAGBs initiated at 450°C in the Ni60 alloy. The increase of annealing temperature and time does not lead to the increase of Mn enrichment at HAGBs while Cr precipitation progresses further to reach a saturated state.

Appendix B. Pile-up correction procedure for indentation testing

Depending on the modulus to hardness ratio, sink-in or pile-up may occur during plastic deformation, which affects the actual contact area and needs to be considered for proper modulus and hardness values [90]. The influence of the observed pile-up on the contact area and thus the mechanical properties can be seen in Fig. B1, where the uncorrected hardness and modulus values given from the Oliver-Pharr method [40] are shown. The hardness and modulus values are shifted to much higher values for the samples showing pile-up behavior. Due to the peak in pile-up height at intermediate temperatures, a peak in modulus is observable for the different compositions in the same annealing temperature regime.

A method for determining the true contact area was proposed by Kese et al. [42] using a Berkovich tip and approximating the pile-up contact perimeter as a semi-ellipse. By knowing the contact area from the Oliver-Pharr method (A_{O-P}), the true contact area can be determined using Eq. (B.1):

$$A = A_{O-P} + A_{pile-up} = A_{O-P} + 5.915 \sum a_i \quad (B.1)$$

with h_c representing the contact depth and a_i the horizontal distance between pile-up contact perimeter and the edge of the indent. The semi-elliptical projected pile-up lobes at the three sides of the Berkovich tip are included in the summation. The contact area determined using Eq. (B.1) is very similar to the value obtained by measuring the area of the residual impression optically (see Fig. B2), therefore the method proposed by Kese et al. [42] is used for contact area corrections throughout Section 3.2.

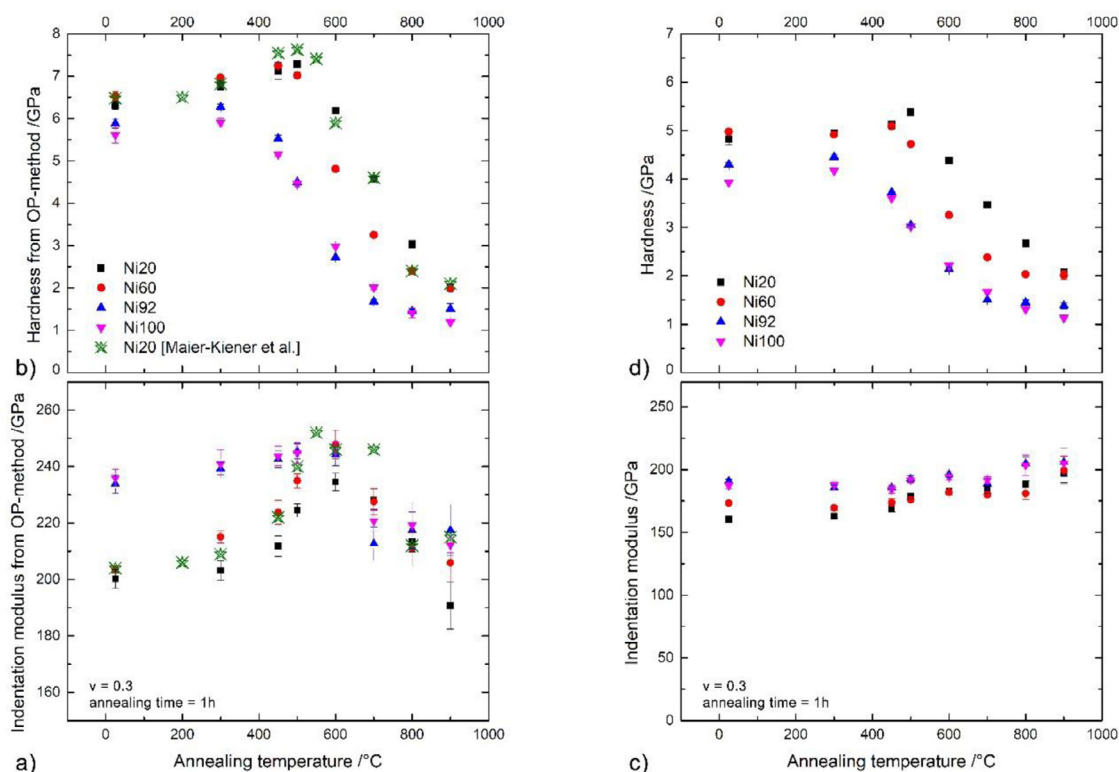


Fig. B1. Indentation modulus and hardness of the deformed Ni-X series after isochronal heat treatment (1 h). (a)–(b) values obtained from the Oliver-Pharr method [40] without pile-up correction (green symbols are taken from Ref. [80]) and (c), (d) values obtained after pile-up correction according to [42]. (For interpretation of the references to colour in this figure legend, the reader is referred to the web version of this article.)

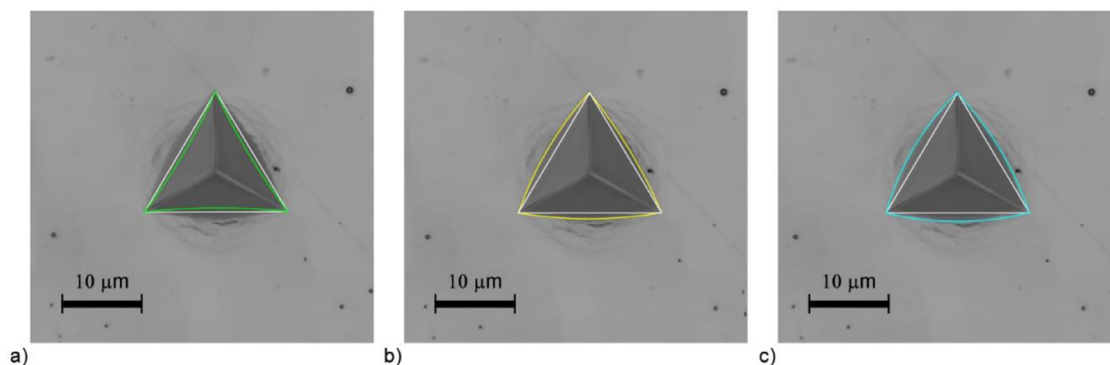


Fig. B2. Comparison of true contact area, determined according to (a) Oliver-Pharr method (green) [21], (b) Kese et al. (yellow) [42] and (c) by means of optical measurement (blue) using the Ni100 sample after HPT deformation. (For interpretation of the references to colour in this figure legend, the reader is referred to the web version of this article.)

References

- [1] B. Cantor, et al., Microstructural development in equiatomic multicomponent alloys, *Mater. Sci. Eng. A* 375 (2004) 213–218–377, doi:10.1016/j.msea.2003.10.257.
- [2] M.V. Klimova, et al., Effect of second phase particles on mechanical properties and grain growth in a CoCrFeMnNi high entropy alloy, *Mater. Sci. Eng. A* 748 (2019) 228–235, doi:10.1016/j.msea.2019.01.112.
- [3] B. Schuh, et al., Mechanical properties, microstructure and thermal stability of a nanocrystalline CoCrFeMnNi high-entropy alloy after severe plastic deformation, *Acta Mater.* 96 (2015) 258–268, doi:10.1016/j.actamat.2015.06.025.
- [4] E.J. Pickering, et al., Precipitation in the equiatomic high-entropy alloy CrMn-FeCoNi, *Scr. Mater.* 113 (2016) 106–109, doi:10.1016/j.scriptamat.2015.10.025.
- [5] Y.J. Li, et al., Phase decomposition in a nanocrystalline CrCoNi alloy, *Scr. Mater.* 188 (2020) 259–263, doi:10.1016/j.scriptamat.2020.07.054.
- [6] L. Li, et al., Segregation-driven grain boundary spinodal decomposition as a pathway for phase nucleation in a high-entropy alloy, *Acta Mater.* 178 (2019) 1–9, doi:10.1016/j.actamat.2019.07.052.
- [7] B.B. Straumal, et al., Grain boundary wetting by a second solid phase in the high entropy alloys: a review, *Materials* 14 (24) (2021) Basel, doi:10.3390/ma14247506.
- [8] B.B. Straumal, et al., Grain boundary phase observed in Al-5 at.% Zn alloy by using HREM, *Philos. Mag. Lett.* 87 (6) (2007) 423–430, doi:10.1080/09500830701225787.
- [9] D.A. Molodov, et al., Acceleration of grain boundary motion in Al by small additions of Ga, *Philos. Mag. Lett.* 72 (6) (1995) 361–368, doi:10.1080/09500839508242475.
- [10] S. Divinski, et al., Grain-boundary melting phase transition in the Cu-Bi system, *Phys. Rev. B* 71 (10) (2005) 104104, doi:10.1103/PhysRevB.71.104104.
- [11] O. Kogtenkova, et al., Grain boundary complexions and phase transformations in Al- and Cu-based alloys, *Metals* 9 (1) (2018), doi:10.3390/met9010010.
- [12] J.W. Cahn, The impurity-drag effect in grain boundary motion, *Acta Metall.* 10 (9) (1962) 789–798, doi:10.1016/0001-6160(62)90092-5.
- [13] K. Lücke, H.P. Stüwe, On the theory of impurity controlled grain boundary motion, *Acta Metall.* 19 (10) (1971) 1087–1099, doi:10.1016/0001-6160(71)90041-1.
- [14] F.J. Humphreys, M. Hatherly, *Recrystallization and Related Annealing Phenomena*, 2nd ed., Elsevier, 2004 edISBN: 978-0-08-044164-1, doi:10.1016/B978-0-08-044164-1.X5000-2.
- [15] D.H. Lee, et al., Nanomechanical behavior and structural stability of a nanocrystalline CoCrFeNiMn high-entropy alloy processed by high-pressure torsion, *J. Mater. Res.* 30 (18) (2015) 2804–2815, doi:10.1557/jmr.2015.239.
- [16] C.C. Koch, Optimization of strength and ductility in nanocrystalline and ultrafine grained metals, *Scr. Mater.* 49 (7) (2003) 657–662, doi:10.1016/S1359-6462(03)00394-4.
- [17] R. Schwaiger, et al., Some critical experiments on the strain-rate sensitivity of nanocrystalline nickel, *Acta Mater.* 51 (17) (2003) 5159–5172, doi:10.1016/S1359-6454(03)00365-3.
- [18] J. Wehrs, et al., Comparison of *in situ* micromechanical strain-rate sensitivity measurement techniques, *JOM* 67 (8) (2015) 1684–1693, doi:10.1007/s11837-015-1447-z.
- [19] Y.J. Li, et al., Deformation kinetics of nanocrystalline nickel, *Acta Mater.* 55 (17) (2007) 5708–5717, doi:10.1016/j.actamat.2007.06.036.
- [20] S.Y. Chen, et al., Phase transformations of HfNbTaTiZr high-entropy alloy at intermediate temperatures, *Scr. Mater.* 158 (2019) 50–56, doi:10.1016/j.scriptamat.2018.08.032.
- [21] B. Schuh, et al., Phase decomposition of a single-phase AlTiVNb high-entropy alloy after severe plastic deformation and annealing, *Adv. Eng. Mater.* 19 (4) (2017) 1600674, doi:10.1002/adem.201600674.
- [22] B. Schuh, et al., Thermodynamic instability of a nanocrystalline, single-phase TiZrNbHfTa alloy and its impact on the mechanical properties, *Acta Mater.* 142 (2018) 201–212, doi:10.1016/j.actamat.2017.09.035.
- [23] F. He, et al., Phase separation of metastable CoCrFeNi high entropy alloy at intermediate temperatures, *Scr. Mater.* 126 (2017) 15–19, doi:10.1016/j.scriptamat.2016.08.008.
- [24] V. Pacheco, et al., Thermal stability of the HfNbTiVZr high-entropy alloy, *Inorg. Chem.* 58 (1) (2019) 811–820, doi:10.1021/acs.inorgchem.8b02957.
- [25] G. Liu, et al., Solute segregation effect on grain boundary migration and hall–petch relationship in CrMnFeCoNi high-entropy alloy, *Mater. Sci. Technol.* (2019) 1–9, doi:10.1080/02670836.2019.1570679.
- [26] G. Braccq, et al., Combining experiments and modelling to explore the solid solution strengthening of high and medium entropy alloys, *Acta Mater.* (2019), doi:10.1016/j.actamat.2019.06.050.
- [27] M. Laurent-Brocq, et al., From diluted solid solutions to high entropy alloys: on the evolution of properties with composition of multi-components alloys, *Mater. Sci. Eng. A* 696 (2017) 228–235, doi:10.1016/j.msea.2017.04.079.
- [28] G. Laplanche, et al., Reasons for the superior mechanical properties of medium-entropy CrCoNi compared to high-entropy CrMnFeCoNi, *Acta Mater.* 128 (2017) 292–303, doi:10.1016/j.actamat.2017.02.036.
- [29] T. Keil, et al., From diluted solid solutions to high entropy alloys: Saturation grain size and mechanical properties after high pressure torsion, *Scr. Mater.* 192 (2021) 43–48, doi:10.1016/j.scriptamat.2020.09.046.
- [30] M. Laurent-Brocq, et al., Combining tensile tests and nanoindentation to explore the strengthening of high and medium entropy alloys, *Materialia* 7 (2019), doi:10.1016/j.mta.2019.100404.
- [31] G. Braccq, et al., The fcc solid solution stability in the Co-Cr-Fe-Mn-Ni multi-component system, *Acta Mater.* 128 (2017) 327–336, doi:10.1016/j.actamat.2017.02.017.
- [32] C. Varvenne, A. Luque, W.A. Curtin, Theory of strengthening in fcc high entropy alloys, *Acta Mater.* 118 (2016) 164–176, doi:10.1016/j.actamat.2016.07.040.
- [33] C.R. LaRosa, et al., Solid solution strengthening theories of high-entropy alloys, *Mater. Charact.* 151 (2019) 310–317, doi:10.1016/j.matchar.2019.02.034.
- [34] M. Glienke, et al., Grain boundary diffusion in CoCrFeMnNi high entropy alloy: kinetic hints towards a phase decomposition, *Acta Mater.* 195 (2020) 304–316, doi:10.1016/j.actamat.2020.05.009.
- [35] J. Kottke, et al., Tracer diffusion in the Ni-CoCrFeMn system: transition from a dilute solid solution to a high entropy alloy, *Scr. Mater.* 159 (2019) 94–98, doi:10.1016/j.scriptamat.2018.09.011.
- [36] P.W. Trimby, Orientation mapping of nanostructured materials using transmission Kikuchi diffraction in the scanning electron microscope, *Ultramicroscopy* 120 (2012) 16–24, doi:10.1016/j.ultramic.2012.06.004.
- [37] V.B. Ozdol, et al., Strain mapping at nanometer resolution using advanced nano-beam electron diffraction, *Appl. Phys. Lett.* 106 (25) (2015), doi:10.1063/1.4922994.
- [38] C. Gammer, et al., Diffraction contrast imaging using virtual apertures, *Ultramicroscopy* 155 (2015) 1–10, doi:10.1016/j.ultramic.2015.03.015.
- [39] J.B. Pethica, W.C. Oliver, Mechanical properties of nanometre volumes of material: use of the elastic response of small area indentations, *MRS Proc.* 130 (1988), doi:10.1557/PROC-130-13.
- [40] W.C. Oliver, G.M. Pharr, An improved technique for determining hardness and elastic modulus using load and displacement sensing indentation experiments, *J. Mater. Res.* 7 (06) (1992) 1564–1583, doi:10.1557/JMR.1992.1564.
- [41] V. Maier, et al., Nanoindentation strain-rate jump tests for determining the local strain-rate sensitivity in nanocrystalline Ni and ultrafine-grained Al, *J. Mater. Res.* 26 (11) (2011) 1421–1430, doi:10.1557/jmr.2011.156.
- [42] K.O. Kese, Z.C. Li, B. Bergman, Method to account for true contact area in soda-lime glass during nanoindentation with the Berkovich tip, *Mater. Sci. Eng. A* 404 (1–2) (2005) 1–8, doi:10.1016/j.msea.2005.06.006.
- [43] K. Edalati, et al., Influence of dislocation-solute atom interactions and stacking fault energy on grain size of single-phase alloys after severe plastic deformation using high-pressure torsion, *Acta Mater.* 69 (2014) 68–77, doi:10.1016/j.actamat.2014.01.036.
- [44] W.H. Liu, et al., Grain growth and the hall–petch relationship in a high-entropy FeCrNiCoMn alloy, *Scr. Mater.* 68 (7) (2013) 526–529, doi:10.1016/j.scriptamat.2012.12.002.

- [45] Y.C. Huang, et al., A Study on the hall-petch relationship and grain growth kinetics in FCC-structured high/medium entropy alloys, *Entropy* 21 (3) (2019) Basel, doi:[10.3390/e21030297](https://doi.org/10.3390/e21030297).
- [46] D. Horton, C.B. Thomson, V. Randle, Aspects of twinning and grain growth in high purity and commercially pure nickel, *Mater. Sci. Eng. A* 203 (1) (1995) 408–414, doi:[10.1016/0921-5093\(95\)09821-6](https://doi.org/10.1016/0921-5093(95)09821-6).
- [47] F. Otto, N.L. Hanold, E.P. George, Microstructural evolution after thermomechanical processing in an equiatomic, single-phase CoCrFeMnNi high-entropy alloy with special focus on twin boundaries, *Intermetallics* 54 (2014) 39–48, doi:[10.1016/j.intermet.2014.05.014](https://doi.org/10.1016/j.intermet.2014.05.014).
- [48] A. Sarkar, K.L. Murty, Anisotropic grain growth kinetics in nanocrystalline nickel, *Philos. Mag. Lett.* 98 (11) (2019) 494–501, doi:[10.1080/09500839.2019.1583391](https://doi.org/10.1080/09500839.2019.1583391).
- [49] H. Hu, B. Rath, On the time exponent in isothermal grain growth, *Metall. Trans.* 1 (11) (1970) 3181–3184.
- [50] M. Chauhan, F.A. Mohamed, Investigation of low temperature thermal stability in bulk nanocrystalline Ni, *Mater. Sci. Eng. A* 427 (1) (2006) 7–15, doi:[10.1016/j.msea.2005.10.039](https://doi.org/10.1016/j.msea.2005.10.039).
- [51] R. Klemm, et al., Thermal stability of grain structure and defects in submicrocrystalline and nanocrystalline nickel, *Scr. Mater.* 46 (9) (2002) 685–690, doi:[10.1016/S1359-6462\(02\)00054-4](https://doi.org/10.1016/S1359-6462(02)00054-4).
- [52] L. Hashemi-Sadraei, et al., The influence of grain size determination method on grain growth kinetics analysis, *Adv. Eng. Mater.* 17 (11) (2015) 1598–1607, doi:[10.1002/adem.201500057](https://doi.org/10.1002/adem.201500057).
- [53] X. Sauvage, et al., Grain boundaries in ultrafine grained materials processed by severe plastic deformation and related phenomena, *Mater. Sci. Eng. A* 540 (2012) 1–12, doi:[10.1016/j.msea.2012.01.080](https://doi.org/10.1016/j.msea.2012.01.080).
- [54] G. Wilde, et al., Plasticity and grain boundary diffusion at small grain sizes, *Adv. Eng. Mater.* 12 (8) (2010) 758–764, doi:[10.1002/adem.200900333](https://doi.org/10.1002/adem.200900333).
- [55] G. Wilde, S. Divinski, Grain boundaries and diffusion phenomena in severely deformed materials, *Mater. Trans.* 60 (7) (2019) 1302–1315, doi:[10.2320/matertrans.MF201934](https://doi.org/10.2320/matertrans.MF201934).
- [56] J. Kottke, et al., Experimental and theoretical study of tracer diffusion in a series of (CoCrFeMn)100–xNi alloys, *Acta Mater.* 194 (2020) 236–248, doi:[10.1016/j.actamat.2020.05.037](https://doi.org/10.1016/j.actamat.2020.05.037).
- [57] M. Naderi, et al., Kinetic, volumetric and structural effects induced by liquid Ga penetration into ultrafine grained Al, *Acta Mater.* 99 (2015) 196–205, doi:[10.1016/j.actamat.2015.07.061](https://doi.org/10.1016/j.actamat.2015.07.061).
- [58] S.V. Divinski, et al., A mystery of "sluggish diffusion" in high-entropy alloys: the truth or a myth? *Diffus. Found.* 17 (2018) 69–104, doi:[10.4028/www.scientific.net/DF.17.69](https://doi.org/10.4028/www.scientific.net/DF.17.69).
- [59] J. Dąbrowa, M. Danielewski, State-of-the-art diffusion studies in the high entropy alloys, *Metals* 10 (3) (2020), doi:[10.3390/met10030347](https://doi.org/10.3390/met10030347).
- [60] W.P. Tong, et al., Nitriding iron at lower temperatures, *Science* 299 (5607) (2003) 686–688, doi:[10.1126/science.1080216](https://doi.org/10.1126/science.1080216).
- [61] J. Schuster, E. Bruder, C. Müller, Plasma nitriding of steels with severely plastic deformed surfaces, *J. Mater. Sci.* 47 (22) (2012) 7908–7913, doi:[10.1007/s10853-012-6566-0](https://doi.org/10.1007/s10853-012-6566-0).
- [62] Y.J. Li, A. Savan, A. Ludwig, Atomic scale understanding of phase stability and decomposition of a nanocrystalline CrMnFeCoNi canton alloy, *Appl. Phys. Lett.* 119 (20) (2021), doi:[10.1063/5.0069107](https://doi.org/10.1063/5.0069107).
- [63] D. Utt, A. Stukowski, K. Albe, Grain boundary structure and mobility in high-entropy alloys: a comparative molecular dynamics study on a Σ 11 symmetrical tilt grain boundary in face-centered cubic CuNiCoFe, *Acta Mater.* 186 (2020) 11–19, doi:[10.1016/j.actamat.2019.12.031](https://doi.org/10.1016/j.actamat.2019.12.031).
- [64] P. Sathiyamoorthi, et al., Thermal stability and grain boundary strengthening in ultrafine-grained CoCrFeNi high entropy alloy composite, *Mater. Des.* 134 (2017) 426–433, doi:[10.1016/j.matdes.2017.08.053](https://doi.org/10.1016/j.matdes.2017.08.053).
- [65] N.D. Stepanov, et al., Mechanical properties of a new high entropy alloy with a duplex ultra-fine grained structure, *Mater. Sci. Eng. A* 728 (2018) 54–62, doi:[10.1016/j.msea.2018.04.118](https://doi.org/10.1016/j.msea.2018.04.118).
- [66] S. Praveen, et al., Exceptional resistance to grain growth in nanocrystalline CoCrFeNi high entropy alloy at high homologous temperatures, *J. Alloy. Compd.* 662 (2016) 361–367, doi:[10.1016/j.jallcom.2015.12.020](https://doi.org/10.1016/j.jallcom.2015.12.020).
- [67] L. Guo, et al., Effects of carbon on the microstructures and mechanical properties of FeCoCrNiMn high entropy alloys, *Mater. Sci. Eng. A* 746 (2019) 356–362, doi:[10.1016/j.msea.2019.01.050](https://doi.org/10.1016/j.msea.2019.01.050).
- [68] A. Bolshakov, G.M. Pharr, Influences of pileup on the measurement of mechanical properties by load and depth sensing indentation techniques, *J. Mater. Res.* 13 (4) (1998) 1049–1058, doi:[10.1557/JMR.1998.0146](https://doi.org/10.1557/JMR.1998.0146).
- [69] J.D. Gale, A. Achuthan, The effect of work-hardening and pile-up on nanoindentation measurements, *J. Mater. Sci.* 49 (14) (2014) 5066–5075, doi:[10.1007/s10853-014-8213-4](https://doi.org/10.1007/s10853-014-8213-4).
- [70] X. Huang, N. Hansen, N. Tsuji, Hardening by annealing and softening by deformation in nanostructured metals, *Science* 312 (5771) (2006) 249, doi:[10.1126/science.1124268](https://doi.org/10.1126/science.1124268).
- [71] D. Terada, H. Houda, N. Tsuji, Effect of strain on "hardening by annealing and softening by deformation" phenomena in ultra-fine grained aluminum, *J. Mater. Sci.* 43 (23–24) (2008) 7331–7337, doi:[10.1007/s10853-008-2809-5](https://doi.org/10.1007/s10853-008-2809-5).
- [72] R.W. Cahn, P. Haasen, *Physical metallurgy*, 4th, rev. and enhanced ed. 1996, Amsterdam: North Holland Elsevier Science B.V. ISBN: 9780080538945.
- [73] H. Shahmir, et al., Effect of annealing on mechanical properties of a nanocrystalline CoCrFeNiMn high-entropy alloy processed by high-pressure torsion, *Mater. Sci. Eng. A* 676 (2016) 294–303, doi:[10.1016/j.msea.2016.08.118](https://doi.org/10.1016/j.msea.2016.08.118).
- [74] M. Zehetbauer, Y.T. Zhu, *Bulk Nanostructured Materials*, Wiley Online Library, 2009 ISBN: 3527315241, doi:[10.1002/9783527626892](https://doi.org/10.1002/9783527626892).
- [75] Y. Zhou, et al., The effects of triple junctions and grain boundaries on hardness and Young's modulus in nanostructured Ni–P, *Scr. Mater.* 48 (6) (2003) 825–830, doi:[10.1016/S1359-6462\(02\)00511-0](https://doi.org/10.1016/S1359-6462(02)00511-0).
- [76] B. Gludovatz, E.P. George, R.O. Ritchie, Processing, microstructure and mechanical properties of the CrMnFeCoNi high-entropy alloy, *JOM* 67 (10) (2015) 2262–2270, doi:[10.1007/s11837-015-1589-z](https://doi.org/10.1007/s11837-015-1589-z).
- [77] H.M. Ledbetter, R.P. Reed, Elastic properties of metals and alloys, I. iron, nickel, and iron-nickel alloys, *J. Phys. Chem. Ref. Data* 2 (3) (1973) 531–618, doi:[10.1063/1.3253127](https://doi.org/10.1063/1.3253127).
- [78] W. Skrotzki, et al., Microstructure and texture evolution during severe plastic deformation of CrMnFeCoNi high-entropy alloy, in: *Proceedings of the IOP Conference Series: Materials Science and Engineering*, 194, 2017, doi:[10.1088/1757-899x/194/1/012028](https://doi.org/10.1088/1757-899x/194/1/012028).
- [79] W. Skrotzki, et al., Microstructure, texture, and strength development during high-pressure torsion of CrMnFeCoNi high-entropy alloy, *Crystals* 10 (4) (2020), doi:[10.3390/cryst10040336](https://doi.org/10.3390/cryst10040336).
- [80] V. Maier-Kiener, et al., Nanoindentation testing as a powerful screening tool for assessing phase stability of nanocrystalline high-entropy alloys, *Mater. Des.* 115 (2017) 479–485, doi:[10.1016/j.matdes.2016.11.055](https://doi.org/10.1016/j.matdes.2016.11.055).
- [81] W. Nix, H. Gao, Indentation size effects in crystalline materials: a law for strain gradient plasticity, *J. Mech. Phys. Solids* 46 (1998) 411–425.
- [82] Z. Sun, et al., Dynamic recovery in nanocrystalline Ni, *Acta Mater.* 91 (2015) 91–100, doi:[10.1016/j.actamat.2015.03.033](https://doi.org/10.1016/j.actamat.2015.03.033).
- [83] Z. Sun, et al., Grain size and alloying effects on dynamic recovery in nanocrystalline metals, *Acta Mater.* 119 (2016) 104–114, doi:[10.1016/j.actamat.2016.08.019](https://doi.org/10.1016/j.actamat.2016.08.019).
- [84] V. Maier-Kiener, et al., Influence of solid solution strengthening on the local mechanical properties of single crystal and ultrafine-grained binary Cu–AlX solid solutions, *J. Mater. Res.* 32 (24) (2017) 4583–4591, doi:[10.1557/jmr.2017.320](https://doi.org/10.1557/jmr.2017.320).
- [85] K. Durst, V. Maier, Dynamic nanoindentation testing for studying thermally activated processes from single to nanocrystalline metals, *Curr. Opin. Solid State Mater. Sci.* 19 (6) (2015) 340–353, doi:[10.1016/j.cossms.2015.02.001](https://doi.org/10.1016/j.cossms.2015.02.001).
- [86] Q. Wei, et al., Effect of nanocrystalline and ultrafine grain sizes on the strain rate sensitivity and activation volume: fcc versus bcc metals, *Mater. Sci. Eng. A* 381 (1–2) (2004) 71–79, doi:[10.1016/j.msea.2004.03.064](https://doi.org/10.1016/j.msea.2004.03.064).
- [87] X.S. Yang, et al., Time, stress, and temperature-dependent deformation in nanostructured copper: Stress relaxation tests and simulations, *Acta Mater.* 108 (2016) 252–263, doi:[10.1016/j.actamat.2016.02.021](https://doi.org/10.1016/j.actamat.2016.02.021).
- [88] M.A. Monclús, J.M. Molina-Aldareguia, High Temperature Nanomechanical Testing. In: Hsueh CH. et al. (eds) *Handbook of Mechanics of Materials*. Springer, Singapore. (2018) doi:[10.1007/978-981-10-6855-3_55-1](https://doi.org/10.1007/978-981-10-6855-3_55-1).
- [89] C. Minnert, K. Durst, Nanoindentation creep testing: advantages and limitations of the constant contact pressure method, *J. Mater. Res.* (2021), doi:[10.1557/s43578-021-00445-6](https://doi.org/10.1557/s43578-021-00445-6).
- [90] A.C. Fischer-Cripps, *Nanoindentation*, 3rd ed., Springer, New York, 2011 ISBN: 978-1-4419-9871-2.



DFG Deutsche
Forschungsgemeinschaft

German Research Foundation

SPP 2006 Compositionally Complex Alloys -
High Entropy Alloys (CCA - HEA)
